Chemostratigraphy of the Boolgeeda Iron Formation and Turee Creek Group, Hamersley Basin, Western Australia

by

Tyler J. Warchola

A thesis submitted in partial fulfillment of the requirements for the degree of

Master of Science

Department of Earth and Atmospheric Sciences
University of Alberta

Abstract

In the most general sense, the Great Oxygenation Event (GOE) refers to the transition from oxygen poor to oxygen rich conditions on ancient Earth (Holland, 2002; Holland, 2006). It has traditionally been defined as the sedimentary intervals in which the isotopic signature for mass independent fractionation of sulfur (MIF-S) disappears (Farquhar et al., 2000), which occurs above oxygen concentrations of 10^{-5} times present atmospheric levels (PAL; Pavlov and Kasting, 2002). In South Africa, this interval corresponds with the Pretoria Group in the Transvaal Basin; specifically, the lower Timeball Hill formation and upper Deutschland Formation (Bekker et al., 2001; Guo et al., 2009). The age for this event is constrained to approximately 2.32 Ga by Re/Os dating of pyrite within the Timeball Hill Formation (Bekker et al., 2001). However, Reinhard et al. (2013) suggested S isotopic signatures defining MIF-S are expected to be preserved for 10-100 million years after the GOE, as minerals hosting the MIF signature are cycled through terrestrial reservoirs and recycled during subduction and volcanic processes. The prospect of MIF-S recycling forces an investigation into the 100 Mya (or more) prior to 2.32 Ga, in hopes of identifying recycling signatures representative of the Reinhard et al. (2013) models, and highlighting proxies that record the initial rise in atmospheric O_2 which eventually eliminated the MIF-S signal. Recently, Philippot et al. (2018) reported a MIF-S recycling signature in the Boolgeeda Iron Formation (IF) and overlying Turee Creek Group (TCG) of Western Australia. These sediments are particularly relevant to those in the Transvaal Basin as they represent time equivalent deposits (2.45-2.209 Ga; Trendall et al., 2004 and Martin et al., 1998, respectively). If the rise of atmospheric O_2 was truly a global event, similar redox proxies should be prevalent in the sediments of both basins at similar stratigraphic intervals. The work presented in this thesis represents a search for O_2 proxies other than MIF-S, that are prevalent within the Boolgeeda IF and TCG. This search was focused around

major and trace element analyses, specifically Ce anomalies, Mn enriched intervals, and intervals portraying anomalous concentrations of redox sensitive trace elements. Results suggest the water column during Boolgeeda IF was persistently oxic in shallow environments, and anoxic and ferruginous in deep water sediments. Periodic weathering of continental and shallow marine sulfides may have also lead to temporary euxinic conditions in marine environments proximal to the continental margin. Thus, it would appear deposition of Boolgeeda and Turee Creek Group sediments occurred after the initial rise of atmospheric O_2, but before levels reached appreciable levels to completely suppress MIF-S recycling signatures. The data presented in this thesis, combined with existing data from time equivalent basins in South Africa and North America, will lead to a better understanding of O_2 dynamics during the early stages of the GOE and a more complete picture of the global rise of O_2 on early Earth.

Bekker, A., Kaufman, A.J., Karhu, J.A., Beukes, N.J., Swart, Q.D., Coetzee, L.L., Eriksson, K.A., 2001. Chemostratigraphy of the Paleoproterozoic Duitschland Formation, South Africa: implications for coupled climate change and carbon cycling. American Journal of Science 301, 261-285.

Farquhar, J., Bao, H., Thiemens, M., 2000. Atmospheric influence of Earth's earliest sulfur cycle. Science 289, 756-758.

Guo, Q., Strauss, H., Kaufman, A.J., Schröder, S., Gutzmer, J., Wing, B., Baker, M.A., Bekker, A., Jin, Q., Kim, S.-T., Farquhar, J., 2009. Reconstructing Earth's surface oxidation across the Archean-Proterozoic transition. Geology 37, 399-402.

Holland, H.D., 2002. Volcanic gases, black smokers, and the Great Oxidation Event. Geochimica et Cosmochimica Acta 66, 3811-3826.

Holland, H.D., 2006. The oxygenation of the atmosphere and oceans. Philosophical Transactions of the Royal Society B: Biological Sciences 361, 903-915.

Martin, D.McB., Li, Z.X., Nemchin, A.A., Powell, C.McA., 1998. A pre-2.2 Ga age for giant hematite ores of the Hamersley Province, Australia. Economic Geology 93, 1084-1090.

Pavlov, A.A., Kasting, J.F., 2002. Mass-independent fractionation of sulfur isotopes in Archean sediments: strong evidence for an anoxic Archean atmosphere. Astrobiology 2, 27-41.

Philippot, P., Ávila, J.N., Killingsworth, B.A., Tessalina, S., Baton, F., Caquineau, T., Muller, E., Pecoits, E., Cartigny, P., Lalonde, S.V., Ireland, T.R., Thomazo, C., van Kranendonk, M.J., Busigny, V., 2018. Globally asynchronous sulphur isotope signals require re-definition of the Great Oxidation Event. Nature Communications 9, 2245

Reinhard, C.T., Planavsky, N.J., Lyons, J.R., 2013. Long-term sedimentary recycling of rare sulphur isotope anomalies. Nature 497, 100-104.

Trendall, A.F., Compston, W., Nelson, D.R., De Laeter, J.R., Bennett, V.C., 2004. SHRIMP zircon ages constraining the depositional chronology of the Hamersley Group, Western Australia. Australian Journal of Earth Science 51, 621-644.

Preface

Research conducted for this thesis is the result of an international collaboration between Dr. Pascal Philippot at the Institut de physique du globe de Paris (IPGP), Paris, France (and later the Université de Montpellier, Montpellier, France), and Dr. Kurt Konhauser at the University of Alberta, Edmonton, Canada. One published journal article resulting from this work has been included in Chapter 2 of this thesis:

> Warchola, T., Lalonde, S.V., Pecoits, E., von Gunten, K., Robbins, L.J., Alessi, D.S., Philippot, P., Konhauser, K.O., 2018. Petrology and geochemistry of the Boolgeeda Iron Formation, Hamersley Basin, Western Australia. Precambrian Research 316, 155-173.

Each author made valuable contributions to article 1. All writing was completed by the first author, aside from contributions made by all co-authors during the editing stage. Petrographic images and trace element figures were all produced by the first author using Excel, Matlab, and Adobe Illustrator, with guidance provided by Dr. Stefan V. Lalonde. The bulk of the geochemical data collected from powder digestions was produced by ACTLABS, after initial powdering was completed and samples were sorted by Dr. Pascal Philippot, Dr. Ernesto Pecoits, Dr. Stefan Lalonde, and myself. Konstantin von Gunten performed bulk digestions and iron speciation sequential extraction analysis on a subset of samples. Initial interpretations and analyses of the research data were made by the first author, with subsequent critiques and suggestions provided by all co-authors. Funding for the project was provided by grants secured by Drs. Philippot, Konhauser, and Alessi. Specific funding sources were the UnivEarths Labex Programme at Sorbonne Paris Cité (ANR-10-LABX-0023 and ANR-11-IDEX-0005-02), the Programme National de Planétologie and the São Paulo Research Foundation (FAPESP, grant 2015/16235-2), and Natural Sciences and Engineering Research Council of Canada (NSERC) Discovery grants to

KOK (RGPIN – 165831) and DSA (RGPIN – 04134). The cores studied in the manuscript were collected by Dr. Philippot as part of the Turee Creek Drilling Project (TCDP) conducted in the Hamersley Basin, Western Australia, between April 2014 and June 2014.

Data collected, and figures produced for Chapters 3 and 4 of this thesis are not currently part of a submitted manuscript. This data may, however, be used in the production of future manuscripts on the topics of Mn enrichment in the TCDP cores and the possibility of magnetofossils in the Boolgeeda Iron Formation. I refer the reader to these chapters for more information.

For Mom and Dad.

"I know that I know nothing."
-Socrates

Acknowledgements

I would first like to acknowledge the mentorship provided by my co-supervisors, Dr. Kurt Konhauser and Dr. Daniel Alessi. I am thankful not only for the professional courtesy and patience they have shown me, but also the friendship we have developed over the duration of my Bachelor's and Master's theses. I would like to thank the Natural Sciences and Engineering Research Council of Canada (NSERC) for endowing me with a Canadian Graduate Scholarship (CGS-M), which provided the much-needed financial support to pursue my studies in full health and devote more time to my research. I would also like to acknowledge the funding sources that supported my Teaching Assistantship and summer salary in the months I was not on NSERC scholarship. This funding was provided by NSERC Discovery grants held by Drs. Kurt Konhauser (RGPIN – 165831) and Daniel Alessi (RGPIN – 04134), and supplemental funding was provided by the University of Alberta. The Métis Nation of Alberta, Aboriginal Students Society at the University of Alberta, and Rupertsland Institute deserve special recognition for the support they provided throughout my Bachelor's and Master's degree. I look forward to one day being able to repay them for their kindness.

I would like to thank Dr. Pascal Philippot for graciously providing all samples investigated in this thesis and for providing helpful comments during the preparation of the resulting manuscript. I would also like to thank Dr. Stefan Lalonde for the numerous discussions and lessons that helped to greatly improve this thesis. Thank you to Dr. Pilar Lecumberri-Sanchez for her help in completing petrography and aiding in identification of sulphide phases. I would also like to thank Dr. Murray Gingras for agreeing to read this oversized document and sit on my defense committee. Your wit and humour over beers and thoughtful input is always appreciated. Thank you to members of the Konhauser Lab, Jamie Robbins, Brendan Bishop, Kaarel Mänd, Marie

Table of Contents

List of Figures

List of Tables

Chapter 1: Introduction

1. Thesis outline

The Great Oxidation Event (GOE) has traditionally been defined by the sedimentary interval in which the isotopic signature for mass independent fractionation of sulfur (MIF-S) disappears. In South Africa, this interval corresponds with the Pretoria Group in the Transvaal Basin; specifically, the lower Timeball Hill Formation and upper Deutschland Formation (Bekker et al., 2001; Guo et al., 2009). The age for this event is constrained to approximately 2.32 Ga by Re/Os dating of pyrite within the Timeball Hill Formation (Bekker et al., 2001). However, Reinhard et al. (2013) suggested S isotopic signatures defining MIF-S are expected to be preserved for 10-100 million years after the GOE, as minerals hosting the MIF signature are cycled through terrestrial reservoirs and recycled during subduction and volcanic processes. The prospect of MIF-S recycling forces an investigation into the 100 Mya (or more) prior to 2.32 Ga, in hopes of identifying recycling signatures representative of the Reinhard et al. (2013) model and highlighting alternative proxies that record the initial rise in atmospheric O_2 which eventually eliminated the MIF-S signal.

Recently, Philippot et al. (2018) reported a MIF-S recycling signature in the Boolgeeda Iron Formation (IF) and overlying Turee Creek Group (TCG) of Western Australia. The TCG represents one of the few units in the world that shows evidence for continuous deposition across the GOE, and therefore, may provide a unique record of O_2 dynamics during the rise of atmospheric oxygen on Earth (Trendall and Blockley, 1970; Trendall, 1979; Thorne and Tyler, 1996). Moreover, the metamorphic grade of the TCG does not exceed the prehnite-pumpellyite-epidote facies, suggesting it has not experienced extensive metamorphism and is likely to preserve primary geochemical signatures (Smith et al., 1982). Boolgeeda and TCG sediments are

particularly relevant to those in the Transvaal Basin as they represent time equivalent deposits (2.45-2.209 Ga; Trendall et al., 2004 and Martin et al., 1998, respectively). If the rise of atmospheric O_2 was truly a global event, similar redox proxies should be prevalent in the sediments of both basins at similar stratigraphic intervals.

Previous analyses of the Turee Creek Group were carried out on outcrops that appear in the hinges of large-scale folds along the southern part of the Hamersley Range in Western Australia (e.g. Swanner et al., 2013; Williford et al., 2011). Recently, however, a drilling project was undertaken by the Institut De Physique Du Globe De Paris (IPGP) in Paris, France, to obtain three cores that span a large section of the Turee Creek. These cores were retrieved as a first attempt to gather a continuous rock record that spans the Great Oxidation Event (GOE) and contains multiple geochemical proxies that can be used as indicators of Archean and Paleoproterozoic atmospheric and oceanic conditions.

The three diamond drill cores obtained from the TCG for geochemical analyses are herein referred to as TCDP1, TCDP2, and TCDP3. They are broadly composed of eight different lithological units that record over 200 Ma of basin evolution. Depth profiles of transition metal concentrations were prepared with the aim of identifying stratigraphic intervals that indicate either subtle or more dramatic changes in redox conditions within the basin. The lithology in which the signatures are present, and their corresponding depositional environment, were used to extract a more detailed picture of the evolution of oxygen within the basin. Of the total ~4 km of sediment that comprises the TCG, approximately 454 m of core was recovered.

Prior to beginning geochemical analyses of core samples, a literature review was conducted to become familiar with information regarding the regional setting, inferred plate-tectonic regime, prior geochemical analyses, and age constraints for the deposition of the Hamersley Group and

Turee Creek Group sediments. Preexisting studies on the GOE and banded iron formations (BIF) were also reviewed to aid in the interpretation of geochemical data. The background information drawn from this literature review is summarized in section II below. The primary question stemming from background reading focused on the cessation of BIF deposition, coinciding with the termination of the Hamersley Group, and subsequent deposition of siliciclastic and glacial sediments comprising the TCG. As TCDP2 and TCDP3 cores lack BIF sediments, initial investigations were focused on TCDP1, which captures a transition from BIF to siliciclastic sediments. The deepest section of TCDP1 (the deepest core drilled) captures the top of the Boolgeeda BIF, which caps the underlying Hamersley Group. As BIF deposition depends on environmental conditions capable of preserving an extensive source of dissolved Fe^{2+}, BIF has traditionally been used as an indicator for low or absent atmospheric O_2. The Boolgeeda BIF layers within the Turee Creek Core, therefore, provided a logical first lithology in which we could assess the distribution and concentration of various transition elements, in hopes of developing a baseline for anoxic (or nearly anoxic) conditions.

From this baseline, trace element concentrations were investigated for enrichments and depletions relative to presumed background conditions. The ~80 m long TCDP1 core was sampled every meter, avoiding areas that appeared altered by secondary fluids. One-hundred and twenty-eight samples were then powdered and sent for major and trace element analyses at ACTLABS. Forty thin sections were also prepared and examined using reflected and transmitted light microscopy. Using the chemostratigraphic profiles produced from these analyses, environmental perturbations and relative fluxes in atmospheric or local oxygen concentration were inferred. The varied behavior of transition elements under anoxic to oxic conditions has been routinely used as a proxy for broadly tracking ancient oxygen levels. The oxidation state of seawater directly affects

the chemical speciation and solubility of transition metals, and as such, the concentration and distribution of trace metals should reflect local to global oxygen conditions at the time of deposition (e.g., Holland, 1984; Scott et al., 2008; Reinhard et al., 2013). The results of this work and a detailed description of the methods are presented and discussed in detail in Chapter 2 of this thesis, which represents a publication published in the peer reviewed journal *Precambrian Research*:

> Warchola, T., Lalonde, S.V., Pecoits, E., von Gunten, K., Robbins, L.J., Alessi, D.S., Philippot, P., Konhauser, K.O., 2018. Petrology and geochemistry of the Boolgeeda Iron Formation, Hamersley Basin, Western Australia. Precambrian Research 316, 155-173.

The chemostratigraphic study of TCDP1 highlighted the presence of manganese (Mn) enriched intervals, approaching 3 wt.% Mn, within the Boolgeeda IF. It was hypothesized that these Mn enrichments could be indicative of oxidizing conditions at the time of deposition during the onset of the GOE, given the high redox potential of Mn: Mn(II) is soluble, and to form MnO_2, a strong oxidant such as O_2 is required. An investigation and description of the Mn phases within TCDP1, TCDP2, and TCDP3 can be found in Chapter 3 of this thesis. These phases are compared to previously described sediments of similar age in South Africa in hopes of identifying correlatable Mn enrichments indicative of a global rise of atmospheric oxygen. Methods used to identify the phases and infer environmental conditions leading to their formation include X-ray fluorescence (XRF) mapping, scanning electron microscope (SEM) imaging, energy dispersive spectroscopy (EDS), XRF core logging calibrated by concentration data acquired from solution mode inductively coupled plasma – mass spectrometry (ICP-MS), X-ray absorption near edge structure (XANES) analyses, extended X-ray absorption fine structure (EXAFS) analyses, powder

X-ray diffraction (XRD), micro X-ray diffraction (μ-XRD), and election microprobe analyses (EPMA). Carbon (C) and molybdenum (Mo) isotopes from companion studies conducted on the same cores are also referenced to provide further context for the Mn enrichments. These methods will be expanded on in Chapter 3.

A fourth chapter was included in this thesis upon the discovery of a thin layer bearing semblance to modern microbial mats, within the Boolgeeda Iron Formation. This layer separates green mudstone below from banded iron formation above and displays distinct mineralogical and textural changes across its transect. Interestingly, this layer was found within a 2 m interval bearing a distinct magnetic anomaly (specifically, a low Verwey transition temperature), previously described in a companion study conducted on these same rocks (Carlut et al., 2015). Upon further investigation, nano-scale Fe-oxide grains were found in the middle of the "mat-like" structure, organized in a thin horizon. It is possible that these grains are biogenically produced magnetite corresponding to magnetosomes from ancient magnetotactic bacteria. If so, this discovery would represent the oldest record of magnetofossils found to date, and have profound implications for the depositional environment of BIF at 2.45 Ga. The observations and results pertaining to this topic are summarized in Chapter 4; however, conclusions remain speculative until further data can be collected.

The work presented in this thesis represents a search for O_2 proxies, other than MIF-S, that are prevalent within the Boolgeeda IF and TCG, in an attempt to better characterize marine conditions in the Paleoproterozoic. This search focused on major and trace element analyses, specifically Ce anomalies, Mn enriched intervals, and intervals portraying anomalous concentrations of redox sensitive trace elements. The goals of this research are as follows:

(1) Produce a chemostratigraphic dataset of all TCDP cores, with emphasis on TCDP1,

(2) Determine whether redox proxies indicative of oxic conditions at the time of deposition are present within the TCDP sediments,

(3) Assess whether sedimentological processes and/or variations in lithology influence the preservation of reliable redox proxies, and if so, to what degree,

(4) Determine if the Mn enrichments present within the TCDP cores represent primary Mn oxides indicative of highly oxidative conditions at the time of deposition,

(5) Attempt to tie any redox proxies found within the TCDP sediments to those found in other time equivalent deposits, specifically Mn enrichments in South Africa, and

(6) Explore the possibility of preserved magnetofossils in the Boolgeeda Iron Formation and consider implications for environmental conditions at this time.

We hypothesize that redox proxies may indicate oxic conditions at the time of TCDP sediments, despite a conflicting S isotope record, as a result of S-MIF recycling up to 100 Ma after the initial rise of atmospheric O_2 (Reinhard et al., 2013; Philippot et al., 2018). Results from this work will lead to a better understanding of the distribution of oxygen within a basin during the initial phases of the GOE, how the interpretation of oxygen levels based on transition element concentrations are influenced by sedimentological processes and sample lithology, and address the possibility of Mn enrichments being present in time equivalent sediments from around the world, suggesting global fluctuations in O_2 concentrations. They may also lead to the identification of the oldest robust record of magnetofossils found to date.

2. Background Information

2.1. The Great Oxidation Event (GOE)

The Great Oxidation Event (GOE) refers to the period in the Palaeoproterozoic Eon when oxygen levels rose above 0.001% of present atmospheric level (PAL) for the first time in Earth's history. The exact timing of the GOE is critical as it provides a minimum boundary for the evolution of oxygenic photosynthesis. Organisms capable of oxygenic photosynthesis are thought to have evolved sometime before 2.7 Ga (Summons et al., 2006; Buick, 2008; Waldbauer et al., 2009). Oxygen produced by bacteria slowly transformed the chemistry of the oceans and the atmosphere until the reservoirs of reduced gases, hydrothermal fluids, and minerals were sufficiently oxidized to allow the buildup of oxygen (Catling and Claire, 2005). The first geological arguments for a rise of oxygen were made by MacGregor (1927), and subsequent studies have constrained the timing of this global rise in atmospheric oxygen to a period between ~2.45 and ~2.32 Ga. The disappearance of mass-independent fractionation of sulfur isotopes between 2.45 and 2.32 Ga is commonly held as the most unequivocal evidence for a permanent change in the redox state of Earth's atmosphere (Farquhar et al., 2000). Other lines of geological evidence for the GOE include the first occurrences of "red beds" (Chandler, 1980; Melezhik et al., 2005), copper deposits (Kirkham and Roscoe, 1993), iron rich paleosols (Rye and Holland, 1998), sulfate evaporates (Schroder et al., 2008; Pope and Grotzinger, 2003; Grotzinger and Kasting, 1993), and the presence of extensive manganese deposits, phosphorites, and glauconite following the GOE (Holland, 2005; Melezhik et al., 2005; Wood, 1973). Further, well-rounded detrital pyrite, uraninite, and siderite grains are only found in clastic deposits before the GOE because these grains are unstable under oxic conditions (Rasmussen and Buick, 1999; Roscoe, 1996; England et al., 2002; Hofmann et al., 2009). Recent examinations of the inventories and isotopic fractionations of redox sensitive trace

elements suggest the initial appearance of oxygenic photosynthesis at ~3.0 Ga (Crowe et al., 2013, Planavsky et al., 2014), while compilations of temporal records for redox sensitive trace elements (e.g., Cr, U) have led to the realization that the onset of the GOE likely began as early as ~2.48 Ga (Konhauser et al., 2011; Partin et al., 2013a, Partin et al., 2013b). Although earlier studies provided a great deal of information regarding the GOE, more recent works have shown that there remain many poorly-understood subtleties regarding the progressive oxygenation of Earth.

2.2. Banded Iron Formations

Banded iron formations (BIF) are marine sedimentary rocks composed of iron oxides, silica (most commonly chert), Fe-carbonates (siderite and ankerite), and Fe-silicates. The precursor phases for BIF sediments are commonly held to be ferric oxyhydroxides, such as ferric hydroxide ($Fe(OH)_3$; see Konhauser et al., 2017 for review), but recently, ferrous iron silicates, such as greenalite, have also been proposed (Rasmussen et al., 2014; Rasmussen et al., 2016; Rasmussen et al., 2017; Tosca et al., 2016). Two types of BIF can be distinguished based on their lateral extent, relationship with volcanic rocks, and tectonic and depositional settings (Gross, 1980; Gross, 1983): Algoma and Superior type BIF. Algoma BIF are characterized by their close association with volcanic rocks and hydrothermal vents, while Superior BIF are more commonly associated with deposition on shallow continental shelf type settings. Both types of BIF are restricted to the Precambrian, with the majority of deposits occurring before 1.8 Ga and reappearing briefly around 700 million years ago (e.g., Bekker et al., 2010).

The presence of BIF in the Precambrian rock record is indicative of high concentrations of dissolved ferrous iron (Fe(II)) in seawater at that time, a condition that is not possible in modern oceans as high concentrations of Fe(II) cannot be maintained in oxygenated water at circumneutral pH. Dissolved Fe(II) can react with oxygen or dissolved sulfide to form insoluble minerals. The

amount of iron required to form extensive Superior type BIF deposits, like those of the Archean and Palaeoproterozoic, demands that the rate of delivery of Fe(II) to the ancient oceans be much higher than the rate of delivery for oxygen, in order to maintain ferruginous seawater over large areas. Furthermore, sulfide concentrations must have remained lower than Fe(II) concentrations, as the widespread precipitation of Fe-sulfide minerals is mineralogically incompatible with BIF deposition (Farquhar et al., 2011). The deposition of Superior type BIF is, therefore, a strong indicator for anoxic conditions on early Earth.

There is a commonly held conception that BIF sediments record contemporary ocean chemistry due to the high surface reactivity of ferric oxyhydroxide particles, as supported by the comparative rare-earth element (REE) signatures between BIF and modern seawater (e.g. Bau and Dulski, 1996; Bau and Dulski, 1999; Alexander et al., 2008). In other words, as the ferric hydroxide particles formed in the ancient water column, they sorbed the trace metals which were present, and in predictable quantities. Therefore, BIF geochemical analyses have been used to reconstruct temporal trends in trace element concentrations throughout Earth history. For instance, it has been shown that the nickel (Ni) content in BIF has changed dramatically over time, driven by a decrease in oceanic Ni availability around 2.7 billion years ago that likely had profound consequences for methane-producing bacteria. These bacteria, called methanogens, have a unique Ni requirement for their methane-producing enzymes. Crucially, methanogens have been implicated in controlling oxygen levels on the ancient Earth as the methane they produce would have reacted with oxygen, keeping atmospheric oxygen levels low. It is possible that a Ni famine led to a cascade of events, beginning with reduced methane production, the expansion of previously marginalized cyanobacteria into shallow-water settings, and culminating with increased oxygenic photosynthesis that tipped the atmospheric balance in favour of oxygen, resulting in the GOE at

ca. 2.5 Ga (Konhauser et al., 2009). Therefore, the ability of BIF to record contemporary trace element signatures make them ideal deposits for analyzing the rise of atmospheric oxygen during the GOE.

2.3. Stratigraphy and Lithology of Western Australia during the Neoarchean-Paleoproterozoic

Prior to deposition of the Hamersley and Turee Creek Groups, the Pilbara Craton was primarily composed of igneous volcanic rocks known as the Pilbara Supergroup. These volcanic rocks can be separated into three distinct stratigraphic units called the Warrawoona, Gorge Creek, and Whim Creek Groups (Hickman, 1983). The 3500 to 3450 Ma Warrawoona Group comprises basalt with minor components of komatiite, dacitic and rhyolitic tuff, agglomerate, and sedimentary rocks (Hickman 1983, Thorpe et al., 1992). The Warrawoona is generally metamorphosed to greenschist facies and contains depositional features characteristic of sedimentary supra- and intertidal facies, including evaporites and stromatolites (Lowe, 1980; Walter et al., 1980). These facies contain fossil cyanobacteria which provide some of the oldest evidence of life on Earth (Awramik et al., 1983; Schopf and Packer, 1987). The Gorge Creek Group overlies the Warrawoona Group, and was deposited between 3300 and 3000 Ma. It is composed of sandstone, minor conglomerate, BIF, and basalt. The Whim Creek Group unconformably overlies the Gorge Creek Group in the west. It is 2950 Ma and composed of basalt and dacite, volcaniclastics, and terrigenous sedimentary rocks. The Whim Creek Group may have developed as a rift structure between strike-slip faults (Barley, 1987; Krapež and Barley, 1987).

The Hamersley Basin developed as a southward-facing rift margin during a WNW-ESE crustal extension that affected the Pilbara Craton during the Mesoarchean (Blake and Barley, 1992). This crustal extension occurred at approximately 2800 Ma and led to the accumulation of

over nine kilometers of sediment by 2200 Ma. Most of these deposits can be classified as the Mount Bruce Supergroup. Sediments of the Mount Bruce Supergroup, which consists of three conformable rock units called the Fortescue, Hamersley, and Turee Creek groups (Trendall, 1979), represent some of most well studied successions with regards to stratigraphic, trace element, and isotopic investigations, and as such, they provide clues regarding the timing of the rise of oxygen. The interval over which the Mount Bruce Supergroup was deposited (~2800 to 2200 Ma) marks one of the most critical periods in Earth history, and contains appreciable evidence for the timing and dynamics of the Great Oxidation Event (GOE).

2.3.1 Fortescue Group

The Fortescue Group was deposited between 2765 and 2687 Ma and consists of basaltic lava and pyroclastic rocks. Smaller amounts of silicic volcanic rocks and non-volcanogenic sedimentary rocks are also present (Arndt et al., 1991; Blake, 1993; Thorne and Trendall, 2001). Units that compose the youngest sections of the Fortescue include the Tumbiana and the Jeerinah formations.

The Tumbiana Formation was deposited at 2724±5 Ma, as indicated by zircon U-Pb dating (Blake et al., 2004), in either a shallow marine or lacustrine environment associated with influx of riverine freshwater derived from the continents (Buick, 1992; Thorne and Trendall, 2001; Bolhar and Van Kranendonk, 2007). It records the Fortescue negative carbon isotope excursion, which is one of the most negative $\delta^{13}C$ signatures preserved in the rock record. This excursion is thought to have occurred as an effect of either condensation of nonbiological organic matter originating from photochemical reactions in the atmosphere when the CH_4/CO_2 ratio reached values >1 (i.e., an "organic haze" as per Pavlov et al., 2001), or is caused by an increased burial of methanotrophic derived biomass (Hayes, 1994; Boetius et al., 2000; Hinrichs, 2002). Thomazo et al. (2009)

performed carbon and sulfur isotope analyses on 41 samples collected from stromatolites, siltstones, laminated mudstones, and homogeneous mudstones, and found $\delta^{13}C$ values ranging from -55‰ to -20‰ (Figure 1.2). This data appeared to display a bimodal distribution, with peaks at -44‰ and -34‰, which was interpreted to reflect variations in the contribution of methanotrophic metabolism to the biomass. Sulfur isotopic values in the same study were found to have $\delta^{34}S$ values that varied from -5.73 to 2.75‰, and $\Delta^{33}S$ values which ranged between -0.25 to 1.64‰ (Figure 1.2). The authors used these values to suggest that sulfate concentrations were low, or the rate of sulfate reduction by sulfate reducing bacteria (SRB) was greater than the rate of sulfate supplied, which pushes $\delta^{34}S$ fractionation towards zero. The $\Delta^{33}S$ values correspond to dampened Mesoarchean sulfur MIF signals, representative of the early stages of oxygen level increase. The authors also note a slight correlation between sulfide mass independent fractionation (MIF-S) and low $\delta^{13}C$ values which they suggest argues for a causal link between methanotrophic activity and the preservation of MIF-S anomalies in the rock record. This may support the conclusions that a methanogenic and/or methanotropic famine may have spurred the rise in global oxygen levels (e.g. Konhauser et al., 2009), as less negative $\delta^{13}C$ values are found in younger Hamersley Basin sediments that do not preserve the MIF-S signal.

Kakegawa and Nanri (2006) performed carbon and sulfur isotope analyses on organic matter and pyrite in stromatolites, cherts, and sandstones of the Jeerinah Formation (~2690-2630 Ma). They used these analyses to determine which microorganisms were active in Precambrian stromatolite formations. The organic matter was interpreted to be synsedimentary based on its finely laminated nature and concordance to sedimentary bedding. $\delta^{13}C$ values of organic matter ranged from -39.7‰ to -27.1‰, which the authors used to suggest that microorganisms capable of photosynthesis were active around stromatolites, in addition to methanotrophic microorganisms.

However, $\delta^{13}C$ values for purple sulfur bacteria (anaerobic photosynthetic *Proteobacteria*) range from approximately -27‰ to -38‰ (Figure 1.3). These bacteria use hydrogen sulfide as opposed to water as the reducing agent in their metabolism and are typically found in stagnant water. It is possible that the signature $\delta^{13}C$ values recorded by Kakegawa and Nanri (2006) indicate the presence of purple sulfur bacteria versus a mixture of methanotrophic and aerobic photosynthetic bacteria. This study also analyzed fine-grained, microscopic pyrite crystals that occurred predominantly inside of the stromatolites. The $\delta^{34}S$ values of the pyrite ranged from -2.5‰ to +5.6‰, suggesting that pyrite formed by either abiotic or biotic sulfate reduction in the stromatolites. The authors also used the heterogeneity of sulfur isotopes within the samples to further support the conclusion that sulfate reduction processes were responsible for pyrite formation (Trudinger and Chamber, 1985; Ohmoto and Goldhaber, 1997). The decrease in $\delta^{13}C$ values could suggest that microbes other than methanogens and methanotrophs began to dominate marine ecosystems by the end of Fortescue deposition. The relatively low range of $\delta^{34}S$ values may even suggest that if SRB were indeed present, they were not abundant in the Archean.

2.3.2 Hamersley Group

Sulfur isotopes of the Jeerinah Formation, as well as the overlying Carawine Dolomite (~2600 Ma), and Mount McRae Shale (~2500 Ma) of the Hamersley Group, were investigated by Ono et al. (2003). The Hamersley Group, which overlies the Fortescue Group, is thought to have been deposited in shallow marine conditions on either the margin of a subdued continent from which there was no significant drainage, or an isolated submerged plateau. It is a finely stratified sequence of BIF, shale, chert, dolomite, and tuff, 2.5 km thick, and contains numerous sills of dolerite and a giant sill of rhyolite (Myers, 1993). Sulfide sulfur isotope analyses of the Jeerinah Formation

yielded $\Delta^{33}S$ values of -0.1 to +8.1‰, over a 50 m section of core, while pyrite analyses of

Carawine Dolomite yielded a broad range in $\delta^{34}S$ (+3.2 to 16.2‰), but a relatively small variation

and negative values in $\Delta^{33}S$ (-2.5 to -1.1‰). The large variation of $\delta^{34}S$ (+3.2 to +16.2‰) and

negative $\Delta^{33}S$ (-2.5 to -0.4‰) of pyrite sulfur in the Carawine Dolomite is attributed to SRB

activity, as this process is expected to produce pyrite with variable $\delta^{34}S$ and negative $\Delta^{33}S$ inherited

from seawater sulfate. Relatively high $\delta^{34}S$ has been used to indicate sulfate reduction in a closed

system with respect to seawater sulfate (Ohmoto, 1992). In the lower Mount McRae Shale, $\Delta^{33}S$

values shift from -1.9 to +6.9‰ over a 22-m section of core. To explain this observation, Ono et

al. (2003) invoked a model in which three distinct sulfur reservoirs were mixed to produce the

observed signatures. These three reservoirs are elemental sulfur produced in the atmosphere (S_8),

sulfuric acid (H_2SO_4) produced in the atmosphere, and seawater sulfate (SO_4; Figure 1.4).

Ono et al. (2003) suggested Archean atmospheric photochemical reactions of volcanic SO_2

partitioned sulfur isotopes such that SO_4 had negative values for $\delta^{34}S$ and $\Delta^{33}S$, while S_8 had

positive values for $\Delta^{33}S$ and $\delta^{34}S$. Bacterial sulfate reduction could have operated as early as 3400

Ma and may have modified atmospheric sulfur isotope fractionations, once the signature was

deposited in a marine setting. Bacterial sulfate reduction and subsequent precipitation of

sedimentary pyrite could have been the main sink for seawater sulfate by the late Archean. SRB

can fractionate $\delta^{34}S$ up to ~50‰ with respect to sulfate (Ohmoto and Goldhaber, 1997; Canfield,

2001). Thus, bacterial reduction of seawater sulfate produces sulfide depleted in [34]S, and the

remaining sulfate becomes enriched in [34]S. Because the isotope fractionation is mass-dependent,

$\Delta^{33}S$ of seawater remains negative, and the MIF-S signal is preserved. The increasing range of $\delta^{34}S$

values from the Jeerinah Formation to the Mount McRae Shale may suggest sulfate reducing

bacteria are becoming more prominent and imparting a stronger S fractionation on the sulfides

they produce, or that sulfate concentrations in marine environments is increasing to the point where it is no longer limiting sulfate reduction and the δ^{34}S signal is beginning to be preserved.

Baur et al. (1985) analyzed several drill cores from the Hamersley Group for evidence of short-range variations in the isotopic compositions of the carbonates. Carbon and oxygen isotope compositions of individual microbands ranged from -2.8 to -19.8‰ and from 10.2 to 20.8‰, respectively, for a set of 32 adjacent microbands within the Marra Mamba Iron Formation (~2593-2590 Ma). The average isotopic contrast between adjacent microbands is 3‰ for carbon and 3.1‰ for oxygen. Isotopically light carbon and oxygen were found to correlate with increased concentrations of iron. This is reflected by the fact that carbonates in BIF were depleted in ^{13}C, whereas those in the Wittenoom Dolomite had δ^{13}C values near zero. Also, the Mara Mamba Iron Formation almost completely lacks hematite, and instead has Fe present as magnetite, ankerite, or fibrous silicate. Carbon isotope lightness increased significantly with increasing magnetite iron and was weakly anti-correlated with ankerite iron. The authors invoked a biological origin of the C signature to justify the correlated variations in ^{13}C and Fe. It is suggested that ^{13}C-depleted carbonates may derive either from fermentative metabolism or from anaerobic respiration, such as dissimilatory Fe(III) reduction (DIR).

Carbon and oxygen isotopes in the Dales Gorge Member of the Brockman Iron Formation, and in the Wittenoom Dolomite where also investigated by Becker and Clayton (1972, 1976; respectively). Iron formation carbonates had δ^{13}C values of -9 to -11‰ while the dolomitic limestones had δ^{13}C values of +2 to -2‰ (Figure 1.5). In both formations, the range of isotopic values for different carbonates was found to be similar and there was no uniform relationship found between δ^{13}C values in coexisting carbonates. In the 1976 study, the authors noted that the oxygen isotopes within the Dales Gorge had undergone isotopic exchange between minerals at

temperatures above 270˚C, and probably less than 310˚C, during burial metamorphism. It appeared that quartz and carbonate had completely equilibrated, while hematite had apparently undergone negligible change. Interestingly, the Mount Bruce Supergroup was interpreted to have been deposited between 2200 and 2000 Ma, based on rubidium-strontium ages for interlayered volcanics (Compston and Arriens, 1968). This age corresponds to the Opthalmian orogenesis, as suggested by Rasmussen et al. (2005). It is possible that the regional heating, folding, and thrusting, as well as extensive fluid flow associated with the Opthalmian fold-and-thrust belt, may have homogenized the isotopic signatures of the carbonates. Becker and Clayton (1972, 1976) concluded that IF was precipitated in a basin isolated from the ocean, that organic activity may have played a significant role in the genesis of the IF, and that the dolomitic limestones were deposited during transgression of the ocean. However, these interpretations must be re-evaluated if the implications of the Opthalmian orogeny on carbon and oxygen isotopic signatures are considered. A diagenetic origin would help to explain apparent similarity of isotopic signatures between the Duck Creek Dolomite and the Wittenoom Dolomite, which are two stratigraphically separate units.

The Dales Gorge BIF of the Brockman Iron Formation was also investigated by Pecoits et al. (2009). Pecoits et al. (2009) interpreted two decoupled sources for the BIF and shale macrobands found within the Dales Gorge. BIF bands are presumed to have formed from hydrothermal solutions while the shale bands appeared to be sourced from mafic source rock weathering. The alternation of BIF and shale macrobands was interpreted to result from competing clastic and chemical sedimentation. Further, the source of clastic sediments was reported to be mafic, perhaps representing the Fortescue basalts. The competing detrital and chemical sources of sediments mimics observations made for the Boolgeeda Iron Formation studied in this thesis.

The upper BIF unit of the Brockman Iron Formation, the Joffre BIF, was investigated by Haugaard et al. (2016). The Joffre Member is the largest BIF in the world, by volume. Unlike the Dales Gorge BIF, these authors suggested there was no evidence for epiclastic material sourced from the continents with the Joffre BIF. However, they did report evidence for volcanogenically sourced detrital material of felsic composition. Fe isotopes (δ^{56}Fe) ranged between +0.04‰ and +1.21‰, averaging +0.46‰. Notably, evidence for elevated levels of redox sensitive trace metals were not found in the Joffre BIF which was interpreted to reflect a lack of oxidative continental weathering. The lack of detrital sediments may also speak to the depth of the depositional environment for the Joffre Member.

The Weeli Wolli Formation of the Hamersley Group remains understudied to date, aside from an investigation into the varve cycles contained within the unit (Trendall, 1973). The Weeli Wolli Formation is approximately 450 m thick, containing ~150 m of iron-formation. The rest of the formation is predominantly dolerite sills. Microbands within the Weeli Wolli Formation display textures similar to those found in the Boolgeeda Iron Formation studied in this thesis. (Figure 3 of Trendall, 1973). To date, no geochemical profiles have been produced though the Weeli Wolli formation.

Sulfur isotope signatures were analyzed in pyrites from a diamictite layer located within the Boolgeeda Iron Formation by Swanner et al. (2013). This horizon has recently been correlated with a similar diamictite horizon found within a pristine drill core (TCDP1) of the Boolgeeda iron formation (Philippot et al., 2018). Results of Swanner et al. (2013) yield a range of Δ^{33}S spanning -0.44 to +6.27‰, suggesting the preservation of a S-MIF signature in the diamictite. Further, they noted the presence of rounded grains of detrital pyrite. Swanner et al. (2013) suggested their results were consistent with deposition under low atmospheric oxygen conditions. Philippot et al. (2018),

on the other hand, suggested the persistent, monotonous, low-amplitude Δ^{33}S signatures recorded throughout the Boolgeeda Iron Formatiion and overlying Turee Creek Group sediments was better attributed to a prolonged MIF-S weathering signatures, congruent with the models of Reinhard et al. (2013).

2.3.3 Turee Creek Group

The Turee Creek Group represents the youngest group within the Mount Bruce Supergroup, and conformably overlies the Boolgeeda Iron Formation of the Hamersley Group along the southern margin of the Pilbara Craton. It is mainly composed of mudstone, siltstone, and immature sandstone (Trendall, 1990). The Turee Creek Group has a total thickness of approximately 3-4 km and is bound by the underlying conformable Boolgeeda IF, and the overlying Wyoloo Group. The contact between the Boolgeeda and the Turee Creek is marked by a change from jaspilitic chert to dark green shale with glaciogenic dropstones (Van Kranendonk et al., 2015). More specifically, a 15 cm "transitional chert" unit conformably overlies the Boolgeeda Iron Formation and comprises thin beds of IF that grade into jaspilitic chert and then into layered grey and jaspilitic chert. This is conformably overlain by a green, pyritic mudstone containing dropstones that represent clastic, glaciomarine deposition (Van Kranendonk et al., 2015). Although many structural events are presumed to have affected the Pilbara craton over the past 2600 Ma, metamorphism within the Turee Creek does not exceed prehnite-pumpellyite-epidote facies (Smith et al., 1982). A low grade metamorphic event (approximately 200-300˚C) is predicted to have affected the Turee Creek Group between ca. 2215 and ca. 2145 Ma. Evidence for this event is provided by monazite and xenotime U-Pb geochronology and may relate to the Opthalmian Orogeny (Rasmussen et al., 2005).

Krapež (1996) developed a sequence stratigraphic interpretation for the Turee Creek Group that consists of five depositional sequences. He also identified fourteen lithofacies assemblages, including offshore, prodelta, delta-front, delta platform, delta plain, and laterally equivalent assemblages of offshore, slope, shelf, and supratidal-intertidal facies tracts of a siliciclastic-carbonate depositional system. He interpreted the basin as an active foredeep, deepening to the north-northeast in advance of a thrust-fold belt system actively approaching from the south-southwest. Horwitz (1982, 1987), Powell and Horwitz (1994), Krapež (1996), Martin (1999), and Martin et al. (2000) also interpreted the Turee Creek Group to have been deposited in a developing foreland basin. They hypothesized this basin was the result of the Capricorn orogeny. Recently, however, Van Kranendonk et al. (2015) proposed a new model in which the Turee Creek represents a northwesterly prograding sedimentary wedge, sourcing material from the southeast and progressively filling up the Turee Creek Basin from the southeast to the northwest. This interpretation is based on paleocurrent data and lithostratigraphic variations across the outcrop that indicate a paleo-shoreline that was oriented ENE-WSW, and a lack of evidence for seismites, internal unconformities, or thrusting, which are typical features of a foredeep basin.

The Turee Creek Group is composed of three major units: the lower Kungarra Formation (which contains the Meteorite Bore Member, MBM), the middle Koolbye Formation, and the upper Kazput Formation (Trendall, 1981; Thorne and Tyler, 1996). The Kungarra Formation represents an overall shallowing-upward succession, with an interpreted sediment source to the southeast (Van Kranendonk et al., 2015). It consists of approximately 1600 m of predominantly fine-grained sandstone, siltstone, and mudstone, in addition to coarse glaciogenic diamictites and other minor lithologies (Van Kranendonk and Mazumder, 2015). The lowest part of the Kungarra Formation comprises relatively deep-water facies formed in an offshore setting below storm wave

base, and includes green-weathered grey shale, thin units of millimetre-bedded grey and jaspilitic chert, and interbedded fine-grained sandstone, siltstone, and mudstone (Van Kranendonk et al., 2015). Krapež (1996) and Martin et al. (2000) interpreted the basal unit of the Kungarra Formation to represent the distal end of a delta. Carbon isotopes of the lower Kungarra Formation were investigated by Lindsay and Brasier (2002). They initially published the paper as a study on the upper Kazput carbonates, but the section has since been reassigned to the lower Kungarra Formation. The $\delta^{13}C$ values in this study appear to sawtooth throughout the section, between values of -6 and +2‰. Covariance in $\delta^{13}C_{carb}/\delta^{18}O_{carb}$ cross-plots have been successfully used as an indicator of diagenetic alteration (Brand and Veizer, 1980; Derry et al., 1992; Lindsay and Brasier, 2000). In general, the cross-plots show that most samples cluster tightly around mean $\delta^{13}C_{carb}$ values and cross correlation is not significant. Stratigraphic field relationships and detailed petrology both suggest most of these Kungarra carbonates formed during diagenesis, and the significant C-isotopic variation recorded in these rocks confirms this interpretation. It is noted that $\delta^{13}C$ values of -6‰ are unusual for carbonates of any age and commonly reflect the incorporation of isotopically light carbon into diagentic carbonates precipitated within sediments (Irwin et al., 1977). The Opthalmian orogeny may be responsible for the diagenesis of the Kungarra Formation, as suggested for the lower Hamersley earlier.

The Meteorite Bore Member (MBM) is interpreted to represent an ancient glacial deposit. This is based on the recognition of striated and faceted boulders near the type locality in the Hardey Syncline (Trendall, 1976; 1981). Also, the bending, penetration, and disruption of fine-scale bedding at the base of large clasts suggests vertical emplacement of ice rafted debris or dropstones. The stratal onlap of clasts by overlying, fine-grained sedimentary rocks further support the dropstone theory (Martin, 1999). Van Kranendonk et al. (2015) and Van Kranendonk and

Mazumder (2015) describe two glacio-eustatic cycles within the Kungarra, defined by falling stage system tracts bracketing diamictite deposits. A recent pyrite Re-Os age and a detrital zircon U-Pb age obtained from drill core samples at the base of the MBM glacial deposit have constrained the age of the oldest glacial event to 2309.0 ± 9.2 Ma and 2340 ± 22 Ma, respectively (Caquineau et al., 2018).

Williford et al. (2011) reported *in situ* multiple sulfur isotope and elemental abundance measurements of sedimentary pyrite at high spatial resolution, as well as the occurrence of detrital pyrite in the MBM. They identified three types of pyrite present within the MBM: (1) authigenic pyrite formed in place as a result of early diagenetic sulfate reduction, (2) detrital pyrite weathered out of older rocks, transported, abraded, and deposited in sedimentary successions, and (3) secondary pyrite resulting from fluid interactions during metamorphism or late diagenesis. Many of the pyrite grains within the MBM were shown to have hydrothermal overgrowths, where the darker cores of grains had δ^{34}S values less than -20‰, and the rims had significantly higher values. The negative δ^{34}S values of the cores suggests a microbial sulfate reduction origin (Machel et al., 1995), while the higher δ^{34}S values and minor element enrichments of >0.5 wt. % (e.g., Co, Ni, As) supports a hydrothermal source for the rims (Ohmoto and Goldhaber, 1997; Ballantyne and Moore, 1988). Using the Ni/Co ratio as a proxy for hydrothermal pyrites, the authors observed that pyrite grains with Ni/Co ratios <0.87 (hydrothermal) had δ^{34}S values from 0 to 6.5‰, whereas those with higher Ni/Co ratios had δ^{34}S values from -37 to 12.8‰. This again supports the hydrothermal origin for the rims and sulfate reducing origin for the cores of the pyrite grains. Williford et al. (2011) invoked microbial sulfate reduction under non-sulfate limiting conditions to explain the 90‰ range in δ^{34}S observed, and proposed that this suggests significant oxidative weathering of sulfides on the continents. Using all evidence gathered, the authors suggested the

MBM was deposited during the final stages of the GOE when pO_2 was high enough to oxidatively weather continental sulfides, but pO_2 remained low enough to preserve the MIF-S signal. In reviewing the data, it is possible that some of the $\Delta^{33}S$ values for detrital grains within the MBM reflect isotopic signatures from deposits much older that the Kungarra Formation. As the MBM is a glacial deposit, older grains preserving the MIF-S signature may have been weathered and transported within a glacier and deposited as the MBM. Although detrital pyrite grains are not typically stable under oxic conditions, studies have shown that they can be preserved in sediments deposited in cold environments where chemical weathering rates are suppressed (Khim and Yoon, 2003). Support for this theory can be found when looking at the distinct differences in $\Delta^{33}S$ values that exist between pyrite grains the authors have identified as authigenic and detrital. The authigenic grains have a significantly narrower range of values than that detrital grains, which suggests relatively oxic authigenic conditions compared to conditions during the formation of detrital grains (Figure 1.6).

The Koolbye Formation is a coastal-fluvial succession conformably overlying the Kungarra Formation (Van Kranendonk et al., 2015). It was interpreted by Mazumder et al. (2015) to represent shallow-marine to beach-aeolian to fluvial sedimentation. It is approximately 100 m thick (based on its type section in the Hardey Syncline) and dominantly composed of medium to fine-grained sandstones (Mazumder et al., 2015). The Koolbye Formation can be broken into four sandstone packages that transition from tidal deposits at the bottom, to beach deposits reworked by aeolian processes in the middle, to fluvial deposits at the top (Mazumder et al., 2015). The general shallowing upwards package recorded by the Koolbye Formation suggests a relative sea level fall throughout its deposition (Posamantier et al., 1988; Posamantier and James, 1993; Catuneanu, 2006; Mazumder et al., 2015). Given that the Koolbye Formation overlies a significant

glacial deposit, represented by the MBM, the shallowing upward package may suggest the beginning of another glacial cycle or local base level uplift due to isostatic rebound. Either global sea-levels were drawn down as water was stored in freshwater glaciers on land, or the massive load removed from the sediment as the glacier retreated allowed for local uplift. Given the lack of a glacial deposit above the Koolbye Formation, preference is given to the latter interpretation.

The Kazput Formation is composed of siltstone, sandstone, conglomerate, grey recrystallized dolomite, and thin beds of IF (Thorne and Tyler, 1996), and is proposed to have been deposited in shallow marine and fluvial settings (Martin et al., 2000). It is approximately 750 m thick and can be divided into three units, which represent a lower dolomite siltstone unit, a middle coarsening-upward arenaceous sandstone unit, and an upper siltstone and fine-grained sandstone unit (Martin et al., 2000). Carbonates within the Kazput Formation represent subtidal stromatolites, grainstones, and micrites proposed to have been deposited on a mixed carbonate-siliciclastic shelf (Martindale et al., 2015). In general, the Kazput Formation represents a movement to deeper water facies relative to the dominantly fluvial Koolbye Formation.

Martindale et al. (2015) looked at carbon isotopes from the Kungarra and Kazput carbonates. They observed a sawtooth δ^{13}C pattern in the Kungarra carbonates, similar to Lindsay and Brasier (2002). The δ^{13}C values varied from -6.15 to -1.61‰ and showed minimal trends, which they used to support a diagenetic origin. The Kazput carbonates they investigated exhibited moderate δ^{13}C values of -2‰ to +1.5‰, which were interpreted as a C-isotope seawater signature. They also used the lack of secondary calcite overgrowths, such as those observed in the Kungarra, as evidence for a primary carbon isotope signature in the Kazput. Alternatively, Barlow et al. (2016) suggested the Kazput carbonates were significantly altered and did not represent primary deposits. They used δ^{18}O values in dolostone that ranged from -14.8 to -9.7‰ to suggest alteration

by hydrothermal fluids. They also observed a positive correlation between $\delta^{13}C$ and $\delta^{18}O$ of carbonates, which supports some degree of alteration. The carbonates of the Turee Creek Group warrant further investigation as to the likelihood that they preserve primary signatures.

2.3.4. Summary of the Geological History of Western Australia

The stable isotope data throughout the Mount Bruce Supergroup of the Hamersley Basin collectively supports general trends in the evolution of Earth's atmospheric and oceanic chemistry through time that have been described in previous literature. A summary of values discussed can be found in Table 1. Three general trends are apparent when analyzing the isotopic signatures of the stratigraphy in ascending order: (1) $\delta^{34}S$ values increase with decreasing age, (2) the range of $\Delta^{33}S$ values decreases with decreasing age, and (3) $\delta^{13}C$ of organic carbon tends to increase with decreasing age. The first point can be explained by either an increase in the prominence of SRB Bthrough time, or an increase in the amount of sulfate supplied to the oceans. If the rate of sulfate supply suddenly became larger than the rate of sulfate reduction, there would be an excess sulfate pool separate from the reduced sulfate which would be required in order to preserve a sulfate fractionation signature.

The second point suggests an increase in atmospheric oxygen over the deposition of the Mount Bruce Supergroup. As oxygen built up in the atmosphere, the increased ozone would dampen or inhibit photolytic reactions and mass-independent sulfur isotope fractionation from taking place. Some of the high $\Delta^{33}S$ values preserved in detrital deposits of the Meteorite Bore Member of the Kungarra Fromation are likely older grains that have been transported into the basin by glaciers. This highlights the need to consider lithologies and depositional settings when interpreting geological data of the Archean and Proterozoic. The recycling of the MIF-S signature

was modelled by Reinhard et al. (2013) and is investigated throughout this section by Philippot et al. (2018). Conclusions drawn from the Philippot et al. (2018) study are alluded to in Chapter 2 of this thesis and will not be discussed further here.

The increase in $\delta^{13}C$ values of organic matter through time may suggest a change in the type of microbes that were dominant as the Mount Bruce Supergroup was deposited. The values could reflect a change from methanotrophic and methanogenic dominated environments of the Tumbiana, to purple sulfur bacteria in the Jeerinah, to cyanobacteria in the Hamersley and Turee Creek Groups. The $\delta^{13}C$ values of carbonates within the Mount Bruce Supergroup, especially the Hamersley and Turee Creek groups, warrant further investigation as there are indications that many of the $\delta^{13}C$ and $\delta^{18}O$ signatures may have been homogenized by metamorphic or diagenetic processes. Progressively less iron content stratigraphically upwards in the Turee Creek Group suggests a progressive decrease in the amount of dissolved iron in seawater, an observation consistent with the observed sulfur-isotopic evidence for a rise of oxygen across this interval and the scrubbing of the world's oceans of dissolved iron (Williford et al., 2011). The subsequent deposition of Mn-rich units may further suggest increasing levels of atmospheric oxygen (explored in Chapter 3). However, the fact that the Turee Creek Group is a shallowing upwards succession, and the increased oxygen could be a function of a stratified water column in which there is a gradient from high oxygen to low oxygen with increasing depth, must also be considered.

The cores collected for this project capture segments of all formations contained within the TCG. TCDP1 contains the top of the Boolgeeda Formation and the bottom section of the Kungarra Formation. The second core, TCDP2, captures the top of the Kungarra Formation and the majority of the Meteorite Bore diamictite layer. The bottom of TCDP3 intersects the Koolbye Sandstone, while the top captures the dolostone and mudstone-siltstone of the lower Kazput Formation. For

the locations of each core within the stratigraphic framework of the Turee Creek, refer to Figure 1.1. These intervals were specifically chosen to provide the best representation of the Turee Creek Group, which, in itself, is one of the few places in the world that documents a near-continuous record of deposition across the rise of atmospheric oxygen within a conformable succession of marine sedimentary rocks (Trendall and Blockley, 1970; Trendall, 1979; Thorne and Tyler, 1996).

3. References (Chapter 1)

Alexander, B.W., Bau, M., Andersson, P., Dulski, P., 2008. Continentally-derived solutes in shallow Archean seawater: Rare earth element and Nd isotope evidence in iron formation from the 2.9 Ga Pongola Supergroup, South Africa. Geochimica et Cosmochimica Acta 72, 378-394.

Arndt N.T., Nelson D.R., Compston W., Trendall A.F., Thorne A.M., 1991. The age of the Fortescue Group, Hamersley Basin, Western Australia, from iron microprobe zircon U-Pb results. Australian Journal of Earth Science, 38, 261-281.

Awramik, S.M., Schopf, J.W., Walter, M.R., 1983. Filamentous fossil bacteria from the Archean of Western Australia. Precambrian Research 20, 357-374.

Ballantyne, J.M., Moore, J.N., 1988. Arsenic geochemistry in geothermal systems. Geochimica et Cosmochimica Acta 52, 475-483.

Barley, M.E., 1987. The archaean Whim Creek Belt, an ensialic fault-bounded basin in the Pilbara Block, Australia. Precambrian Research 37, 199-215.

Barlow, E., Van Kranendonk, M. J.., Yamaguchi, K. E., Ikehara, M., 2016. Lithostratigraphic analysis of a new stromatolite – thrombolite reef from across the rise of atmospheric oxygen in the Paleoproterozoic Turee Creek Group, Western Australia.

Bau, M., Dulski, P., 1996. Distribution of yttrium and rare-earth elements in the Penge and Kuruman iron-formations, Transvaal Supergroup, South Africa. Precambrian Research 79, 37–55.

Bau, M., Dulski, P., 1999. Comparing yttrium and rare earths in hydrothermal fluids from the Mid-Atlantic Ridge: implications for Y and REE behavior during near-vent mixing and for the Y/Ho ratio of Proterozoic seawater. Chemical Geology 155, 77-90.

Baur, M.E., Hayes, J.M., Studley, S.A., Walter, M.R., 1985. Millimeter-Scale Variations of Stable Isotope Abundances in Carbonates from Banded Iron-Formations in the Hamersley Group of Western Australia. Economic Geology, 80, 270-282.

Becker, R. H., Clayton, R. N., 1972. Carbon isotopic evidence for the origin of a banded iron-formation in Western Australia. Geochimica et Cosmochimica Acta 36, 577-595.

Becker, R. H., Clayton, R. N., 1976. Oxygen isotope study of a Precambrian banded iron-formation, Hamersley Range. Western Australia. Geochimica et Cosmochimica Acta 40, 1153-1165.

Bekker, A., Kaufman, A.J., Karhu, J.A., Beukes, N.J., Swart, Q.D., Coetzee, L.L., Eriksson, K.A., 2001. Chemostratigraphy of the Paleoproterozoic Duitschland Formation, South Africa: implications for coupled climate change and carbon cycling. American Journal of Science 301, 261-285.

Bekker, A., Slack, J., Planavsky, N., Krapež, B., Hofmann, A., Konhauser, K.O., Rouxel, O.J., 2010. Iron formation: the sedimentary product of a complex interplay among mantle, tectonic, oceanic, and biospheric processes. Economic Geology 105, 467-508.

Blake, T.S., 1993. Late Archaean crustal extension, sedimentary basin formation, flood basalt volcanism and continental rifting: the Nullagine and Mount Jope Supersequences, Western Australia. Precambrian Research 60, 185-241.

Blake T.S., and Barley M.E., 1992. Tectonic evolution of the Late Archaean to Early Proterozoic Mount Bruce Megasequence. Tectonics II, 1415-1425.

Blake T.S., Buick R., Brown S.J.A., Barley M.E., 2004. Geochronology of a late Archaean flood basalt province in the Pilbara Craton, Australia: constraints on basin evolution, volcanic and sedimentary accumulation and continental drift rates. Precambrian Research 133, 143-173.

Boetius A., Ravenschlag K., Schubert C.J., Rickert D., Widdel F., Gieseke A., Amann R., Jorgensen B.B., Witte U., Pfannkuche O., 2000. A marine microbial consortium apparently mediating anaerobic oxidation of methane. Nature, 407, 623-626.

Bolhar, R., Van Kranendonk, M.J., 2007. A non-marine depositional setting for the northern Fortescue Group, Pilbara Craton, inferred from trace element geochemistry of stromatolitic carbonates. Precambrian Research, 155, 229-250.

Brand, U., Veizer J., 1980. Chemical diagenesis of multicomponent carbonate system-1. Trace elements. Journal of Sedimentary Petrology 50, 1219-1250.

Buick R., 1992. The antiquity of oxygenic photosynthesis: evidence from stromatolites in sulphate-deficient Archean lakes. Science 255, 74-77.

Buick R., 2008. When did oxygenic photosynthesis evolve? Philosophical Transactions of the Royal Society B: Biological Sciences 363, 2731-2743.

Canfield, D.E., 2001. Isotope fractionation by natural populations of sulfate-reducing bacteria. Geochimica et Cosmochimica Acta, 65, 1117-1124.

Caquineau, T., Paquette, J.-L., Philippot, P., 2018. U-Pb detrital zircon geochronology of the Turee Creek Group, Hamersley Basin, Western Australia: timing and correlation of the Paleoproterozoic glaciations. Precambrian Research 307, 34-50.

Carlut, J., Isambert, A., Bouquerel, H., Pecoits, E., Philippot, P., Vennin, E., Ader, M., Thomazo, C., Buoncristiani, J-F., Baton, F., Muller, E., Deldicque, D., 2015. Low temperature magnetic properties of the Late Archean Boolgeeda iron formation (Hamersley Group, Western Australia): environmental implications. Frontiers in Earth Science 3 (Article 18), 1-14.

Catuneanu, O. Principles of Sequence Stratigraphy. Elsevier, Amsterdam, 2006, 375 pp.

Catling D.C. and Clair M.W., 2005. How Earth's atmosphere evolved to an oxic state: a status report. Earth and Planetary Science Letters 237, 1-20.

Chandler, F.W., 1980. Proterozoic redbed sequences of Canada. In: Canadian Geological Survey Bulletin. 311 pp. 1-53.

Compston, W., Arriens, P.A., 1968. The Precambrian geochronology of Australia. Canadian Journal of Earth Sciences 5, 561-583.

Crowe, S.A., Døssing, L.A., Beukes, N.J., Bau, M., Kruger, S.J., Frei, R., Canfield, D.E., 2013. Atmospheric oxygenation three billion years ago. Nature 501, 535-538.

Derry, L.A., Kaufman, A.J., Jacobsen, S.B., 1992. Sedimentary cycling and environmental change in the late Proterozoic; evidence from stable and radiogenic isotopes. Geochimica et Cosmochimica Acta 56, 1317-1329.

England, G.L., Rasmussen, B., Krapez, B., Groves, D.I., 2002. Paleoenvironmental significance of rounded pyrite in siliciclastic sequences of the Late Archean Witwatersrand Basin: oxygen-deficient atmosphere or hydrothermal alteration? Sedimentology 49, 1133-1156.

Farquhar, J., Bao, H., Thiemens, M., 2000. Atmospheric influence of Earth's earliest sulfur cycle. Science 289, 756-758.

Farquhar, J., Zerkle, A.L., Bekker, A., 2011. Geological constraints on the origin of oxygenic photosynthesis. Photosynthesis Research 107, 11-36.

Gross, G.A., 1980. A classification of iron-formation based on depositional environments. The Canadian Mineralogist 18, 215-222.

Gross, G.A., 1983. Tectonic systems and the deposition of iron-formation. Precambrian Research 20, 171-187.

Grotzinger, J.P., Kasting, J.F., 1993. New constraints on Precambrian ocean composition. The Journal of Geology 101, 235-243.

Guo, Q., Strauss, H., Kaufman, A.J., Schröder, S., Gutzmer, J., Wing, B., Baker, M.A., Bekker, A., Jin, Q., Kim, S.-T., Farquhar, J., 2009. Reconstructing Earth's surface oxidation across the Archean-Proterozoic transition. Geology 37, 399-402.

Haugaard, R., Pecoits, E., Lalonde, S., Rouxel, O., Konhauser, K.O., 2016. The Joffre banded iron formation, Hamersley Gorup, Western Australia: Assessing the palaeoenvironment through detailed petrology and chemostratigraphy. Precambrian Res. 273, 12-37.

Hayes, J.M., 1994. Global methanotrophy at the Archean-Proterozoic transistion. In: Bengtson, S. (Ed.), Early life on Earth. Columbia University Press, New York.

Hickman, A.H., 1983. Geology of the Pilbara Block and its environs. Geological Survey of Western :Australia, Bulletin 127, 268 pp.

Hinrichs, K.U., 2002. Microbial fixation of methane carbon at 2.7 Ga: was an anaerobic mechanism possible. Geochemistry, Geophysics, Geosystems 3, 1-10.

Hofmann, A., Bekker, A., Rouxel, O.J., Rumble, D., Master, S., 2009. Multiple sulphur and iron isotope composition of detrital pyrite in Archaean sedimentary rocks: a new tool for provenance analysis. Earth and Planetary Science Letters 286, 436-445.

Holland, H.D., 1984. The Chemical Evolution of the Atmosphere and Oceans. Princeton University Press, Princeton NJ, pp. 1-598

Holland, H.D., 2005. Sedimentary mineral deposits and evolution of Earth's near surface environments. Econ. Geol. 100, 1489-1509.

Horwitz, R.C., 1982. Geological history of the Early Proterozoic Paraburdoo hinge zone, Western Australia. Precambrian Research 19, 191-200.

Irwin, H., Curtis, C.D., Coleman, M.L., 1977. Isotopic evidence for the source of diagenetic carbonates formed during the burial of organic-rich sediments. Nature 269, 209-213.

Kakegawa, T., Nanri, H., 2006. Sulfur and carbon isotope analyses of 2.7 Ga stromatolites, cherts and sandstones in the Jeerinah Formation, Western Australia. Precambrian Research, 148, 115-124.

Khim, B.K., Yoon, H.I., 2003. Postglacial marine environmental changes in Maxwell Bay, King George Island, West Antarctica. Polar Research 22, 341-353.

Kirkham, R.V., Roscoe, S.M., 1993. Atmospheric evolution and ore deposit formation. Resource Geology Special Issue 15, 1-17.

Konhauser K.O., Pecoits E., Lalonde S.V., Papineau D., Nisbet E.G., Barley M.E., Arndt N.T., Zahnle K., Kamber B.S., 2009. Oceanic nickel depletion and a methanogen famine before the Great Oxidation Event. Nature 458, 750-753.

Konhauser, K.O., Lalonde, S.V., Planavsky, N.J., Pecoits, E., Lyons, T.W., Mojzsis, S.J., Rouxel, O.J., Barley, M.E., Rosiere, C., Fralick, P.W., Kump, L.R., Bekker, A., 2011. Aerobic bacterial pyrite oxidation and acid rock drainage during the Great Oxidation Event. Nature 478, 369-373.

Konhauser, K.O., Planavsky, N.J., Hardisty, D.S., Robbins, L.J., Warchola, T.J., Haugaard, R., Lalonde, S.V., Partin, C.A., Oonk P.B.H., Tsikos, H., Lyons, T.W., Bekker, A., Johnson, C.M., 2017. Iron Formations: A global record of Neoarchaean to Palaeoproterozoic environmental history. Earth-Science Reviews 172, 140-177.

Krapež, B., 1996. Sequence-stratigraphic concepts applied to the identification of basin-filling rhythms in Precambrian successions. Australian Journal of Earth Sciences, 43, 355-380.

Krapež, B., Barley, M.E., 1987. Archaean strike-slip faulting and related ensialic basins: evidence form the Pilbara Block, Australia. Geological Magazine 1124, 555-567.

Lindsay, J.F., Brasier, M.D., 2000. A carbon isotope reference curve for ca. 1700-1575 Ma, McArthur and Mount Isa Basins, Northern Australia. Precambrian Research 99, 271-308.

Lindsay, J.F., Brasier, M.D., 2002. Did global tectonics drive early biosphere evolution? Carbon isotope record from 2.6 to 1.9 Ga carbonates of Western Australian basins. Precambrian Research, 114, 1-34.

Lowe, D.R., 1980. Stromatolites 3,400-myr old from the Archean of Western Australia. Nature 284, 441-443.

MacGregor, A.R., 1927. The problem of the Precambrian atmosphere. South African Journal of Science 24, 155-172.

Machel, H.G., Krouse, H.R., Sassen, R., 1995. Products and distinguishing criteria of bacterial and thermochemical sulfate reduction. Applied Geochemistry 10, 373-389.

Martin, D.M., Li., Z.X., Nemchin, A.A., Powell, C.M., 1998. A pre-2.2 Ga age for giant hematite ores of the Hamersley Province, Australia? Economic Geology 93, 1084-1090.

Martin, D.M., 1999. Depositional setting and implications of Paleoproterozoic glaciomarine sedimentation in the Hamersley Province, Western Australia. Geological Society of America Bulletin 111, 189-203.

Martin, D.M., Powell, C.M., George, A.D., 2000. Stratigraphic architecture and evolution of the early Paleoproterozoic McGrath Trough, Western Australia. Precambrian Research 99, 33-64.

Martindale, R. C., Strauss, J. V, Sperling, E. A., Johnson, J. E., Van Kranendonk, M. J., Flannery, D., French, K., Lepot, K., Mazumder, R., Rice, M.S., Schrag, D.P, Summons, R., Walter, M., Abelson, J., Knoll, A. H., 2015. Sedimentology, chemostratigraphy, and stromatolites of lower Paleoproterozoic carbonates, Turee Creek Group, Western Australia. Precambrian Research 266, 194–211.

Mazumder, R., Van Kranendonk, M. J., 2013. Palaeoproterozoic terrestrial sedimentation in the Beasley River Quartzite, lower Wyloo Group, Western Australia. Precambrian Research 231, 98–105.

Mazumder, R., Van Kranendonk, M.J., Altermann, W., 2015. A marine to fluvial transition in the Paleoproterozoic Koolbye Formation, Turee Creek Group, Western Australia. Precambrian Research 258, 161-170.

Melezhik, V.A., Fallick, A.E., Hanski, E.J., Kump, L.R., Lepland, A., Prave, A.R., Strauss, H., 2005. Emergence of the aerobic biosphere during the Archean-Proterozoic transition: challenges of future research today. GSA Today 15, 4-11.

Myers, J.S., 1993. Precambrian History of the West Australian Craton and Adjacent Orogens. Annual Review of Earth and Planetary Sciences, 21, 453-485.

Ohmoto, H., 1992. Biogeochemistry of sulfur and the mechanisms of sulfide-sulfate mineralization in Archean oceans, In: M. Schidlowski (Ed.), Early Organic Evolution: Implications for Mineral and Energy Sources, Springer-Verlag, Berlin, 378-397.

Ohmoto, H., Goldhaber, M., 1997. Applications of sulfur and carbon isotopes in ore deposit research. In: Barnes H.L (Ed.), Geochemistry of Hydrothermal Ore Deposits, third ed. John Wiley and Sons, 517-611.

Ono, S., Eigenbrode, J.L., Pavlov, A.A., Khareecha, P., Rumble III, D., Kasting, J.F., Freeman, K.H., 2003. New insights into Archean sulfur cycle from mass-independent sulfur isotope records from the Hamersley Basin, Australia. Earth and Planetary Science Letters, 213, 15-30.

Partin, C.A., Lalonde, S.V., Planavsky, N.J., Bekker, A., Rouxel, O.J., Lyons, T.W., Konhauser, K.O., 2013a. Uranium in iron formations and the rise of atmospheric oxygen. Chemical Geology 362, 82–90.

Partin, C.A., Bekker, A., Planavsky, N.J., Scott, C.T., Gill, B.C., Li, C., Podkovyrov, V., Maslov, A., Konhauser, K.O., Lalonde, S.V., Love, G.D., Poulton, S.W., Lyons, T.W., 2013b. Large-scale fluctuations in Precambrian atmospheric and oceanic oxygen levels from the record of U in shales. Earth and Planetary Science Letters 369-370, 284–293.

Pavlov A.A., Kasting J.F., Eigenbrode J.L., Freeman K.H., 2001. Organic haze in Earth's early atmosphere: Source of low-C-13 Late Archean kerogens? Geology 29, 1003-1006.

Pecoits, E., Gingras, M.K., Barley, M.E., Kappler, A., Posth, N., Konhauser, K.O., 2009. Petrography and geochemistry of the Dales Gorge banded iron formation: Paragenetic sequence, source and implications for palaeo-ocean chemistry. Precambrian Research 172, 163–187.

Philippot, P., Ávila, J.N., Killingsworth, B.A., Tessalina, S., Baton, F., Caquineau, T., Muller, E., Pecoits, E., Cartigny, P., Lalonde, S.V., Ireland, T.R., Thomazo, C., van Kranendonk, M.J., Busigny, V., 2018. Globally asynchronous sulphur isotope signals require re-definition of the Great Oxidation Event. Nature Communications 9, 2245

Planavsky, N.J., Asael, D., Hofmann, A., Reinhard, C.T., Lalonde, S.V., Knudsen, A., Wang, X., Ossa Ossa, F., Pecoits, E., Smith, A.J.B., Beukes, N.J., Bekker, A., Johnson, T.M., Konhauser, K.O., Lyons, T.W., Rouxel, O.J., 2014. Evidence for oxygenic photosynthesis half a billion years before the Great Oxidation Event. Nature Geoscience 7, 283-286.

Pope, M.C., Grotzinger, J.P, 2003. Paleoproterozoic stark formation, Athapuscow Basin, Northwest Canada: record of cratonic-scale salinity crisis. Journal of Sedimentary Research 73, 280-295.

Posamantier, H.W., Jervey, M.T., Vail, P.R., 1988. Eustatic controls on clastic depositional sequeces and systems tract models. In: C.K. Wilgus et al. (Eds.), Sea Level Changes: An Integrated Approach. Special publications of the Society of Economic Paleontologists and Mineralogists 42, 109-124.

Posamantier, H.W., James, D.P., 1993. An overview of sequence stratigraphic concepts: uses and abuses. In : H.W. Posamentier, C.P. Summerhayes, B.U. Haq, G.P. Allen (Eds.), Sequence Stratigraphy and Facies Associations. International Association of Sedimentologists Special Publication 18, 3-18.

Powell, C.M., Horwitz, R.C., 1994. Late Archaean and Early Proterozoic tectonics and basin formation of the Hamersley Ranges. In: 12th Australian Geological Convention, Geological Society of Australia, Perth, Excursion Guidebook 4.

Rasmussen, B., Buick, R., 1999. Redox state of the Archean atmosphere: Evidence from detrital heavy minerals in ca. 3250-2750 Ma sandstones from the Pilbara Craton, Australia. Geology 27, 115-118.

Rasmussen, B., Fletcher, I.R., Sheppard, S., 2005. Isotopic dating of the migration of a low-grade metamorphic front during orogenesis. Geology, 33, 773-776.

Rasmussen, B., Krapež, B., Meier, D.B., 2014. Replacement origin for hematite in 2.5 Ga banded iron formation: evidence for postdepostional oxidation of iron-bearing minerals. Geological Society of America Bulletin 126, 438-446.

Rasmussen, B., Muhling, J.R., Suvorova, A., Krapež, B., 2016. Dust to dust: evidence for the formation of "primary" hematite dust in banded iron formations via oxidation of iron silicate nanoparticles. Precambrian Research 284, 49-63.

Rasmussen, B., Muhling, J.R., Suporova, A., Krapež, B., 2017. Greenalite precipitation linked to the deposition of banded iron formations downslope from a late Archean carbonate platform. Precambrian Research. 290, 49-62.

Reinhard, C.T., Planavsky, N.J., Lyons, J.R., 2013. Long-term sedimentary recycling of rare sulphur isotope anomalies. Nature 497, 100-104.

Roscoe, S.M., 1996. Paleoplacer uranium gold. In: Eckstrand OR, Sinclair WD, Thorpe RI (eds) Geology of Canadian mineral deposit types, vol P-1. Geological Society of America, The Geology of North America, Boulder, 10-23.

Rye, R., Holland, H.D., 1998. Paleosols and the evolution of atmospheric oxygen: a critical review. American Journal of Science 298, 621-672.

Schopf, J.W., Packer, B.M., 1987. Early archean (3.3-billion to 3.5-billion-year-old microfossils from Warrawoona Group, Australia. Science 237, 70-73.

Schröder, S., Bekker, A., Beukes, N.J., Strauss, H., van Niekerk, H.S., 2008. Rise in seawater sulphate concentration associated with the Paleoproterozoic positive carbon isotope excursion: evidence from sulphate evaporites in the 2.2-2.1 Gyr shallow-marine Lucknow Formation, South Africa. Terra Nova 20, 108-117.

Scott, C., Lyons, T.W., Bekker, A., Shen, Y., Poulton, S., Chu, X., Anbar, A., 2008. Tracing the stepwise oxygenation of the Proterozoic ocean. Nature 452, 456-459.

Smith R.E., Perdrix J.L., Parks J.C., 1982. Burial metamorphism in the Hamersley province, Western Australia. Journal of Petrology 23, 75-102.

Summons R.E., Bradley A.S., Jahnke L.L., and Waldbauer J.R., 2006. Steroids, triterpenoids and molecular oxygen. Philosophical Transactions of the Royal Society B: Biological Sciences 361, 951-968.

Swanner, E.D., Bekker, A., Pecoits, E., Konhauser, K.O., Cates, N.L., Mojzsis, S.J., 2013. Geochemistry of pyrite from diamictites of the Boolgeeda Iron Formation, Western Australia with implications for the GOE and Paleoproterozoic ice ages. Chemical Geology 362, 131-142.

Thomazo C., Ader M., Farquhar J., Philippot P., 2009. Methanotrophs regulated atmospheric sulfur isotope anomalies during the Mesoarchean (Tumbiana Formation, Western Australia). Earth and Planetary Science Letters, 279, 65-75.

Thorne, A.M., Trendall, A.F., 2001. Geology of the Fortescue Group, Pilbara Craton, Western Australia. Geological Survey of Western Australia Bulletin 144.

Thorne, A.M., Tyler, L.M., 1996. Roy Hill, Western Australia Sheet 50-12: Geological Survey of Western Australia. 1:250 000 Map Series.

Thorpe, R.A., Hickman, A.H., Davis, D.W., Mortensen, J.K., Trendall, A.F., 1992. U-Pb zircon geochronology of Archaean felsic units in the Marble Bar region, Pilbara Craton, Western Australia. Precambrian Research 56, 169-189.

Tosca, N.J., Guggenheim, S., Pufahl, P.K., 2016. An authigenic origin for Precambrian greenalite: implications for iron formation and the chemistry of ancient seawater. Geological Society of America Bulletin 128, 511-530.

Trendall A.F., and Blockley J.G., 1970. The iron formations of the Precambrian Hamersley Group, Western Australia. Geological Survey of Western Australia Bulletin, 119.

Trendall, A.F., 1973. Varve Cycles in the Weeli Wolli Formation of the Precambrian Hamersley Group, Western Australia. Economic Geology 68, 1089-1097.

Trendall, A.F., 1976. Striated and faceted boulders from the Turee Creek Formation – Evidence for a possible Huronian glaciation on the Australian continent: Geological Survey of Western Australia Annual Report 1975, 88-92.

Trendall A.F., 1979. A revision of the Mount Bruce Supergroup. Geological Survey of Western Australia Annual Report for 1978, 63-71.

Trendall, A.F., 1981. The Lower Proterozoic Meteorite Bore Member, Hamersley Basin Western Australia. In: Hambrey, M.J., Harland, W.B. (Eds.), Earth's Pre-Pleistocene Glacial Record. Cambridge University Press, Cambridge, 555-557.

Trendall, A.F., 1990. Hamersley Basin, in Geology and mineral resources of Western Australia. Western Australia Geological Survey, Memoir 3, 77-119, in Geology and mineral resources of Western Australia. Western Australia Geological Survey, Memoir 3, 163-191.

Trendall, A.F., Conpston, W., Nelson, D.R., De Laeter, J.R., Bennett, V.C., 2004. SHRIMP zircon ages constraining the depositional chronology of the Hamersley Group, Western Australia. Australian Journal of Earth Sciences 51, 621-644.

Trudinger, P.A., Chamber, L.A., 1985. Low-temperature sulphate reduction: biological versus abiological. Canadian Journal of Earth Sciences 22, 1910-1918.

Van Kranendonk, M. J., Mazumder, R., 2015. Two Paleoproterozoic glacio-eustatic cycles in the Turee Creek Group, Western Australia, (3), 596–607.

Van Kranendonk, M. J., Mazumder, R., Yamaguchi, K. E., Yamada, K., Ikehara, M., 2015. Sedimentology of the Paleoproterozoic Kungarra Formation, Turee Creek Group, Western Australia: A conformable record of the transition from early to modern Earth. Precambrian Research, 256, 314–343.

Waldbauer J.R., Sherman L.S., Sumner D.Y., and Summons R.E., 2009. Late Archean molecular fossils from the Transvaal Supergroup record the antiquity of microbial diversity and aerobiosis. Precambrian Res. 169, 28-47.

Walter, M.R., Buick, R., Dunlop, J.S.R., 1980. Stromatolites 3,400-3,500 Myr old from the North Pole area, Western Australia: Nature 284, 443-445.

Williford, K. H., Van Kranendonk, M. J., Ushikubo, T., Kozdon, R., Valley, J. W., 2011. Constraining atmospheric oxygen and seawater sulfate concentrations during Paleoproterozoic glaciation: In situ sulfur three-isotope microanalysis of pyrite from the Turee Creek Group, Western Australia. Geochimica et Cosmochimica Acta, 75, 5686–5705.

Wood, J., 1973. Stratigraphy and depositional environments of upper Huronian rocks of the Rawhide Lake-Flack Lake area, Ontario. In: Young GM (ed) Huronian Stratigraphy and Sedimentation, vol 12. Geological Association of Canada Special Paper, Geological Association of Canada, 73-95.

4. Figures (Chapter 1)
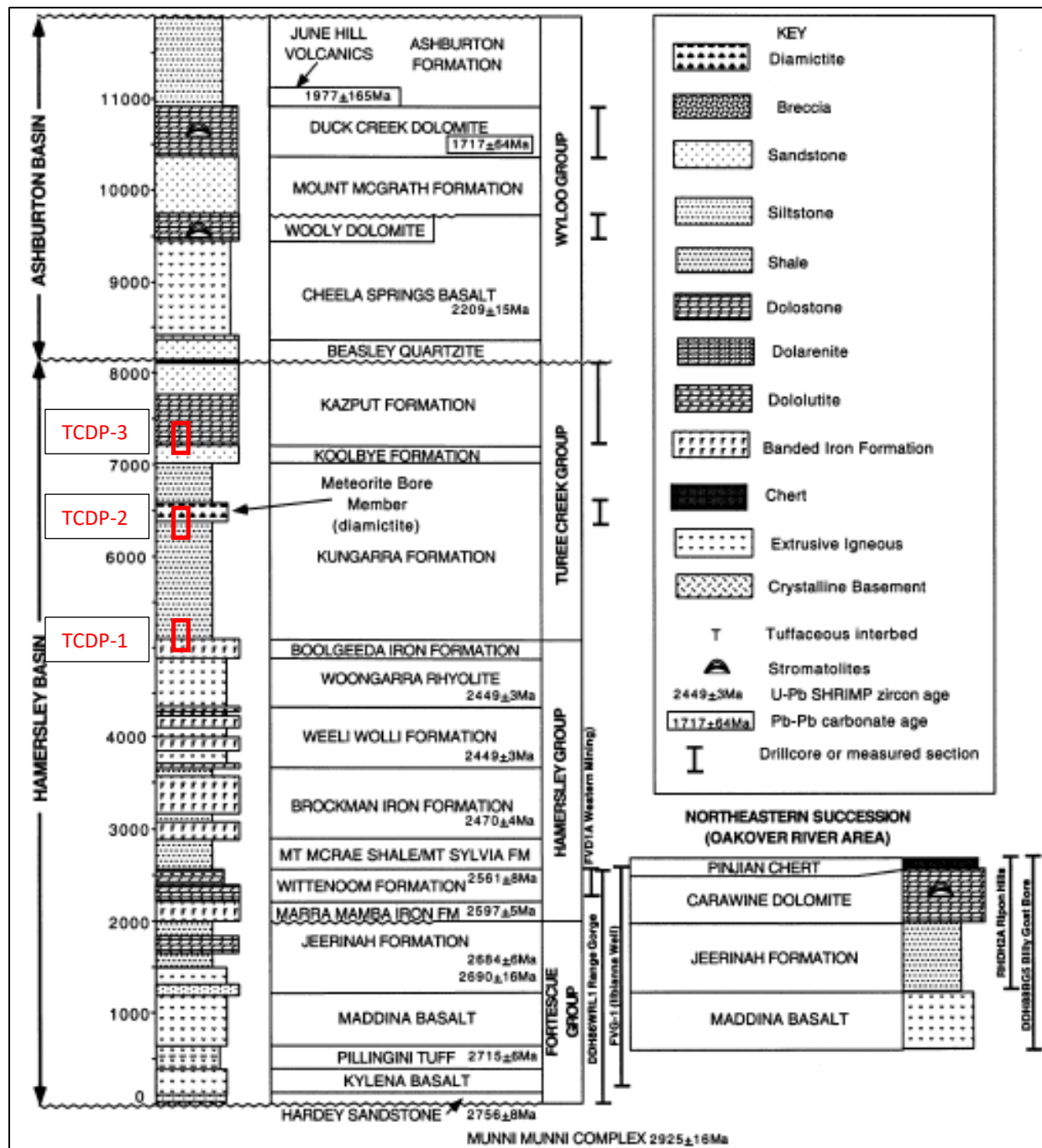
Figure 1.1. Stratigraphy of the Mount Bruce Supergroup, noted here as the Hamersley Basin. Figure taken from Lindsay and Brasier (2002). Ages gathered from multiple sources (Barley et al., 1997; Trendall et al., 1998; Arndt et al., 1991). Location of TCDP cores within the stratigraphic framework are highlighted by the red boxes.
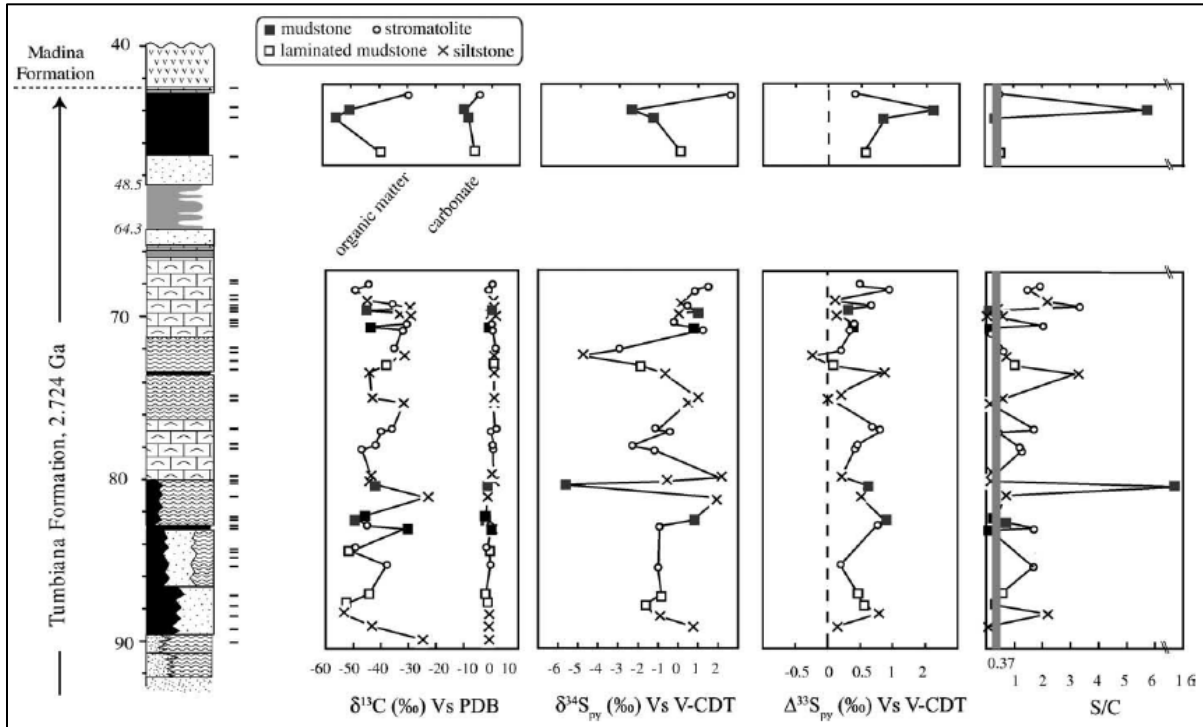
Figure 1.2. δ^{13}C, δ^{34}S, Δ^{33}S, and S/C values obtained in Thomazo et al. (2009).
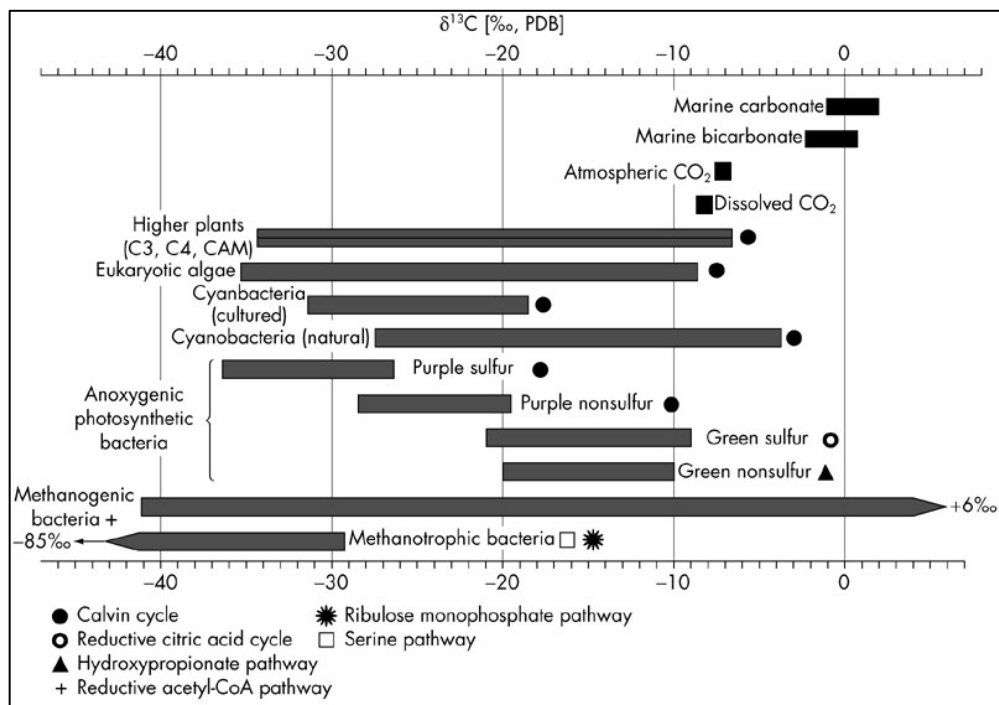
Figure 1.3. General δ^{13}C ranges for various organic matter produced by different metabolisms (Courtesy of Manfred Schidlowski and Kurt Konhauser).
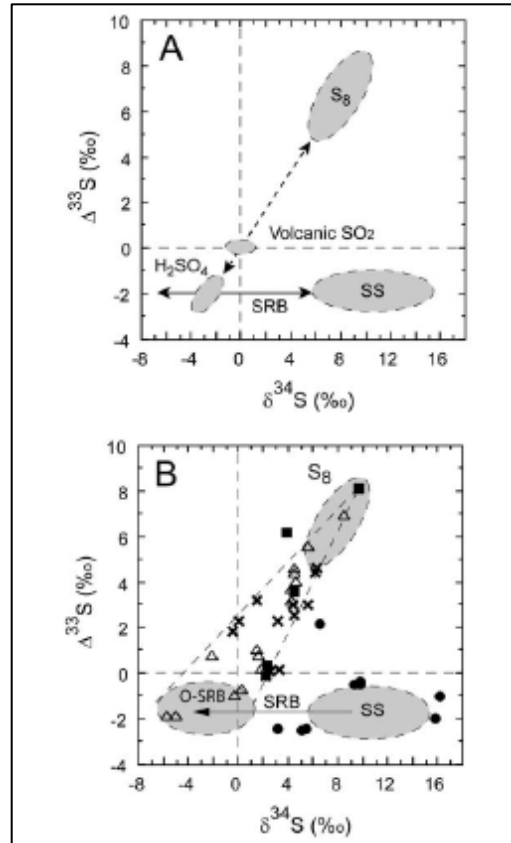
Figure 1.4. Part A shows the three reservoirs pertaining to different $\Delta^{33}S$ and $\delta^{34}S$ values. Part B overlays the data from Ono et al. (2003). Figure taken from Ono et al. (2003).
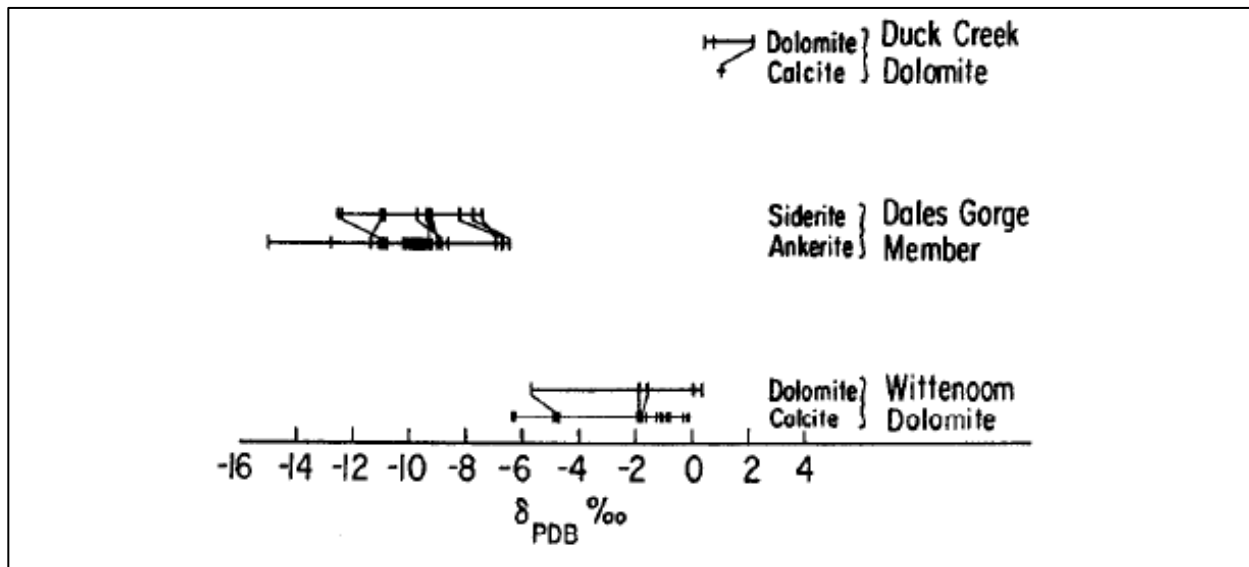
Figure 1.5. $\delta^{13}C$ values for the iron formations and dolomitic limestones investigated by Becker and Clayton (1972).
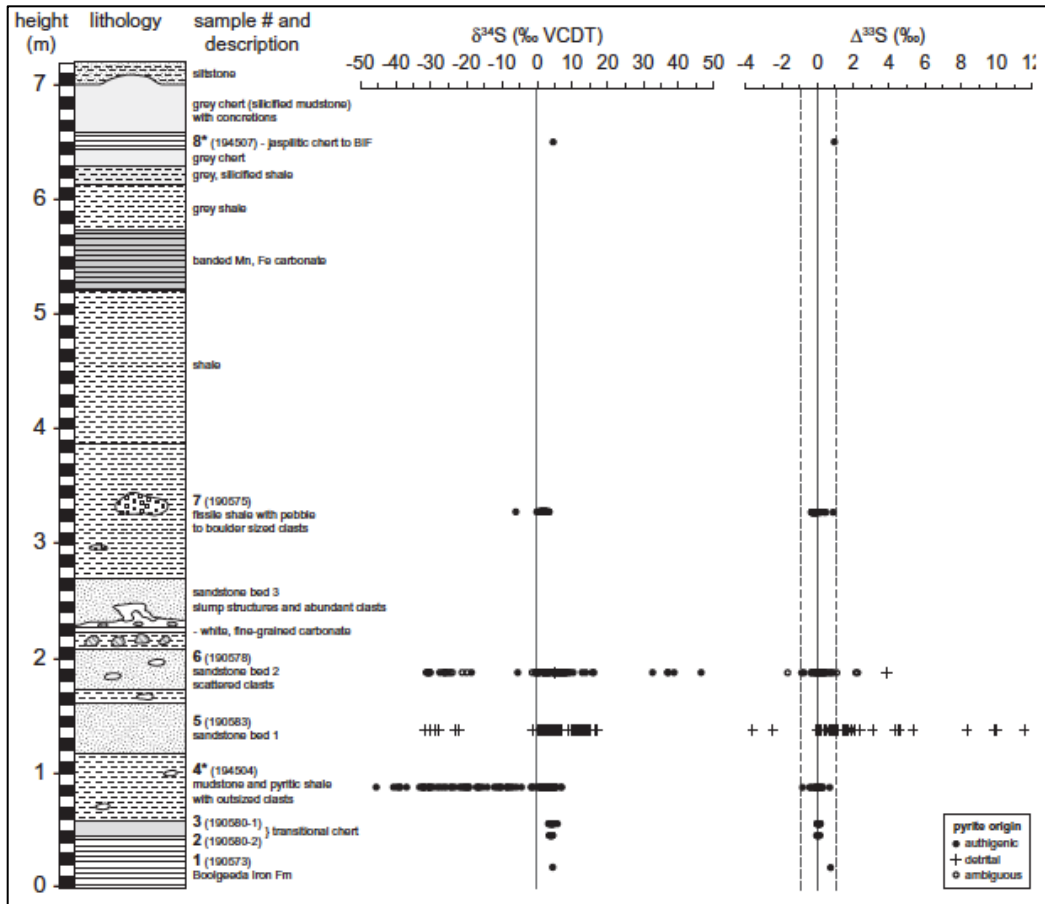
Figure 1.6. δ^{34}S and Δ^{33}S values of pyrites through the Meteorite Bore Member of the Kungarra Formation. Dashed lines indicate the range of Δ^{33}S measured in unambiguously authigenic pyrite and crosses indicate pyrite of detrital or ambiguous origin. From Williford et al. (2011).

5. Tables (Chapter 1)

Author	Formation (age in Ga)	δ34S Range (‰)	Δ33S Range (‰)	δ13C Organic Range (‰)	δ13C Carbonate Range (‰)
Thomazo et al. (2009)	Tumbiana (2.72)	-5.73 to 2.75	-0.25 to 1.64	-23.8 and -55.9	-9.2 to 1.9
Kakegawa and Nanri (2006)	Jeerinah Formation (2.69)	-2.5 to 5.6	-----	-39.7 to -27.1	-----
Kakegawa et al., ref29	Jeerinah Formation (2.69)	0.4 to 10.2	-----	-----	-----
Ono et al. (2003)	Jeerinah Formation (2.69)	~1 to 14	-0.1 to 8.1	-----	-----
Baur et al. (1985)	Marra Mamba (2.59)	-----	-----	-37.8	-7.35
Baur et al. (1985)	Marra Mamba (2.59)	-----	-----	-43	0.36
Ono et al. (2003)	Carawine Dolomite (2.59)	3.2 to 16.2	-2.5 to -1.1	-----	-----
Bottomley et al. (1992)	Carawine Dolomite (2.59)	4.6 to 20.9	-----	-----	-----
Ono et al. (2003)	Mount McRae Shale (2.5)	-5.4 to 8.4	-1.9 to 6.9	-----	-----
Kakegawa et al.,	Mount McRae Shale (2.5)	-6.3 to 11.8	-----	-----	-----
Baur et al. (1985)	Mount Sylvia	-----	-----	-18.6	-12
Baur et al. (1985)	Brockman (Dales Gorge)	-----	-----	-25.9	-8.52
Baur et al. (1985)	Brockman (Dales Gorge)	-----	-----	-21.4	-9.35
Williford et al. (2011)	Kungarra (MBM; 2.45-2.2)	-45.5 to 46.4	-1.0 to 1	-----	-----
Martindale et al. (2015)	Kazput (2.45-2.2)	-----	-----	-----	-2 to 1.5

Table 1.1. Literature survey of δ^{34}S, Δ^{33}S, δ^{13}C$_{organic}$, and δ^{13}C$_{carbonate}$ values. Values interpreted to be affected by digenesis and metamorphism were omitted from the table.

Chapter 2: Petrology and Geochemistry of the Boolgeeda Iron Formation, Hamersley Basin, Western Australia[*]

1. Introduction

Precambrian iron formations (IF) are marine sedimentary rocks composed of iron oxides, silica (most commonly chert), Fe-carbonates (siderite and ankerite), and Fe-silicates (Bekker et al., 2010; 2014; Konhauser et al., 2017). The presence of IF in the rock record is indicative of both high concentrations of dissolved ferrous iron (Fe^{2+}) in seawater (Isley, 1995) and anoxic ocean conditions (e.g. Cloud, 1973; Konhauser et al., 2002; Klein, 2005). The combination of these two factors promoted the transport of Fe(II) from submarine hydrothermal sources to relatively shallow continental shelves where large Superior-type IF were deposited (e.g., Beukes and Klein, 1990; Morris, 1993). Although BIF were deposited throughout the Precambrian, perhaps as much as 60% of the global volume of BIF were deposited between 2.50 and 2.45 Ga (Islay and Abbott, 1999). Accordingly, peak BIF deposition may be related to either a major pulse of dissolved iron from hydrothermal input (e.g. Derry and Jacobsen, 1988, 1990; Klein and Buekes, 1993; Buhn and Stanistreet, 1997; Trompette et al., 1998; Walde and Hagemann, 2007) or a significant redox transition in the surface oceans that facilitated widespread Fe(II) oxidation into a ferric oxyhydroxide, such as ferric hydroxide, $Fe(OH)_3$; this iron phase may then have combined with amorphous silica to form a water-rich Fe(III)-Si gel (e.g., Percak-Dennett et al., 2011) or silica-rich Fe(III)-oxyhydroxide, likely precursor phases of IF (see Konhauser et al., 2017 for review).

The Hamersley Group in Western Australia hosts the world's largest IF deposits by mass, and records over 150 million years of geological history. A number of studies have investigated the chemical composition, mineralogy, geochronology, and sedimentology of the major Hamersley Basin IF units, including the 2.60 Ga Marra Mamba Iron Formation (Blockley, 1979; Ewers and Morris, 1981; Blockley et al., 1993; Trendall et al., 1998; Lascelles, 2000), the Brockman Iron Formation, specifically the 2.48 Ga Dales Gorge Member (Ayres, 1972; Konhauser et al., 2002; Hamade et al., 2003; Pickard et al., 2004; Pecoits et al., 2009; Steinhofel et al., 2010; Konhauser et al., 2015) and the 2.46 Ga Joffre Member (McConchie, 1984; Haugaard et al., 2016a), and the 2.45 Ga Weeli Wolli Formation (Trendall, 1973; Davy, 1992), or have compared and contrasted IF units in the context of the entire Hamersley Group (Trendall and Pepper, 1977; Morris and Horwitz, 1983; Baur et al., 1985; Alibert and McCulloch, 1993; Morris, 1993; Trendall et al., 2004; Partridge et al., 2008). In contrast, investigations of the youngest iron deposit and terminal unit of the Hamerlsey Group, the Boolgeeda Iron Formation, have been restricted to samples from sparse surface outcrops that appear in the hinges of large-scale folds along the southern part of the Hamersley (e.g. Swanner et al., 2013, Williford et al., 2011). Recently however, in order to obtain constraints on the rise of atmospheric oxygen and associated glacial events concomitant with the Paleoproterozoic Great Oxidation Event (GOE), the Turee Creek Drilling Project (TCDP) was undertaken to acquire three drill cores that capture representative portions of the Boolgeeda IF, different formations within the overlying Turee Creek group (TCG), and the stratigraphic boundaries between them. These cores, referred to as TCDP1, TCDP2, and TCDP3, provide a representative sample of over 4 km of conformable sediment that comprises the Boolgeeda IF and TCG (Philippot et al., 2018).

Deposition of the Boolgeeda Iron Formation and TCG occurred between 2.45 and 2.22

billion years ago, making them important units for the study of early Paleoproterozoic oxygen dynamics. Geochronological constraints on the deposition of these formations include a U-Pb zircon age of 2449±3 Ma for the conformably underlying Woongarra Rhyolite (Barley et al., 1997), a U-Pb zircon age of 2209±15 Ma for the unconformably overlying Cheela Springs Basalt of the Wyloo Group (Martin et al., 1998), and a U-Pb baddeleyite age of 2208±10 Ma for a dolerite sill intruding the Turee Creek Group, interpreted to be coeval with the eruption of the Cheela Springs Basalt (Müller et al., 2005). Stratigraphically, the Cheela Springs Basalt lies unconformably above the Turee Creek Group and, therefore, the lower age constraint represents the minimum age of the Boolgeeda IF and Turee Creek package. Recently, Philippot et al. (2018) and Caquineau et al. (2018) reported a pyrite Re-Os age of 2309 ± 9.2 Ma and a detrital zircon U-Pb age of 2340 ± 22 Ma obtained from drill core samples at the base of the main glacial deposit of the Meteorite Bore Member of the Kungarra Formation (Hardey Syncline). In addition, a meter-scale layer of diamictite identified within the Boolgeeda IF yielded a zircon U-Pb age of 2454 ± 23 Ma (see Figure 2.2; Philippot et al., 2018; Caquineau et al., 2018). The samples, sample depth scale, and sample IDs employed by Caquineau et al. (2018) are identical to those used in this study, and we direct the reader there for an in-depth discussion on the geochronology of the Boolgeeda IF.

Using a combination of the above age constraints and multiple sulphur isotope analyses performed throughout the three drill cores, Philippot et al (2018) showed the persistence of a monotonous small-magnitude mass-independent sulfur isotope (MIF-S) signal in sedimentary sulfides from the base of the Boolgeeda IF to about 1000 meters above the Meteorite Bore Member diamictite, which is punctuated by short episodes of sulphur isotope perturbations attributed to oxidative weathering of the Archaean continental surface. Given the age constraints and

uninterrupted sequence of Boolgeeda IF and Turee Creek deposition, this is inconsistent with an abrupt, globally synchronous, atmospheric transition at about 2.32–2.33 Ga as previously advocated (Bekker et al., 2004 ; Guo et al., 2009 ; Luo et al., 2016). Rather, it is consistent with the view of the GOE as a transitional period (Reinhard et al., 2013), where an early (>2.45 Ga) rise of atmospheric oxygen above the threshold value of 10^{-5} Present Atmospheric Level (PAL) was followed by a long period of continued delivery of MIF-S anomalies to the oceans until their exhaustion from weathering catchments. In the case of the Boolgeeda-Turee Creek sedimentary basin, the source MIF-S rocks were not weathered out until after 2.25 Ma, thus indicating that the exhaustion process took at least 200 Myr. Asynchrony in the extinction of MIF-S signals between the Superior, Kaapvaal, and Pilbara cratons underline the need to better constrain the timing and dynamics of the GOE through the detailed study of sedimentary sequences deposited between 2.5 and 2.32 Ga.

In this study, we analyzed the uppermost 45 meters of the Boolgeeda Iron Formation and an additional 30 meters of the overlying Kungarra mudstones, as sampled in the Turee Creek Drilling Project 1 drill core (TCDP1). This interval captures the termination of IF deposition in the Hamersley basin and coincides with a decline in global IF deposition in the Paleoproterozoic. Using geochemical and mineralogical analyses, we provide a continuous, high resolution chemostratigraphic dataset of major and trace element concentrations and variations, as well as Fe speciation depth plots, in order to better understand the relationship between the rise of atmospheric oxygen and subsequent decline in IF deposition, and to further test the model for atmospheric oxygenation proposed by Philippot et al. (2018) based on S-isotopic systematics. The data presented here represents the highest resolution whole-rock geochemical dataset of a BIF produced to date.

2. Core, sampling, and analytical methods

The three drill cores (TCDP1, TCDP2, TCDP 3) retrieved as part of the Turee Creek Drilling Project (TCDP; Figure 2.1) represent a combined 454 m of core recovered over 746 m of drilling. The core samples were split, and half is archived at Géosciences Montpellier. Samples discussed in this study were subsampled from TCDP1.

Samples were collected at regular intervals between 174.13 and 99.0 m depth. The Boolgeeda Iron Formation in this section of core is largely comprised of Fe-rich and silica-dominated IF (including jasper), with a distinct clastic package occurring around 152 m (see section 3.1). The overlying Kungarra Formation is dominated by relatively homogeneous grey shales and siltstones. Forty thin sections representing drilling depths between 172.1 m and 130.39 m were prepared and examined using reflected and transmitted light microscopy. Detailed mineralogical analyses of these thin sections are presented in section 3.1.

One hundred and twenty-eight TCDP1 rock chip samples were submitted to Actlabs for major and trace metal analyses, along with 12 pulp samples to monitor for contamination during the milling and/or analysis processes. Nickel, Zn, Cd, S%, Cu, Ag, and Pb measurements were made using the total digestion inductively coupled plasma mass spectrometry (TD-ICP-MS) method. Rock powder samples (~0.25 g/sample) were completely digested by first treating them in concentrated hydrofluoric acid, and subsequently treating them with a mixture of nitric and perchloric acids. Samples were then heated and dried using precise programmer-controlled heating in several ramping and holding cycles, and finally re-suspended in hydrochloric acid. Analyses were completed using a Varian Vista 735 ICP-MS. Standards used for TD-ICP-MS were GXR-4,

SDC-1, GXR-6, SAR-M (U.S.G.S.), DNC-1a, and SBC-1. Detection limits for Ag, Cd, Cu, Ni, Pb, Zn, and S, as reported by Actlabs, are 0.3, 0.5, 1, 1, 5, 1 ppm, and 0.001%, respectively.

All other major and trace element values were obtained using a lithium metaborate/tetraborate fusion (FUS)-ICP-MS method. Samples were mixed with a flux of lithium metaborate and lithium tetraborate and fused in an induction furnace. The melt was immediately poured into a 5% nitric acid solution containing an internal standard, and then mixed continuously until completely dissolved (~30 minutes). The fused sample was diluted and analyzed using a Perkin Elmer Sciex ELAN 6000, 6100, or 9000 ICP-MS. Three blanks and five controls (three before the sample group and two following) were analyzed. Duplicate samples were analyzed every 15 samples and the instrument was recalibrated every 40 samples. Following the reported Actlabs procedure, custom standard materials were prepared for the project and generally accepted results for these standards were those within three standard deviations on either side of the certified values. Standards used for FUS-ICP-MS were NIST 694, DNC-1, W-2a, SY-4, BIR-1a, LKSD-3, TDB-1, NCS DC70009 (GBW07241), OREAS 100a (Fusion), OREAS 101a (Fusion), OREAS 101b (Fusion), and JR-1. Upper and lower limits of detection for each element analyzed are readily available on the Actlabs commercial website. Blank measurements for all analyses were below the detection limits. Raw data for all analyses are compiled in SI Table 1, and a quality control table is reported in SI Table 2. A summary of major and minor element analyses can be found below in Tables 1 and 2, respectively.

Fe speciation was evaluated for selected samples using the method of Poulton and Canfield (2005). Sequential extractions targeted 7 fractions: (1) exchangeable Fe (Fe_{Ex}), (2) carbonate associated Fe (Fe_{Carb}), (3) easily reducible oxides ($Fe_{Ox1;}$ e.g. ferrihydrite, lepidocrite), (4) reducible oxides ($Fe_{Ox2;}$ e.g. goethite, akaganéite, hematite), (5) magnetite (Fe_{Mag}), (6) poorly

reactive sheet silicate Fe (Fe_{PRS}), and (7) pyrite Fe and unreactive silicate Fe (Fe_{Py+U}). Iodometric titrations to determine the exact fraction of pyrite bound Fe (Fe_{Py}) were not performed as robust silicates containing Fe unreactive with H_2S are relatively rare compared to pyrite in Boolgeeda sediments. This has been confirmed by the absence of robust Fe silicate phases in XRD diffraction patterns of samples analyzed (SI Figure 2.1). Therefore, the Fe_{Py+U} fraction will here-on be treated as representative of the Fe_{Py}. All chemicals used were ACS grade and obtained from Fisher Scientific (Toronto, Ontario, Canada). Procedures 1 through 5 were performed using 0.2 g of sample weighed into 50 mL polypropylene centrifuge tubes. The Fe_{Ex} fraction (1) was extracted using 1 M magnesium chloride; solutions reacted at pH 7 for 2 h at room temperature. The Fe_{Carb} fraction (2) was extracted with 1 M sodium acetate at pH 4.5 and 50°C for 24 h on a heating block. To adjust to pH 4.5, 8.6% v/v acetic acid was used. The Fe_{Ox1} fraction (3) was extracted over 48 h at room temperature using 1 M hydroxylamine hydrochloride in 25% v/v acetic acid. The Fe_{Ox2} fraction (4) was extracted with 50 g/L sodium dithionite, buffered to a pH of 4.8 using 0.35 M acetic acid, 0.2 M sodium citrate, and sodium hydroxide; solutions reacted for 2 h at room temperature. For magnetite (5), 0.2 M ammonium oxalate and 0.17 M oxalic acid solution were used to leach samples over 6 h, at pH 3.2 and room temperature. The extraction volume in steps 1-5 was 10 mL After each step, tubes were centrifuged at 15000 g for 20 min, and 5 mL of the supernatant was collected and diluted 10 times for analysis using a 2% nitric acid and 0.5% hydrochloric acid solution. The remaining supernatant was discarded.

To extract Fe_{PRS} (6), samples were transferred into Thermo Scientific Teflon FEP centrifuge tubes by rinsing with 18.2 Ω Milli-Q water. The water was then removed by centrifugation prior to the next extraction. This extraction was performed using boiling 37% hydrochloric acid. To do so, a heating block was preheated to 210 °C. Five mL of hot hydrochloric

acid were added to the tubes, which were then placed in the preheated heating block, brought to a boil (3-5 min), and boiled for another 1 min. The boiling was stopped by removing the tubes from the heating block and adding 10 mL of cold ultrapure water. The tubes were centrifuged (15000 g, 20 min), and 5 mL of the supernatant was diluted 3 times with 2% nitric acid and 0.5% hydrochloric acid for analysis. Another 5 mL were discarded, and the remaining 5 mL was left in the tubes for the final digestion step. The final digestion (7) was performed by adding 5 mL of 70% nitric acid and 3 mL of 48-51% hydrofluoric acid, and subsequently heating the mixtures at 155 °C until near dryness. One mL of 37% hydrochloric acid was added to the remaining solution and the mixture was heated again at 155 °C for 4 h. The remains were then diluted to 50 mL with 2% nitric acid and 0.5% hydrochloric acid.

All solutions were analyzed for Fe using an Agilent 8800 Triple Quadrupole ICP-MS in high matrix introduction mode, using Ar as carrier and dilution gas and He (5 mL/min) as collision gas to minimize polyatomic interferences (Sakai, 2015). Germanium and In were used as internal standards. Elemental recovery was verified using the certified standard STSD-3 (CANMET Mining and Mineral Sciences Laboratories, Natural Resources Canada), yielding an average total recovery of 107%.

3. Petrography and mineralogy

3.1. Lithologies in TCDP1

Based on mineralogy and grain size, Philippot et al., (2018) defined five major lithologies within TCDP1: (1) banded iron formation (BIF), (2) silica-dominated iron formation (3) green mudstone/siltstone, (4) diamictite associated with sandstone/siltstone, and (5) grey siltstone/argillite (Figure 2.2). Lithologies 1 through 4 are the major components of the Boolgeeda

IF, while lithology 5 comprises the overlying Kungarra Formation. Although in variable proportions, iron oxides (mostly magnetite, but also hematite), quartz, carbonate, chlorite, and pyrite, are present within the banded iron formation, silica-dominated iron formation, and green mudstone/siltstone. Rare occurrences of muscovite, plagioclase, apatite, and zircon are also present. These three lithologies are generally gradational, with subtle transitions and fine-scale (mm to cm) intercalations occurring within, and between, them. On the other hand, the diamictite and grey siltstone/argillite are defined within specific intervals of the core and represent distinct sediment packages separate from the other lithologies. Each lithology is discussed in more detail below.

3.1.2 Banded iron formation

The BIF is mainly composed of iron oxides (magnetite and hematite), quartz, and lesser amounts of carbonate, with minor chlorite and rare muscovite. Magnetite grains are typically large and euhedral relative to hematite grains (Figure 2.3A), and in some instances, contain inclusions of elongated to rounded hematite and quartz (Figure 2.3B). Macroscopic banding is well- to poorly-developed by alternating layers of almost pure iron oxides (±quartz and occasionally chlorite) and quartz±carbonate±chlorite. Banding on the cm-scale is most clearly defined by alternating quartz and Fe-oxide rich layers. Thin mm-scale carbonate-rich bands typically occur at the transition between iron- and quartz-rich bands. Within the Fe-oxide-rich layers, slightly darker bands contain abundant microplaty hematite (Figure 2.3A and 2.3B, SI Figure 2.2). Notably, microplaty hematite grains in Fe-oxide-rich bands below 160 m depth are larger, more bladed, and more abundant relative to those above 160 m depth (Figures 2.4A and 2.4B). Microplaty hematite within the quartz bands is restricted to mm-scale jasper microbands that alternate with mm-scale carbonate-rich

microbands (Figures 2.3C and 2.3D). In sections of the core where quartz-rich bands are jasper dominated, microplaty hematite is associated with, or replaced by, fine disseminated hematite dust (SI Figure 2.3). Within thick jasper intervals, cm-scale "sub-bands" can also be found which appear opaque in PPL. We attribute these darker bands to the transition from disseminated hematite to large euhedral magnetite that are clearly visible in thin section (Figure 2.4D).

Figure 2.4 displays typical textural associations of magnetite and hematite. Microbands of hematite, magnetite, and quartz are similar to those described by Trendall (1973) for the underlying Weeli Wolli Iron Formation; specifically, Figures 2.4C and 2.4D represent Trendall's (1973) microbanding types A and B, respectively. In sections lacking hematite, euhedral magnetite is the only abundant oxide phase. The size distribution of magnetite crystals is bimodal, as two populations of large well defined euhedral crystals and smaller, more abundant subhedral crystals exist (SI Figure 2.4). When green mudstone/siltstone is interbedded with the BIF, layers of the latter are finer grained than usual and contain pyrite, which is otherwise generally absent from the BIF lithology aside from rare isolated euhedral grains (see Philippot et al., 2018 for description and composition of pyrite).

Veins within the BIF are infilled by carbonate±quartz±chlorite. Crosscutting relationships show quartz and carbonate veins disrupting hematite, magnetite, and carbonate beds. In rare cases, flecks of microplaty hematite can be seen within both the quartz and carbonate veins in sections where the veins disrupt beds containing these minerals (SI Figure 2.5). However, there is no visible gradation in microplaty hematite abundance moving away from the veins, and microplaty hematite distal to veins is restricted to thin beds, parallel to iron banding, which typically contain what appear to be primary depositional structures.

3.1.3 Silica-dominated iron formation

The distinction between BIF and silica-dominated IF is centered on variations in the Si content observed from bulk geochemistry data, with the Si-dominated IF generally containing ~10% more Si by weight than the BIF. Petrographic distinctions of this lithology from the BIF are subtle, but most obvious in the chert content. Microcrystalline quartz layers are largely present as two distinct varieties: (1) laminated red chert (jasper) and (2) massive white chert. Individual layers range from chert microbands (<1 mm) to thicker chert bands up to 15 cm thick. White layers tend to be thicker, usually massive, and are composed of almost pure quartz. Jasper layers tend to form microlayered units composed of microcrystalline quartz with disseminated fine hematite dust interbedded with carbonate- or chlorite-rich layers. Occasionally, magnetite and carbonate crystals are dispersed in the quartz-rich layers, and magnetite dispersed in the carbonate- or chlorite-rich layers. Jasper underwent a less advanced stage of silicification than the white chert, as indicated by the preserved original microlayering and partially preserved original mineralogy. In jasper intervals that appear to have been "bleached", the red jasper colour has been removed from the chert, hematite has recrystallized into semi-continuous wavy microbands of "sutured" grains, and quartz has recrystallized into larger grains. Notably, although white chert can be found throughout TCDP1, it appears to be more common towards the contact between the Boolgeeda IF and Kungarra Formation. Veins in the silica-dominated iron formation are infilled by carbonate±quartz±chlorite.

3.1.4 Green mudstone/siltstone

The green mudstone/siltstone forms three distinct intervals. The lower mudstone/siltstone around 160 m depth, ranging in color from greenish to light grey, is mainly composed of quartz, carbonate, and magnetite, with lesser amounts of muscovite and chlorite. Apatite is also present as

microscopic grains associated with iron oxides in green mudstones; specifically, magnetite+apatite+carbonate microbands alternate on the scale of 100s-of-μm to mm-scale with quartz+pyrite microbands (see SI Figure 6 of Philippot et al, 2018). Pyrite is present as both small dispersed crystals, and several large idiomorphic crystals with inclusions of quartz, carbonate, muscovite, and chlorite. Microbands of pyrite can also be found within the shale, which intermingle between large euhedral magnetite grains (Figure 2.5). Texturally, pyrite can be found as small, rounded inclusions within magnetite crystals closely associated with the bands, in irregular contact with magnetite, and overgrowing euhedral magnetite crystals (Figure 2.5C), suggesting that generations of pyrite pre-dated, co-precipitated, and post-dated the large euhedral magnetite crystals. Veins infilled with carbonate±iron oxides±quartz are also present.

The middle and upper green siltstones at ca. 148 m and 132 m depths consist of chlorite, quartz, car bonate, magnetite, and lesser amounts of pyrite. Lamination and bedding are marked by variable proportions of carbonate and chlorite. Pyrite is present either as minute crystals forming micro-layers parallel to bedding, or scarce, large idiomorphic crystals, occasionally displaying pressure shadows and hosting iron oxide inclusions. Veins are filled with chlorite±quartz±carbonate±iron oxides. Between 130 m and 128 m, a transition is observed from green (chlorite-rich) siltstones to grey (muscovite-rich) siltstones, corresponding with the transition from the Boolgeeda Iron Formation to the Kungarra Formation. This transition also coincides with a significant decrease in the iron oxide concentration from the chlorite-rich bands to the grey siltstone. Additionally, the overall proportion of carbonate increases across transitions to the grey siltstone.

3.1.5 Clastic diamictite horizon

A ca. 2 m-thick layer of clastic diamictite sediment between 151.6 m and 153.4 m depth consists of white, rounded to angular mm- to cm-scale carbonate and quartz clasts embedded within a matrix of variably sized quartz grains and chlorite, with minor amount of carbonate, apatite, ilmenite, and various sulfides. As shown by Philippot et al. (2018), this horizon is similar to the glacial diamictite described at the Duck Creek Syncline and Yerra Bluff locality (Martin, 1999; Martin et al., 2000). Generally, clasts are poorly sorted throughout the section with grains ranging in size from mm- to cm-scale, contained within a mudstone matrix. The presence of dropstones in this interval has previously been noted (SI Figure 2 from Philippot et al., 2018).

3.1.6 Grey siltstone/argillite (Kungarra Formation)

The grey siltstone is mainly composed of muscovite and quartz, with subordinate amounts of carbonate. Scarce, but large, idiomorphic crystals of pyrite may also be present. Likewise, rare and minute crystals of pyrite and magnetite occur dispersed throughout the rock. Ripple-cross lamination is a common feature throughout this lithology and local veinlets are infilled by carbonate±pyrite±quartz. The presence of abundant muscovite typically imprints a clear cleavage to the siltstone beds. Small laminae and layers (<5 cm) of calcareous mudrock, ranging in colour from light grey to greenish, can be found within the grey siltstone. These intercalations are typical in the upper part of TCDP1, the Kungarra Formation.

4. Bulk rock geochemistry

4.1 Major and trace elements

Chemostratigraphic depth profiles for selected major and trace elements are presented in Figures 2.6 and 2.7, respectively (see also Table 1 and Table 2). Two distinct intervals at 160 and 153 m depth show anomalous levels of major and redox sensitive trace elements. The interval at 160 m depth is associated with the S-rich lower green mudstone/siltstone, while the interval at 153 m depth represents the diamictite. Two smaller perturbations in trace element profiles are also found at 148 m and 132 m depth.

Iron concentrations generally decrease up-section, but anomalously low concentrations are found at 160 m, 148 m, and 132 m depth. A significant drop in Fe concentration occurs at the transition from the Boolgeeda Iron Formation to the overlying grey mudstones/argillite of the Kungarra Formation. Silica concentrations are relatively constant throughout the core, aside from the anomalous layers at 160, 148, and 132 m depth. Within these intervals, silica concentrations vary widely, comprising two distinct populations with either high SiO_2 (~80 wt. %) or low SiO_2 (~20 wt. %) contents. Generally, green mudstone/siltstone samples are included in the low Si population, while Si-dominated IF samples comprise the high Si-population.

Titanium, Al, and Mg depth plots (Figure 2.6) are almost identical, aside from higher concentrations of Ti and Al in the diamictite. All three plots display an increase in concentration above 160 m depth, apart from depleted values in Si-rich samples at 160 m, 148 m, and 132 m depth. This increase is marked by the positive shift in concentration between the lower and upper sections of the BIF lithology, and further increases accompanying the transition to the overlying Kungarra Formation mudstone/argillite.

Calcium concentrations are relatively stable throughout the core and typically less than 3 wt.%, aside from minor enrichments in the green mudstone/siltstone intervals. Concentrations of K, Na, and P are typically <1 wt.% throughout the core. Exceptions include a spike in K concentrations to 4-6 wt.% in the diamictite interval and higher concentrations (~5 wt. %) within the Kungarra Formation, Na enrichments leading up to the diamictite layer and at 132 m, and a P enrichment at 160 m. Loss on ignition (LOI) values are higher in the green mudstone/siltstone and grey siltstone/argillite intervals, as expected, given the prevalence of carbonate in these lithologies.

Sulfur concentrations are noticeably elevated within the lower green mudstone/siltstone at 160 m depth, and the diamictite at 153 m depth. Between these two intervals, concentrations increase up until the diamictite, and then progressively decrease up-section until 145 m depth. Sulfur values above 145 m in the upper BIF indicate a permanent increase in S concentrations, as S values shift from <100 ppm in the lower BIF to >400 ppm in the upper BIF. During the transition from the upper Boolgeeda Iron Formation to the Kungarra Formation, S values appear to be stable, aside from a slight increase at 130 m and a subtle decrease at 120 m depth.

Two intervals of Mn enrichment (up to 3 wt. % MnO) are present at 150-151 m and 130 m depth. Aside from these thin intervals and a subtle increase in Mn leading up to the diamictite layer, Mn concentrations remain low and stable throughout the core.

To account for detrital contributions and reveal primary enrichments in the sediments, trace element profiles are normalized to Ti where appropriate (Figure 2.7). Our decision to normalize to Ti opposed to other lithogenic elements (i.e. Al, Zr, Th, Sc) did not influence the depth profiles (SI Figure 2.6-2.8). As stated above and congruent with major element patterns, generally, large perturbations are found at 160 m and 153 m depths, with smaller anomalies at 148 m and 132 m depths.

Barium concentrations decrease above 160 m, with an order of magnitude drop in abundance from the lower to upper BIF. This shift is maintained into the overlying Kungarra Formation. Aside from this general trend, anomalies in Ba abundance include a large spread of data between 160 m to 148 m depth, and low concentrations at the transition from the Boolgeeda Iron Formation to the Kungarra Formation mudstone/argillite at 130 m.

The V depth profile peaks at 160 m and 148 m depth. The Cu profile is almost identical to V, aside from more pronounced enrichments at 132 m and 148 m. Apart from three anomalous intervals at 160 m, 148 m, and 132 m, concentrations of V and Cu remain relatively unchanged throughout the core. Cobalt concentrations are relatively stable throughout the Boolgeeda Iron Formation aside from a slight depletion at 160 m and occasional spikes in concentration in samples of green mudstone/siltstone. Cobalt concentrations decrease slightly in the Kungarra Formation. The Zn profile appears to decrease slightly up section and displays a large positive spike at 160 m depth. Other discrepancies are relatively small or represented by a single data point. Uranium enrichments relative to Ti are pronounced at 160 m, 148 m, and 132 m, but otherwise stable throughout the core. Chromium enrichments occur at 172 m, 157 m, 148 m, and 132 m. They approach 400 ppm at 157 m depth, and Ti normalized enrichments breach 10,000. These values are comparable to those reported by Konhauser et al. (2011) for the 2.32 Ga Timeball Hill formation (Figure 2.8). Lead concentrations are highest at 160 m, 148 m, and 132 m depth, and generally decrease up-section with the Kungarra Formation containing the lowest concentrations.

It is interesting to note that Ba, V, Cu, Co, Zn, and U concentration plots that are not normalized to Ti (SI Figure 2.9) exhibit near identical patterns, with peak concentrations of 1900 ppm, 200 ppm, 100 ppm, 25 ppm, 85 ppm, and 5 ppm, respectively, within the diamictite layer. All elemental concentrations increase towards the diamictite layer, and then gradually decrease

moving stratigraphically up from it. Concentrations of all six elements again increase significantly in the Kungarra Formation, suggesting a predominantly clastic origin for these elements. Correlation plots of elemental concentrations vs TiO_2 (%) confirm a strong detrital component for V, Co, Zn, and U (SI Figure 2.11). Barium and Cu have weaker, but still significant, correlations with TiO_2 (%), while Pb and Cr do not correlate at all. The non-normalized Cr abundance profile displays a similar trend, but the peak concentration occurs just below the diamictite layer at 157 m depth. Further, the ~400 ppm Cr concentration measured in this interval is greater than that found in any detrital lithology within the core, including the overlying Kungarra Formation. When not normalized to Ti, the Pb trend displays a large spike at 160 m (up to 100 ppm), and a smaller increase at 148 m. One sample within the diamictite also approaches 70 ppm. Notably, the Pb depth plot appears most similar to the S depth plot and concentrations of both elements display a linear correlation (r^2=0.6904; SI Figure 2.10).

4.2 Rare earth element and yttrium features

The REE+Y patterns for samples containing less than 1 wt.% Al_2O_3 are presented in Figure 2.9. Elevated total REE+Y concentrations are apparent above 160 m depth, along with increased Al_2O_3 and TiO_2, especially between 150-160 m within the Boolgeeda Iron Formation (Figure 2.10A). This interval coincides with a higher propensity for current structures and the observation that red jaspilitic bands are clearly disrupted. Similar to the Al_2O_3 and TiO_2 depth plots, total REE+Y concentrations appear to undergo a permanent increase above 160 m, as demonstrated by the higher values recorded in the upper BIF compared to the lower BIF. A second increase in total REE concentrations occurs coincident to the transition from the Boolgeeda Iron Formation to the

Kungarra Formation. Total REE+Y concentrations display a strong positive correlation with Al_2O_3 concentrations (Figure 2.10C).

All non-clastic lithologies within the Boolgeeda Iron Formation display a La/Lu ratio < 1, which is indicative of HREE enrichment. The highest La/Lu values within the Boolgeeda Iron Formation occur at 160 m depth and within the diamictite layer, above which there appears to be a progressive decrease back to subdued values found in the BIF. Within the overlying Kungarra Formation, the REE+Y profile flattens, and La/Lu ratios often exceed 1 (Figure 2.10A).

Y/Ho ratios vary widely throughout the core. Most igneous rocks and epiclastic sediments have a Y/Ho weight ratio of 28 and a molar ratio of 52 (Bau, 1996; and references therein), whereas large Y/Ho ratios are typical of aqueous and highly evolved magmatic systems (Bau et al, 1996). Aqueous fluids and their precipitates are commonly characterized by superchondritic Y/Ho ratios (values > 26.22 w/w as per Pack et al., 2007), with molar ratio values as high as 90 being reported in modern seawater (Zhang et al., 1994; Bau et al., 1997; Nozaki et al., 1997; Bau and Dulski, 1999). Elevated Y/Ho ratios are prevalent throughout the Boolgeeda Iron Formation, typically ranging between 35 and 50 (w/w). The Y/Ho ratio appears to decrease slightly up-section, with the lowest values displayed in the Kungarra Formation. Further, Y/Ho data appear to vary sinusoidally throughout the core, with depressions possibly corresponding to periods of enhanced detrital input (Figure 2.10A).

Post Archean Australian Shale normalized Eu anomalies (Eu/Eu*$_{PAAS}$; Taylor and McLennan, 1985) were calculated using Eu/Eu$^*_{PAAS}$ = Eu/([2/3]Sm + [1/3]Tb) (Bau and Dulski, 1996). A positive Eu anomaly is prevalent throughout all lithologies of the TCDP1 core, but overall the Eu anomaly decreases up-section, with the lowest values found in the Kungarra Formation (Figure 2.11A). Generally, samples with less Al_2O_3 have higher Eu anomalies (Figure 2.11C).

Detecting the presence of Ce anomalies in seawater precipitates can be complicated by anomalous abundances of La. To avoid false negative Ce anomalies that may appear when using the equation Ce/Ce* = Ce/(0.5La + 0.5Pr), we plotted Ce/Ce* versus Pr/Pr* to identify true negative Ce anomalies as prescribed by Bau and Dulksi (1996), where (Pr/Pr*) = Pr/(0.5Ce + 0.5Nd) (Figure 2.11B). Here it can be seen that while some true negative Ce anomalies (Ce/Ce*<1.05 and Pr/Pr* >1.05) and a few probable positive Ce anomalies (Pr/Pr*<0.95) exist, most of the data show false negative Ce anomalies due to positive La anomalies (Ce/Ce*<0.95, 0.95<Pr/Pr*<1.05). We thus focus on Pr/Pr* as an indicator of true Ce anomalies. The Pr anomaly shows significant variation throughout the core, with the most positive values (most negative true Ce anomalies) in upper iron formation interval, bracketed by rare negative Pr anomalies (positive Ce anomalies) (Figure 2.11A). Similar to Eu/Eu*, true Ce anomalies indicated by Pr/Pr* appear progressively attenuated with increasing detrital input, approaching crustal values with increasing Al_2O_3 (Figure 2.11C).

4.3 Chemical Index of Alteration (CIA) and intervals of anomalous enrichment

The Al_2O_3-(CaO°+Na_2O)-K_2O plot for detrital lithologies in the TCDP1 core is presented in Figure 2.12, where CaO° represents the proportion of total Ca in the silicate fraction only. Data from the green mudstone/siltstone lithology plot close to the boundary of the ternary diagram defined by Al_2O_3 and CaO°+Na_2O, with K_2O proportions rarely exceeding 10%. The range of these values can be explained by the weathering of ultramafic to mafic source rocks (see discussion below). Conversely, data for the grey siltstone/argillite of the Kungarra Formation lies to the right of the boundary, and typically displays higher K_2O proportions, between 10 and 20%, reflected in the higher proportions of muscovite present in this section. This trend is typical of felsic source rock

weathering, suggesting that a change in source material occurred during the transition from the Boolgeeda Iron Formation to the Kungarra Formation. The sandstone/siltstone and diamictite contain the highest proportion of K_2O (25-30%) (Figure 2.12). These points fall within the average cluster of Fortescue shales, Jeerinah shales, and Mount McRae shales as plotted by Pecoits et al. (2009). As all shale formations listed above were deposited before, and lie stratigraphically beneath the Boolgeeda Iron Formation, it is possible that the diamictite represents an average of the weathering products of these formations and their source-rocks. In general, the chemical index of alteration (CIA) values for shales in the TCDP1 core are relatively high, with some values approaching 90, suggesting intense chemical weathering of some source rocks.

4.4 Fe speciation

The concentration of Fe contained within each sequential extraction fraction, collected using the method of Poulton and Canfield (2005), is shown in Figure 2.13A. Iron is dominantly contained in the Fe_{Mag} and Fe_{PRS} fractions, with lesser amounts present in the Fe_{Py}, Fe_{Carb}, and Fe_{Ox1} fractions. Iron concentrations in the Fe_{Ex} and Fe_{Ox2} fractions were negligible in all samples. Highly reactive Fe (Fe_{HR}) is defined as the sum of all fractions of Fe highly reactive towards H_2S on short diagenetic time scales (i.e. $Fe_{HR} = Fe_{Carb} + Fe_{Ox1} + Fe_{Ox2} + Fe_{Mag} + Fe_{Py}$; Canfield et al., 1992; Raiswell and Canfield, 1998; Poulton et al., 2004). Total Fe (Fe_T) represents the sum of Fe in all sequential extraction fractions. The degree of pyritization is defined as the proportion of pyritized Fe within the highly reactive Fe pool (Fe_{Py}/Fe_{HR}; Berner, 1970). Total Fe to Ti (Fe_2O_3/Ti) decreases up core, with particularly low ratios occurring within the diamictite and higher ratios present around 160 m, 148 m, and 132 m (Figure 2.13B). Ratios of Fe_{HR}/Fe_T and Fe_{Py}/Fe_{HR} increase up core, with clear increases in the ratios occurring at 160 m depth (Figure 2.13C). The Fe_{HR}/Fe_T ratio exceeds

0.4 above 160 m depth, and remains above this value aside from a single point at 155.56 m. The Fe_{Py}/Fe_{HR} ratio exceeds 0.7 at 109 m within the Kungarra Formation but remains below this threshold in all other samples. The Fe_{Ox}/Fe_{HR} and Fe_{Carb}/Fe_{HR} ratios both display the highest values at ~148m. The Fe_{Carb}/Fe_{HR} depth profile also displays a pronounced enrichment at 160 m whereas the Fe_{Ox}/Fe_{HR} depth profile does not.

5. Discussion

5.1 Boolgeeda Iron Formation Composition and Genesis

It is commonly held that IF sediments record contemporary ocean chemistry due to the high surface reactivity of primary precipitates (i.e. ferric oxyhydroxide particles or Fe(III)-Si gels) and their propensity to adsorb elements directly from seawater, as supported by the comparable rare-earth element (REE) signatures of IF and modern seawater (e.g. Bau and Dulski, 1996; Bau, 1999; Alexander et al., 2008). Therefore, IF geochemical analyses have been used to reconstruct temporal trends in marine trace element concentrations throughout Earth history (e.g. Konhauser et al., 2009). Minerals composing IF are not primary, but instead reflect diagenetic and metamorphic transformation of primary precipitates (Klein, 2005; Konhauser et al., 2017). However, if the system has remained closed, IF should preserve primary geochemical signatures of the water column. A detailed assessment of petrogenesis of the Boolgeeda Iron Formation is required in order to determine whether or not diagenesis, metamorphism, or secondary fluids have significantly altered sample composition at the whole-rock scale.

Hematite is interpreted to be an early diagenetic phase resulting from the dehydration and crystallization of a primary Fe(III)-Si gel (Fischer and Knoll, 2009; Percak-Dennett et al., 2011) or ferric oxyhydroxides precipitated from the water column (Konhauser et al., 2005). Three forms

of hematite are prevalent in the Boolgeeda Iron Formation: (1) microplaty hematite, (2) fine disseminated hematite dust, and (3) thin continuous bands of "sutured" hematite grains. Microplaty hematite and disseminated hematite dust are interpreted to be the most primary Fe phases preserved in the Boolgeeda Iron Formation, supported by textural relationships with other minerals such as inclusions of microplaty hematite in large euhedral magnetite grains (Figures 2.3A, 2.3B). This conclusion is consistent with the previous work of Spencer and Percival (1952), James (1954), Trendall (1973), Ahn and Buseck (1990), Beukes and Gutzmer (2008), Pecoits et al. (2009), Bekker et al. (2010), and Sun et al. (2015). However, Rasmussen et al. (2015, 2016, 2017) have recently proposed that hematite dust is neither primary nor an early diagenetic component of IF. Instead, they consider microplaty hematite to be an alteration product of earlier ferrous iron-silicate nanoparticles. If conclusions drawn by these authors hold true and hematite is a product of oxidizing fluids modifying the redox state and minerology of IF post deposition, then intervals containing hematite may be inappropriate for examining ancient redox conditions. We do, in rare cases, see flecks of microplaty hematite within quartz and carbonate veins in sections where the veins disrupt beds containing these minerals (SI Figure 2.5). These flecks were likely incorporated into the veins as fluids pulled grains from the adjacent primary beds. With that said, as there is no visible gradation in microplaty hematite abundance moving away from the veins, we have no reason to believe that hydrothermal alteration led to the genesis of microplaty hematite. Further, microplaty hematite distal to veins is restricted to thin beds, parallel to iron banding, which typically contain primary depositional structures. If oxidizing fluids produced the microplaty hematite, we would expect grains to be present on a larger scale throughout the section, and not restricted to cm scale beds. We, therefore, consider microplaty hematite grains and disseminated hematite dust to be relatively early diagenetic features, resulting from the dehydration and

crystallization of primary ferric oxyhydroxide particles or Fe(III)-Si gel formed in the water column.

Microplaty hematite is more common in Fe-rich mesobands while disseminated hematite dust is prevalent in Si-rich mesobands (jasper). The microplaty hematite and disseminated hematite dust are interpreted to have formed from the same primary Fe(III)-Si gel phase, but to have undergone different diagenetic modifications as a result of their contrasting background matrices (i.e. Si dominated vs Fe dominated). These contrasting matrices on the mesoband scale are likely the result of temporal changes in seawater Fe and Si content during deposition (Trendall, 2002) as amorphous Si was carried to the ocean floor by precipitated ferric oxyhydroxides (Fischer and Knoll, 2009) in the form of an Fe(III)-Si gel. Silica rich bands resulted when hydrothermal Fe concentrations were depressed relative to Si, and Fe rich bands resulted when Fe(III) precipitation outpaced Si precipitation, perhaps with seawater Si drawdown due to extensive Fe precipitation.

Primary Fe(III) precipitates trapped in Si-rich layers were likely prevented from ripening into microplaty hematite as a result of insufficient space due to rapid lithification of chert bands during early diagenesis. It is possible that extensive burial and heating led to silica dissolution-precipitation creep (DPC) within some of the Si-rich microbands (den Brok and Spiers, 1991; Egglseder et al., 2016; Egglseder et al., 2018). Dissolution-precipitation creep can occur at pressures as low as 2-3 bar (Greene et al., 2009) when applied stress causes Si dissolution at quartz grain boundaries. Silica is then transported by diffusion to areas of low Si concentrations where it precipitates (Bons and den Brok, 2000). This mechanism would have allowed disseminated hematite dust to concentrate within Si mesobands and coalesce into thin bands of sutured hematite or magnetite depending on the amount of buried carbon present. Evidence for this process occurring include bands of sutured Fe oxides that have formed within pure Si layers (Figure 2.4C).

Further, cm-scale "sub-bands" are present within thick jasper intervals that appear more opaque and darker red in PPL (Figure 2.4D). These layers capture the transition from primary disseminated hematite dust to large euhedral magnetite grains. These sub-bands likely represent periods when sufficient organic C was buried with Si rich Fe(III)-Si gel to promote the transformation of disseminated hematite dust into magnetite during DPC and metamorphism. Iron oxide-rich mesobands containing significant microplaty hematite are likely the result of a shortage of reduced C input during burial, allowing the preservation and ripening of large microplaty hematite grains. Conversely, the lack of hematite in sections dominated by euhedral magnetite suggests primary Fe(III) phases within these intervals have been consumed by the formation of magnetite during metamorphism, likely the result of a reaction with reduced C compounds buried originally with the sediments. Similarly, the prevalence of large "bladed" microplaty hematite in iron oxide-rich mesobands below 160 m depth, and apparent absence above, may reflect a larger scale change in reduced C supply separating depositional conditions above and below 160 m.

Two varieties of chert exist in the Boolgeeda Iron Formation: (1) laminated red chert (jasper) and (2) massive white chert. Both varieties of chert are interpreted to be diagenetic; however, jasper is interpreted to have formed before the massive white chert. Quartz composing the massive white chert appears to have recrystallized into larger euhedral quartz grains lacking any trace of disseminated hematite thereby giving it a "bleached" appearance. Preserved reaction fronts captured in thin section highlight lateral mineralogical changes within microbands and mesobands of bleached and jasper zones; most notably, disseminated hematite has concentrated into sutured wavy microbands. As alluded to above, it is likely that "bleaching" occurred as an artifact of DPC during diagenesis and regional-scale deformation (Egglseder et al., 2016). The

competency contrast between the Boolgeeda IF and Kungarra Formtion may therefore explain the increased prevalence of white chert towards the contact between the two units.

The large euhedral magnetite within the Boolgeeda BIF lithology is clearly secondary, and likely metamorphic. Magnetic remanence and susceptibility analyses (Carlut et al., 2018) as well as sequential Fe extractions (Figure 2.13) confirm the ubiquitous presence of magnetite throughout the Boolgeeda IF. Inclusions of hematite and quartz within magnetite (Figure 2.3B) and the even distribution of euhedral magnetite throughout the Boolgeeda BIF (i.e. little association with "primary" banding features) support the interpretation that this is a relatively late phase overprinted on sediments of earlier diagenetic origin. The bimodal size distribution of euhedral magnetite (SI Figure 2.4) is likely the result of two separate regional scale metamorphic events that promoted the growth of euhedral magnetite from earlier sediments. The larger magnetite likely formed first while the smaller magnetite formed during a second event when BIF sediments were under higher pressures, resulting in their smaller size. Notably, Carlut et al. (2018) detected 2 Verwey transition temperatures in TCDP1 magnetite between 148 m and 146 m depth, and suggested localized Si-substitution into magnetite to explain this signature. It is possible a secondary silicification event affected this 2 m interval. However, the anomalous Verwey transition temperature is not found anywhere else in TCDP1, and therefore, there is no reason to believe alteration of the core in this manner was pervasive.

Chlorite within all lithologies, particularly prevalent in the green mudstone/siltstones, suggests low-grade metamorphism; the upper limit is prehnite-pumpellyite to lower greenschist facies. Notably, martite and geothite are absent from thin sections, suggesting microplaty hematite within the Boolgeeda Iron Formation is not a paragenetic product of alteration typically associated with the formation of high grade hematite ore. Further, minnesotaite and stilpnomelane appear

absent from thin section, attesting to the pristine nature of the iron bands. The prevalence of chlorite in the green mudstone/siltstones is likely the result of metamorphic alteration of primary clay material that composed these intervals.

Philippot et al. (2018) documented the presence of multiple pyrite textures within TCDP1, including nodular pyrite aggregates, clusters of microcrystalline pyrite, inclusion free pyrite overgrowths around pyrite framboids, finely disseminated euhedral to subhedral pyrite crystals, euhedral to subhedral pyrite crystals aligned with bedding and conforming to soft sediment deformation features, as well as bands of densely packed microcrystalline pyrite aggregates. The two most prevalent phases of pyrite in the Boolgeeda Iron Formation, primarily within the green mudstone/siltstone intervals, are: 1) large euhedral pyrites are commonly found in thin horizontal layers parallel to primary bedding and 2) smaller euhedral crystals that cross-cut horizontal bedding and are brighter in reflected light. We suggest the large euhedral pyrites are a relatively primary phase formed early during diagenesis in shallow pore waters, and may represent the diagentic product of primary mackinawite ($Fe_{1+x}S$; Berner, 1970). Support for this exists in inclusions of this phase within large euhedral magnetite crystals. The brighter euhedral pyrite postdates and is systematically associated with primary pyrite. The systematic association of secondary pyrite with primary pyrite and lack of it elsewhere suggest that no additional input of sulfur or iron has occurred. Instead, secondary pyrite is likely the result of local remobilization or recrystallization of pre-existing pyrite. Trace element composition of pyrite acquired by LA-ICP-MS further supports the early diagenetic to syngenetic formation of pyrite layers (Philippot et al., 2018).

Carbonates within the Boolgeeda Iron Formation are primarily found in the green mudstone/siltstone intervals in thin bands, as reflected in the high LOI values found within these

layers. The carbonates are typically dolomitized, supported by the high Mg concentrations in the green mudstones/siltstones. The P enrichment at 160 m is tied to the presence of apatite in this interval. Notably, microbands of Fe-oxide+apatite+carbonate can be found alternating with microbands of quartz+pyrite down to the 10s-100s of μm scale in the green mudstone/siltstone (SI Figure 6 of Philippot et al., 2018). The Fe-oxide+apatite+carbonate bands are likely the diagenetic product of remnant P-rich organic debris deposited with the detrital sediments at 160 m depth. The influx of organic rich debris at 160 m depth may have occurred as a result of increased primary productivity in shallow marine settings. Inter-banded quartz+pyrite layers, on the other hand, may reflect remnants of microbial sulfate reduction spurred by increased organic carbon input. This conclusion is supported by strong S-isotope fractionations (δ^{34}S approaching -40‰) in the pyrites, suggesting microbial sulfate reduction under non-S-limiting conditions (Philippot et al., 2018). In short, pyrite layers reflect preserved interfaces where rising sulfide produced by SRB reacted with reduced iron in the water column to form pyrite. Apatite rich layers reflect intervals where organic carbon delivered to the sediment outpaced consumption by microbial metabolism, and thus excess C and P not used up in post depositional Fe reduction were diagenetically transformed into apatite.

5.2 Precipitated and detrital components in the Boolgeeda Iron Formation

A transition from precipitated sediments reflecting marine conditions to sediments increasingly dominated by continentally sourced detrital input is observed stratigraphically upward through the TCDP1 core. This progressive increase of clastic material up-section is also reported in surface expressions of the Boolgeeda Iron Formation (Morris, 1993), as the BIF grades into the overlying siltstones of the Kungarra Formation.

The BIF lithology marks the marine endmember of the TCDP1 core as reflected by its REE+Y composition. Shale normalized (PAAS) REE+Y patterns for samples that contain less than 1 wt.% Al_2O_3 display consistent LREE depletions (La/Lu values < 1), high Y/Ho ratios (>26), and positive La, Y, and Eu anomalies (Figure 2.9). Notably, LREE depletion, positive La and Gd anomalies, and elevated Y/Ho ratios, have characterized seawater since the early Archean (Bau and Dulski, 1996; Nozaki et al., 1997; Bolhar et al., 2004; Alexander et al., 2008; Frei et al., 2016). Metal oxyhydroxides, the proposed precursor phases of IF, have long been known to play an important role in the removal of REE+Y from seawater (e.g., Bau, 1991; Koeppenkastrop and De Carlo, 1992; Bau, 1999; Ohta and Kawabe, 2001; Bau and Koschinsky, 2009), and thus chemically precipitated early Precambrian IFs (>2.3 Ga) typically display Sm/Yb < 1 and Eu/Sm > 1, large positive Eu anomalies, and significant LREE depletion (Bau and Möller, 1993; Planavsky et al., 2010).

Sediments within the sandstone/siltstone and diamictite layers, as well as the grey siltstone/argillite of the Kungarra Formation, display relatively flat PAAS normalized REE+Y patterns, and lack anomalies characteristic of seawater (SI Figure 2.14). This departure from a seawater-like REE+Y and elevated levels of lithogenic elements (i.e. Al, Ti) are characteristic of continentally-derived shales. These lithologies are strongly influenced by, or perhaps represent, the continental endmember of the depositional system at various periods in basin history.

Generally, total REE, La/Lu ratios, and concentrations of lithogenic elements increase up section, while Y/Ho ratios decrease. Decreasing Fe concentrations up-section further reflect the transition from deeper shelf conditions promoting IF deposition to shallow water conditions with high detrital input. This general pattern is interrupted by a more pronounced influx of detrital material between 160 and 148 m depth, as indicated by low Y/Ho ratios, high La/Lu ratios, and a

spike in total REE, TiO$_2$, and Al$_2$O$_3$ concentrations (Figure 2.10A). This interval coincides with the appearance of current generated structures, the loss of a positive La anomaly in sediments, and the appearance of abundant chlorite in thin section that likely resulted from low grade metamorphism of the original clay material. Collectively, these indicators are similar to the detrital contamination pattern observed by Veihmann et al. (2015). The variable Fe concentration data between 160 and 148 m depth is the result of sampling alternating Fe-rich and Fe-poor (Si-rich) bands within the BIF lithology, as well as the mixing of the BIF lithologies and detrital input containing moderate Fe concentrations.

Detrital input appears to subside above 148 m depth, and it remains low until deposition of the Kungarra Formation. A hiatus in detrital input is supported by a sharp drop in total REE, declining concentrations of TiO$_2$ and Al$_2$O$_3$, a progressive increase in the Y/Ho ratio, a progressive decrease in the La/Lu ratio, and a return to BIF lithologies at 148 m depth (Figure 2.10A). Although indicators of detrital influx are subdued between 148 m and 132 m, they remain higher than levels within the BIF located below 160 m depth. This suggests a permanent change in the amount of clastic input, and perhaps a significant shift in the depositional environment leading up to deposition of the Kungarra Formation.

The periodic nature of detrital influx is interpreted to reflect changes in base level within the basin. As base level fell, detritus became an increasingly dominant component of the sediment. As base level rose, the depositional setting moved seaward and detritus-starved deposition resumed deeper on the shelf. The result is the sinusoidal pattern observed in all three plots – La/Lu, Y/Ho, and total REE (Figure 2.10A).

The dichotomy in Si concentration at 160 m, 148 m, and 132 m depth is the result of interlaying between chert-rich sections of the BIF lithology and green mudstone/siltstone in these

intervals. This is highlighted by plotting total Fe_2O_3 (wt. %) vs. SiO_2 (wt. %) (Figure 2.10B). The log-log plot displays two curved trends that are distinguished by the lithologies that compose them. The high SiO_2 population follows the trend defined by the BIF and silica-dominated IF samples, while the low SiO_2 population represents a merger of the first trend and a second trend defined by detrital lithologies (i.e. sandstone, diamictite, grey siltstone/argillite, green mudstone/siltstone). Where the green mudstone/siltstone is interbedded with BIF, BIF bands become thinner and pyrite becomes more prevalent. The inter-banding in this interval represents deposition on the boundary of conditions promoting BIF conditions and those promoting the influx of detrital material. Pyrite formation may be the result of higher concentrations of S and organic C accompanying the influx of detrital material, as illustrated in Figure 2.14. Higher sulfate in the water column and increased input of clastic and organic matter would intermittently prevent IF deposition and promote pyrite rich green mudstone/siltstone deposition. Further, higher S and reduced C delivery to sediments may have resulted in the microbanding of Fe-oxides+apatite+carbonate and quartz+pyrite down to the 10s-100s of μm scale within the green mudstone/siltstone, as discussed above.

The spike in K concentrations within the diamictite interval and the Kungarra Formation are attributed to a compositional change in source rock being weathered. Detrital input in these intervals was likely sourced from felsic source rocks containing higher proportions of K-rich minerals, which were subsequently broken down into K-rich clays during burial. Support for this theory is found in Figure 2.12. Two weathering trends are defined by the green mudstone/siltstone samples and the diamictite and Kungarra Formation samples. Shales from the Kungarra Formation and diamictite appear to be sourced from more felsic lithologies in the Hamersley Basin, while the green mudstone/siltstone appears to be sourced from rocks with compositions similar to Pilbara, Fortescue, and Weeli Wolli basalts.

5.3 Redox proxies, oxidative weathering, and trace element enrichments during deposition of the Boolgeeda Iron Formation

The establishment of mildly oxidizing surface waters during deposition of the Boolgeeda Iron Formation are supported by true negative Ce anomalies (as indicated by positive Pr/Pr*) captured by the BIF lithology (Figure 2.11). The presence of negative Ce anomies is typical for Paleoproterozoic and Neoproterozoic IF (Laajoki, 1975; Fryer, 1977a,b; Graf, 1978; Barrett et al., 1988; Klein and Beukes, 1989; Viehmann et al., 2016), but is generally absent from IF older than 2.5 Ga, as oxygen levels were too low to oxidize Ce^{3+} to Ce^{4+}. The presence of negative Ce anomalies in the Boolgeeda Iron Formation, which are not artifacts of positive La anomalies (Figure 2.11B), confirms the conclusions of Philippot et al (2018) that oxygen levels in shallow marine settings had reached appreciable levels by 2.45 Ga. The distribution of Ce anomalies in Boolgeeda Iron Formation sediments further suggests that elevated oxygen levels were pervasive within the shallow marine realm and stable above the threshold required to produce a negative Ce anomaly.

The largest negative Ce anomalies are found within the middle of the upper and lower BIF intervals (Figure 2.11A). The sinusoidal nature of the Ce anomaly depth plot is interpreted to reflect background negative Ce anomalies captured by primary BIF precipitates being suppressed by detrital influxes. Support for this theory exists in the depression of negative Ce anomalies (as indicated by Pr/Pr*) with increasing Al_2O_3 (%) content (Figure 2.11C); the largest negative Ce anomalies occur in samples with the lowest Al_2O_3 concentrations. This would suggest detrital material lacking a Ce anomaly masks the background negative Ce anomaly of the water column during periods of high detrital input. This interpretation fits with our prior discussion on intervals of high detrital influx and associated changes in the Ti, Al, and Total REE+Y depth plots, as well

70

as the La/Lu and Y/Ho plots. A few points indicating positive Ce anomalies appear to cap both the upper and lower BIF unit; this may indicate oxidative scrubbing of Ce from waters containing lesser or no Ce background negative anomaly (e.g., slightly lower degrees of water column oxygenation or potential stratification).

The mechanism responsible for imparting the Ce anomaly pattern on Boolgeeda Iron Formation sediments is outlined in Figure 2.14. As reduced hydrothermal solutions containing dissolved Fe(II) were upwelled onto the shelf, they interacted with oxygen and precipitated as Fe(III) oxyhydroxides, which subsequently sorbed Si and settled as an Fe(III)-Si gel. Particles precipitating in the shallow, more oxic zone captured a Ce depleted REE+Y signature from seawater, while less oxic waters resulted in minor Ce oxidation without generating significantly Ce-depleted seawater, resulting in iron precipitates that bore a mild positive Ce anomaly by direct enrichment in particle-reactive Ce(IV).

Some Boolgeeda Iron Formation samples contain both a negative Ce anomaly and a positive Eu anomaly (Figure 2.9). It may have been possible to preserve positive Eu anomalies from hydrothermal vent fluids emerging at depth and to also capture negative Ce anomalies from an overlying oxic water column at the transition from anoxic to oxic conditions. Anoxic conditions would have promoted the long-distance transport of REE+Y in the deep ocean, as REE+Y removal from the water column by precipitating Fe(III) and Mn(IV) oxyhydroxides would have been limited to shallow oxic environments. As deep reducing ocean waters were upwelled onto the continental shelf, positive Eu anomalies could have been captured by Fe(III) oxyhydroxides precipitating at, or above, the chemocline.

Positive Eu anomalies disappear up section, best demonstrated by the moving average curve (black line) in Figure 2.11A. This is attributed to waning hydrothermal influence as the

depositional environment became shallower, approaching the onset of Kungarra Formation deposition. The loss of a positive Eu anomaly may have been compounded by detrital dilution of primary seawater signatures (Figure 2.11C), similar to the Ce anomaly.

Amongst the large-scale transition from deep to shallow water deposition - corresponding to waning hydrothermal fluids and higher detrital input - there are periods of punctuated trace element influx into the sediments. Two major intervals occur at 160 m and 153 m depth, while two relatively minor intervals are found at 148 m and 132 m depth (Figure 2.7). The interval at 153 m represents the clastic diamictite, while the intervals at 160 m, 148 m, and 132 m depth represent interlaying of green mudstone/siltstone and Si-dominated IF associated with variable TiO_2 and Al_2O_3 concentrations and dichotomous SiO_2 concentrations (>65% or <40%).

By comparing the TiO_2 normalized (Figure 2.7) and un-normalized (SI Figure 2.9) major and trace element depth plots, the role of detrital versus autochthonous controls on IF trace element profiles can be distinguished. In the un-normalied plots, Ba, V, Cu, Co, Zn, U, and Cr all display elevated concentrations between 160 m and 148 m depth, peaking within the diamictite layer. Concentrations are also relatively high within the green mudstone/siltstone intervals and the Kungarra Formation, suggesting a strong detrital component contributes to total elemental concentrations. In fact, correlation plots of V, Co, Zn, and U versus Ti concentrations suggests detrital material represents the largest proportion of these elements' concentrations throughout the Boolgeeda Iron Formation (SI Figure 2.11). Deposition of the diamictite likely occurred at the climax of base level fall within the basin; the progressive increase in trace element concentrations leading up to the diamictite and subsequent decreases moving stratigraphically up from it likely reflects a regressive-transgressive cycle. The onset of this cycle may have coincided with glaciation, as supported by dropstones previously identified within the diamictite interval

(Philippot et al., 2018). The green mudstone/siltstone intervals inter-banded with the Si-dominated IF lie at the margins of the regressive-transgressive cycle. As discussed above, these represent periods when the depositional environment was on the boundary between depositional conditions promoting primary BIF deposition and conditions dominated by detrital influx.

When normalized to TiO_2, only thin intervals of trace element enrichment at 160 m, 148 m, and 132 m remain. This suggests that Ba, V, Cu, Co, Zn, U, and Cr are all enriched in continental material, but that autochthonous enrichments are also important at 160 m, 148 m, and 132 m depth. The largest autochthonous enrichment occurs at 160 m, as concentrations of all elements in the Ti normalized plots are highest at this depth. Notably, iron speciation suggests a major change in the redox state of the water column at 160 m, supported by an increase in the Fe_{HR}/Fe_T ratio (Figure 2.13). This dramatic change in Fe speciation may be reflected in the disappearance of coarse grained microplaty hematite above 160 m depth, and is accompanied by a shift in S concentrations from <100 ppm in the lower BIF to >400 ppm in the upper BIF interval (Figure 2.6), which may indicate an increase in the background marine S reservoir. This transition is also reflected by the S-isotopic data from pyrites at 160 m depth, which show the disappearance of S-MIF ($\Delta^{33}S = 0‰$) and $\delta^{34}S$ values approaching -40‰ (Philippot et al., 2018). This suggests oxic atmospheric conditions capable of preventing MIF-S preservation and marine S concentrations high enough to sustain sulfate reduction under non-S-limiting conditions see Philippot et al., 2018 for a discussion). Textural evidence for strong sulfate reduction near 160 m depth may be found in pyrite microbeds (Figure 2.5), in which small euhedral grains of pyrite lie parallel to primary bedding and are interstitial between larger magnetite grains. Small rounded pyrite inclusions are also found in some of the larger euhedral magnetite grains, supporting the

early diagenetic formation of pyrite in this interval. It is possible these beds were produced biogenically during *in situ* sulfate reduction in shallow pore waters.

Following Philippot et al (2018), we suggest the oxidative weathering of continental sulfides can explain the observations listed above. Support for continental weathering of sulfides is found in the Cr/Ti ratios, which are comparable to elevated values within the Timeball Hill formation previously reported by Konhauser et al. (2011). Those authors attributed the elevated Cr concentrations to acid weathering events occurring as O_2 began to increase in the lead up to the GOE. Values from the Boolgeeda Iron Formation, superimposed on the temporal Cr/Ti trend of Konhauser et al. (2011), correspond well with elevated Cr/Ti ratios observed around the GOE (Figure 2.8). High S concentrations associated with pyrite grains in the diamictite suggest that a reduced continental S source was, at the very least, available for oxidation, transport, and precipitation in marine sediments (Philippot et al., 2018).

Although marine S concentrations appear to have increased between deposition of the upper and lower BIF intervals, euxinic conditions were not prevalent. The Fe_{Py}/Fe_{HR} ratio approaches the threshold of euxinic conditions (0.7) at 160 m but does not breach this threshold aside from one sample at 109 m depth within the Kungarra Formation mudstone (Figure 2.13). This is not unexpected, as euxinic conditions would prevent the deposition of the IF. It is possible that euxinic conditions occurred in shallower environments proximal to continental margins. Fed by the oxidative weathering of continental sulfides, sulfate generated by sulfide oxidation would have dissipated further into the basin. The Kungarra Formation data suggests that euxinic conditions are approached as the depositional setting shallows towards a more sulfate-rich environment.

Aside from the diamictite layer and interval at 160 m depth, S concentrations do not exceed 1 wt. %, and MIF-S does not disappear at any other depth in the core (Philippot et al., 2018). The lack of significant S enrichments within anomalous intervals at 148 m and 132 m depth indicates against oxidative weathering of continental sulfides as a driver for these trace element enrichments, at least to the extent of that observed at 160 m depth. We propose enrichments at 148 m and 132 m are mechanistically different; they are more likely the result of local base level dynamics transferring material across the chemocline separating anoxic and oxic settings and concentrating trace elements at the interface between IF deposition and clastic sedimentation. This interface represents a geochemical boundary separating input from shallow waters with a more active sulfur cycle from anoxic Fe(II)-rich deep waters, favouring iron precipitation and trace element enrichment at their intersection.

6. Summary and Conclusion

The Boolgeeda Iron Formation and overlying sediments of the Kungarra Formation provide a snapshot of marine conditions around GOE time. Major and trace element concentrations coupled with Fe speciation suggest shallow marine conditions that were mildly oxic and anoxic ferruginous conditions in deep water. These background conditions appear to have been intermittently perturbed by interaction with shallow waters that were more trace-element and sulfur rich. We suggest that these events were driven by oxic weathering of sulfides and locally increased marine S concentrations, particularly in shallow marine environments proximal to the continental margin. Within the Boolgeeda IF, one such event is preserved at 160 m depth. This horizon is marked by a dramatic change in Fe speciation, a large increase in Ti normalized trace element concentrations, S isotope signatures characteristic of atmospheric oxygenation (Philippot et al., 2018), and perhaps

an increase in reduced carbon input as reflected by the disappearance of coarse grained microplaty hematite above 160 m depth. Further, it separates two intervals of BIF with drastically different S concentrations. These events may mark significant changes in the balance between continental and marine S sources and sinks.

Traditional proxies for redox conditions may be masked by the influx of detrital materials. Shifts in detrital flux are most likely the result of baselevel fluctuation and represent local changes rather than a global phenomenon. The TCDP1 core preserves a shallowing upward sequence associated with waning hydrothermal input, and a punctuated interval of detrital input between 160 m and 148 m depth. Iron speciation suggests that the shallower deposits record coastal waters that approached euxinic conditions.

The transition from the Boolgeeda IF to the overlying Kungarra Formation marks a significant change in the local depositional environment. Yet, the termination of BIF deposition and eventual deposition of glacial sediments that comprise the Meteorite Bore Member of the Kungarra Formation indicate a significant global transition that overprints the local signatures preserved in TCDP1. The Boolgeeda IF and Kungarra Formation appear to mark the onset of these global changes, culminating in the GOE.

7. References (Chapter 2)

Ahn, J.H., Buseck, P.R., 1990. Hematite nanospheres of possible colloidal origin from a Precambrian banded iron formation. Science 250, 111-113.

Alexander, B.W., Bau, M., Andersson, P., Dulski, P., 2008. Continentally-derived solutes in shallow Archean seawater: Rare earth element and Nd isotope evidence in iron formation from the 2.9 Ga Pongola Supergroup, South Africa. Geochimica et Cosmochimica Acta 72, 378-394.

Alibert, C., McCulloch, M.T., 1993. Rare earth element and neodymium isotopic compositions of banded iron formations and associated shales from Hamersley, Western Australia. Geochimica et Cosmochimica Acta 57, 187-204.

Ayres, D.E., 1972. Genesis of Iron-bearing minerals in banded iron formation mesobands in the Dales Gorge Member, Hamersley Group, Western Australia. Economic Geology 67, 1214-1233.

Barley, M.E., Pickard, A.L., Sylvester, P.J., 1997. Emplacement of a large igneous province as a possible cause of banded iron formation 2.45 billion years ago. Nature 385, 55-58.

Barrett, T.J., Fralick, P.W., Jarvis, I., 1988. Rare-earth-element geochemistry of some Archean iron formations north of Lake Superior, Ontario. Canadian Journal of Earth Sciences 25, 570-580.

Bau, M., 1991. Rare-earth element mobility during hydrothermal and metamorphic fluid-rock interaction and the significance of the oxidation state of europium. Chemical Geology 93, 219-230.

Bau, M., Möller, P., 1993. Rare earth element systematics of the chemically precipitated component in Early Precambrian iron formations and the evolution of the terrestrial atmosphere-hydrosphere-lithosphere system. Geochimica et Cosmochimica Acta 57, 2239-2249.

Bau, M., 1996. Controls on the fractionation of isovalent trace elements in magmatic and aqueous systems: Evidence from Y/Ho, Zr/Hf, and lanthanide tetrad effect. Contributions to Mineralogy and Petrology 123, 323-333.

Bau, M., Dulski, P., 1996. Distribution of yttrium and rare-earth elements in the Penge and Kuruman iron-formations, Transvaal Supergroup, South Africa. Precambrian Research 79, 37–55.

Bau, M., Möller, P., Dulski, P., 1997. Yttrium and lanthanides in eastern Mediterranean seawater and their fractionation during redox-cycling. Marine Chemistry 56, 123-131.

Bau, M., Dulski, P., 1999. Comparing yttrium and rare earths in hydrothermal fluids from the Mid-Atlantic Ridge: implications for Y and REE behavior during near-vent mixing and for the Y/Ho ratio of Proterozoic seawater. Chemical Geology 155, 77-90.

Bau, M., 1999. Scavenging of dissolved yttrium and rare earths by precipitating iron oxyhydroxide: experimental evidence for Ce oxidation, Y-Ho fractionation, and lanthanide tetrad effect. Geochimica et Cosmochimica Acta 63, 67-77.

Bau, M., Koschinsky, A., 2009. Oxidative scavenging of cerium on hydrous Fe oxide: Evidence from the distribution of rare earth elements and yttrium between Fe oxides and Mn oxides in hydrogenetic ferromanganese crusts. Geochemical Journal 43, 37-47.

Baur, M.E., Hayes, J.M., Studley, S.A., Walter, M.R., 1985. Millimeter-scale variations of stable isotope abundances in carbonates from banded iron-formations in the Hamersley Group of Western Australia. Economic Geology 80, 270-282.

Bekker, A., Holland, H.D., Wang, P.-L., Rumble III, D., Stein, H.J., Hannah, J.L., Coetzee, L.L., Beukes, N.J., 2004. Dating the rise of atmospheric oxygen. Nature 427, 117-120.

Bekker, A., Slack, J.F., Planavsky, N., Krapez, B., Hofmann, A., Konhauser, K.O., Rouxel, O.J., 2010. Iron Formation: The sedimentary product of complex interplay among mantle, tectonic oceanic, and biospheric processes. Economic Geology 105, 467-508.

Bekker, A. and Planavsky, N. and Rasmussen, B. and Krapez, B. and Hofmann, A. and Slack, J. and Rouxel, O. et al. 2014. Iron Formations: Their origins and implications for ancient seawater chemistry, in Holland, H. and Turekian, K. (ed), Treatise on Geochemistry, Vol. 9, pp. 561-628. Netherlands: Elsevier.

Berner, R.A., 1970. Sedimentary pyrite formation. American Journal of Science 268, 1-23.

Beukes, N.J., Klein, C., 1990. Geochemistry and sedimentology of a facies transition – from microbanded to granular iron-formation – in the early Proterozoic Transvaal Supergroup, South Africa. Precambrian Research 47, 99-139.

Beukes, N.J., Gutzmer, J., 2008. Origin and paleoenvironmental significance of major iron formations at the Archean-Paleoproterozoic boundary. Society of Economic Geology Reviews 15, 5-47.

Blockley, J.G., 1979. A contribution to the stratigraphy of the Marra Mamba Iron Formation. Geologial Survey of Western Australia Annual Report.

Blockley, J.G., Tehnas, I.J., Mandyczewsky, A., Morris, R.C., 1993. Proposed stratigraphic subdivisions of the Marra Mamba Iron Formation and the lower Wittenoom Dolomite, Hamersley Group, Western Australia. Geological Survey of Western Australia Report.

Bolhar, R., Kamber, B.S., Moorbath, S., Fedo, C.M., Whitehouse, M.J., 2004. Characterisation of early Archaean chemical sediments by trace element signatures. Earth and Planetary Science Letters 222, 43-60.

Bons, P.D., den Brok, B., 2000. Crystallographic preferred orientation development by dissolution-precipitation creep. Journal of Structural Geology 22, 1713-1722.

Bühn, B., Stanistreet, I.G., 1997. Insight into the enigma of Neoproterozoic manganese and iron formations from the perspective of supercontinental break-up and glaciation. Geological Society, London, Special Publications 119, 81-90.

Canfield, D.E., Raiswell, R., Bottrell, S.H., 1992. The reactivity of sedimentary iron minerals toward sulfide. American Journal of Science, 296, 818-834.

Caquineau, T., Paquette, J.-L., Philippot, P., 2018. U-Pb detrital zircon geochronology of the Turee Creek Group, Hamersley Basin, Western Australia: timing and correlation of the Paleoproterozoic glaciations. Precambrian Research 307, 34-50.

Carlut, J., Isambert, A., Bouquerel, H., Pecoits, E., Philippot, P., Vennin, E., Ader, M., Thomazo, C., Buoncristiani, J-F., Baton, F., Muller, E., Deldicque, D., 2015. Low temperature magnetic

properties of the Late Archean Boolgeeda iron formation (Hamersley Group, Western Australia): environmental implications. Frontiers in Earth Science 3 (Article 18), 1-14.

Cloud, P., 1973. Paleoecological significance of the banded iron-formation. Economic Geology 68, 1135-1143.

Davy, R., 1992. Mineralogy and chemical composition of a core from the Weeli Wolli formation in the Hamersley Basin. Record - Geological Survey of Western Australia, 1991/6.

den Brok, S.W.J., Spiers, C.J., 1991. Experimental evidence for water weakening of quartzite by microcracking plus solution-precipitation creep. Journal of the Geological Society of London 148, 541-548.

Derry, L.A., Jacobsen, S.B., 1988. The Nd and Sr isotopic evolution of Proterozoic seawater. Geophysical Research Letters 15, 397-400.

Derry, L.A., Jacobsen, S.B., 1990. The chemical evolution of Precambrian seawater: Evidence from REEs in banded iron formations. Geochimica et Cosmochimica Acta 54, 2965-2977.

Egglseder, M.S., Cruden, A.R., Tomkins, A.G., Wilson, C.J.L., 2016. Deformation-induced silica redistribution in banded iron formation, Hamersley Province, Australia. Lithos 266-267, 87-97.

Egglseder, M.S., Cruden, A.R., Tomkins, A.G., Wilson, S.A., Langerdam, A.D., 2018. Colloidal origin of microbands in banded iron formations. Geochemical Perspectives Letters 6, 43-49.

Ewers, W.E., Morris, R.C., 1981. Studies of the Dales Gorge Member of the Brockman Iron Formation, Western Australia. Economic Geology 76, 1929-1953.

Farquhar., J., Bao, H.M., Thiemens, M., 2000. Atmospheric influence of Earth's earliest sulfur cycle. Science 289, 756-758.

Farquhar, J., Bao, H., Thiemens, M., 2001. Atmospheric influence of Earth's earliest sulfur cycle. Science 289, 756-758.

Fischer, W.W., Knoll, A.H., 2009. An iron shuttle for deepwater silica in late Archean and early Paleoproterozoic iron formation. Geological Society of America Bulletin 121, 222-235.

Greene, G.W., Kristiansen, K., Meyer, E.E., Boles, J.R., Israelachvili, J.N., 2009. Role of electrochemical reactions in pressure solutions. Geochimica et Cosmochimica Acta 73, 2862-2874.

Guo, Q., Strauss, H., Kaufman, A.J., Schröder, S., Gutzmer, J., Wing, B., Baker, M.A., Bekker, A., Jin, Q., Kim, S-T., Farquhar, J., 2009. Reconstructing Earth's surface oxidation across the Archean-Proterozoic transition. Geology 37, 399-402.

Frei, R., Crowe, S.A., Bau, M., Polat, A., Fowle, D.A., Dossing, L.N., 2016. Oxidative elemental cycling under the low O2 Eoarchean atmosphere. Scientific Reports 6, 1-9.

Fryer, B.J., 1977a. Rare earth evidence in iron formations for changing Precambrian oxidation states. Geochimica et Cosmochimica Acta 41, 361-367.

Fryer, B.J., 1977b. Trace element geochemistry of the Sokoman Iron Formation. Canadian Journal of Earth Science 14, 1598-1610.

Graf, J.L., 1978. Rare earth elements, iron formations and seawater. Geochimica et Cosmochimica Acta 42, 1845-1850.

Hamade, T., Konhauser, K.O., Raiswell, R., Goldsmith, S., Morris, R.C., 2003. Using Ge/Si ratios to decouple iron and silica fluxes in Precambrian banded iron formations. Geology 31, 35-38.

Haugaard, R., Pecoits, E., Lalonde, S., Rouxel, O., Konhauser, K.O., 2016a. The Joffre Banded Iron Formation, Hamersley Gorup, Western Australia: Assessing the palaeoenvironment through detailed petrology and chemostratigraphy. Precambrian Research 273, 12-37.

Holland, H.D., 2002. Volcanic gases, black smokers, and the great oxidation event. Geochimica et Cosmochimica Acta 66, 3811-3826.

Holland, H.D., 2006. The oxygenation of the atmosphere and oceans. Philosophical Transactions of the Royal Society B 361, 903-915.

Isley, A.E., 1995. Hydrothermal plumes and the delivery of iron to banded iron formations. The University of Chicago Press Journals 103, 169-185.

Isley, A.E., Abbott, D.H., 1999. Plume-related mafic volcanism and the deposition of banded iron formation. Journal of Geophysical Research 104, 15461-15477.

James, H.L., 1954. Sedimentary facies of iron-formation. Economic Geology 49, 235-293.

Klein, C., Beukes, N.J., 1989. Geochemistry and sedimentology of a facies transition from limestone to iron-formation deposition in the Early Proterozoic Transvaal Supergroup, South Africa. Economic Geology 84, 1733-1742.

Klein, C., Beukes, N.J., 1993. Sedimentology and geochemistry of the glaciogenic late Proterozoic Rapitan Iron-Formation in Canada. Economic Geology 88, 542-565.

Klein, C., 2005. Some Precambrian banded iron-formations (BIFs) from around the world: Their age, geologic setting, mineralogy, metamorphism, geochemistry, and origin. American Minerologist 90, 1473-1499.

Koeppenkastrop, D., De Carlo, E.H., 1992. Sorption of rare-earth elements from seawater onto synthetic mineral particles: An experimental approach. Chemical Geology 95, 251-263.

Konhauser, K.O., Hamade, T., Raiswell, R., Morris, R.C., Ferris, F.G., Southam, G., Canfield, D.E., 2002. Could bacteria have formed the Precambrian banded iron formations? Geology 30, 1079-1082.

Konhauser, K.O., Newman, D.K., and Kappler, A., 2005. The potential significance of microbial Fe(III)-reduction during Precambrian banded iron formations. Geobiology 3,167-177

Konhauser, K.O., Pecoits, E., Lalonde, S.V., Papineau, D., Nisbet, E.G, Barley, M.E., Arndt, N.T., Zahnle, K., Kamber, B.S., 2009. Oceanic nickel depletion and a methanogen famine before the Great Oxidation Event. Nature 458, 750-754.

Konhauser, K.O., Lalonde, S.V., Planavsky, N.J., Pecoits, E., Lyons, T.W., Mojzsis, S.J., Rouxel, O.J., Barley, M.E., Rosiere, C., Fralick, P.W., Kump, L.R., Bekker, A., 2011. Aerobic bacterial pyrite oxidation and acid rock drainage during the Great Oxidation Event. Nature 478, 369-373.

Konhauser, K.O., Robbins, L.J., Pecoits, E., Peacock, C., Kappler, A., Lalonde, S.V., 2015. The Archean nickel famine revisited. Astrobiology 15, 804-815.

Konhauser, K.O., Planavsky, N.J., Hardisty, D.S., Robbins, L.J., Warchola, T.J., Haugaard, R., Lalonde, S.V., Partin, C.A., Oonk, P.B.H., Tsikos, H., Lyons, T.W., Bekker, A., Johnson,

C.M., 2017. Iron Formations: A global record of Neoarchaean to Palaeoproterozoic environmental history. Earth-Science Reviews 172, 140-177.

Laajoki, K., 1975. Rare-earth elements in Precambrian iron formations in Vayrlankyla, South Puolanka area, Finland. Bulletin of the Geological Society of Finland 47, 93-107.

Lascelles, D.F., 2000. Marra Mamba Iron Formation stratigraphy in the eastern Chichester Range, Western Australia. Australian Journal of Earth Sciences 47, 799-806.

Luo, G., Ono, S., Beukes, N.J., Wang, D.T., Xie, S., Summons, R.E., 2016. Rapid oxygenation of Earth's atmosphere 2.33 billion years ago. Science Advances 2, 1-9.

Martin, D.McB., Li, Z.X., Nemchin, A.A., Powell, C.McA., 1998. A pre-2.2 Ga age for giant hematite ores of the Hamersley Province, Australia. Economic Geology 93, 1084-1090.

Martin, D.M., 1999. Depositional setting and implications of Paleoproterozoic glaciomarine sedimentation in the Hamersley Province, Western Australia. Geological Society of America Bulletin 111, 189-203.

Martin, D.M., Powell, C.M., George, A.D., 2000. Stratigraphic architecture and evolution of the early Paleoproterozoic McGrath Trough, Western Australia. Precambrian Research 99, 33-64.

McConchie, D.M., 1984. The geology and geochemistry of the Joffre and Whaleback Shale members of the Brockman Iron Formation, Western Australia. University of Western Australia.

Morris, R.C., 1993. Genetic modelling for banded iron-formation of the Hamersley Group, Pilbara Craton, Western Australia. Precambrian Research 60, 243-286.

Morris, R.C., Horwitz, R.C., 1983. The origin of the iron-formation-rich Hamersley Group of Western Australia – deposition on a platform. Precambrian research 21, 273-297

Müller, S.G, Krapež, B., Barley, M.E., Fletcher, I.R., 2005. Giant iron-ore deposits of the Hamersley province related to the breakup of Paleoproterozoic Australia: New insights from in situ SHRIMP dating of baddeleyite from mafic intrusions. Geology 33, 577-580.

Nesbitt, H.W., Young, G.M., 1989. Formation and diagenesis of weathering profiles. The Journal of Geology 97, 129-147.

Nozaki, Y., Zhang, J., Amakawa, H., 1997. The fractionation between Y and Ho in the marine environment. Earth and Planetary Science Letters 148, 329-340.

Ohta, A., Kawabe, I., 2001. REE (III) adsorption onto Mn dioxide (delta-MnO2) and Fe oxyhydroxide: Ce(III) oxidation by delta-MnO2. Geochimica et Cosmochimica Acta 65, 695–703.

Pack, A., Russell, S.S., Shelley, J.M.G., van Zuilen, M., 2007. Geo- and cosmochemistry of the twin elements yttrium and holmium. Geochimica et Cosmochimica Acta 71, 4592-4608.

Partridge, M.A., Golding, S.D., Baublys, K.A., Young, E., 2008. Pyrite paragenesis and multiple sulfur isotope distribution in late Archean and early Paleoproterozoic Hamersley Basin sediments. Earth and Planetary Science Letters 272, 41-49.

Pecoits, E., Gingras, M.K., Barley, M.E., Kappler, A., Posth, N., Konhauser, K.O., 2009. Petrography and geochemistry of the Dales Gorge banded iron formation: Paragenetic sequence, source and implications for palaeo-ocean chemistry. Precambrian Research 172, 163–187.

Percak-Dennett, L., Roden, E.E., Beard, B.L., Johnson, C.M., 2011. Iron isotope fractionation during dissimilatory iron reduction under simulated Archean conditions. Geobiology 9, 205-220.

Philippot, P., Ávila, J.N., Killingsworth, B.A., Tessalina, S., Baton, F., Caquineau, T., Muller, É., Pecoits, E., Cartigny, P., Lalonde, S.V., Ireland, T.R., Thomazo, C., Van Kranendonk, M.J., and Busigny, V., 2018, Globally asynchronous sulphur isotope signals require re-definition of the Great Oxidation Event. Nature Communications 9, 2245, doi: 10.1038/s41467-018-04621-x.

Pickard, A.L., Barley, M.E., Krapež, B., 2004. Deep-marine depositional setting of banded iron formation: Sedimentological evidence from interbedded clastic sedimentary rocks in the early Palaeoproterozoic Dales Gorge Member of Western Australia. Sedimentary Geology 170, 37-62.

Planavsky, N., Bekker, A., Rouxel, O.J., Kamber, B., Hofmann, A., Knudsen, A., Lyons, T.W., 2010. Rare Earth Element and yttrium compositions of Archean and Paleoproterozoic Fe formations revisited: new perspectives on the significance and mechanisms of deposition. Geochimica et Cosmochimica Acta 74, 6387-6405.

Planavsky, N.J., Asael, D., Hofmann, A., Reinhard, C.T., Lalonde, S.V., Knudsen, A., Wang, X., Ossa Ossa, F., Pecoits, E., Smith, A.J.B., Beukes, N.J., Bekker, A., Johnson, T.M., Konhauser, K.O., Lyons, T.W., Rouxel, O.J., 2014. Evidence for oxygenic photosynthesis half a billion years before the Great Oxidation Event. Nature Geosciences 7, 283-286.

Poulton, S.W., Krom, M.D., Raiswell, R., 2004. A revised scheme for the reactivity of iron (oxyhydr)oxide minerals towards dissolved sulfide. Geochimica et Cosmochimica Acta 68, 3703-3715.

Poulton, S.W., Canfield, D.E., 2005. Development of a sequential extraction procedure for iron: implications for iron partitioning in continentally derived particulates. Chemical Geology 214, 209-221.

Raiswell, R., Canfield, D.E., 1998. Sources of iron for pyrite formation in marine sediments. American Journal of Science 298, 219-245.

Rasmussen, B., Krapež, B., Muhling, J.R., Suvorova, A., 2015. Precipitation of iron silicate nanoparticles in early Precambrian oceans marks Earth's first iron age. Geology 43, 303–306.

Rasmussen, B., Muhling, J.R., Suvorova, A., Krapež, B., 2016. Dust to dust: Evidence for the formation of "primary" hematite dust in banded iron formations via oxidation of iron silicate nanoparticles. Precambrian Research 284, 49-63.

Rasmussen, B., Muhling, J.R., Suvorova, A., Krapez, B., 2017. Greenalite precipitation linked to the deposition of banded iron formations downslope from a late Archean carbonate platform. Precambrian Research 290, 49-62.

Reinhard, C.T., Planavsky, N.J., Lyons, T.W., 2013. Long-term sedimentary recycling of rare sulphur isotope anomalies. Nature 497, 100-104.

Sakai, K., 2015. Routine soil analysis using an Agilent 8800 ICP-QQQ. Application note 5991-6409EN. Agilent Technologies.

Satkowski, A.M., Beukes, N.J., Li, W., Beard, B.L., Johnson, C.M., 2015. A redox-stratified ocean 3.2 billion years ago. Earth and Planetary Science Letters 430, 43-53.

Spencer, E., Percival, F.G., 1952. The structure and origin of the banded hematite jaspers of Singhbhum, India. Economic Geology 47, 365-383.

Steinhofel, G., von Blackenburg, F., Horn, I., Konhauser, K.O., Beukes, N., Gutzmer, J., 2010. Deciphering formation processes of banded iron formations from the Transvaal and the Hamersley Sequence by combined Si and Fe isotope analysis using UV femtosecond laser ablation. Geochimica et Cosmochimica Acta 74, 2677–2696.

Sun, S., Konhauser, K.O., Kappler, A., Li, Y-L., 2015. Primary hematite in Neoarchean to Paleoproterozoic oceans. Geological Society of America Bulletin 127, 850-861.

Swanner, E.D., Bekker, A., Pecoits, E., Konhauser, K.O., Cates, N.L., Mojzsis, S.J., 2013. Geochemistry of pyrite from diamictites of the Boolgeeda Iron Formation, Western Australia with implications for the GOE and Paleoproterozoic ice ages. Chemical Geology 362, 131-142.

Taylor, S.R., McLennan, S.M., 1985. The continental crust: Its composition and its evolution, Blackwell, Oxford, 312 pp.

Trendall, A.F., 1973. Varve cycles in the Weeli Wolli Formation of the Precambrian Hamersley Group, Western Australia. Economic Geology 68, 1089-1097.

Trendall, A.F., Pepper, R.S., 1977. Chemical composition of the Brockman Iron Formation. Geological Survey of Western Australia, 1976/25.

Trendall, A.F., Nelson, D.R., De Laeter, J.R., Hassler, S.W., 1998. Precise zircon U-Pb ages from the Marra Mamba Iron Formation and Wittenoom Formation, Hamersley Group, Western Australia. Australian Journal of Earth Sciences 45, 137-142.

Trendall, A.F., 2002. The significance of iron-formation in the Precambrian stratigraphic record. In: Altermann W. & Corcorane P.L. eds. Precambrian Sedimentary Environments: a Modern Approach to Depositional Systems, pp. 33-66. International Association of Sedimentologists Special Publication 44.

Trendall, A.F., Compston, W., Nelson, D.R., De Laeter, J.R., Bennett, V.C., 2004. SHRIMP zircon ages constraining the depositional chronology of the Hamersley Group, Western Australia. Australian Journal of Earth Science 51, 621-644.

Trompette, R., De Alvarenga, C.J.S., Walde, D., 1998. Geological evolution of the Neoproterozoic Corumbá graben system (Brazil). Depositional context of the stratified Fe and Mn ores of the Jacadigo Group. Journal of South American Earth Sciences 11, 587-597.

Viehmann, S., Bau, M., Hoffmann, J.E., Muenker, C., 2015. Geochemistry of the Krivoy Rog Banded Iron Formation, Ukraine, and the impact of peak episodes of increased global magmatic activity on the trace element composition of Precambrian seawater. Precambrian Research 270, 165-180.

Viehmann, S., Bau, M., Bühn, B., Dantas, E.L., Andrade, F.R.D., Walde, D.H.G., 2016. Geochemical characterisation of Neoproterozoic marine habitats: Evidence from trace elements and Nd isotopes in the Urucum iron and manganese formations, Brazil. Precambrian Research 282, 74-96.

Walde, D.H.G., Hagemann, S.G., 2007. The Neoproterozoic Urucum/Mutun Fe and Mn deposits in W-Brazil/SE-Bolivia: assessment of ore deposits models. Zeitschrift-Deutschen Gesellschaft Fur Geowissenschaften 158, 45-56.

Williford, K.H., Van Kranendonk, M.J., Ushikubo, T., Kozdon, R, Valley, J.W., 2011. Constraining atmospheric oxygen and seawater sulfate concentrations during Paleoproterozoic glaciation: In situ sulfur three-isotope microanalysis of pyrite from the Turee Creek Group, Western Australia. Geochimica et Cosmochimica Acta 75, 5686-5705.

Zhang, J., Amakawa, H., Nozaki, Y., 1994. The comparative behaviors of yttrium and lanthanides in the seawater of the north Pacific. Geophysical Research Letters 21, 2677-2680.

8. Figures (Chapter 2)
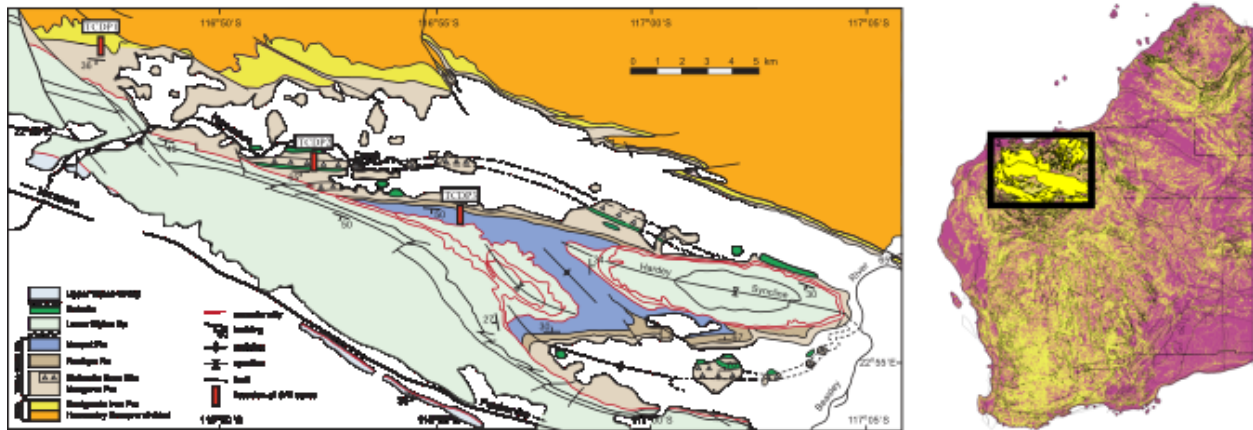
Figure 2.1. Geological map of the Hardey Syncline, edited from Philippot et al. (2018; left), and location of the Hardey Syncline in relation to Western Australia (right). Locations of sampling for the Turee Creek Drilling Project (TCDP) cores are highlighted on the left.
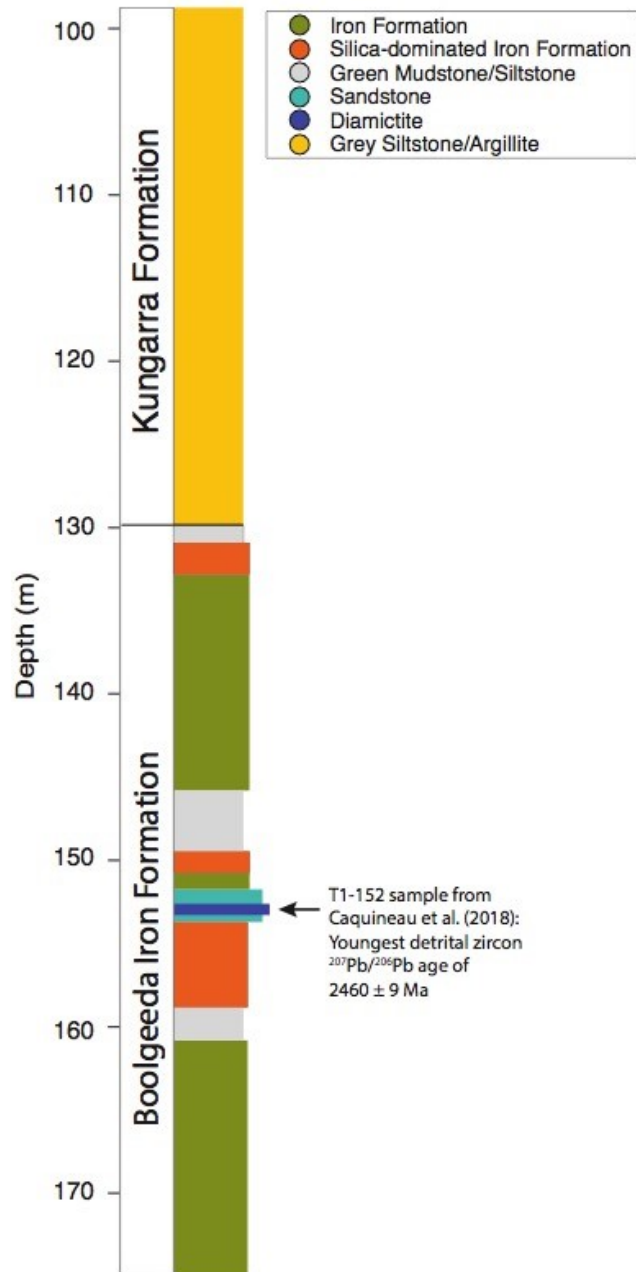
Figure 2.2. Litholog for Turee Creek Drilling Project core 1 (TCDP1) after Philippot et al. (2018), displaying the stratigraphic position and relationship between different lithologies within the core.
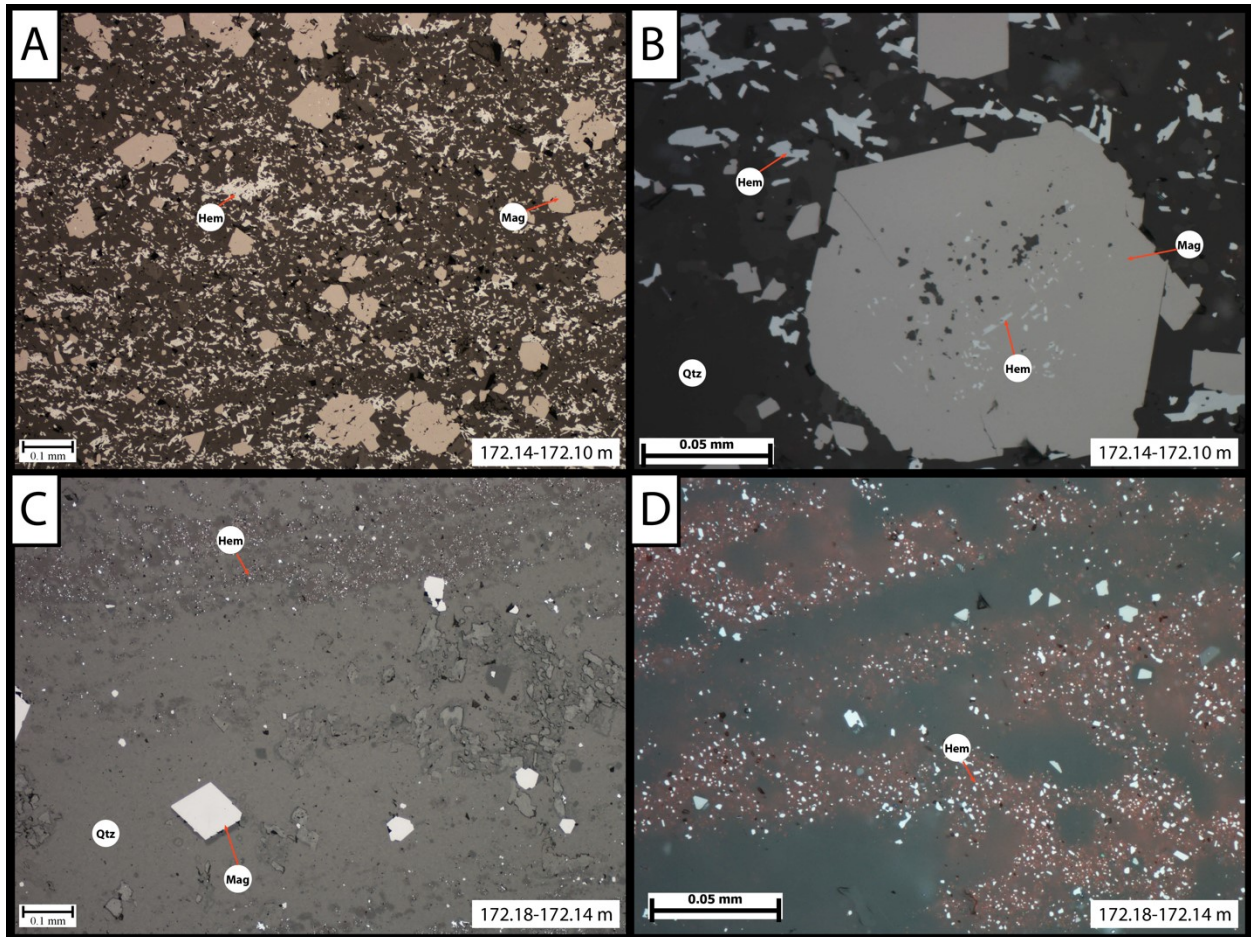
Figure 2.3. Typical textural relationships of iron minerals in the Boolgeeda Iron Formation under reflected light. A: General appearance of relatively large euhedral magnetite grains compared to smaller platy hematite grains. B: A large euhedral magnetite grain containing inclusions of hematite and quartz, suggesting magnetite crystals formed after quartz and hematite. C: Relationship of microplaty hematite bands (top) to silica dominated bands containing euhedral magnetite (bottom). D: Magnified image of microplaty hematite bands, displaying individual platy hematite grains and fine hematite dust yielding the red staining colour of the silica matrix.
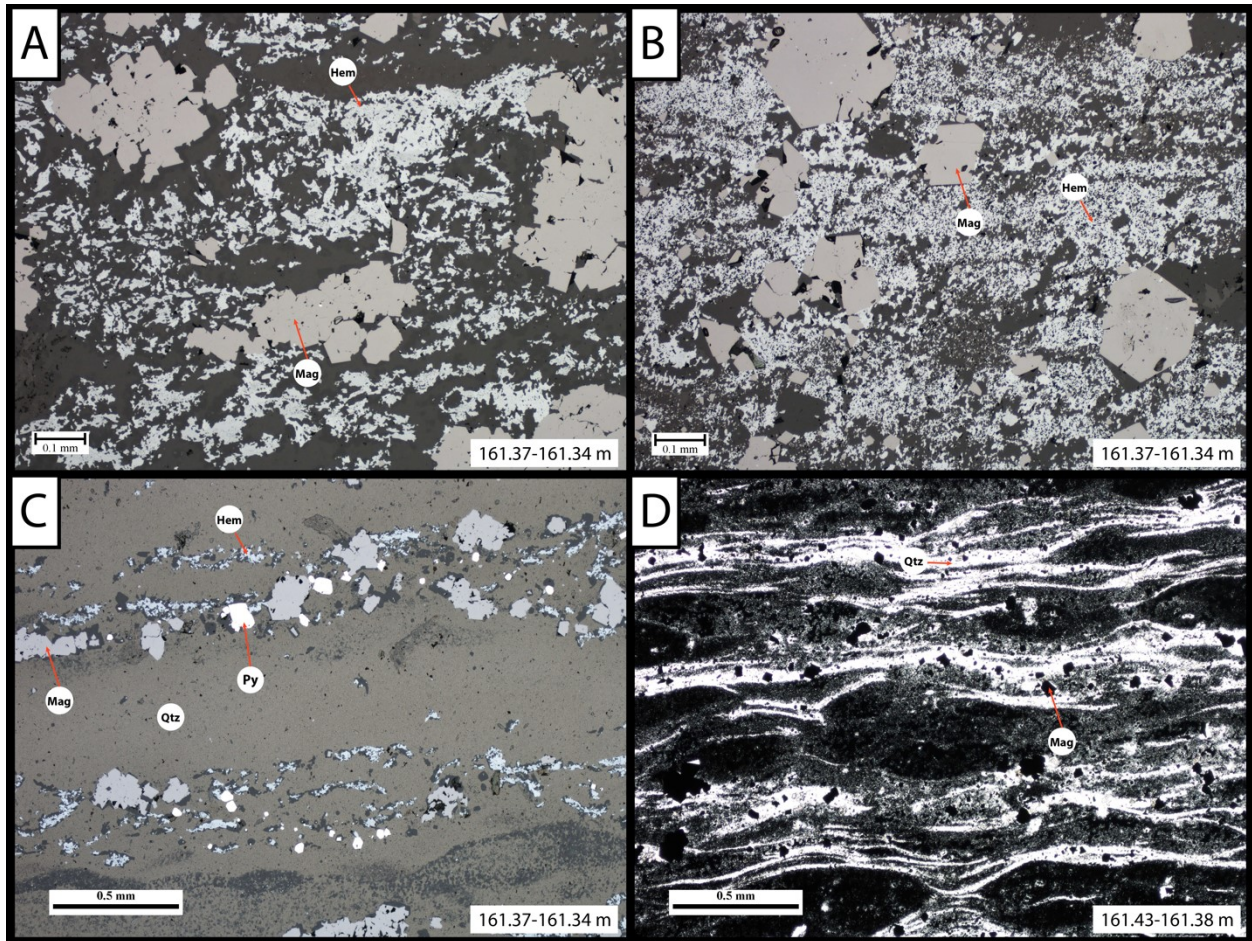
Figure 2.4. Typical textural associations of hematite and magnetite. A-B: Varying appearance of magnetite and hematite grains within closely spaced bands (<3 cm apart) under reflected light; hematite grains in B are smaller, less bladed, and more abundant than grains in A; magnetite grains in B are larger and more euhedral than in A. C: Microbanding similar to Trendall's (1973) type A under reflected light. D: Microbanding similar to Trendall's (1973) type B under transmitted light.
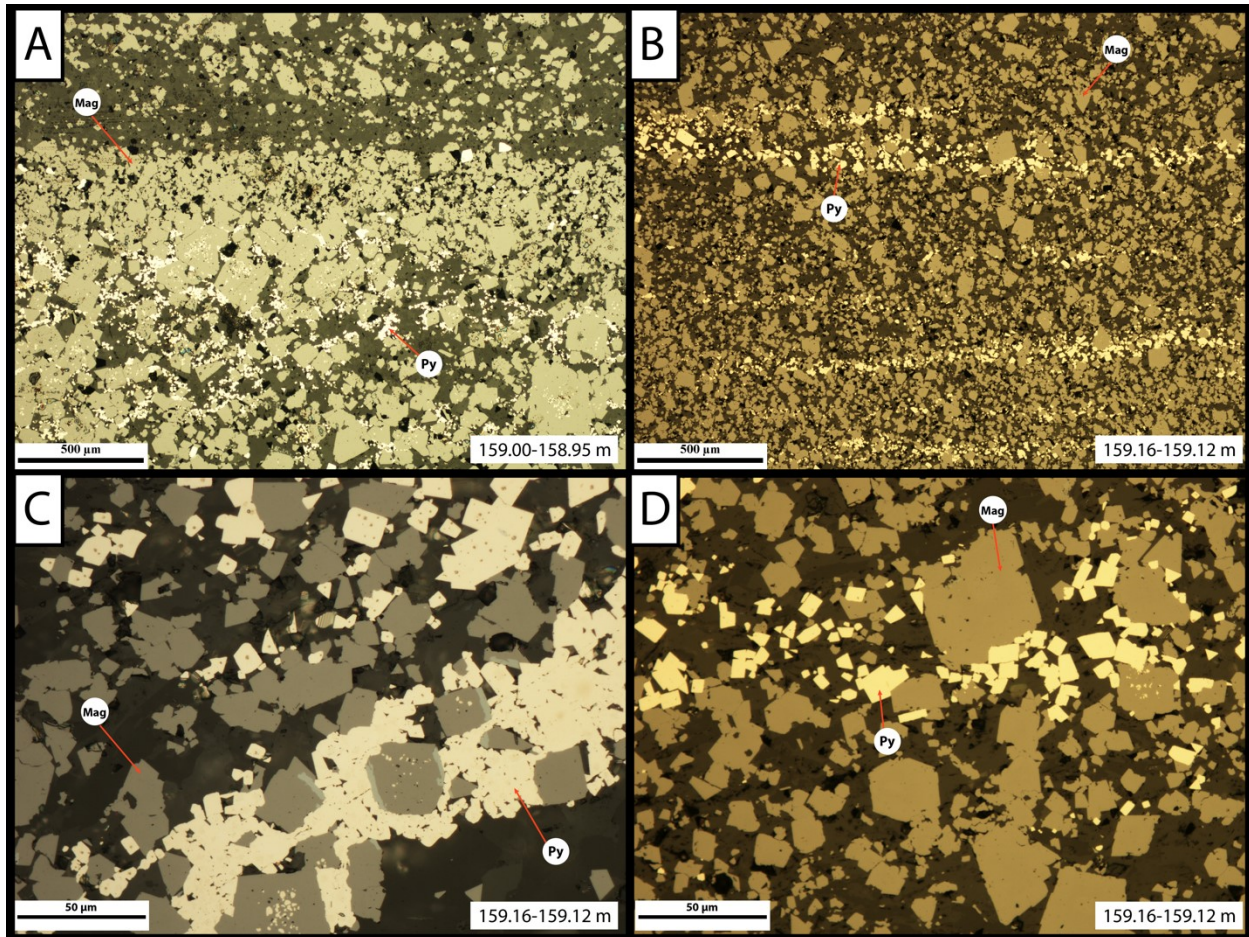
Figure 2.5. Typical pyrite textures found within the TCDP1 under reflected light. A: Small euhedral pyrite crystals intermingled between large euhedral magnetite grains; note the sharp boundary where magnetite grains become less prevalent and pyrite is absent. B: Thin microbands of pyrite grains that lie parallel to primary bedding; presumably from *in situ* sulphate reduction in shallow pore waters. C: Small rounded inclusions of pyrite within euhdral magnetite crystals closely associated with pyrite microbands; association suggests pyrite is more primary than magnetite. D: Textural association of euhedral magnetite and pyrite grains.
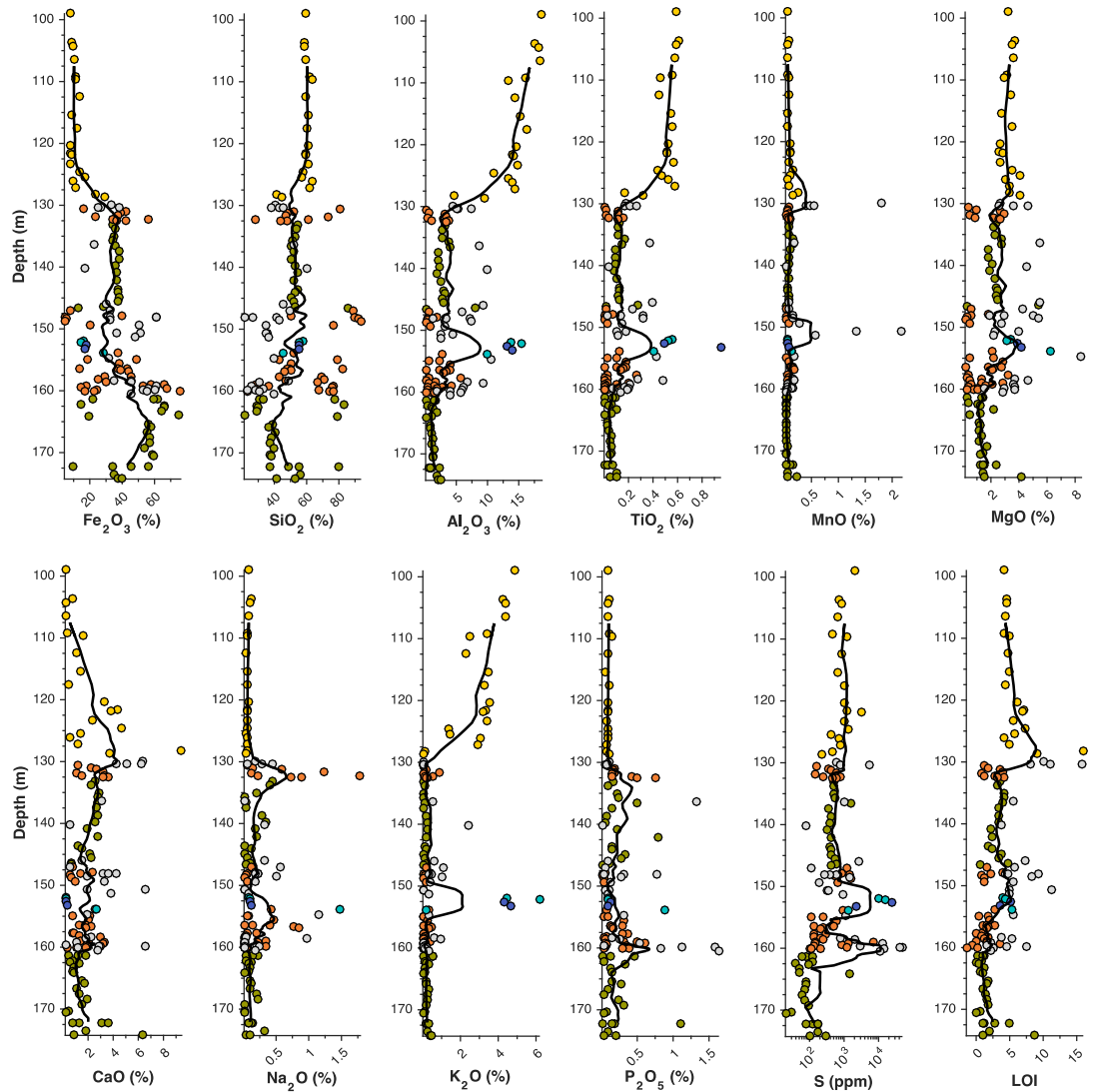
Figure 2.6. Major element contents and chemostratigraphic depth profiles.
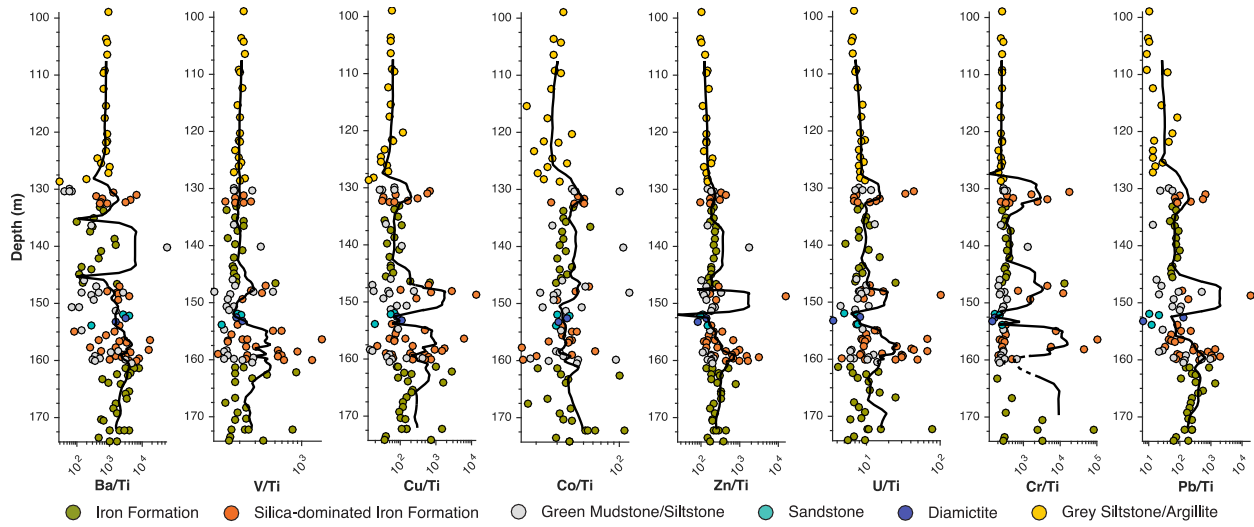
Figure 2.7. Trace element contents and chemostratigraphic depth profiles normalized to titanium. Note that normalization to Al, Zr, Th, and Sc result in similar trends (SI Figures 2.6-2.8).
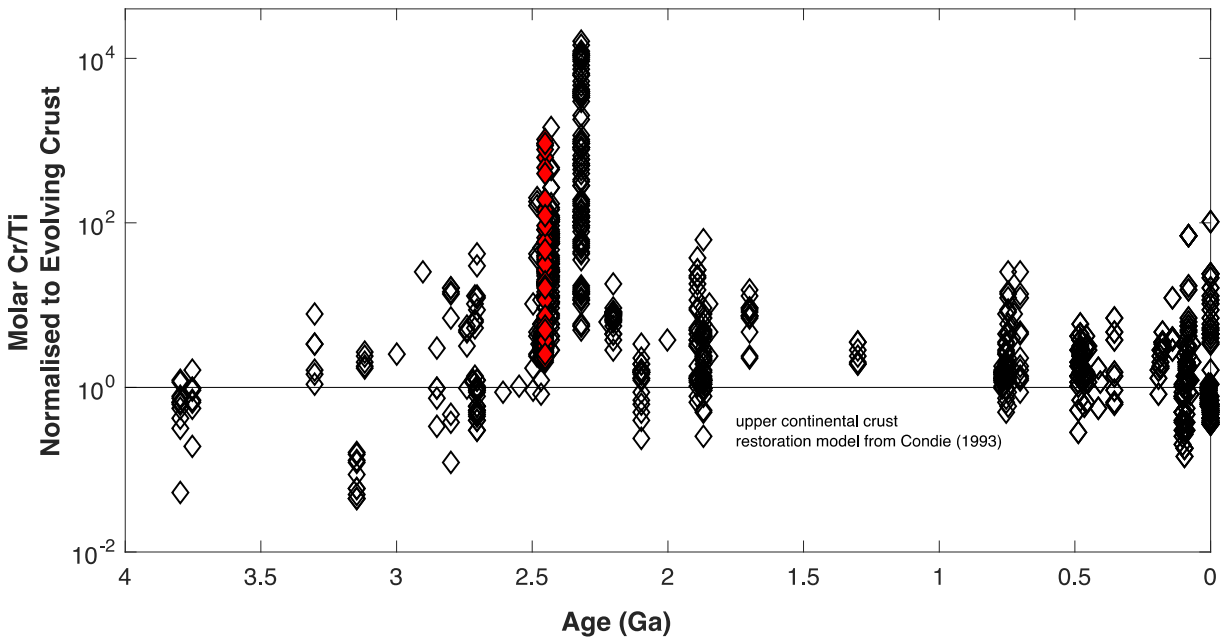
Figure 2.8. Cr/Ti data from TCDP1 (red diamonds) overlain on the Cr/Ti through time from Konhauser et al. (2011; hollow diamonds). Sediments of the Boolgeeda Iron Formation and Turee Creek Group are consistent with the trend of increased oxidative weathering of continental sulphide minerals, peaking in the 2.32 Ga Timeball Hill Formation, South Africa.
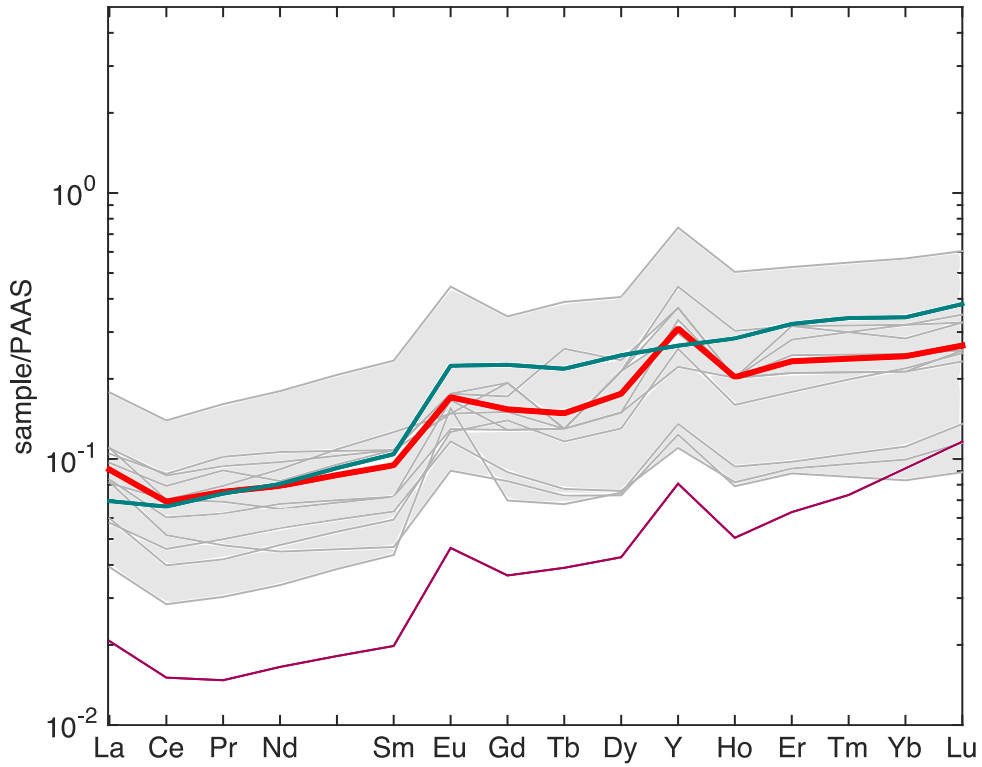
Figure 2.9. REE+Y patterns for samples within TCDP1 containing less than 1 wt.% aluminium. All samples are from either the BIF or silica-dominated IF lithology. Light grey lines represent individual measurements, and bright red lines represent the average pattern of the sample set. The REE+Y patterns for the Dales Gorge BIF (purple) from Pecoits et al. (2009) and the Joffre BIF (green) from Haugaard et al. (2016) have been included for comparison.
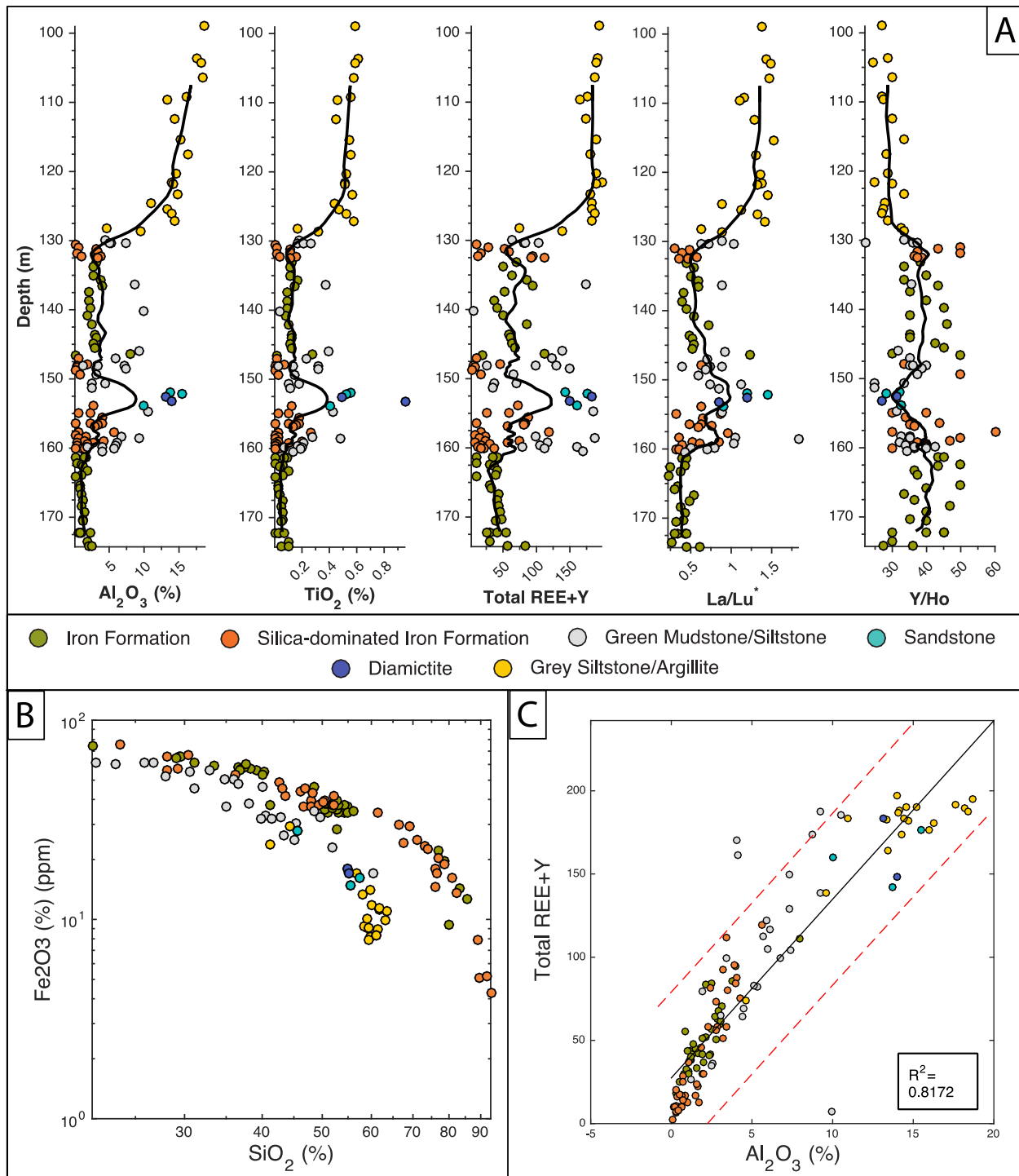
Figure 2.10. Proxies for detrital influx in TCDP1. A: Profiles highlighting detrital influx between 160 m and 148 m depth, and the loss of REE proxies associated with marine deposition. The sinusoidal nature of the Y/Ho plot is interpreted to represent a regressive-transgressive cycle. B: Two trends defined by varying Fe concentration with increasing Si concentration. The upper trend is dominated by lithologies presumed to represent primary precipitates (i.e. BIF), while the lower trend is composed of detrital lithologies. C: Plot demonstrating the strong correlation between REE concentrations and detrital input.
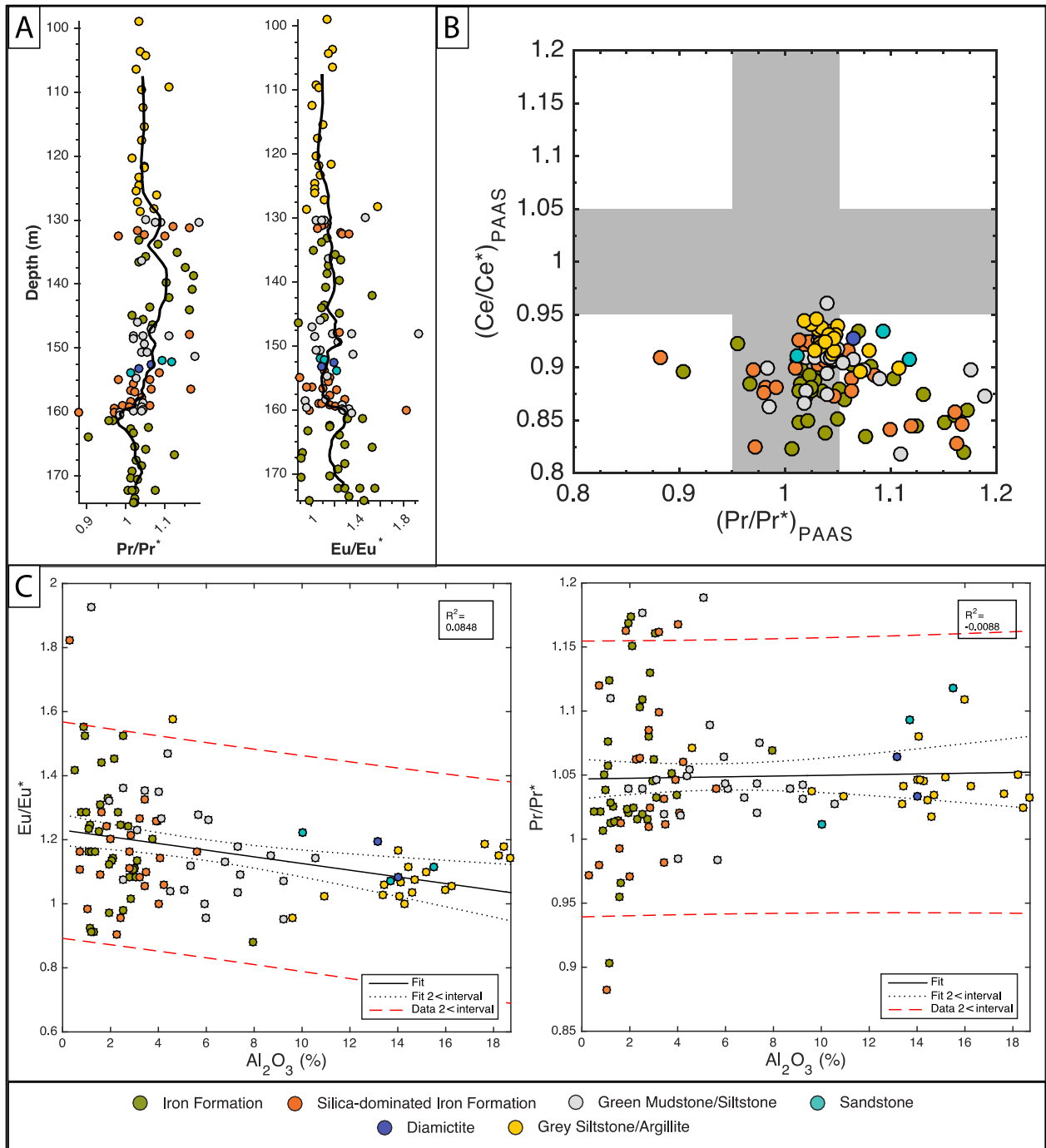
Figure 2.11. Ce, Pr, and Eu anomaly trends through TCDP1. A: Depth profiles of Pr and Eu anomalies. B: Ce anomaly vs. Pr, highlighting the presence of true negative Ce anomalies. C: Eu and Pr anomaly versus Al_2O_3 concentrations for TCDP1 lithologies.
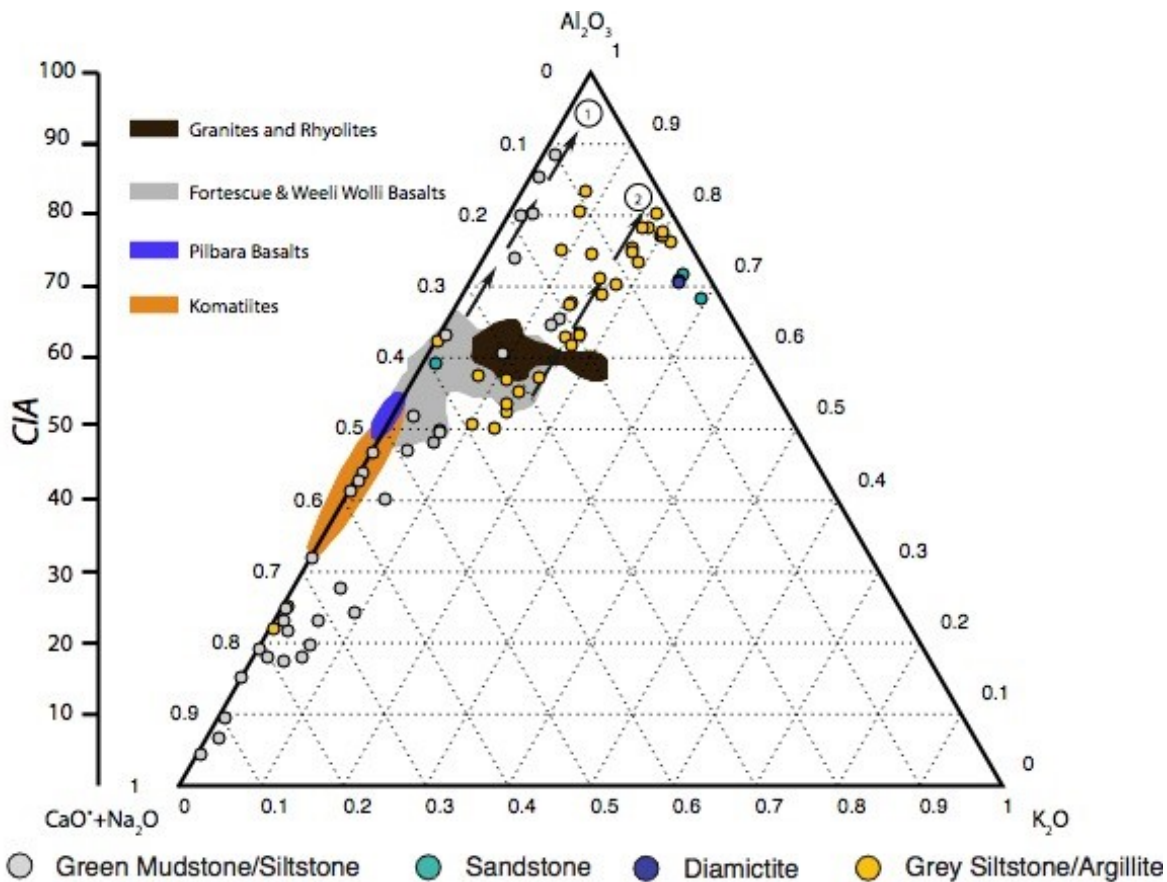
Figure 2.12. CIA plot for TCDP1 detrital sediments. Kungaara Formation shales appear to be weathered from a granite or rhyolite source, whereas shales within the Boolgeeda Iron Formation appear to represent an ultramafic to mafic source. Potassium enrichment can result from conversion of Al-rich clays to those more potassic in composition, such as illite or muscovite (Nesbitt and Young, 1989). Arrows 1 and 2 indicate weathering pathways of mafic and felsic rocks, respectively.
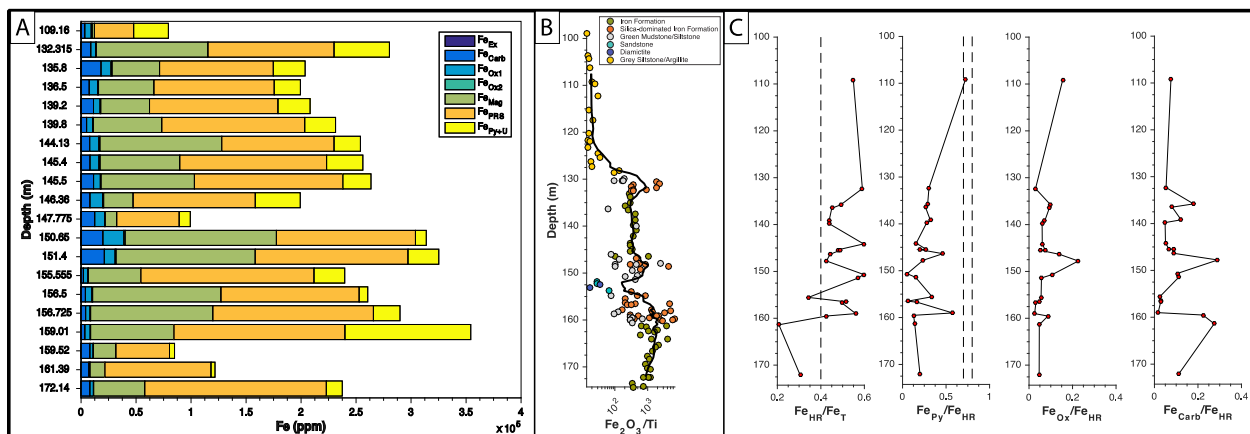
Figure 2.13. Fe budget and Fe speciation. The majority of Fe is concentrated in magnetite and poorly reducible silicate phases such as chlorite. Depth plots suggest anoxic

ferruginous conditions present during deposition. Drastic changes in profiles are observed at 160 m depth.
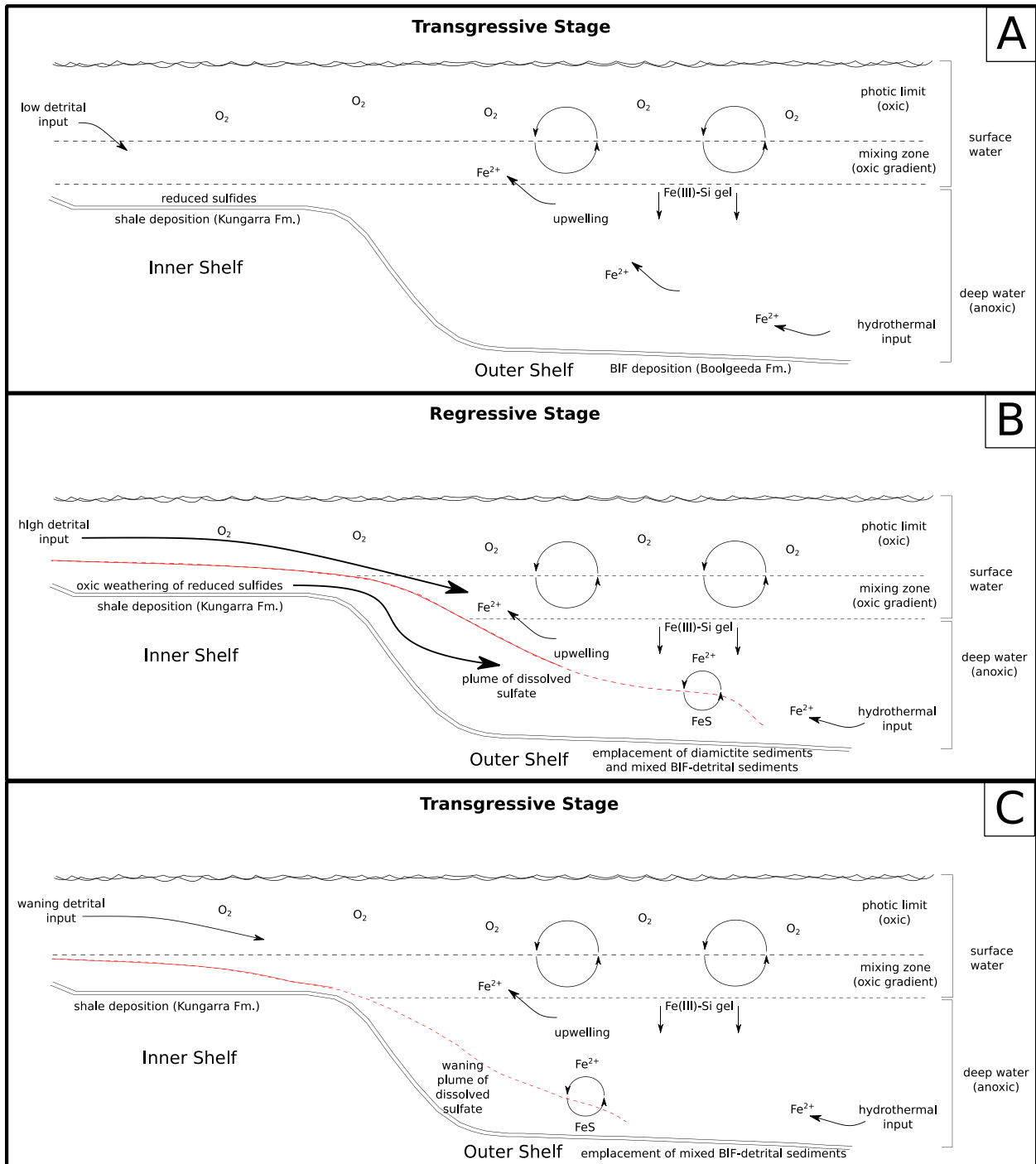
Figure 2.14. Panel A: Schematic diagram of conditions leading to deposition of "pure" BIF intervals within the Boolgeeda Iron Formation. Upwelling hydrothermal Fe(II) is oxidized to Fe(III) in the persistently oxygenated shallow water column. Fe(III)-oxyhydroxides subsequently sorb dissolved Si to form an Fe(III)-Si gel, the primary phase

of the Boolgeeda BIF. Europium anomalies from the hydrothermal source and the negative Ce anomaly prevalent in the oxygenated shallow water column are captured as the precipitated Fe(III)-Si gel phase sorbs REE+Y from the water column. Panel B: A fall in base level results in the deepening of the oxic-anoxic chemocline, and results in the weathering of sulfide minerals previously associated with submerged shelf sediments. The resulting dissolved sulfate is transported deeper into the basin (red line). Further, a decrease in base level leads to increased riverine incision and transport of terrestrially-sourced detrital sediments. These processes inhibited the precipitation of "pure" BIF intervals, and resulted in intervals of mixed detrital-BIF sediments. Panel C: A transgression leads to the resumption of BIF deposition as sulfate concentrations dissipate and detrital influx wanes. Note: the interval at 160 m represents a temporary coupling of the ocean-atmosphere system, resulting in the oxidation of reduced continental sulfides. This event can be viewed as an extreme case of panel B. Sulfate is generated and transported to the ocean, where it is then reduced to sulfide. Large amounts of detrital input also occurred as a result of changes in base level and increased local weathering. The combined effects led to the deposition of S-rich shale at 160 m depth. At 160 m depth, $\Delta^{33}S$ goes to 0‰, and $\delta^{34}S$ approaches -40‰ (Philippot et al., 2018).

9. Supplementary Figures (Chapter 2)

SI Figure 2.1. XRD profiles for samples used to determine Fe speciation.
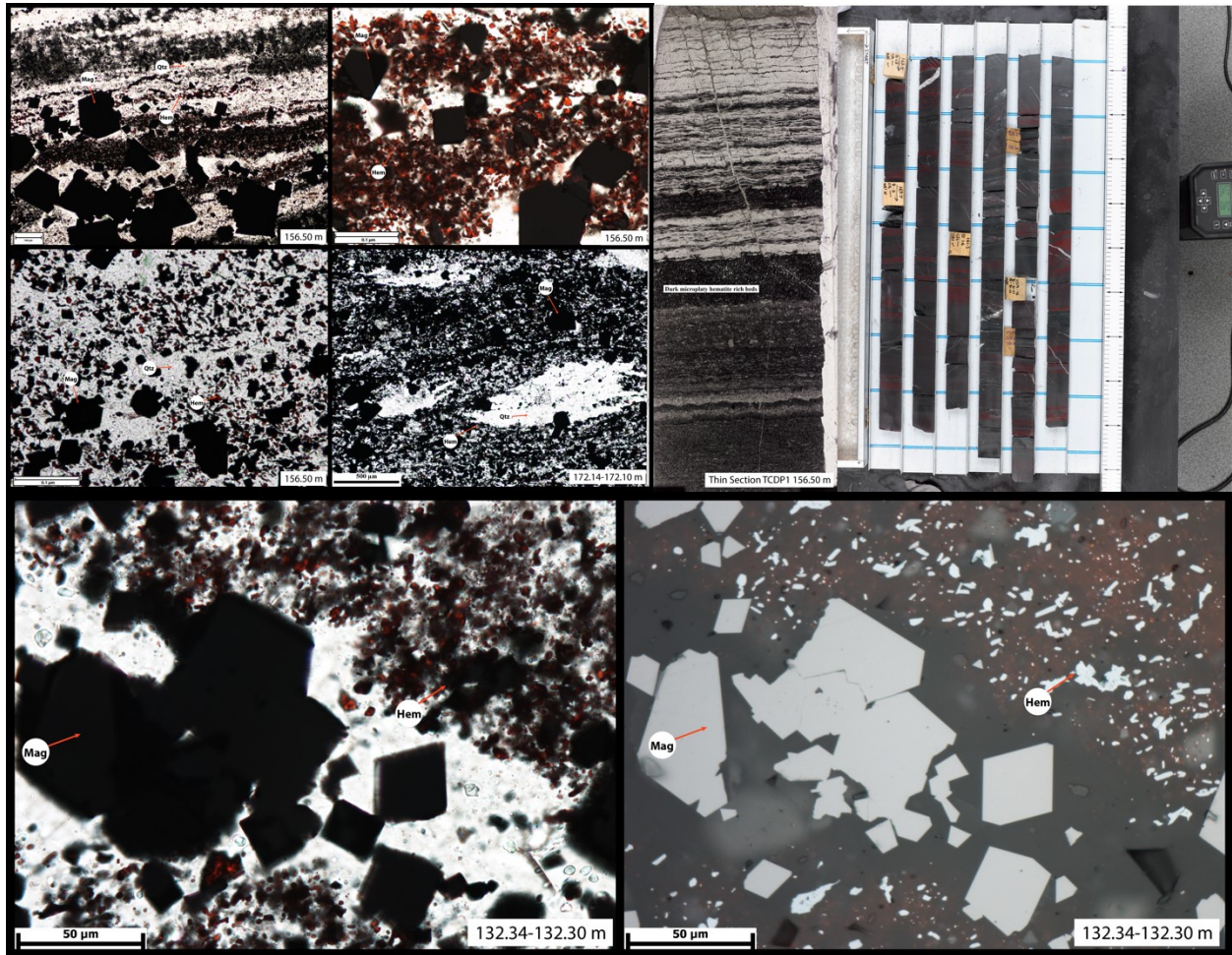
SI Figure 2.2. Example of microplaty hematite in thin section, its location in cm-scale beds, and the location of these beds within the TCDP1 core. Bottom pannel: PPL (left) and reflected light (right) images of microplaty hematite and euhedral magnetite. Only hematite plates that are sufficiently thin to allow the transmission of PPL and yield a bright blood red colour. This is best demonstrated by the transition from opaque sections to bright red sections within a single crystal, as the crystal thins (left).
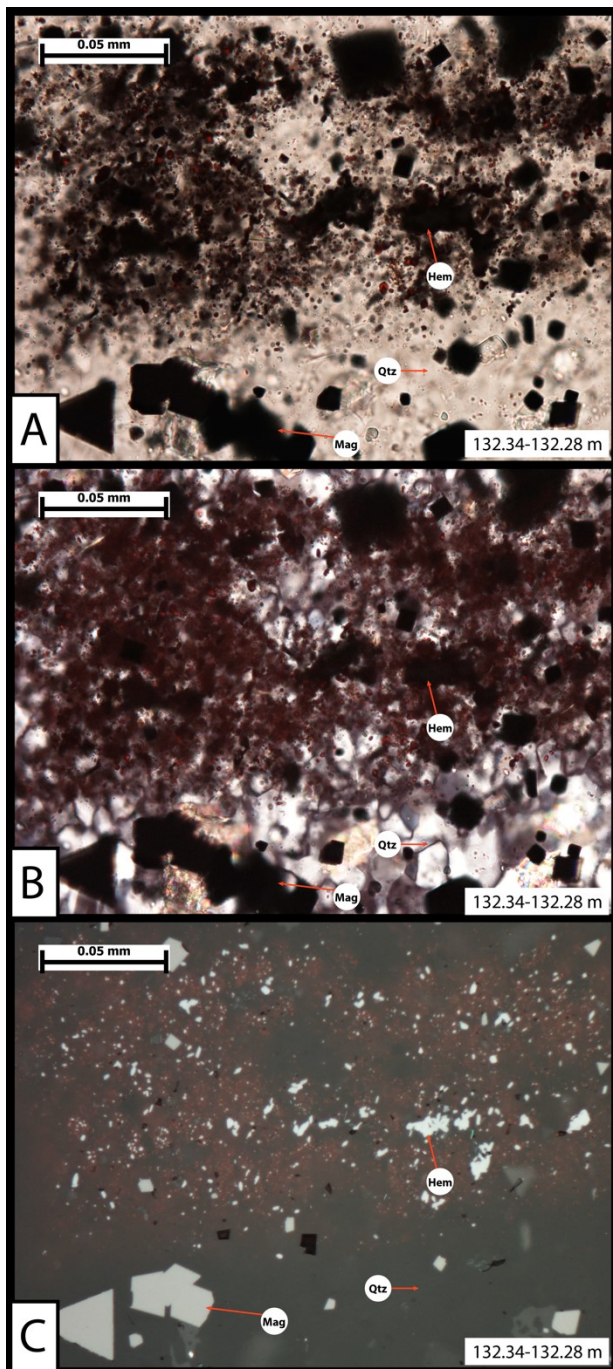
SI Figure 2.3. Texture of disseminated hematite dust at 132 m depth, in plane-polarized light (A), cross-polarized light (B), and reflected light (C).
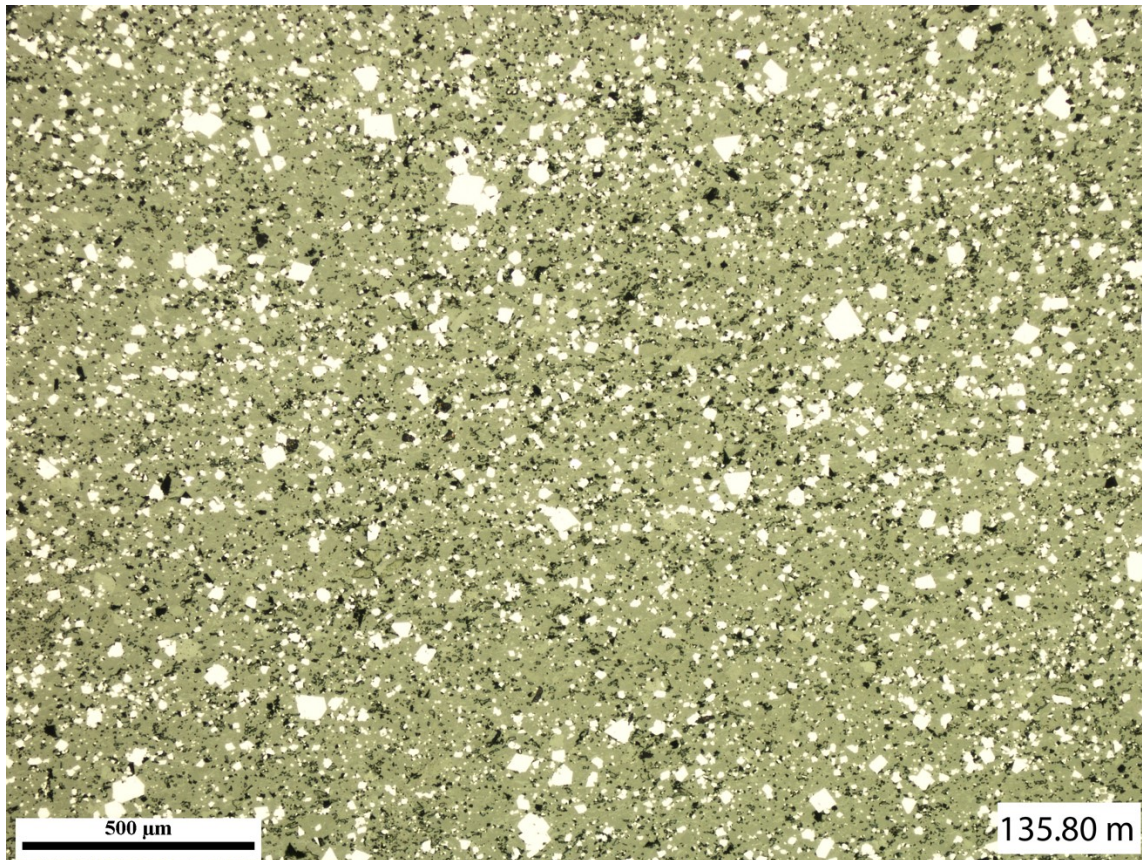
SI Figure 2.4. General texture of the IF lithology within the Boolgeeda Iron Formation. Note the presence of two forms of magnetite: one large eudral form and one smaller subhedral form.
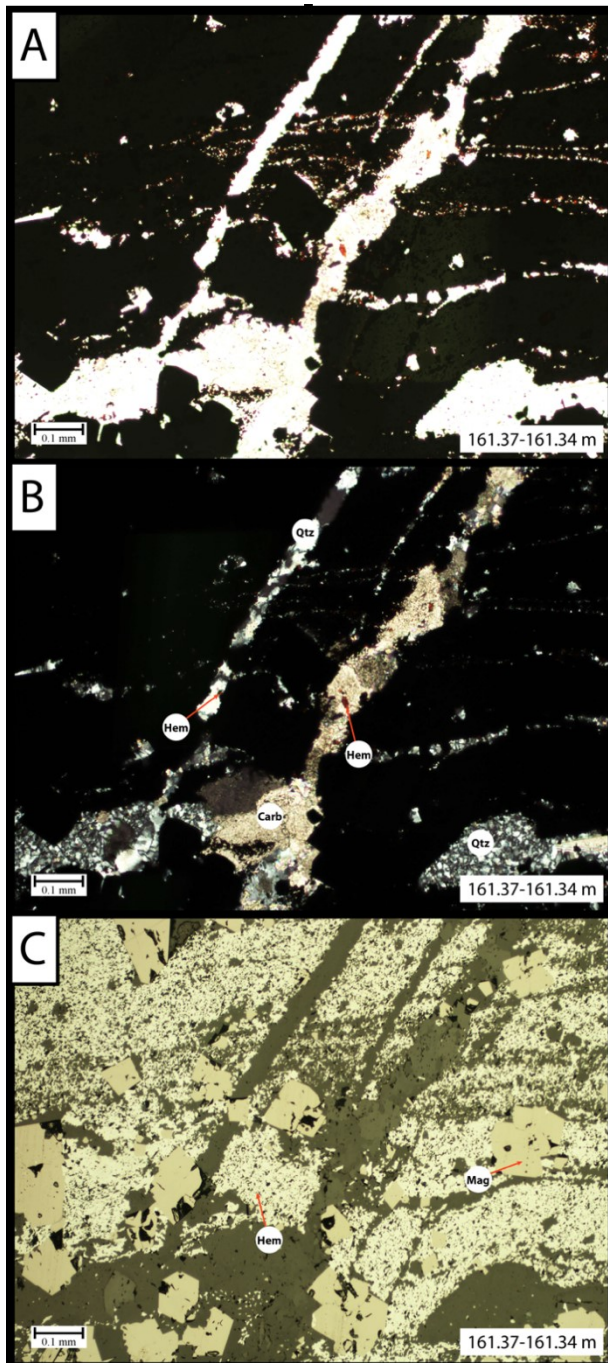
SI Figure 2.5. Microplaty hematite in quartz and carbonate veins, displayed in plane-polarized light (A), cross-polarized light (B), and reflected light (C). Small grains of microplaty hematite can be found in both the quartz vein (left) and the carbonate vein (right). Notably, hematite does not appear vary gradationally away from the vein and, in general, the association of microplaty hematite and veins is rare.
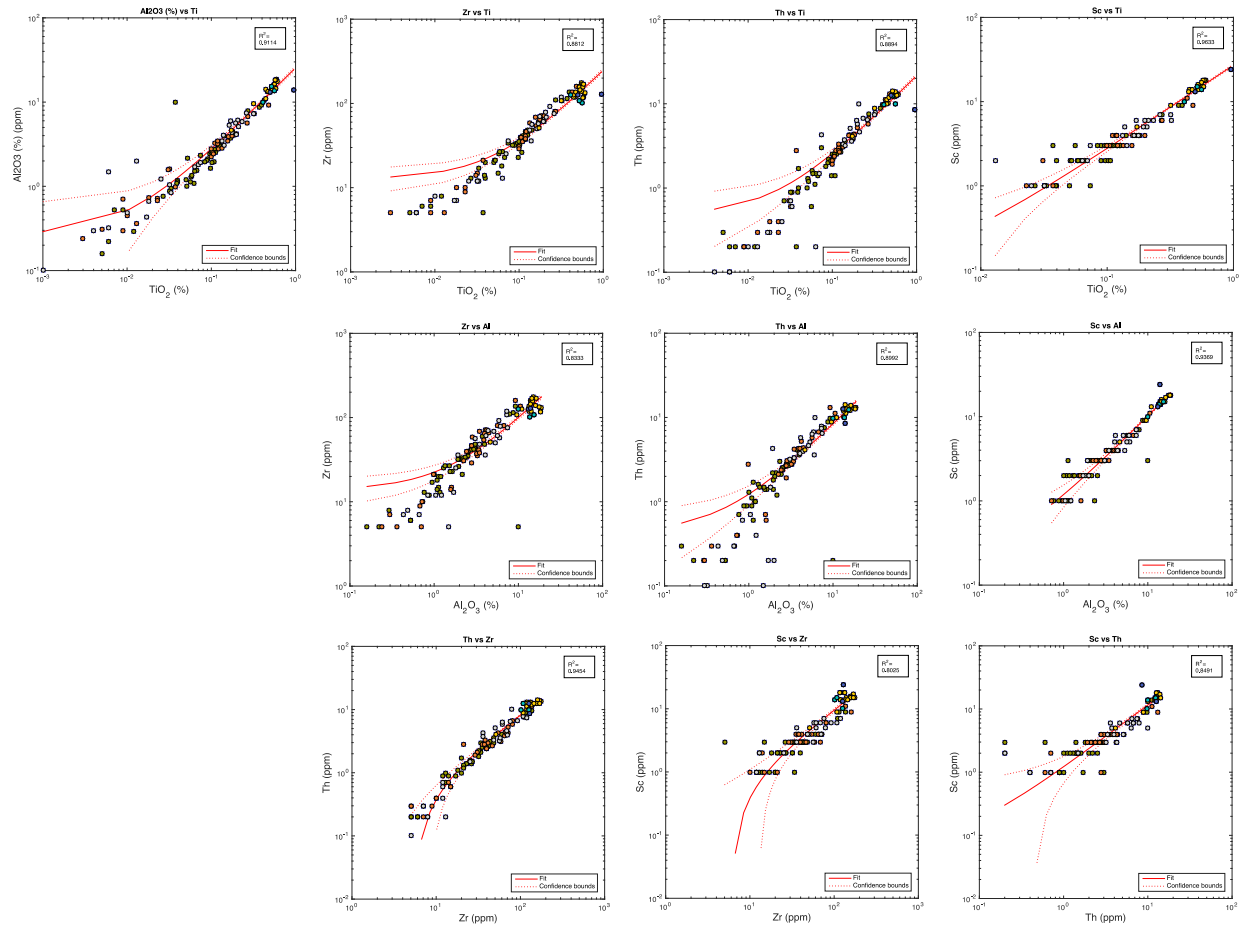
SI Figure 2.6. Crossplots of all lithogenic elements showing R2 values.
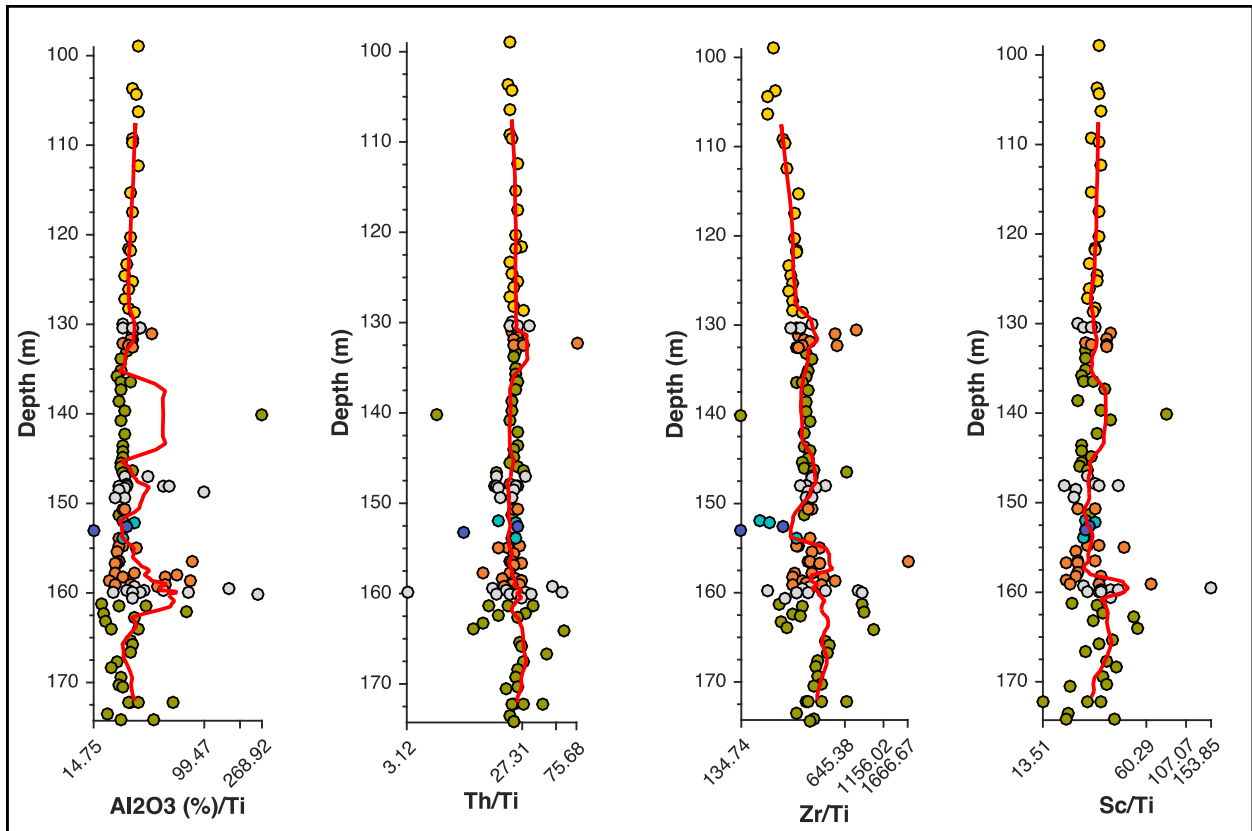
SI Figure 2.7. Lithogenic elements normalized to Ti to provide a sense of where fractionations in lithogenic elements occur.
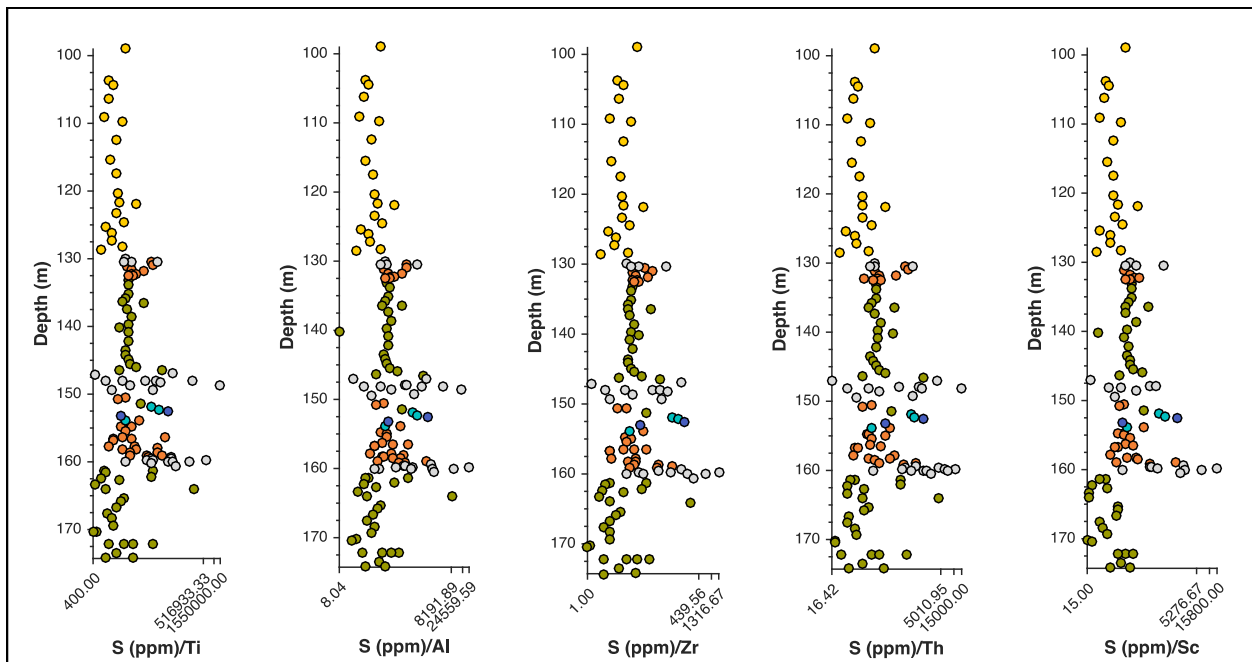
SI Figure 2.8. Variation in depth plots of S based on which lithogenic element is used to normalize. Plots are almost identical, thereby suggesting our choice of Ti does not influence depth profiles.
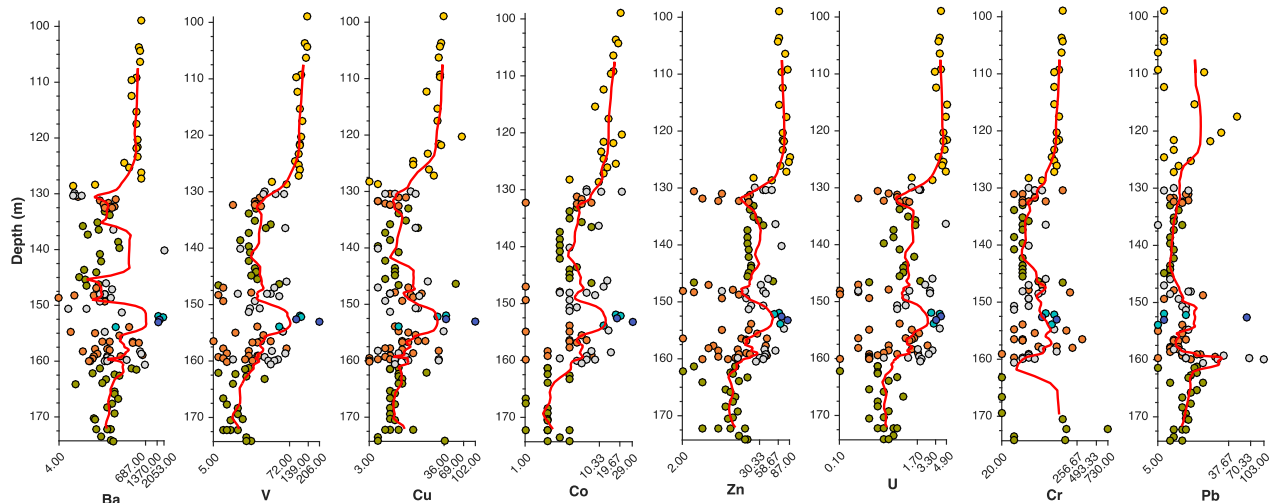
SI Figure 2.9. Trace element profiles not normalized to Ti.
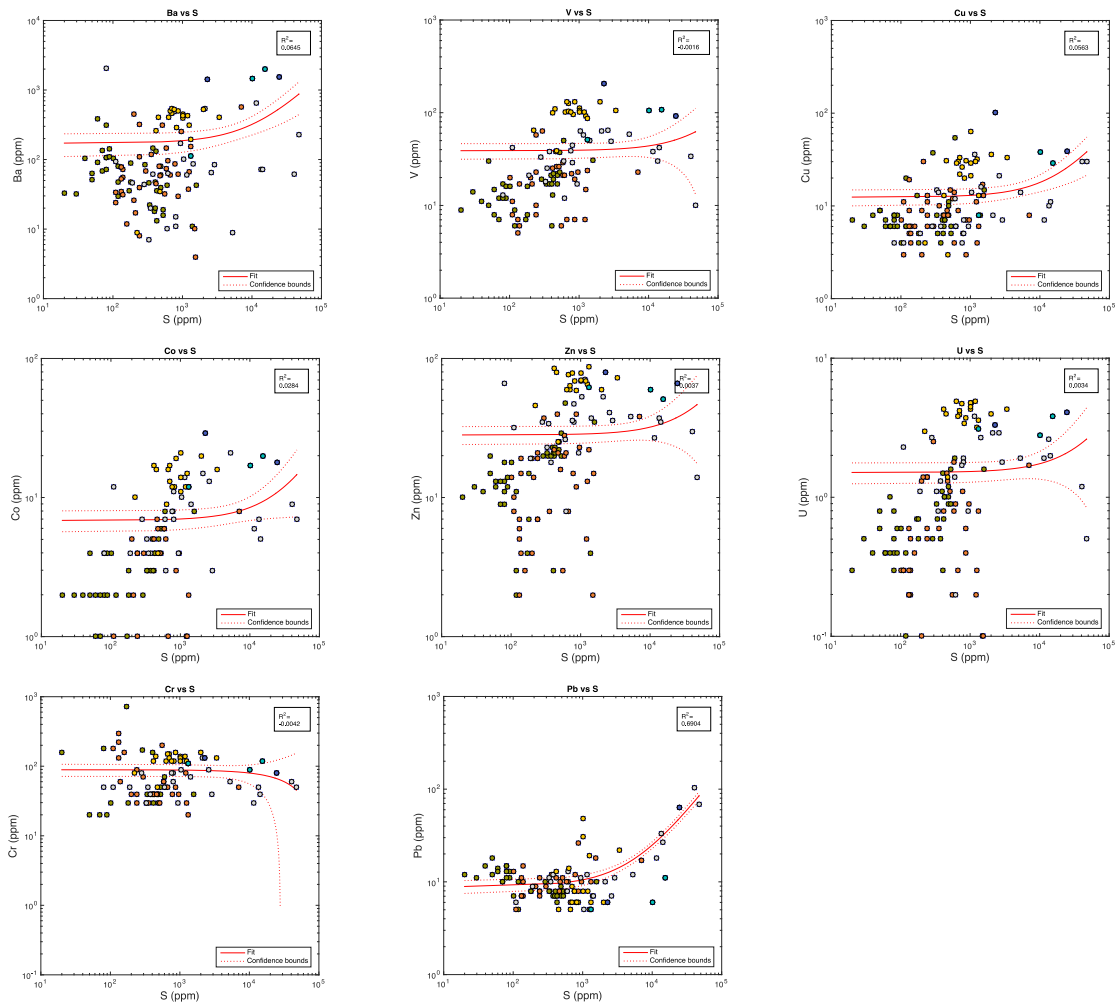
SI Figure 2.10. Correlation plots of sulfur vs trace element concentrations. Only Pb shows a significant correlation with S.
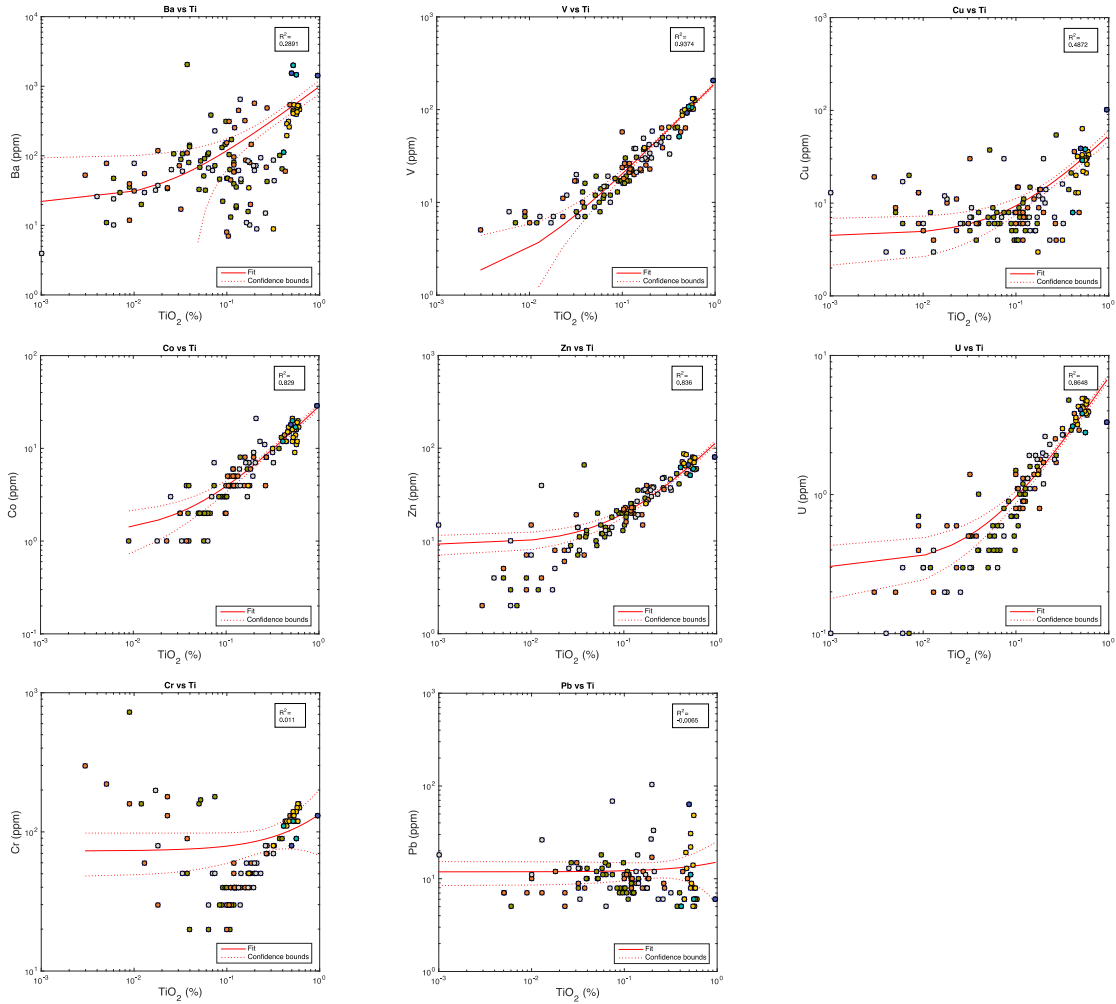
SI Figure 2.11. Trace element concentrations vs titanium concentrations. Strong correlations suggest trace element concentration is dominated by detrital input.
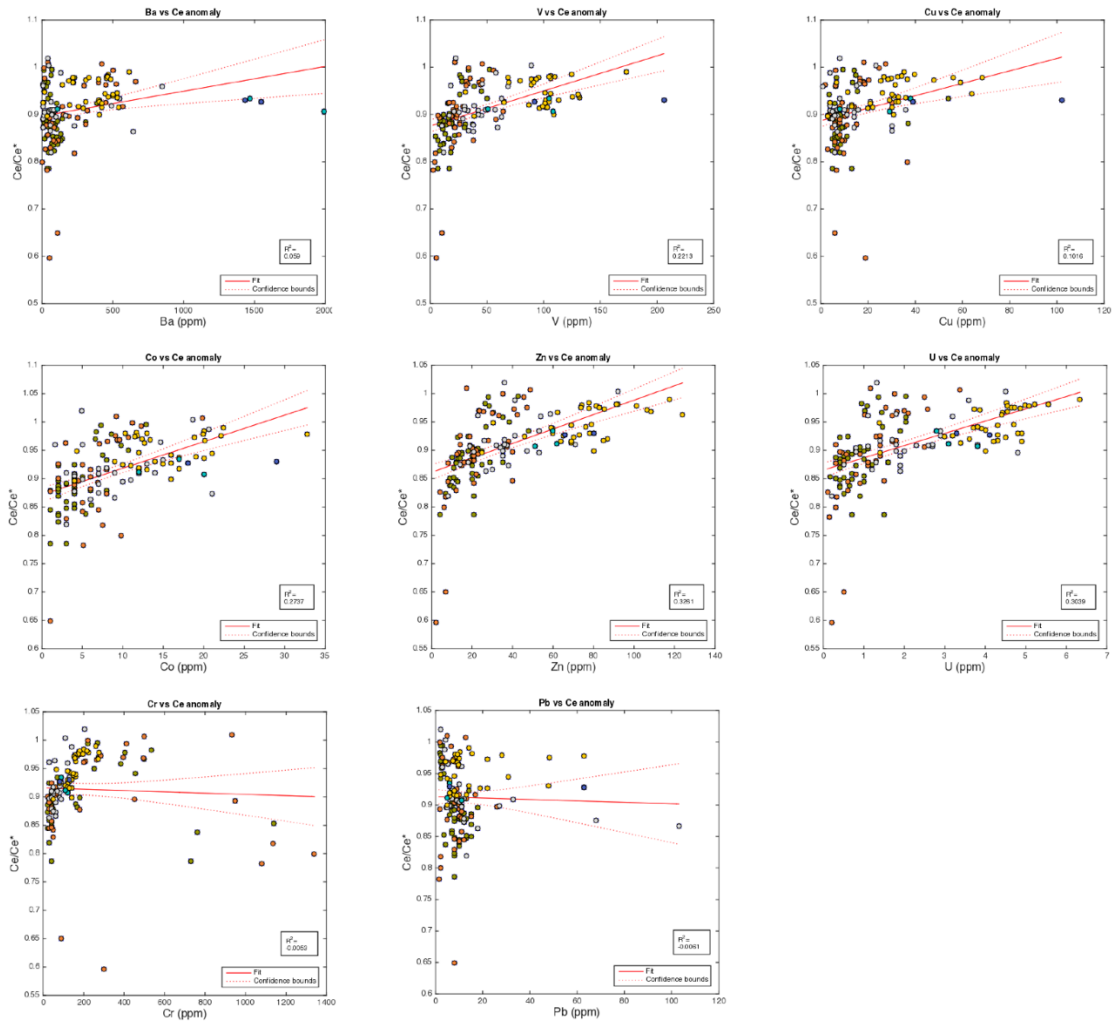
SI Figure 2.12. Ce anomaly vs trace element concentration plots. V, U, Co and Zn show weak correlations (above r^2=0.2) while Ba, Cu, Cr, and lead show no correlation.
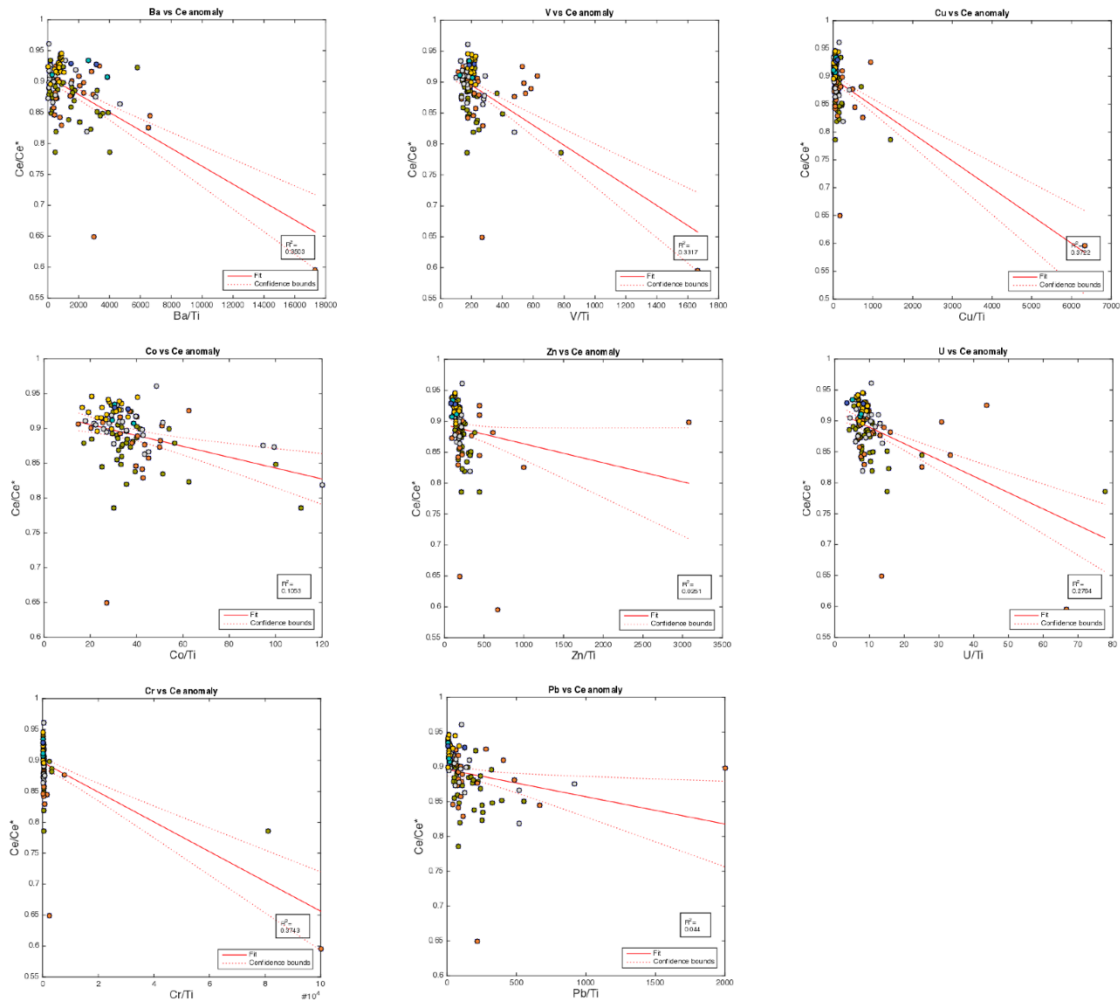
SI Figure 2.13. Cross plots of Ce anomaly vs trace element concentrations normalized to Ti.
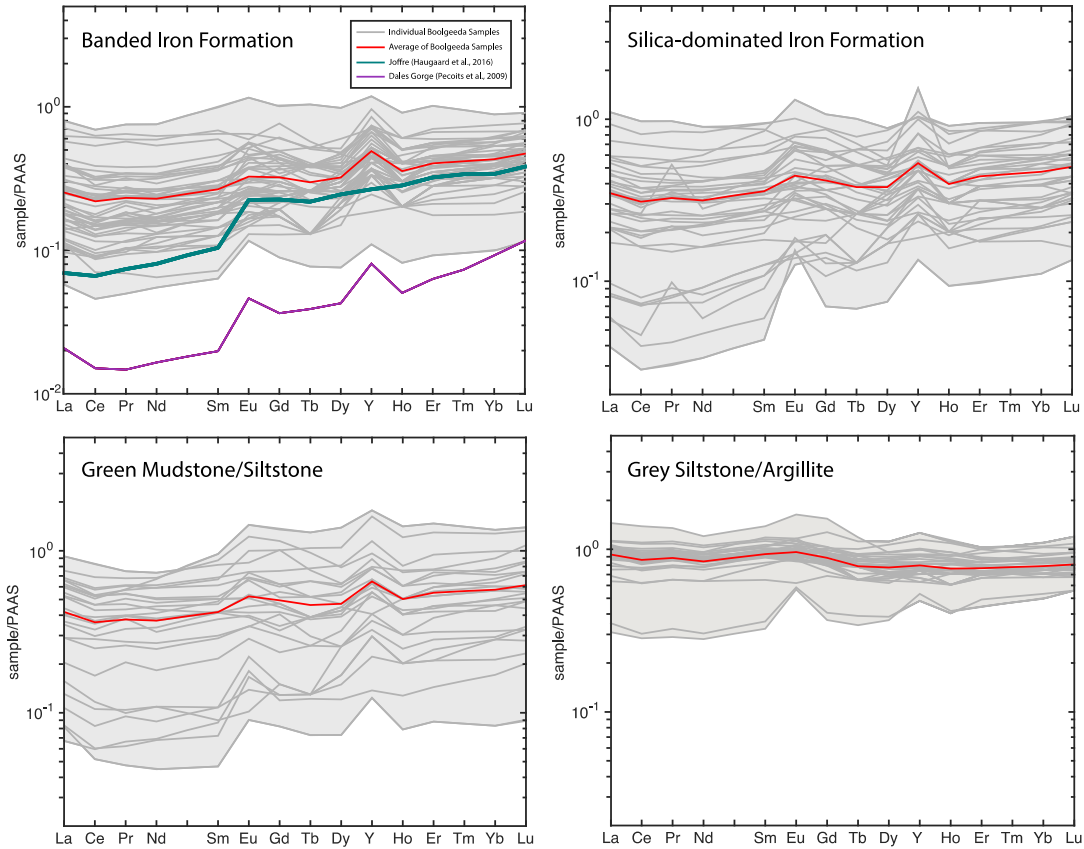
SI Figure 2.14. REE+Y patterns for lithologies within TCDP1 (no limit on Al content). Light grey lines represent individual measurements, and bright red lines represent the average pattern of each sample set. The REE+Y patterns for the Dales Gorge BIF (purple) and the Joffre BIF (Green) generated from the data of Pecoits et al. (2009) and Haugaard et al. (2016), respectively, have been included in the Banded Iron Formation Panel.

10. Tables (Chapter 2)

Table 2.1. Average, minimum, and maximum major element concentrations within TCDP1.

(ppm)	Iron Formation (n=51)			Silica-dominated Iron Formation (n=53)			Green Mudstone/Siltstone (n=30)			Sandstone (n=3)			Diamictite (n=2)			Grey Siltstone/Argilite (n=35)		
Element	Avg	Min	Max	Avg	Min	Max	Avg	Min	Max	Avg	Min	Max	Avg	Min	Max	Avg	Min	Max
SiO$_2$ (%)	50.35	21.29	85.78	57.09	23.68	93.39	38.25	21.58	60.55	52.79	45.61	57.35	55.14	55.02	55.25	58.72	41.15	64.84
TiO$_2$ (%)	0.09	0.01	0.27	0.09	0.00	0.27	0.22	0.03	0.48	0.50	0.41	0.56	0.72	0.50	0.95	0.50	0.16	0.65
Al$_2$O$_3$ (%)	2.14	0.16	7.94	2.25	0.10	6.22	5.89	1.21	11.11	13.06	10.02	15.49	13.58	13.15	14.01	13.99	4.34	18.80
Fe$_2$O$_3$ (%)	41.71	9.48	74.85	35.06	4.29	76.17	41.83	17.09	61.34	19.69	14.85	28.06	17.44	16.97	17.90	11.72	7.21	29.30
MnO (%)	0.07	0.02	0.22	0.16	0.03	2.65	0.36	0.03	2.18	0.08	0.05	0.13	0.07	0.07	0.08	0.10	0.05	0.26
MgO (%)	1.86	0.27	5.40	1.63	0.16	4.13	3.96	1.52	8.45	4.24	3.11	6.19	4.01	3.84	4.18	3.25	2.55	4.51
CaO (%)	1.79	0.20	6.30	1.95	0.32	6.77	2.98	0.29	6.60	1.03	0.19	2.67	0.30	0.28	0.31	2.37	0.18	10.39
Na$_2$O (%)	0.14	0.00	0.82	0.28	0.00	1.79	0.24	0.00	1.15	0.55	0.08	1.47	0.12	0.11	0.13	0.07	0.02	0.43
K$_2$O (%)	0.18	0.00	0.55	0.20	0.00	0.91	0.40	0.01	2.39	3.62	0.22	6.17	4.49	4.32	4.66	2.81	0.03	4.88
P$_2$O$_5$ (%)	0.22	0.02	1.15	0.21	0.01	0.83	0.39	0.01	1.63	0.36	0.09	0.89	0.12	0.10	0.13	0.06	0.06	0.26
S (ppm)	341.79	20.00	1570.00	706.53	100.00	7100.00	5274.61	80.00	47400.00	8870.00	1310.00	15200.00	13595.00	2290.00	24900.00	965.13	220.00	3350.00
LOI	2.22	0.05	8.73	1.71	-1.46	4.12	6.40	1.51	15.76	4.49	3.88	5.31	4.37	3.66	5.07	6.13	4.08	17.15

Table 2.2. Average, minimum, and maximum trace element concentrations within TCDP1.

(ppm)	Iron Formation (n=51)			Silica-dominated Iron Formation (n=53)			Green Mudstone/Siltstone (n=30)			Sandstone (n=3)			Diamictite (n=2)			Grey Siltstone/Argilite (n=35)		
Element	Avg	Min	Max	Avg	Min	Max	Avg	Min	Max	Avg	Min	Max	Avg	Min	Max	Avg	Min	Max
Y	12.41	2.97	26.00	11.29	2.00	41.87	18.04	2.00	48.00	19.67	16.00	26.00	20.50	19.00	22.00	21.52	13.00	34.11
Zr	32.94	4.74	110.00	36.45	3.30	117.64	75.93	5.00	160.00	111.33	101.00	126.00	127.00	126.00	128.00	147.72	44.98	214.20
Ba	75.67	11.00	389.00	148.32	4.00	660.86	206.79	7.00	2053.00	1192.33	113.00	1994.00	1494.00	1437.00	1551.00	359.09	9.00	616.87
La	8.14	1.10	21.90	8.51	0.60	28.10	19.54	1.00	42.20	31.00	27.60	36.20	31.70	27.20	36.20	35.46	11.82	55.43
Ce	14.54	1.80	42.60	15.59	0.90	55.31	35.67	1.80	77.20	58.63	53.30	68.40	60.60	52.70	68.50	68.53	22.58	110.45
Pr	1.71	0.22	5.06	1.80	0.14	5.86	4.12	0.33	8.59	7.02	6.22	8.36	7.16	6.29	8.02	7.82	2.55	11.94
Nd	6.50	0.90	18.20	6.85	0.50	21.79	15.41	0.80	30.40	25.10	22.50	28.30	26.50	24.30	28.70	28.59	9.51	40.86
Sm	1.23	0.20	3.30	1.30	0.10	4.69	2.84	0.20	5.50	4.63	4.10	5.10	4.80	4.60	5.00	5.18	1.80	7.70
Eu	0.30	0.07	0.61	0.35	0.05	1.42	0.66	0.19	1.56	0.95	0.77	1.09	1.01	0.90	1.11	1.04	0.61	1.77
Gd	1.30	0.20	2.86	1.40	0.20	5.00	2.58	0.20	6.30	3.63	3.10	4.30	3.80	3.70	3.90	4.13	1.71	7.20
Tb	0.21	0.06	0.40	0.27	0.05	0.77	0.40	0.10	1.00	0.50	0.40	0.60	0.55	0.50	0.60	0.61	0.26	0.91
Dy	1.34	0.30	2.40	1.29	0.20	4.12	2.40	0.20	6.50	3.17	2.70	3.70	3.55	3.50	3.60	3.62	1.72	5.23
Ho	0.34	0.08	0.60	0.32	0.08	0.84	0.55	0.20	1.40	0.63	0.50	0.80	0.70	0.70	0.70	0.75	0.40	1.10
Er	1.05	0.26	1.90	0.93	0.10	2.50	1.66	0.20	4.20	1.97	1.70	2.30	2.25	2.20	2.30	2.18	1.27	2.93
Tm	0.16	0.04	0.29	0.17	0.03	0.39	0.26	0.07	0.61	0.31	0.27	0.36	0.33	0.32	0.34	0.33	0.20	0.45
Yb	1.13	0.28	1.90	0.99	0.10	2.70	1.71	0.20	3.80	2.00	1.70	2.40	2.15	2.10	2.20	2.22	1.40	3.09
Lu	0.19	0.05	0.30	0.18	0.04	0.42	0.29	0.08	0.60	0.30	0.26	0.36	0.35	0.34	0.36	0.35	0.24	0.51
Hf	0.85	0.10	2.59	1.20	0.14	3.42	2.08	0.80	5.34	2.73	2.40	3.10	3.10	3.10	3.10	3.77	1.20	6.21
Th	2.26	0.20	7.60	2.48	0.10	8.59	6.51	0.20	18.94	10.70	9.80	12.40	10.60	8.60	12.60	12.31	3.93	20.90
U	0.86	0.10	2.04	0.96	0.10	3.37	2.09	0.20	4.80	3.23	2.80	3.80	3.70	3.30	4.10	4.22	1.37	6.34
Sc	2.80	0.47	7.48	3.41	0.19	8.36	5.93	1.00	11.51	13.00	10.00	15.00	18.50	13.00	24.00	14.73	4.98	24.94
V	19.78	4.31	52.16	23.52	2.29	64.00	40.19	10.00	88.89	88.00	51.00	108.00	149.00	92.00	206.00	98.84	30.72	172.80
Cr	203.47	20.00	1138.86	259.37	20.00	1340.31	72.88	30.00	205.93	106.67	90.00	120.00	105.00	80.00	130.00	155.24	50.00	277.40
Co	4.49	1.00	12.83	6.22	1.00	19.80	8.65	1.60	21.00	16.33	12.00	20.00	23.50	18.00	29.00	14.95	4.00	32.79
Cu	9.75	3.43	54.00	10.61	1.86	36.63	11.68	1.01	36.00	25.00	8.00	38.00	70.50	39.00	102.00	30.57	3.00	68.41
Pb	8.19	1.98	18.00	8.62	1.39	26.00	15.76	2.26	103.00	7.33	5.00	11.00	34.50	6.00	63.00	14.87	2.10	62.89
Zn	18.83	2.00	48.00	19.48	2.00	48.58	38.47	8.00	92.23	57.67	51.00	62.00	73.00	66.00	80.00	76.02	25.00	123.90

Table 2.3. Raw data used in Chapter 2.

Sample name	Lithology	SiO$_2$ (%)	TiO$_2$ (%)	Al$_2$O$_3$ (%)	Fe$_2$O$_3$ (%)
99.0-99.09	Kungarra mudstone	59.62	0.594	18.72	8.21
103.68-103.77	Kungarra mudstone	58.91	0.606	17.61	9.01
T1 104.38	Kungarra mudstone	58.35	0.647	18.803	9.377
104.38	Kungarra mudstone	58.35	0.586	18.19	9.22
T1 104.4	Kungarra mudstone	62.76	0.495	11.795	8.164
106.29-106.35	Kungarra mudstone	59.12	0.576	18.41	10.09
T1 109.16	Kungarra mudstone	57.2126867	0.61810649	17.4837186	12.5622402
T1 109.18	Kungarra mudstone	64.84	0.472	10.925	9.436
109.14-109.2	Kungarra mudstone	61.87	0.552	15.99	11.16
T1 109.7	Kungarra mudstone	62.28	0.47	13.536	11.127
109.7	Kungarra mudstone	63.69	0.46	13.43	11.05
112.3-112.41	Kungarra mudstone	59.64	0.446	14.28	14.06
T1 113.95	Kungarra mudstone	58.75	0.404	12.378	16.165
T1 115.35	Kungarra mudstone	61.11	0.535	15.94	9.108
115.32-115.43	Kungarra mudstone	61.31	0.545	15.18	9
117.51-117.42	Kungarra mudstone	60.14	0.56	16.24	11.8
T1 119.9	Kungarra mudstone	60.51	0.524	15.25	8.161
T1 120.3	Kungarra mudstone	60.8	0.545	15.625	7.66
120.3	Kungarra mudstone	61.05	0.52	14.59	8.33
T1 121.6	Kungarra mudstone	58.91	0.531	13.846	7.477
121.6-121.75	Kungarra mudstone	59.32	0.518	14.01	7.84
T1 121.8	Kungarra mudstone	58.39	0.493	13.35	9.03
121.8-121.9	Kungarra mudstone	59.55	0.514	14.13	9.07
123.29-123.36	Kungarra mudstone	60.97	0.568	14.73	8.3
T1 123.43	Kungarra mudstone	62.18	0.522	14.433	7.205
T1 124.45	Kungarra mudstone	57.72	0.413	11.758	13.17
124.47-124.57	Kungarra mudstone	57.98	0.441	10.94	13.32
125.3-125.37	Kungarra mudstone	56.87	0.469	13.36	16.99
T1 126.05	Kungarra mudstone	64.71	0.531	14.135	9.741
126.09-126.17	Kungarra mudstone	63.19	0.528	14.04	9.9
127.17-127.26	Kungarra mudstone	61.92	0.579	14.44	11.38
T1 125-30	Kungarra mudstone	55.53	0.458	13.634	17.435
T1 128.24	Boolgeeda IF	42.04	0.157	4.34	22.57
128.24-128.31	Boolgeeda IF	41.15	0.173	4.62	23.76
128.55-128.65	Boolgeeda IF	44.42	0.319	9.59	29.3
129.88-130.01	Boolgeeda IF	40.62	0.177	4.38	33.47
130.38	Boolgeeda IF	43.4	0.163	5.36	26.54
T1 130.39	Boolgeeda IF	43.2	0.259	7.32	28.63
130.39	Boolgeeda IF	38.06	0.211	5.1	37.93
130.4	Boolgeeda IF	45.1	0.26	7.42	25.09
130.46-130.51	Boolgeeda IF	81.1	0.009	0.3	16.27
130.95-131.04	Boolgeeda IF	52.18	0.018	0.73	41.94
131.04-131.17	Boolgeeda IF	48.01	0.111	3.23	39.22

131.65-131.75	Boolgeeda IF	46.75	0.118	3.42	37.07
131.76-131.82	Boolgeeda IF	73.04	0.013	0.36	23.57
132.23	Boolgeeda IF	28.05	0.16	3.9	56.43
T1 132.25A	Boolgeeda IF	50.0043317	0.05781675	1.68772881	46.9399368
T1 132.25B	Boolgeeda IF	79.2643101	0.0121377	0.53021086	20.1497958
132.38-132.5	Boolgeeda IF	48.03	0.118	3.21	36.92
132.5-132.59	Boolgeeda IF	43.65	0.119	3.44	42
133.05-133.15	Boolgeeda IF	54.15	0.121	3.13	34.1
133.75-133.85	Boolgeeda IF	53.83	0.119	2.81	35.48
135.04-135.14	Boolgeeda IF	53.07	0.119	2.85	34.53
T1 135.8	Boolgeeda IF	50.2264765	0.15940034	3.81242408	37.6316175
135.8	Boolgeeda IF	51.14	0.169	3.76	34.42
136.4-136.46	Boolgeeda IF	51.97	0.368	8.71	22.82
T1 136.5	Boolgeeda IF	56.6958957	0.15004488	3.47740073	35.9075371
136.5	Boolgeeda IF	50.54	0.142	3.98	35.57
137.3-137.4	Boolgeeda IF	52.24	0.09	2.11	37.97
138.6-138.73	Boolgeeda IF	50.69	0.089	2.03	38.28
T1 139.2	Boolgeeda IF	52.5431193	0.22050133	5.17026176	35.485226
T1 139.76	Boolgeeda IF	49.6262872	0.08612412	2.15865528	41.8224849
139.74-139.83	Boolgeeda IF	52.78	0.095	2.41	35.54
T1 139.8	Boolgeeda IF	57.4607868	0.13615209	3.38207876	36.8091527
140.09	Boolgeeda IF	60.55	0.037	9.95	17.09
140.75	Boolgeeda IF	54.81	0.084	1.95	36.57
T1 142.13	Boolgeeda IF	53.1808074	0.10728193	2.80769166	40.1227366
142.13-142.23	Boolgeeda IF	51.99	0.1	2.52	36.33
143.55-143.6	Boolgeeda IF	54.16	0.125	3	37.19
T1 144.1	Boolgeeda IF	53.8496178	0.13399716	3.31237391	38.3291843
144.1	Boolgeeda IF	53.21	0.127	3.07	37.41
144.87	Boolgeeda IF	50.39	0.111	2.74	38.28
T1 145.05	Boolgeeda IF	46.4642998	0.12345302	3.1959712	47.2471642
T1 145.4	Boolgeeda IF	49.9140662	0.10293976	2.78281435	42.4167249
145.45	Boolgeeda IF	51.77	0.125	2.93	37.38
146	Boolgeeda IF	45.34	0.393	9.23	30.37
T1 146.36	Boolgeeda IF	40.5045147	0.28645548	11.1076509	34.928649
146.36	Boolgeeda IF	52.67	0.273	7.94	28.41
146.49-146.54	Boolgeeda IF	85.78	0.012	0.29	12.75
146.95-147.0	Boolgeeda IF	89.08	0.018	0.67	7.95
147.0-147.05	Boolgeeda IF	49.73	0.234	5.91	32.54
T1 147.05	Boolgeeda IF	50.4634706	0.2411578	6.14906083	33.9739006
T1 147.7A	Boolgeeda IF	75.8698263	0.10720517	2.84899474	14.6847755
T1 147.7B	Boolgeeda IF	81.7970655	0.01554932	0.31119027	19.2517855
147.93-147.97	Boolgeeda IF	50.48	0.07	1.82	39.73
148.02	Boolgeeda IF	26.72	0.025	1.21	61.12
148.085	Boolgeeda IF	21.58	0.133	3.45	61.34
148.1	Boolgeeda IF	41.37	0.324	7.29	32.12

148.12	Boolgeeda IF	89.45	0.006	0.32	5.08
148.2-148.25	Boolgeeda IF	92.02	0.017	0.43	5.17
148.6	Boolgeeda IF	42.88	0.319	7.33	32.61
148.65	Boolgeeda IF	93.39	0.001	0.1	4.29
149.31-149.36	Boolgeeda IF	76.82	0.033	0.84	20.3
149.36-149.4	Boolgeeda IF	34.81	0.143	3.09	50.28
T1 150.58A	Boolgeeda IF	34.1063838	0.19294964	4.57512759	43.1151039
T1 150.58B	Boolgeeda IF	35.9250468	0.10999858	2.92573802	53.3292076
150.58-150.64	Boolgeeda IF	35.97	0.103	2.54	50.89
150.64-150.72	Boolgeeda IF	35.06	0.178	4.48	36.95
151.33-151.38	Boolgeeda IF	36.63	0.112	2.52	48.19
T1 151.4	Boolgeeda IF	34.6500586	0.1102769	2.86173449	54.5814929
151.83-151.91	Boolgeeda IF	57.35	0.56	13.68	16.17
152.2-152.28	Boolgeeda IF	55.4	0.519	15.49	14.85
152.53-152.59	Boolgeeda IF	55.02	0.497	13.15	17.9
153.1-153.14	Boolgeeda IF	55.25	0.95	14.01	16.97
153.78-153.84	Boolgeeda IF	45.61	0.409	10.02	28.06
153.87-153.945	Boolgeeda IF	52.09	0.121	2.77	37.63
154.84-154.8	Boolgeeda IF	39.89	0.43	10.54	32.03
154.84-154.87	Boolgeeda IF	42.6	0.099	2.26	48.54
154.87-154.9	Boolgeeda IF	78.71	0.023	0.72	18.93
T1 155.45D	Boolgeeda IF	50.678045	0.19788097	4.73418091	37.9894194
T1 155.45A	Boolgeeda IF	56.5767792	0.25922972	6.21506219	27.2070157
T1 155.45E	Boolgeeda IF	60.7528537	0.24713561	5.56766262	22.1471128
155.46-155.56	Boolgeeda IF	49.99	0.182	4.06	38.05
156.4	Boolgeeda IF	49.26	0.177	3.99	37.37
T1 156.5A	Boolgeeda IF	49.3029011	0.13654192	3.20802931	43.0251407
156.5	Boolgeeda IF	48.14	0.105	2.42	43.42
T1 156.62A	Boolgeeda IF	45.6450776	0.1290821	3.03503155	46.3811261
156.72-156.62	Boolgeeda IF	50.15	0.158	3.48	38.79
156.72-156.83	Boolgeeda IF	46.11	0.135	2.86	44.12
T1 156.83	Boolgeeda IF	48.8284563	0.15823266	3.77271462	42.5030816
157.74	Boolgeeda IF	43.17	0.267	5.63	45.86
157.76	Boolgeeda IF	69.11	0.023	0.68	29.39
159.035-159.07	Boolgeeda IF	71.14	0.005	0.31	25.07
158.24-158.26	Boolgeeda IF	48.46	0.273	6.77	34.7
158.26-158.29	Boolgeeda IF	46.8	0.032	1.62	45.7
158.58	Boolgeeda IF	66.65	0.009	0.71	29.73
158.6	Boolgeeda IF	31.06	0.476	9.25	45.85
158.96-159	Boolgeeda IF	29.2	0.2	4.24	57.57
159-159.035	Boolgeeda IF	28.1	0.031	1.57	66.16
T1 159.08	Boolgeeda IF	27.2675926	0.11509773	3.86174565	66.3118989
T1 159.08A	Boolgeeda IF	28.0470641	0.12353866	3.11330377	64.9550226
T1 159.08B	Boolgeeda IF	76.4308637	0.01516204	0.8855673	19.5263453
159.13-159.19	Boolgeeda IF	36.29	0.099	2.78	53.21

159.22	Boolgeeda IF	76.27	0.01	0.45	17.95
159.3	Boolgeeda IF	25.85	0.207	6.09	61.22
T1 159.5A	Boolgeeda IF	81.2041924	0.02501195	1.47133663	15.1960246
159.5A	Boolgeeda IF	75.88	0.013	1.98	14.47
T1 159.54	Boolgeeda IF	29.0692164	0.22889547	6.95537578	59.2848147
159.63B	Boolgeeda IF	32.86	0.169	5.99	55.95
159.71-159.735	Boolgeeda IF	30.48	0.01	0.49	67.42
159.735-159.76	Boolgeeda IF	67.77	0.064	1.7	24.22
159.8	Boolgeeda IF	27.92	0.074	1.93	52.75
159.95-159.93	Boolgeeda IF	23.18	0.199	4.12	60.04
159.965-159.98	Boolgeeda IF	23.68	0.032	1.04	76.17
159.98-160.015	Boolgeeda IF	73.75	0.004	0.3	22.67
160.02-160.075	Boolgeeda IF	30.52	0.194	5.66	55.62
160.075-160.12	Boolgeeda IF	76.44	0.006	1.5	17.02
160.5-160.64	Boolgeeda IF	40.09	0.138	4.03	45.92
T1 161.3A	Boolgeeda IF	78.7445101	0.01920682	0.39047107	21.6747177
161.28-161.32	Boolgeeda IF	31.12	0.097	1.63	61.54
161.32-161.41	Boolgeeda IF	77.01	0.006	0.22	22.12
161.41-161.48	Boolgeeda IF	33.5	0.067	1.55	59.4
162.10-162.15	Boolgeeda IF	83.23	0.007	0.52	14.43
162.32-162.38	Boolgeeda IF	29.48	0.062	1.09	65.95
162.61-162.67	Boolgeeda IF	29.57	0.04	1.18	65.87
163.32-163.2	Boolgeeda IF	29.07	0.107	1.94	64.72
163.97-164.01	Boolgeeda IF	21.29	0.056	1.12	74.85
164.1-164.04	Boolgeeda IF	78.73	0.005	0.16	19.58
165.3-165.4	Boolgeeda IF	39.11	0.027	0.76	55.94
165.8-165.9	Boolgeeda IF	36.66	0.033	0.94	58.01
166.67-166.74	Boolgeeda IF	40.38	0.04	1.12	55.61
167.6-167.67	Boolgeeda IF	38.22	0.058	1.3	56.76
168.38-168.31	Boolgeeda IF	37.14	0.051	1.01	57.2
169.32-169.39	Boolgeeda IF	40.11	0.063	1.51	53.38
170.19-170.26	Boolgeeda IF	37.44	0.059	1.34	58.31
170.40-170.47	Boolgeeda IF	37.71	0.05	1.2	59.76
T1 172.1C	Boolgeeda IF	55.7902495	0.04132843	1.2182806	38.048547
172.1-172.18 A	Boolgeeda IF	48.62	0.039	1.08	45.91
172.1-172.18 B	Boolgeeda IF	79.83	0.009	0.53	9.48
172.1-172.18 C	Boolgeeda IF	54.93	0.032	0.87	34.13
172.15-172.23	Boolgeeda IF	36.88	0.074	2.33	56.5
173.46-173.52	Boolgeeda IF	56.07	0.102	1.91	35.27
174.24-174.31	Boolgeeda IF	41.22	0.052	2.14	37.4
174.07-174.13	Boolgeeda IF	52.77	0.106	2.5	39.44

MnO (%)	MgO (%)	CaO (%)	Na$_2$O (%)	K$_2$O (%)	P$_2$O$_5$ (%)	S (ppm)
0.051	3.18	0.2	0.09	4.88	0.1	2020
0.071	3.72	0.78	0.13	4.21	0.11	700
0.0558	3.874	0.223	0.156	4.467	0.11	NaN
0.057	3.54	0.24	0.1	4.4	0.1	860
0.1225	3.194	3.861	0.427	2.188	0.12	NaN
0.06	3.57	0.22	0.08	4.38	0.09	660
0.06129445	3.50632859	0.17596124	0.02722683	3.58757652	0.11785764	442.653465
0.093	2.728	2.682	0.039	1.985	0.13	NaN
0.058	3.17	0.32	0.07	3.38	0.11	450
0.0756	3.06	1.66	0.05	2.552	0.15	NaN
0.075	2.92	1.65	0.06	2.51	0.14	1260
0.085	3.44	1.13	0.05	2.27	0.1	830
0.0978	4.509	0.627	0.023	1.075	0.26	NaN
0.0631	2.859	1.232	0.063	3.747	0.09	NaN
0.066	2.73	1.43	0.07	3.44	0.06	640
0.059	3.51	0.41	0.06	3.27	0.11	1000
0.0805	2.826	2.198	0.058	3.71	0.1	NaN
0.079	2.747	2.27	0.06	3.924	0.09	NaN
0.097	2.65	3.28	0.08	3.58	0.09	1010
0.1154	2.58	4.929	0.053	3.377	0.1	NaN
0.106	2.55	4.37	0.07	3.37	0.1	1190
0.107	2.843	4.087	0.051	2.999	0.09	NaN
0.104	2.8	3.8	0.07	3.19	0.1	3350
0.083	2.7	2.34	0.07	3.39	0.07	1020
0.0767	2.63	2.281	0.058	3.615	0.09	NaN
0.1381	3.724	3.553	0.027	1.438	0.08	NaN
0.153	3.55	4.71	0.06	1.37	0.1	1300
0.104	4.07	1.41	0.05	1.45	0.1	420
0.049	3.162	0.566	0.048	3.013	0.09	NaN
0.057	3.01	0.6	0.06	3.05	0.09	710
0.081	3.31	1.2	0.07	2.9	0.08	750
0.1051	4.406	0.97	0.026	1.302	0.1	NaN
0.2622	3.382	10.385	0.028	0.063	0.06	NaN
0.264	3.36	9.45	0.07	0.11	0.07	470
0.159	4.1	3.71	0.04	0.03	0.12	220
1.79	2.61	6.39	0.19	0.02	0.11	600
0.401	2.55	4.21	0.28	0.03	0.09	810
0.5402	4.884	5.482	0.074	0.017	0.05	NaN
0.463	3.57	5.04	0.07	0.05	0.06	5280
0.551	4.61	6.28	0.45	0.03	0.08	800
0.08	0.39	1.16	0.06	0.03	0.1	160
0.054	0.93	2.26	0.15	0.14	0.18	360
0.067	2.7	2.69	0.58	0.16	0.16	420

0.078	2.97	3.22	1.24	0.91	0.18	590
0.039	0.48	1.08	0.12	0.03	0.14	140
0.076	2.17	3.26	1.79	0.51	0.42	790
0.05890925	1.25669406	1.82763613	0.26474375	0.1604714	0.13953785	259.447086
0.06554616	0.38076163	0.8677193	0.00628172	0.02164751	0.18857896	NaN
0.093	2.55	3.58	0.88	0.24	0.49	610
0.078	2.61	3.22	0.72	0.21	0.75	470
0.085	2.35	2.54	0.44	0.07	0.16	490
0.071	2.16	2.22	0.41	0.14	0.1	490
0.088	2.31	2.9	0.2	0.06	0.23	490
0.18925374	2.80497276	3.32951572	0	0.01626769	0.25186761	424.394381
0.151	2.72	2.78	0.02	0.05	0.24	530
0.177	5.51	3.07	0.02	0.53	1.32	1030
0.10548526	2.087269	1.07379512	0	0.03486409	0.1165589	458.626674
0.151	2.72	2.72	0.04	0.09	0.5	1570
0.101	1.83	2.71	0.05	0.05	0.14	340
0.083	1.84	2.78	0.29	0.17	0.07	420
0.09374236	3.09413691	2.22999985	0.82271735	0.08392797	0.1222483	665.238837
0.07922574	2.19520524	2.47452904	0.11958975	0.21626837	0.12558624	253.610417
0.076	2.13	2.56	0.35	0.29	0.06	370
0.03149852	1.77163083	0.79432758	0.56717627	0.32040396	0.1113531	282.619529
0.032	4.5	0.58	0.32	2.39	0.01	80
0.057	1.9	1.94	0.19	0.26	0.22	330
0.08412139	2.31771403	2.02552464	0.16553935	0.18749247	0.25866951	248.076617
0.075	2.25	2.72	0.2	0.22	0.8	410
0.051	2.42	1.23	0.03	0.09	0.15	390
0.04036957	2.51728582	1.25254906	0.06182905	0.18954019	0.23824818	298.239257
0.051	2.51	1.47	0.12	0.21	0.15	430
0.076	2.4	2.11	0.03	0.08	0.34	430
0.06887674	2.44233804	1.55524358	0	0.02684487	0.20645867	1260.27515
0.09704703	2.38983069	2.13685141	0.00019846	0.05982682	0.27958177	230.866831
0.088	2.49	2.21	0.06	0.1	0.28	530
0.09	5.47	1.55	0.32	0.61	0.1	2620
0.07608565	7.61067998	0.65483313	0.07170192	0.1620782	0.12039641	383.860021
0.067	5.4	0.7	0.1	0.19	0.12	600
0.038	0.29	0.62	0.05	0.06	0.02	410
0.041	0.56	0.75	0.12	0.19	NaN	1210
0.076	4.26	0.57	0.56	1.12	0.06	110
0.08575731	4.65184406	0.69816238	0.55644849	1.14706847	0.10967884	577.176052
0.06101445	1.93680154	0.9076274	0.1616749	0.37231837	0.06327634	579.692699
0.02964896	0.29762412	0.61487856	0	0	0.0655653	1164.12828
0.089	1.8	2.33	0.19	0.36	0.06	870
0.133	1.9	3.19	0.23	0.43	0.04	610
0.123	2.93	3.57	0.23	0.44	0.77	370
0.162	5	4.26	0.18	0.32	0.32	280

0.072	0.54	1.4	0.06	0.07	0.01	1500
0.037	0.27	0.58	0.05	0.09	0.02	550
0.159	5.4	1.91	0.5	1.01	0.28	1440
0.033	0.16	0.66	0.03	0.01	0.04	1550
0.085	0.51	0.93	0.07	0.18	0.04	670
0.275	2.77	3.25	0.19	0.36	0.13	190
2.65417106	4.12990906	6.77205438	0.00893004	0.01019548	0.12513491	1202.49721
1.57395742	2.33989565	2.4772104	0.00679634	0.00537249	0.16607723	336.866496
1.339	2.24	1.88	0.02	0.01	0.11	330
2.182	3.96	6.57	0.02	0.04	0.05	350
0.575	2.16	3.86	0.08	0.33	0.09	940
0.63098106	2.60527905	4.14320108	0	0.02455998	0.15912116	1276.63906
0.06	3.41	0.22	0.08	4.47	0.09	10100
0.049	3.11	0.19	0.11	6.17	0.1	15200
0.066	3.84	0.28	0.11	4.32	0.13	24900
0.083	4.18	0.31	0.13	4.66	0.1	2290
0.134	6.19	2.67	1.47	0.22	0.89	1310
0.124	2.05	2.51	0.42	0.31	0.08	970
0.167	8.45	1.88	1.15	0.33	0.31	1160
0.097	2.16	2.17	0.08	0.03	0.03	240
0.03	0.52	0.79	0.06	0.04	0.1	110
0.08663102	3.1852516	1.71308394	0.4167647	0.29917552	0.16046579	579.651189
0.08560867	3.58869896	2.27191801	0.76278555	0.69572466	0.83153196	975.703146
0.13780687	3.61495592	3.56468812	0.26405502	0.80824884	0.09074424	763.127221
0.085	2.81	2.06	0.46	0.26	0.31	590
0.149	2.77	1.75	0.14	0.14	0.3	460
0.14925865	2.08132643	1.86151069	0.42564475	0.33486569	0.21753984	191.765764
0.141	1.77	1.78	0.41	0.31	0.13	510
0.18494712	2.10230747	1.80035105	0.86913745	0.31972092	0.22557235	165.315665
0.164	2.23	2.29	0.76	0.49	0.15	240
0.172	2.07	1.86	0.84	0.3	0.17	200
0.16402809	2.34494065	2.05795187	0.71712946	0.4763471	0.20700907	279.313152
0.079	3.24	0.77	0.2	0.12	0.37	300
0.054	0.42	0.83	0.06	0.07	0.29	130
0.075	0.3	1.27	0.04	0.1	0.07	130
0.166	3.66	2.21	0.04	0.6	0.15	760
0.14	1.37	2.98	0.01	0.02	0.03	210
0.065	0.48	2	0.02	0.07	0.05	240
0.177	4.67	1.8	0.98	0.96	0.25	2090
0.106	2.89	1.85	0.35	0.37	0.5	7100
0.082	1.35	1.45	0.02	0.12	0.31	140
0.09191626	2.64850733	1.46742597	0.07707474	0.19630029	0.21070952	472.288212
0.07988886	2.06961542	1.62809817	0.16543297	0.14687995	0.56588857	2891.4612
0.08562243	0.50243343	1.79392991	0	0.05708866	0.09016353	NaN
0.131	2.11	3.29	0.23	0.13	0.6	1330

0.102	0.62	2.02	0.02	0.04	0.05	140
0.05	3.56	1.04	0.02	0.07	0.54	13500
0.05931236	1.03452553	1.56587452	0	0.02316486	0.08746044	571.700621
0.091	1.65	3.16	0.02	0.02	0.07	870
0.05131737	4.34921173	1.44641077	0	0.22452244	1.1412545	1026.06552
0.053	3.71	0.29	0.21	0.09	0.04	2850
0.051	0.39	1.91	0.03	0.15	0.35	130
0.097	1.04	3	0.34	0.15	0.06	1260
0.162	1.52	6.6	0.24	0.19	1.12	47400
0.122	2.98	2.88	0.02	0.05	1.59	40400
0.059	0.78	0.32	0.03	0.05	0.03	100
0.043	0.29	1.07	0.03	0.02	0.39	200
0.046	3.73	1.19	0.03	0.09	0.83	14300
0.05	1.01	1.82	0.06	0.07	0.3	110
0.042	2.84	2.78	0.18	0.33	1.63	11400
0.0540481	0.39795764	0.55958851	0	0.00139625	0.06471542	106.3604
0.05	1.45	1.83	0.22	0.52	0.46	80
0.035	0.27	0.43	0.04	0.06	0.02	120
0.043	1.35	1.23	0.15	0.55	0.13	60
0.04	0.37	0.73	0.04	0.09	0.04	120
0.023	1.01	0.51	0.12	0.22	NaN	40
0.033	1.22	1.31	0.09	0.3	0.34	90
0.029	2.18	0.85	0.1	0.11	0.13	50
0.027	1.28	0.81	0.08	0.1	0.15	50
0.038	0.51	0.9	0.03	0.04	NaN	1390
0.043	1.14	1.54	0.1	0.21	0.14	80
0.043	1.28	1.72	0.12	0.22	0.27	80
0.04	1.16	1.11	0.11	0.31	0.09	70
0.042	1.3	1.3	0.2	0.27	0.03	60
0.042	1.11	1.88	0.22	0.23	0.24	70
0.051	1.75	1.46	0.03	0.22	0.32	90
0.026	1.43	0.44	0.02	0.09	0.08	30
0.019	1.24	0.2	0.02	0.07	0.04	20
0.10845369	1.3942479	3.48570675	0.05567214	0.24392707	1.14769219	1353.00188
0.062	1.23	1.32	0.08	0.21	0.19	120
0.151	1.49	3.1	0.14	0.18	0.02	170
0.115	1.4	3.66	0.12	0.27	1.1	180
0.038	2.33	0.76	0.08	0.32	0.14	80
0.067	1.46	1.82	0.32	0.28	0.1	180
0.217	4.15	6.3	0.04	0.41	0.2	290
0.048	1.49	0.84	0.11	0.49	0.03	100

LOI	Total on CaCO$_3$ basis for samples >5% CaO	Y	Zr	Ba	La
4.08	99.71	19	131	533	40.7
4.56	99.71	20	135	467	39.4
4.52	100.58	20.86	139.9	470.5	37.47
4.58	99.36	17	119	502	39.5
6.73	99.85	26.79	181.4	224	24.28
4.27	100.9	18	117	503	39
NaN	95.35299726	26.9763755	210.446898	616.871833	55.431403
5.5	98.83	31	214.2	217.1	28.69
4.21	100.9	19	138	407	35.2
4.78	99.74	27.3	132.7	310	33
4.93	100.9	22	119	309	31.5
4.72	100.2	18	118	291	35.5
4.56	98.84	34.11	132	146.7	36.65
4.71	99.46	21.91	183.3	460.2	43.13
4.87	98.71	20	175	407	39.3
4.35	100.5	17	170	399	38.4
5.67	99.08	25.2	200.2	463	42.64
5.47	99.27	19.93	172.2	459.2	38.93
6.19	100.4	20	158	445	38.9
7.37	99.29	23.57	184.3	401.6	35.17
7.03	99.28	20	160	425	40.4
7.16	98.61	24.56	171.2	334.9	34.66
6.88	100.2	21	158	406	37.9
5.55	98.78	20	156	424	37.6
5.54	98.63	20.46	183.4	463.3	39.62
6.71	98.73	22.52	138.1	188.1	30.16
7.24	99.86	25	126	196	34.6
5.64	100.5	22	136	258	36.1
4.22	100.27	19.08	163	488.1	33.82
4.13	98.64	19	145	540	38.6
4.89	100.8	20	170	529	37.5
5.26	99.23	24.48	130	220.6	36.07
17.15	100.44	14.37	44.98	18.99	11.82
15.89	98.92	13	51	35	13.4
9.11	100.9	20	107	9	26.2
10.08	99.84	10	70	10	11.7
15.76	98.79	11	50	11	15.3
10.44	100.9	14.12	83.63	7.051	15.57
8.07	98.62	18	69	9	14
10.99	100.9	15	75	15	20.1
1.16	100.7	3	7	12	1.8
1.7	100.3	10	10	119	3.7
3.62	100.6	13	35	45	8.1

4.02	99.98	15	41	74	8.9
0.88	99.76	5	5	55	2.5
2.8	99.56	22	54	86	16
NaN	102.3978065	8.84013929	20.410216	190.988584	7.97443543
NaN	101.4869897	7.00675463	4.46872738	38.6688031	2.28648645
4.12	100.3	27	37	96	13.2
3.09	99.88	30	38	59	17.7
3.62	100.8	19	43	60	10.5
3.1	100.4	10	46	80	8.7
4.22	100.6	16	44	40	9.7
NaN	98.42179591	19.3654108	65.1479172	15.6005362	16.6720275
4.24	99.68	20	60	16	14.4
5.53	100	32	115	102	30.4
NaN	99.6488507	9.04976092	65.8884249	28.9034814	10.2209821
3.97	100.4	26	48	43	15.1
3.37	100.7	14	33	22	7.8
3.42	99.73	8	32	132	6.3
NaN	99.86588116	11.7938953	89.765099	70.2731531	14.5580721
NaN	98.90395587	10.0888122	35.2676425	68.1840242	6.84445082
3.37	99.67	9	34	147	7.2
NaN	101.3845606	9.71586649	56.4341204	231.609901	11.5590548
3.81	99.27	2	5	2053	1
2.11	100.1	14	32	46	8.1
NaN	101.2575789	14.0569661	41.7336067	58.7454867	11.9125696
2.41	99.62	23	35	48	15.4
1.87	100.3	14	44	18	9.5
NaN	99.92499502	12.3559715	53.055102	40.606603	12.6453141
2.29	100.6	14	48	36	10.1
3.86	100.4	17	41	13	10.6
NaN	101.3306501	12.9328254	40.0314335	21.6759243	9.4678005
NaN	100.1798814	9.76042333	49.9570747	11.4787704	9.93437177
3.35	100.8	18	42	19	10.7
7.23	100.7	19	136	65	27.1
NaN	95.52304538	10.9767824	135.968318	49.0554662	23.8907722
4.77	100.7	12	110	43	21.9
0.66	100.6	5	8	20	3.3
1.56	100.9	3	7	37	1.6
5.73	100.8	21	92	94	23.2
NaN	98.07654938	21.50742	118.258026	131.079269	35.3407016
NaN	97.01351474	8.775265	44.9266849	43.3866876	11.0808104
NaN	102.3833074	3.33682443	4.84270976	5.41442306	3.13163236
4.05	101	10	25	61	7.8
4.45	99.46	8	12	63	4.1
4.73	99.29	21	48	62	16.9
9.34	100.7	18	108	44	25.2

2.23	99.24	2	NaN	10	0.7
0.87	99.55	NaN	7	32	2
8.39	100.8	31	119	87	26
1.21	99.93	NaN	NaN	4	0.6
1.13	101	5	12	60	2.6
5.53	100.8	15	56	46	11.1
NaN	101.1262722	7.19082273	46.4866478	14.7270458	9.99367634
NaN	98.85930051	10.4094151	77.1502983	21.3608669	13.4117145
4.94	100	5	40	7	6.6
11.32	100.8	10	66	20	14
4.9	99.43	5	39	169	6.1
NaN	99.76670525	6.62800169	48.5913531	42.8547643	5.3563579
3.88	99.98	16	101	1470	27.6
4.28	100.3	17	107	1994	36.2
5.07	100.4	22	126	1551	36.2
3.66	100.3	19	128	1437	27.2
5.31	101	26	126	113	29.2
2.77	100.9	13	46	251	12.9
5.53	100.7	28	137	60	35.6
1.79	99.86	9	31	8	11.5
0.5	100.4	8	10	34	3.1
NaN	99.46089887	27.749403	117.638585	420.120007	22.5688658
NaN	98.49435459	15.7639901	79.4055024	210.921966	17.1117507
NaN	97.19526377	17.2874038	101.325105	504.38041	28.096179
1.94	100.2	17	71	147	15.2
2.8	98.85	22	65	80	13.2
NaN	100.7427591	41.8712357	58.5686341	399.164274	21.3590617
1.58	100.2	18	40	311	13.3
NaN	100.6923537	11.2510056	59.7649525	660.857464	15.68994
1.72	100.4	14	69	323	14.7
1.68	100.3	11	59	450	10
NaN	101.2298914	13.6193317	75.8549546	531.344887	18.5239035
0.87	100.6	18	80	68	22.3
0.02	100.9	6	9	35	2.2
0.74	99.11	3	NaN	79	0.9
3.82	100.9	13	81	493	20.5
1.79	100.5	7	15	17	3.1
1.12	100.9	5	5	39	1.8
5.34	100.8	14	160	546	42.2
1.63	98.91	14	71	569	13.6
-0.02	99.17	7	14	72	3.2
NaN	102.2482691	6.31309136	40.7289766	448.240027	10.6031095
NaN	100.8947331	10.0909923	43.048585	296.894703	8.19452036
NaN	99.38717635	3.65719998	3.29853886	229.483571	1.499038
1.62	100.5	15	29	153	8.2

1.95	99.48	3	NaN	31	1
2.13	100.8	16	78	72	23.8
NaN	100.6669032	3.71220574	5.32967201	54.5914431	2.56214323
3.5	100.9	8	NaN	30	5
NaN	102.7510192	26.0347228	84.493755	849.71996	28.8194292
1.51	100.9	17	57	85	21.1
-0.52	100.8	8	8	79	2.2
2.4	100.9	4	13	66	1.5
7.48	99.99	17	36	230	13.4
4.63	99.81	44	61	62	25.1
-1.46	100.7	11	12	#DIV/0!	6
0.3	98.89	6	NaN	26	3.2
2.56	100.5	24	61	72	19.9
1.93	100.2	7	5	24	1.7
2.15	100.1	48	36	647	22.7
NaN	101.9066117	2.97225888	4.74060525	73.5076233	2.19986602
1.16	100.1	13	23	309	5.5
0.31	100.5	4	5	47	1.3
0.91	98.88	9	23	389	5.2
0.83	100.3	3	6	30	1.3
0.05	98.52	10	18	105	4.5
0.44	100.4	13	13	143	4.6
1.15	100.4	11	26	64	6.3
0.6	100.4	15	15	51	4.1
0.98	101	4	5	11	1.1
1.82	100.8	10	13	106	4.2
1.52	100.8	12	17	106	4
0.96	100.9	10	20	136	7.3
1.44	100.9	11	25	91	6.9
1.57	100.7	14	21	69	6.3
1.76	100.7	12	27	110	6.8
0.67	99.91	14	27	32	6.9
0.06	100.4	12	20	33	5.8
NaN	101.5341052	19.6570186	14.9548015	109.566512	7.7569159
1.22	99.97	9	14	80	4.3
4.94	99.87	9	6	36	4.2
2.85	99.47	20	12	89	6.8
1.1	100.6	9	34	72	6.8
2	99.4	9	32	48	3.7
8.73	100.9	18	21	85	14.9
0.99	98.82	11	40	104	9.5

Ce	Pr	Nd	Sm	Eu	Gd	Tb
75.8	8.56	31.4	5.2	1.09	3.8	0.6
73.8	8.35	30.5	5.3	1.15	4	0.6
76.53	8.59	31.45	5.772	1.21	4.462	0.6284
74.7	8.51	30.4	5.4	1.13	3.9	0.6
49.51	5.741	21.63	4.441	0.967	4.218	0.7038
73	8.18	30.2	5.1	1.11	3.9	0.6
110.454709	11.9364628	40.8628367	7.69763409	1.76889817	7.20127447	0.91289684
60.12	6.999	26.59	5.174	1.029	4.726	0.7735
66.3	8.22	28.7	5	0.97	3.7	0.6
66.53	7.554	28.21	5.405	1.146	4.618	0.7208
59	6.85	25.4	4.6	0.93	3.9	0.6
65.2	7.63	28.3	5	0.93	3.8	0.6
73.71	8.507	32.65	6.575	1.258	5.946	0.8616
87.66	9.878	35.85	6.405	1.222	4.82	0.6749
73.4	8.42	30.4	5.2	1	3.8	0.5
70.6	7.96	28.6	5	0.93	3.4	0.5
85.91	9.569	34.84	6.252	1.169	4.812	0.7166
78.17	8.768	31.57	5.654	1.083	4.313	0.6006
72.8	8.11	30.2	5.5	0.98	4	0.5
70.65	7.959	29.09	5.379	1.08	4.314	0.6485
74.3	8.66	31.9	5.8	1.26	4.4	0.7
70.53	7.984	29.37	5.418	1.082	4.45	0.6645
70.8	8.18	29.9	5.5	1.06	4.1	0.6
68.9	7.87	29.1	5	0.95	3.7	0.5
80.23	8.994	32.59	5.927	1.132	4.435	0.6147
61.34	7.049	26.26	5.037	0.9997	4.233	0.6293
64.4	7.54	28.6	5.3	1.04	4.6	0.7
66.3	7.7	29.3	5.2	0.98	4.1	0.6
67.63	7.57	27.23	4.931	0.9107	3.81	0.5461
71.9	8.5	29.8	5.2	0.93	3.9	0.5
70.4	7.85	28.5	5.1	1	3.9	0.5
72.12	8.184	30.02	5.527	1.01	4.478	0.65
22.58	2.551	9.508	1.803	0.6119	1.712	0.2631
24.1	2.87	10.3	2	0.63	1.9	0.3
49.2	5.75	21.6	3.6	0.67	3.2	0.5
22.1	2.64	9.9	1.8	0.48	1.4	0.2
28.2	3.49	12.6	2.3	0.49	2.2	0.3
30.97	3.524	12.96	2.342	0.4487	1.953	0.2908
26	3.37	10.7	2.1	0.43	1.6	0.3
36.9	4.47	16.2	2.8	0.55	2.1	0.3
2.9	0.4	1.2	0.2	0.08	0.3	NaN
6.3	0.8	2.8	0.6	0.19	0.8	0.2
14.7	1.93	6.5	1.2	0.27	1.3	0.2

16.2	1.92	7.4	1.4	0.29	1.4	0.2
3.8	0.36	1.9	0.3	0.11	0.4	NaN
27.9	3.39	13	2.3	0.61	2.4	0.4
12.8570098	1.34206281	5.53670209	1.09738308	0.36686778	1.37822422	0.1841394
3.1680752	0.37035301	1.61053506	0.32784687	0.13652597	0.65106143	0.08963133
22.7	2.93	10.8	2.4	0.69	2.6	0.5
29.9	3.43	14.1	2.5	0.74	2.9	0.5
19.2	2.31	9	1.7	0.41	1.8	0.3
16.1	1.95	7	1.2	0.27	1.2	0.2
17.9	2.3	8	1.5	0.34	1.5	0.3
30.8385874	3.35134694	13.0046416	2.53812945	0.56056112	2.85574198	0.3912876
25.2	3.03	11.4	2	0.48	2	0.3
55.2	6.65	25.6	5.5	1.25	4.7	0.8
19.0560919	2.04575389	7.70126324	1.26968179	0.26369927	1.33975137	0.17280944
25.9	3.05	11.6	2.3	0.61	2.3	0.4
14.2	1.91	6.7	1.3	0.3	1.2	0.2
11.1	1.41	4.5	1	0.2	0.8	0.1
28.5993888	3.01225219	11.5522412	2.15645162	0.49088731	2.27056696	0.31224912
13.5143832	1.46949427	5.67513467	1.03722575	0.25669456	1.17699669	0.17134897
12.9	1.55	5.3	1	0.22	0.9	0.1
22.2716414	2.37781263	9.01615266	1.53651524	0.33694549	1.50391546	0.19447135
1.8	0.33	0.8	0.2	#DIV/0!	0.2	NaN
13.6	1.81	6.1	1.2	0.28	1.2	0.2
21.3553644	2.27833844	8.75223509	1.58076351	0.4019188	2.02159383	0.26774639
22.6	2.82	9.9	2	0.61	1.9	0.3
17.6	2.13	7.9	1.5	0.32	1.4	0.2
24.6394709	2.7268695	10.7056219	2.04132314	0.46023511	2.16833046	0.299147
18.4	2.44	8.3	1.7	0.34	1.4	0.2
17.9	2.04	7.8	1.4	0.4	1.5	0.3
18.4561701	2.03252527	7.99615361	1.5511923	0.43949347	1.87996133	0.25807159
19.6816799	2.09695199	7.90783675	1.51237944	0.32361287	1.75455051	0.23047658
19.2	2.23	8.2	1.7	0.4	1.7	0.3
50	5.71	21.2	3.6	0.7	2.8	0.4
48.6042246	5.22422303	20.0166776	3.80393542	0.64077785	3.57081801	0.44226778
42.6	5.06	18.2	3.3	0.5	2.3	0.3
4.9	0.58	2	0.4	0.1	0.4	NaN
2.8	0.41	1.1	0.2	0.08	0.2	NaN
41.7	4.82	17	2.8	0.55	2.6	0.4
65.7662013	6.60350379	24.8138874	4.5399979	0.91244342	4.7187715	0.58350853
22.7077934	2.42605767	9.1313082	1.66245672	0.36826443	1.89205633	0.22855955
4.11821672	0.4182785	1.52002162	0.25893853	0.09756769	0.38419538	0.05603509
13.5	1.81	6.2	1.2	0.31	1.1	0.2
6.6	0.84	3	0.6	0.24	0.7	0.1
29.4	3.52	14	2.7	0.79	2.9	0.5
45.8	5.37	20	3.4	0.74	2.9	0.4

1.3	0.64	0.8	0.2	0.08	0.2	NaN
3.2	0.4	1.3	0.2	0.05	0.2	NaN
46.9	5.42	20.8	3.8	0.8	3.5	0.6
0.9	0.14	0.5	0.1	#DIV/0!	NaN	NaN
4.6	0.6	1.9	0.4	0.1	0.4	NaN
19.9	2.3	8.4	1.6	0.37	1.4	0.2
20.5485226	2.25311942	8.59028558	1.64313513	0.34882608	1.54962418	0.20925058
25.6716685	2.73748108	10.4843859	1.95877134	0.49853666	2.05991294	0.27247423
13.1	1.5	5.5	1	0.19	0.9	0.1
24.9	2.87	10.3	1.8	0.34	1.3	0.2
12.3	1.63	5.4	1	0.24	0.8	0.1
11.7619547	1.32081914	5.05750203	1.01786669	0.2777287	1.02495913	0.15504419
54.2	6.49	22.5	4.1	0.77	3.1	0.4
68.4	8.36	28.3	5.1	1	3.5	0.5
68.5	8.02	28.7	5	1.11	3.9	0.6
52.7	6.29	24.3	4.6	0.9	3.7	0.5
53.3	6.22	24.5	4.7	1.09	4.3	0.6
23.8	2.93	10.6	1.9	0.43	1.9	0.3
64.2	7.42	28.1	5.2	1.09	4.1	0.6
20.2	2.38	8.6	1.5	0.26	1.1	0.2
5.6	0.7	3.1	0.7	0.16	0.9	0.1
45.9292939	4.90621543	20.3004182	4.68667821	1.42305735	4.99685695	0.77435005
32.9781454	3.5643057	13.9116674	2.66612373	0.69505278	2.90440619	0.4042468
55.3108949	5.8582502	21.7949607	3.82861644	0.86458884	4.02756002	0.54463377
27.9	3.24	12.5	2.2	0.54	2.2	0.4
23.6	3.14	10.6	2	0.4	2.1	0.3
40.6178181	4.37285501	17.5336158	3.42277481	0.84395107	3.55743842	0.48274314
23.9	2.96	11.2	2.1	0.44	2.4	0.4
29.8169536	3.19866214	12.2381485	2.24300715	0.71594391	2.38112764	0.31391392
26.4	3.05	11.9	2	0.44	1.9	0.3
18.6	2.15	8.2	1.5	0.35	1.3	0.2
34.7473539	3.70543626	14.0835309	2.58234378	0.77958513	3.00253005	0.40624814
40.9	4.86	18.5	3.4	0.73	3	0.4
3.8	0.46	1.9	0.4	0.16	0.5	NaN
1.5	0.16	0.8	0.1	0.06	0.2	NaN
36.5	4.08	14.8	2.4	0.51	2	0.3
5.7	0.65	2.5	0.6	0.16	0.5	0.1
3.1	0.33	1.3	0.3	0.1	0.4	NaN
77.2	8.59	30.4	4.8	0.77	2.9	0.4
25.2	2.96	10.7	1.9	0.41	1.7	0.3
5.8	0.72	3.1	0.7	0.15	0.7	0.1
19.5607164	2.057171	7.80136153	1.3205905	0.37978405	1.31620266	0.16416628
16.1180307	1.82547913	7.44067798	1.56093346	0.48345509	1.70530727	0.24639268
2.26543417	0.26762628	1.13785469	0.24174073	0.16777533	0.32528041	0.05207049
15.2	1.85	7.6	1.5	0.39	1.7	0.3

1.6	0.2	0.8	0.1	0.07	0.2	NaN
42.1	4.77	17.3	2.9	0.71	2.4	0.4
4.74660634	0.58603377	2.34307517	0.4834205	0.19585045	0.55603941	0.09390543
8.4	0.92	3.7	0.6	0.15	0.6	0.1
54.6857936	5.97668037	23.1034673	4.8513138	1.32149494	5.35689389	0.74916667
37	4.14	14.7	2.3	0.42	1.5	0.3
3	0.36	1.3	0.3	0.1	0.4	NaN
2.9	0.37	1.7	0.4	0.13	0.4	NaN
23.7	2.91	11.4	2.3	0.58	2.2	0.3
42.4	5.06	20.1	3.7	1.08	4.7	0.8
9.3	0.88	3.7	0.5	0.11	0.7	0.1
4.8	0.55	2.3	0.4	0.18	0.6	0.1
34.2	3.84	15.4	2.6	0.73	2.8	0.5
3	0.38	1.5	0.4	0.15	0.5	NaN
40.3	5.11	22.7	5.3	1.56	6.3	1
3.65064673	0.4410265	1.86464727	0.35239868	0.12580121	0.41537942	0.0593819
9.9	1.21	5.4	1.1	0.34	1.3	0.2
2	0.23	0.9	0.2	0.07	0.3	NaN
9.2	1.01	4.2	0.7	0.18	0.8	0.1
2.1	0.26	1.2	0.2	0.08	0.3	NaN
7.6	0.9	3.3	0.7	0.16	0.9	0.1
8	1.03	4.4	1	0.26	1.1	0.2
11	1.34	5.4	1.1	0.23	1.1	0.2
7.3	0.86	4.2	0.7	0.23	1	0.2
1.8	0.22	1	0.2	0.07	0.2	NaN
6.9	0.83	3.3	0.6	0.16	0.7	0.1
7	0.9	3.6	0.6	0.19	0.9	0.1
12.6	1.62	5.7	1.2	0.23	1.2	0.2
11.7	1.36	5.2	0.8	0.18	0.9	0.2
10.3	1.27	5	0.9	0.27	1.1	0.2
11.9	1.41	5.6	1.1	0.29	1.2	0.2
12	1.44	5.8	1.2	0.29	1.2	0.2
10	1.16	4.4	0.8	0.18	1	0.2
12.7149449	1.57606706	6.69521274	1.37768392	0.55151291	2.0650381	0.29063262
7.2	0.92	3.5	0.7	0.17	0.9	0.1
5.6	0.61	2.2	0.4	0.14	0.6	0.1
11.1	1.42	6.1	1.3	0.48	1.6	0.3
12	1.39	5.4	0.9	0.27	1.1	0.2
7.1	0.91	3.8	0.8	0.2	0.8	0.1
25.2	2.9	11	2.1	0.6	2	0.3
17.9	2.1	8.2	1.4	0.27	1.4	0.2

Dy	Ho	Er	Tm	Yb	Lu	Hf
3.3	0.7	2	0.3	2	0.33	3.2
3.4	0.7	2.1	0.29	1.9	0.31	3.2
3.693	0.7569	2.085	0.3054	2.109	0.3253	3.887
3.3	0.7	2	0.3	2	0.3	3
4.494	0.9511	2.495	0.3526	2.327	0.3701	4.75
3.2	0.6	2	0.3	2	0.3	2.9
4.46290116	0.90050718	2.85713518	0.4480639	3.09310326	0.51498598	6.20682689
4.996	1.079	2.847	0.4056	2.647	0.4107	5.543
3.4	0.7	2.1	0.32	2.1	0.34	3.4
4.509	0.9493	2.54	0.3577	2.438	0.3766	3.735
3.7	0.8	2.2	0.33	2.1	0.32	2.9
3.3	0.6	2	0.31	2	0.31	3
5.227	1.1	2.932	0.4218	2.94	0.4662	3.796
3.952	0.8132	2.235	0.3275	2.355	0.3693	4.885
3.2	0.6	2	0.3	2	0.29	3.9
3	0.6	1.9	0.32	2.1	0.33	4.2
4.345	0.9179	2.456	0.3626	2.576	0.4087	5.454
3.54	0.73	2.04	0.3025	2.193	0.3444	4.676
3.4	0.7	2.1	0.33	2.2	0.32	3.8
4.007	0.8351	2.274	0.3331	2.303	0.3585	4.926
3.9	0.8	2.3	0.34	2.1	0.33	4
4.119	0.8751	2.378	0.3497	2.468	0.3861	4.662
3.7	0.7	2.2	0.34	2.2	0.32	4
3.1	0.6	1.9	0.28	1.9	0.29	3.5
3.62	0.7408	2.04	0.3083	2.216	0.35	4.917
3.904	0.8411	2.375	0.3562	2.594	0.4141	3.638
4.2	0.9	2.7	0.43	2.9	0.44	2.8
3.8	0.8	2.4	0.37	2.4	0.36	3.2
3.323	0.7039	1.971	0.3023	2.165	0.3497	4.441
3.1	0.7	2	0.31	2.1	0.33	3.3
3.1	0.7	2	0.3	2	0.3	3.6
4.004	0.855	2.366	0.3499	2.44	0.3781	3.735
1.716	0.4139	1.268	0.1966	1.403	0.2397	1.222
1.8	0.4	1.4	0.22	1.5	0.24	1.2
2.9	0.6	2	0.32	2.1	0.33	2.5
1.4	0.3	1	0.16	1	0.15	1.8
2.1	0.5	1.5	0.23	1.6	0.24	1.8
1.838	0.4258	1.256	0.196	1.425	0.2349	2.301
1.9	0.5	1.6	0.25	1.7	0.25	1.6
2	0.4	1.3	0.2	1.4	0.22	1.8
0.3	NaN	0.2	NaN	0.3	NaN	NaN
1.1	0.2	0.9	0.14	0.8	0.14	NaN
1.4	0.3	1.1	0.16	1.1	0.19	0.8

1.7	0.4	1.4	0.21	1.5	0.25	0.8
0.5	0.1	0.4	0.07	0.4	0.07	NaN
2.3	0.6	1.9	0.3	2	0.31	1.3
1.0423862	0.22326903	0.68643312	0.10309646	0.75604953	0.13597233	0.53982621
0.60949914	0.15801361	0.5095661	0.08674322	0.61786688	0.1074686	NaN
3	0.7	2.4	0.38	2.7	0.41	1
3.4	0.8	2.5	0.39	2.7	0.42	0.8
2.1	0.5	1.6	0.25	1.7	0.26	1
1.2	0.3	1	0.15	0.9	0.18	1.1
1.7	0.4	1.3	0.21	1.4	0.22	0.9
2.25673648	0.49318701	1.54495474	0.2383103	1.70356215	0.29598405	1.85484498
2.2	0.6	1.7	0.26	1.7	0.27	1.3
4.6	0.9	2.9	0.42	2.5	0.39	3
1.08246246	0.25471448	0.86796073	0.14317947	1.08470933	0.20539362	1.96050222
2.4	0.6	1.9	0.29	1.9	0.29	1.1
1.5	0.4	1.1	0.17	1.2	0.21	0.8
1	0.2	0.8	0.12	1	0.18	0.8
1.64228545	0.36455601	1.21066502	0.20053746	1.55663882	0.28631624	2.59065908
1.12555322	0.25369299	0.95374063	0.14128466	1.04901527	0.18750965	0.98311563
1	0.2	0.8	0.12	0.9	0.18	0.7
1.11167857	0.25066986	0.86155047	0.14257388	1.09976223	0.21452588	1.73170349
0.2	NaN	0.2	NaN	0.2	NaN	NaN
1.4	0.4	1.2	0.17	1.1	0.17	0.7
1.48829972	0.32826856	1.10130311	0.17420127	1.21632055	0.22087043	1.14919244
2	0.5	1.6	0.23	1.5	0.24	0.9
1.7	0.4	1.3	0.19	1.3	0.22	0.9
1.58666767	0.34913443	1.14733214	0.18510921	1.32958504	0.24037174	1.5845103
1.6	0.4	1.2	0.18	1.3	0.22	1
1.8	0.4	1.3	0.19	1.3	0.22	0.9
1.47898435	0.33143959	1.06555321	0.15505142	1.13578031	0.20149	1.09552127
1.21582834	0.27557419	0.93227139	0.15152935	1.11807411	0.20930066	1.32367424
1.8	0.4	1.5	0.22	1.5	0.23	1
2.8	0.6	2	0.31	2.1	0.33	3.3
2.18649851	0.45648092	1.45128652	0.23473956	1.74897792	0.29393703	5.34465941
1.9	0.4	1.2	0.18	1.2	0.2	2.3
0.5	0.1	0.5	0.07	0.5	0.08	NaN
0.3	NaN	0.2	NaN	0.2	NaN	NaN
2.6	0.6	2	0.31	2.2	0.37	1.9
2.94718348	0.74796183	2.19306907	0.35126493	2.53394026	0.46474093	3.24089254
1.20014325	0.24590072	0.80764523	0.12335117	0.8278274	0.14626591	1.16471176
0.34173629	0.07813102	0.25133689	0.034394	0.23452878	0.03833291	NaN
1.2	0.3	0.9	0.13	0.9	0.14	0.6
0.8	0.2	0.6	0.11	0.8	0.12	NaN
2.8	0.6	1.8	0.26	1.7	0.26	1.1
2.5	0.5	1.7	0.27	1.9	0.32	2.6

0.3	NaN	0.2	NaN	0.2	NaN	NaN
0.2	NaN	0.1	NaN	0.1	NaN	NaN
3.8	0.8	2.7	0.42	2.8	0.43	2.7
0.2	NaN	0.1	NaN	0.1	NaN	NaN
0.4	0.1	0.3	NaN	0.3	0.05	0.2
1.5	0.4	1.2	0.18	1.2	0.21	1.2
1.10678848	0.234579	0.76310279	0.11936619	0.8660581	0.15296086	1.38134897
1.47818608	0.31733547	1.05417524	0.15508449	1.11933095	0.19182708	2.45860331
0.8	0.2	0.6	0.09	0.6	0.1	0.9
1.2	0.3	0.8	0.12	0.8	0.14	1.4
0.8	0.2	0.5	0.07	0.5	0.08	0.9
0.92660591	0.20058457	0.63969093	0.0981557	0.69542144	0.12128542	1.32242965
2.7	0.5	1.7	0.27	1.7	0.26	2.4
3.1	0.6	1.9	0.29	1.9	0.28	2.7
3.6	0.7	2.2	0.32	2.1	0.34	3.1
3.5	0.7	2.3	0.34	2.2	0.36	3.1
3.7	0.8	2.3	0.36	2.4	0.36	3.1
2	0.4	1.3	0.21	1.4	0.23	1
4	0.9	2.7	0.4	2.7	0.45	3.4
1.2	0.3	0.9	0.13	0.9	0.15	0.6
1	0.2	0.7	0.1	0.7	0.11	NaN
4.11995364	0.8374046	2.42721561	0.35364509	2.36086011	0.3921335	3.41562502
2.31953357	0.50755955	1.77421894	0.27342189	1.88802604	0.3295038	2.46199851
2.62566393	0.57998791	1.8999018	0.315562	2.26462087	0.40460132	2.88375111
2.2	0.5	1.6	0.24	1.6	0.26	1.6
2.1	0.5	1.8	0.28	2	0.31	1.5
2.42203734	0.49165422	1.50191907	0.24105772	1.64601636	0.27763287	1.63132869
2.4	0.5	1.7	0.25	1.6	0.24	0.8
1.66482408	0.36994297	1.2046416	0.19070804	1.28473815	0.22978587	1.7382255
2	0.4	1.4	0.2	1.4	0.22	1.6
1.6	0.3	1.1	0.17	1.2	0.19	1.3
2.15306125	0.449056	1.42295935	0.23819166	1.57768431	0.26401569	2.19843724
2.7	0.6	1.7	0.26	1.7	0.26	1.9
0.6	0.1	0.4	0.06	0.4	0.06	0.2
0.3	NaN	0.2	NaN	0.3	0.04	NaN
1.8	0.4	1.2	0.19	1.5	0.22	2.1
0.8	0.2	0.5	0.08	0.6	0.1	0.2
0.5	0.1	0.4	0.06	0.4	0.06	NaN
2.1	0.4	1.4	0.21	1.6	0.26	4
1.6	0.3	1.1	0.16	1.1	0.18	1.7
0.8	0.2	0.5	0.08	0.5	0.07	0.2
0.84559362	0.19034799	0.63784822	0.10527881	0.80255773	0.14862945	1.20877106
1.368273	0.29960154	0.89333151	0.13209153	0.93043929	0.16417152	1.32363514
0.34954843	0.09265217	0.2780852	0.04347028	0.31371174	0.05818023	NaN
1.7	0.4	1.1	0.16	1.1	0.15	0.6

0.3	NaN	0.2	NaN	0.2	NaN	NaN
2.2	0.5	1.5	0.23	1.6	0.26	1.9
0.56628463	0.12630385	0.41095074	0.07227004	0.48347047	0.08671971	0.13753521
0.8	0.2	0.7	0.12	0.8	0.14	NaN
3.69756333	0.72979116	2.17059524	0.30357025	2.08607784	0.36337686	2.63579069
2	0.5	1.7	0.26	1.8	0.31	1.3
0.5	0.2	0.5	0.08	0.5	0.08	NaN
0.4	0.1	0.3	0.06	0.4	0.06	0.3
2.1	0.4	1.3	0.21	1.3	0.19	0.9
4.9	1.2	3.7	0.55	3.6	0.57	1.5
1.2	0.3	1.1	0.19	1.3	0.21	NaN
0.7	0.2	0.6	0.1	0.6	0.1	NaN
2.9	0.6	2.1	0.32	2	0.32	1.4
0.7	0.2	0.6	0.1	0.7	0.11	0.3
6.5	1.4	4.2	0.61	3.8	0.6	0.8
0.35512357	0.08089717	0.26252939	0.03946424	0.28021344	0.04947678	0.09941123
1.4	0.3	1	0.16	1.1	0.16	0.4
0.3	NaN	0.3	0.05	0.4	0.06	NaN
1.1	0.2	0.8	0.13	0.9	0.13	0.4
0.4	NaN	0.3	0.05	0.4	0.06	NaN
0.9	0.2	0.7	0.11	0.8	0.12	0.3
1.3	0.3	1.2	0.18	1.2	0.21	0.3
1.2	0.3	1	0.16	1.1	0.19	0.5
1.4	0.4	1.2	0.2	1.3	0.21	0.3
0.3	NaN	0.3	0.06	0.4	0.06	NaN
1	0.2	0.8	0.14	0.9	0.14	NaN
1	0.3	0.9	0.15	0.9	0.15	0.3
1.3	0.3	0.9	0.14	0.9	0.15	0.4
1.1	0.3	0.9	0.14	0.9	0.16	0.6
1.3	0.3	1.1	0.18	1.2	0.19	0.4
1.4	0.3	1.1	0.17	1.1	0.18	0.6
1.5	0.4	1.3	0.2	1.3	0.19	0.5
1.3	0.3	1.2	0.19	1.2	0.2	0.3
1.75954047	0.41096608	1.25163744	0.17501555	1.26982038	0.18565092	0.33856014
0.9	0.2	0.8	0.12	0.8	0.14	0.2
0.7	0.2	0.6	0.09	0.6	0.11	NaN
1.9	0.5	1.5	0.24	1.6	0.26	0.2
1.2	0.3	1	0.15	1.1	0.17	0.7
1	0.3	0.8	0.13	1	0.16	0.7
2.2	0.5	1.6	0.24	1.6	0.27	0.4
1.5	0.4	1.2	0.2	1.5	0.24	0.8

Th	U	Sc	V	Cr	Co	Cu
13	4	18	132	160	20	36
12.8	3.9	18	125	150	17	33
14.25	4.517	18.87	124.8	202.5	20.03	39.72
13	3.7	18	131	160	19	31
10.84	4.427	11.63	69.6	271.2	20.18	59.04
12.5	3.8	18	130	150	16	30
20.8965263	6.33586313	24.938072	172.795614	260.873611	22.4152747	35.1896504
11.06	4.55	11.44	68.43	277.4	19.96	56.17
12.1	4	15	109	140	16	31
11.66	3.726	14.05	90.83	170.5	18.88	47.9
10.2	3.2	14	92	120	15	32
11.3	3.4	14	96	120	12	20
13.36	4.401	12.89	89.2	163	12.66	31.46
14.88	4.976	16.98	109.5	175.1	10.27	32.69
13.4	4.9	15	102	120	9	29
13.8	4.8	17	113	140	14	29
16.27	5.559	15.95	106.1	179.6	11.68	34.42
14.14	4.65	17.28	106.3	172	11.81	29.88
12.6	4.3	16	106	130	21	64
13.7	4.872	14.7	89.31	158.5	11.45	28.43
14.2	4.9	15	102	140	12	30
13.35	5.072	14.98	95.29	223.4	32.79	68.41
12.5	4.3	15	105	130	16	33
12.4	4.5	15	101	120	11	21
13.89	5.222	15.8	104.5	218.3	12.98	26.75
10.42	3.867	12.97	79.32	151.5	12.33	25.23
10	3.6	13	87	110	12	13
11.9	4.3	14	99	120	17	13
12.83	4.72	15.59	93.24	196	22.16	36.55
12.4	4.2	14	103	130	13	22
12.5	4.7	15	101	120	12	26
11.96	4.55	14.53	91.48	157.7	13.35	6.616
3.932	1.373	4.98	30.72	65.77	4.313	11.36
4.1	1.4	5	39	50	4	3
8.8	3	9	65	80	10	4
4	1.4	4	30	50	7	12
5.1	1.9	4	29	60	7	5
6.402	1.801	7.64	45.55	57.83	14.7	16.13
4.6	1.9	6	59	60	21	14
6.5	1.8	7	45	80	11	7
0.2	0.4	NaN	NaN	160	NaN	6
0.4	0.6	NaN	NaN	30	NaN	10
2.8	0.8	4	25	40	5	8

3	0.8	4	21	60	6	4
0.3	0.2	NaN	NaN	60	NaN	4
4.3	1.1	4	22	40	8	5
1.81949823	0.47654517	2.48211935	19.1613573	452.687477	4.54803937	10.5313331
0.14821154	0.1589261	0.34976983	2.28729345	1078.02725	5.07448557	6.77489762
2.8	0.9	4	21	50	5	6
3.3	1.3	4	26	40	6	8
2.9	1	3	22	40	5	11
2.8	0.9	3	17	30	4	8
2.9	1.2	3	21	40	4	10
5.38406253	2.04390581	5.83531986	44.9857284	253.49885	10.7111005	15.6376671
4.1	1.6	4	37	50	6	6
8.9	4.8	9	63	90	10	14
4.7368104	2.03681055	4.29243112	38.6035853	382.431349	9.82311249	6.34831401
3.6	1.6	4	31	40	8	15
2.2	0.7	3	17	40	3	5
2	0.7	2	13	30	3	6
6.81807758	2.04307811	7.48019135	52.1593919	267.154951	12.8288823	9.30975418
2.81983993	0.95123573	3.74004558	25.8486388	534.593729	6.7593473	14.994016
2.1	0.5	3	17	40	3	4
4.2315342	1.07518311	3.60287781	27.3303017	404.466197	8.6049365	6.68469903
0.2	NaN	3	13	50	4	4
1.8	0.9	3	18	30	3	8
3.52863997	1.4644846	3.79804372	26.2121836	456.716815	7.46279071	3.42931401
2.5	1.5	3	17	40	3	5
3.1	1.1	3	21	40	5	7
4.30330707	1.44116215	4.62973214	32.5998461	500.02969	9.35975623	13.3770769
3	1	3	22	40	4	7
2.6	1	3	19	40	4	7
3.22520959	1.02805571	4.01593733	27.7250227	274.389055	6.60879327	18.0082741
4.00908774	1.36166715	4.54041928	34.0815583	221.622569	7.33433545	14.0683522
2.7	0.9	3	23	40	4	5
9.7	2.9	9	65	90	13	21
18.9351685	4.508494	11.5145019	88.8877775	108.850672	18.6067948	23.440277
7.6	1.9	7	50	70	8	54
0.2	0.3	NaN	6	160	NaN	8
0.3	0.2	NaN	7	80	1	11
6.7	2.3	6	42	50	12	4
11.8999207	3.58009819	11.3892521	58.207197	140.355121	20.5858454	4.01725473
3.55516404	1.16336662	3.58206015	21.9996189	934.13724	9.21272784	18.2619855
0.19444997	0.31801794	0.19201326	3.68481774	1340.305	9.79181234	36.6292491
1.5	0.6	2	19	50	3	7
0.4	0.2	1	12	NaN	3	6
3.3	1.3	4	38	40	4	6
7.8	2.7	6	33	80	7	6

0.1	0.1	NaN	NaN	NaN	NaN	17
0.3	0.2	NaN	6	200	NaN	12
7.4	2.7	7	50	70	9	16
NaN	0.1	NaN	NaN	NaN	NaN	13
0.6	0.3	NaN	7	50	1	9
3.2	1.1	3	21	50	4	5
3.87460133	1.76792943	3.78358301	33.505464	220.805696	11.1646742	24.6908902
6.01670698	1.53997149	5.55578943	35.5036425	183.737007	9.06753728	16.5123629
2.4	1.1	3	18	30	5	15
4.4	0.8	4	25	50	4	14
2.5	0.8	3	17	30	4	6
3.96790946	1.3239632	3.10470645	22.6614013	205.933131	4.94199486	7.91635199
9.9	2.8	14	105	90	17	38
12.4	3.8	15	108	120	20	29
12.6	4.1	13	92	80	18	39
8.6	3.3	24	206	130	29	102
9.8	3.1	10	51	110	12	8
2.7	0.9	3	23	40	4	7
11.2	3.8	11	57	120	14	36
2.1	1.4	3	58	30	4	8
0.4	0.3	1	11	180	1	11
8.3306879	3.37118884	8.36143929	45.5757236	498.150058	19.8023989	27.3865875
6.06710302	2.58444906	6.11083961	46.1391445	285.701207	10.6489874	20.3929236
8.59138406	2.49641017	8.06959386	55.9249198	412.540908	12.2799909	6.39347793
4.3	1.8	4	29	60	6	14
3.8	1.5	4	38	40	7	9
4.64585404	1.82380068	4.48533012	43.1253894	494.922667	9.27880102	18.3516448
2.4	1.1	3	26	30	4	15
5.01251155	2.00408093	3.85201308	31.4985658	396.561519	9.60945394	16.6173074
4.2	1.4	3	23	40	4	11
3.1	1.3	3	20	40	5	9
6.34966419	2.10336684	4.39846475	33.3229238	265.338851	8.10900875	18.7156968
5.8	2.5	6	64	70	4	6
0.3	0.6	NaN	7	130	NaN	5
NaN	0.2	NaN	NaN	220	NaN	9
6.7	1.7	6	39	80	8	4
0.6	1.4	1	17	NaN	2	30
NaN	0.6	NaN	8	NaN	NaN	13
13	2.9	9	63	130	15	8
5.2	1.7	4	23	50	8	8
0.7	0.5	2	17	NaN	NaN	6
3.70350194	1.018618	5.17612451	44.4429216	207.372444	2.90131092	1.86210691
3.62180375	1.69176762	4.03381451	31.716795	199.13839	7.15500116	6.37956504
0.12599412	0.33300998	0.46507811	4.38622835	1136.90139	7.53672773	9.63837376
1.9	0.8	3	24	20	2	6

NaN	0.3	NaN	6	NaN	NaN	5
10	2.6	5	30	50	7	10
0.46975306	0.56526123	1.86323413	8.21191542	947.093552	6.94394409	4.98813311
0.2	0.4	2	7	NaN	NaN	3
12.3849375	3.18585392	9.22529191	68.2520388	120.514755	1.60360684	1.00502012
3.6	1.8	6	49	40	3	7
0.2	0.3	NaN	NaN	NaN	NaN	6
0.2	0.3	2	15	30	1	4
4.3	0.5	3	10	50	7	30
5.8	1.2	6	34	60	9	30
0.7	0.3	1	20	NaN	NaN	7
0.1	0.1	NaN	NaN	NaN	NaN	3
6.3	2	5	42	40	5	11
0.1	0.3	NaN	8	NaN	NaN	3
3.7	1.9	5	38	30	6	7
0.34815071	0.1713346	0.47431306	4.3148769	1138.85641	6.07223835	11.039104
1.4	0.4	2	17	NaN	2	8
0.2	NaN	NaN	NaN	NaN	NaN	6
1.4	0.4	2	15	NaN	2	6
0.2	0.1	NaN	6	NaN	NaN	20
1.1	0.4	2	11	NaN	2	8
1	0.4	2	16	NaN	4	8
1.4	0.8	3	30	20	4	9
0.6	0.6	3	10	NaN	2	9
0.3	NaN	NaN	NaN	NaN	NaN	8
0.7	0.3	1	NaN	NaN	NaN	6
0.9	0.5	1	NaN	NaN	NaN	7
1.7	1	1	7	20	1	6
1.6	0.4	2	8	NaN	1	7
1.3	0.4	2	12	NaN	2	6
1.5	0.6	2	12	20	2	6
1.5	0.5	2	14	NaN	2	6
1	0.3	1	9	160	2	7
1.22853864	0.64805323	1.43555377	10.7358945	761.054828	5.45354862	8.32737375
0.9	0.4	1	9	NaN	2	6
0.2	0.7	NaN	7	730	1	13
0.9	0.5	1	8	NaN	2	5
3	0.8	1	12	180	4	8
2.2	0.7	2	16	30	3	4
1.2	0.5	2	19	170	2	37
2.5	0.6	2	16	30	4	4

Pb	Zn
6	60
6	60
10.4039	77.59
6	59
9.4764	62.25
5	76
14.0421249	117.59307
28.0505	81.41
5	80
21.9033	85.19
19	65
6	69
9.6965	123.9
8.2011	74.18
14	60
48	78
15.4114	92.22
9.0221	82.94
31	69
10.2211	77.74
8	69
62.8885	101.4
22	73
8	70
9.306	91.09
7.4593	106.2
6	87
13	85
48.2521	73.92
9	64
8	79
4.3624	108.5
2.1046	30.46
NaN	25
NaN	46
8	26
NaN	35
5.1432	58.73
12	38
6	47
NaN	3
12	8
11	22

8	20
7	4
12	15
4.74029809	13.2920061
1.38638626	NaN
10	21
10	21
7	25
9	22
8	25
3.57336431	38.3448236
8	29
5	53
2.38958928	35.3428995
10	35
8	20
7	20
2.96690101	42.6538407
1.97774251	26.4270568
7	20
2.35281402	28.5459807
NaN	66
8	21
2.13558166	26.8026845
8	21
7	23
2.25054364	30.45103
7	23
6	21
2.16085693	23.1601981
2.148373	27.9793416
7	20
7	41
4.35233709	92.2265755
NaN	48
NaN	3
NaN	5
6	32
3.96339837	41.1133958
4.99534749	17.4854702
2.13806365	6.20318882
8	12
13	8
12	18
NaN	35

NaN	2
NaN	3
7	37
18	15
6	8
9	19
2.02086178	35.0023388
2.91589258	47.1117989
11	23
10	34
11	21
2.26026996	36.0716398
6	60
11	51
63	66
6	80
5	62
10	23
12	71
11	21
5	8
12.771582	48.5836741
7.52905816	40.8355357
6.68493271	45.5794444
10	28
8	40
5.56378505	25.6160599
11	16
7.90471761	23.8377601
8	19
9	19
9.61542727	30.1201196
9	37
7	6
7	5
8	36
9	14
7	7
10	53
17	38
15	19
2.98763116	42.5441904
9.79006601	33.1015042
2.33708115	7.15853571
10	22

10	15
33	37
1.77038685	12.6956431
26	40
2.78639129	54.0806354
11	36
11	7
5	13
68	14
103	30
13	14
NaN	4
27	35
NaN	10
18	27
3.61557023	NaN
15	13
5	3
14	13
NaN	2
15	11
13	12
12	20
18	15
7	4
15	9
13	11
10	13
13	12
10	9
11	14
11	12
12	10
4.37875919	9.63611611
10	11
NaN	4
8	7
11	18
8	15
10	20
7	18

Table 2.4. Fe-speciation data table. See text for description of steps 1 through 7.

Fe Speciation Data											
Sample	Depth in Core (m)	step1	step2	step3	step4	step5	step6	step7	sum	certificate	recovery
STSD-3	-	80.18	1497.44	6385.73	3050.82	2483.86	11428.46	14522.32	39448.80	44000	90%
109.16	109.16	152.50	3304.45	5871.57	876.25	1983.10	35633.86	31548.51	79370.25		
132.25-132.38	132.315	109.31	8812.55	4442.96	516.07	101540.99	114638.45	50284.91	280345.24		
135.8	135.8	238.65	18001.45	8881.41	1077.01	43209.05	103407.71	28880.31	203695.58		
136.5	136.5	212.96	7309.02	7499.20	871.04	50368.96	109399.64	23721.73	199382.55		
139.2	139.2	191.07	11142.86	6020.87	583.21	44282.99	116880.98	29098.06	208200.04		
139.8	139.8	133.19	4966.59	5329.18	784.22	62216.14	129910.78	28025.23	231365.34		
144.1-144.16	144.13	261.71	7656.92	8189.63	1059.06	110704.50	102197.31	23861.61	253930.73		
145.4	145.4	163.00	8097.61	8109.35	948.77	72417.35	133481.70	32967.10	256184.87		
145.5	145.5	85.16	11324.59	6199.61	597.02	84874.87	134906.17	25587.59	263575.02		
146.36	146.36	197.36	7989.91	11543.16	829.01	26829.47	111075.13	40786.63	199250.66		
147.7-147.85	147.775	163.05	12305.49	8888.92	695.45	10427.89	56814.51	9988.45	99283.76		
150.58-150.72	150.65	196.86	19761.03	18888.47	1302.38	137455.69	126423.39	9813.86	313841.67		
151.4	151.4	176.69	21020.07	9832.25	805.62	126503.37	138959.20	27886.59	325183.80		
155.45-155.66	155.555	71.19	2121.56	4114.06	441.11	47622.80	157455.05	27856.43	239682.19		
156.5	156.5	97.83	3921.11	5975.69	511.44	116698.16	125647.66	7770.55	260622.43		
156.83-156.62	156.725	53.69	4124.98	4083.43	422.07	111116.61	145966.23	24148.33	289915.33		
159.08-158.94	159.01	150.48	3384.81	4829.70	320.21	75793.73	155508.92	114245.31	354233.16		
159.5-159.54/63	159.52	48.14	8078.84	2926.73	218.70	20424.69	48710.79	4594.36	85002.25		
161.3-161.48	161.39	22.68	6921.55	1042.03	147.84	13564.57	96539.08	3549.36	121787.10		
172.18-172.1	172.14	49.56	8047.16	3157.78	210.37	46474.17	165044.47	14518.34	237501.85		

Chapter 3: Manganese enrichments in the Boolgeeda Iron Formation and implications for oxygen levels during the Great Oxidation Event

1. Introduction

The history of Earth's oxygenation is intimately tied to the evolution of oxygenic photosynthesis, and in this regard, a number of studies have provided geochemical evidence indicative of cyanobacteria – likely the first O_2 producers - in the marine realm as early as 2.7 Ga (e.g., Summons et al., 1999; Eigenbrode and Freeman, 2006; Godfrey and Falkowski, 2009; Thomazo et al., 2011), but potentially even earlier (Crowe et al., 2013; Planavsky et al., 2014; Satkowski et al., 2015). However, despite the apparent early rise of cyanobacteria – a suggestion that has received significant resistance based on genomic data (e.g., Shih et al., 2017; Soo et al., 2017) – the first evidence for an accumulation of oxygen in the atmosphere is not until ca. 2.45 Ga, the so-called Great Oxidation Event (Philippot et al., 2018).

Geological arguments for a rise of oxygen were initially made by MacGregor (1927), and subsequent studies linked the first occurrences of "red beds" (Chandler, 1980; Melezhik et al., 2005), copper deposits (Kirkham and Roscoe, 1993), iron rich paleosols (Rye and Holland, 1998), and sulfate evaporates (Schroder et al., 2008; Pope and Grotzinger, 2003; Grotzinger and Kasting, 1993). Other lines of geological evidence for the GOE include the preservation of well-rounded detrital pyrite, uraninite, and siderite grains in clastic deposits of the Archean Eon (Grandstaff, 1980) but not thereafter because these grains are unstable under oxic conditions (Rasmussen and Buick, 1999; Roscoe, 1996; England et al., 2002; Hofmann et al., 2009). The timing for the GOE has subsequently been pushed back in time to between ~2.45 and ~2.32 Ga with the observations that mass-independent fractionation of sulfur isotopes (MIF-S) disappeared at that time (Farquhar

et al., 2000). Recently, however, Philippot et al. (2018) noted recycling of the MIF-S signal within the Hamersley and Turee Creek Basins of Western Australia that may have lasted up to 140 Ma after the onset of the GOE, supporting earlier models of Reinhard et al. (2013). The prospect of MIF-S recycling for 100-150 Ma after the GOE begs an investigation into other proxies for atmospheric and shallow marine oxygenation, in hopes of providing a more detailed record of O_2 dynamics spanning this crucial time in Earth's history.

One important piece of evidence for marine oxygenation is the presence of extensive manganese deposits between 2.4 to 2.2 Ga (Wood, 1973; Holland, 2005; Melezhik et al., 2005; Holland, 2006). Manganese enriched intervals are rare throughout the Archean, and their sparsity has traditionally been attributed to a paucity of oxidants for dissolved Mn^{2+} in seawater to form the precursor Mn(IV) oxide phases. The high redox potential required to oxidize Mn(II) necessitates the presence of molecular oxygen, superoxide, or hydrogen peroxide (Kopp et al., 2005; Clement et al., 2009; Hansel and Learman, 2016) and the lack of evidence for the latter two on ancient Earth (Pecoits et al., 2015) make molecular O_2 the most likely candidate for Mn(II) oxidation. Recently, it has also been proposed that some of these Mn enrichments may be attributable to an ancient and now extinct prototype of photosystem II, dependent on Mn(II) photooxidation for energy (Johnson et al., 2013).

Sediments deposited during the GOE provide an opportunity to investigate, characterize, and compare time-equivalent Mn phases from around the world. In doing so, it may be possible to define a global transition in Mn speciation, and perhaps correlate thick Mn deposits between major depositional basins at that time, such as those in South Africa and Australia. The Hotazel Formation represents the largest Mn deposit in the world, and it is hosted in the Postmasburg Group of the Griqualand West Basin in South Africa, constrained in age by a 2.426 Ga U-Pb baddeleyite

date from the underlying Ongeluk volcanics (Gumsley et al., 2017) and a Pb-Pb age of 2.394 Ga from the overlying Mooidraai dolomite (Bau et al., 1999). Previous authors have suggested that the Hotazel was formed by the combined effects of distal hydrothermal activity and transgression-regression cycles; iron and manganese were effused from hydrothermal vents, and the rise and fall of sea level shifted the marine chemoclines up and down, which promoted temporal precipitation of Fe(III) and Mn(IV) oxyhydroxides as the primary metal phases (Beukes, 1983; Nel et al., 1986).

The Hotazel is composed of three Mn-rich units, all of which contain up to 40 wt.% Mn (Tsikos and Moore, 1997), with a mineralogy dominated by braunite $[Mn^{2+}(Mn^{3+})_6O_8SiO_4]$, kutnahorite $[(CaMn^{2+}(CO_3)_2]$, and hausmannite $[Mn^{2+}(Mn^{3+})_2O_4]$ – the present mineralogy represents the post-burial alteration to the primary oxyhydroxide phases (Tsikos et al., 2003). The BIF that comprise the Hotazel Formation generally have Mn concentrations below 0.5 wt.% but display slightly higher values in hematite- and carbonate-rich samples (Tsikos and Moore, 1997). Thinner Mn deposits are found in the Koegas Subgroup, which lies stratigraphically below the Hotazel Formation, separated by the Ongeluk Andesite, the Makganyene Diamictite, and an unconformity. The Koegas Subgroup has recently been proposed to have been deposited between 2.426 Ga (Gumsley et al., 2017 – based on SIMS and ID-TIMS U-Pb baddeleyite age for Ongeluk volcanics) and 2.460 Ga (Pickard, 2003 – based on SHRIMP U-Pb zircon ages of the underlying Kuruman BIF).

In this study, we report a similar sequence of Mn-enrichments from the uppermost Hamersley Group and the overlying Turee Creek Group, Western Australia (Figure 3.1). At the stratigraphic bottom of the sequence, the Boolgeeda Iron Formation, the youngest of the Hamersley Group iron formations, has recently been dated at 2.45 Ga using detrital zircons from a thin diamictite layer found within the unit (Caquineau et al., 2018), making it possible that the

Koegas Subgroup and Boolgeeda IF represent time equivalent deposits. The Boolgeeda is overlain by the Kungarra Formation, an approximately ~2.5 km thick package of shale and siltstone that in addition to several thick dolerite intrusions, hosts the ~400 m-thick Meteorite Bore Member diamictite. The Meteorite Bore Member diamictite is expressed in two major packages, a thicker (~300 m) lower occurrence and a thinner (<100 m) upper occurrence that are hosted in the upper third of the Kungarra Formation. New detrital zircon U-Pb ages (Caquineau et al., 2018) and a Re-Os age (Philippot et al., 2018) from the thicker lower occurrence constrain its age to <2.31 Ga. Overlying the Kungarra Formation is the ~200 m thick Koolbye Formation quartzite, which itself is overlain by the ~400 m thick Kazput Formation. The Kazput Formation is characterized by at least three dolomitic carbonate units, at times stromatolitic, separated by thick units (up to ~200 m) of shale and siltstone. The Turee Creek Group is capped by the Beasley River Quartzite upon which the Cheela Spring's Basalt is unconformably overlain; a SHRIMP U-Pb zircon age of 2209 +/- 15 Ma for the latter (Martin et al., 1998), along with a similar Pb-Pb baddeleyite age of 2208 +/- 10 Ma for dolerite sills intruding the Turee Creek Group (Müller et al., 2005), constitute an upper age limit for the Turee Creek Group.

No less than four major Mn enrichment zones, reaching up to ~15 m thick and up to 7 wt.% Mn in bulk-rock analysis, were discovered in drill cores obtained in the context of the Turee Creek Drilling Project (TCDP). Here we examine in detail the chemostratigraphic expression of these enrichments and the mineralogy of Mn-hosting phases responsible for these excursions. Stable molybdenum isotope systematics, collected in a companion study conducted on the same cores (Thoby et al., in prep), are also presented to better understand the origin of these enrichments and their significance in the context of competing theories for possible phototrophic metabolisms in

operation ca. 2.45 to 2.31 Ga and their role in the evolution of marine and atmospheric redox conditions during this critical transition period.

2. Methods and Results

2.1 X-ray fluorescence scanning

Drill core from the Turee Creek Drilling Project was analyzed by X-ray Fluorescence (XRF) core scanning using an Avaatech X-ray fluorescence (XRF) core scanner at IFREMER, Brest, France, to acquire geochemical profiles through the TCDP cores at 3 cm intervals. Data were cross-calibrated using the program AvaaXelerate (Bloemsma, 2015; Weltje et al., 2015) and the approach of Weltje and Tjallingii (2008) against high-precision bulk-rock major and trace element compositions determined by ICP-OES and HR-ICP-MS, respectively. To determine ideal AvaaXelerate program parameters for accurate cross-calibration, a limited calibration dataset containing only bulk-rock major and trace element data from TCDP1 was initially used. This limited the number of variables (e.g., lithology) and saved time during preliminary testing.

Nine calibration figures were produced under different program settings or using different calibration data to test which method of XRF calibration best reflected the true concentrations of elements. A summary table (Appendix A Table 1) and the calibration plots can be found in Appendix A. AvaaXelerate lists three settings that can be adjusted during sample selection: 1) the calibration method, 2) the sample depth tolerance (mm), and 3) the significance level.

As prescribed in Weltje et al. (2015), we used the multivariate log-ratio calibration (MLC) opposed to a univariate log-ratio calibration (ULC) as it incorporates absorption and enhancement effects on intensities into the model, which the ULC does not. Further, it accounts for an "undefined" variable, which represents all elements not selected for detection on the scanner. This

makes MLC the most likely transformation to produce quantitative intensity-concentration relationships. In order for the MLC calibration to work within AvaaXelerate all NaN and 0 values in calibration samples needed to be removed. Thus, any wet chemistry data with elemental concentrations missing were not included to calibrate the XRF data.

Baseline conditions used for XRF calibration were a sample depth tolerance of 100 mm, a significance level of 0.05, and the MLC method. We believe the sample depth tolerance of 100 mm is justified as some of our calibration samples are the average of 10 cm of core. To test the impact of reducing this tolerance, we performed a sample set of XRF calibrations using a 50 mm depth tolerance interval. All R^2 values were lower in the 50 mm depth tolerance case when compared to the 100 mm depth tolerance case, aside from Ca and Mg which remained approximately the same (Appendix A Table 1).

We also tested the impact of decreasing the significance level from 0.05 to 0.01. This change had no effect on the plots. Similarly, increasing the significance level to 0.2 also had no effect on the plots (Appendix A Table 1). This result may be an effect of our sample depth tolerance level being large enough (100mm) to allow the program to pick a calibration sample set with the smallest significance level automatically. Further, we also collected a surplus of calibration points and therefore the program may have automatically omitted samples with high significance levels when calibration samples were selected statistically.

The impact of separately calibrating XRF data measured at different energies (i.e. 10 kV or 30 kV) was also tested. When the 30 kV data are plotted without the 10 kV data, R^2 values for all elements drop or stay the same, while the value for the Undef variable increases. When the 10kV data are plotted without the 30 kV data, all R^2 values tend to increase or remain similar, including the Undef variable.

To test the impacts of matrix effects, three plots of the 10 kV, 30 kV, and 10 kV+30 kV dataset calibrated using only samples from the Kungarra formation were also produced. R^2 values were significantly higher for all plots when compared to plots using calibration data from the entire core, aside from Zn, Zr, and the Undef variable. This is also the case when comparing the 10 kV only and 30 kV only Kungarra datasets to their respective whole datasets.

The Kungarra-only datasets also show that R^2 values are generally highest in the 10 kV calibrations, mid-range in the 10 kV + 30 kV calibrations, and lowest in the 30 kV calibrations; an identical pattern to that observed for the entire TCDP1 dataset.

It would appear that the most accurate calibrations occur when 10 kV XRF data from the Kungarra formation is calibration with solution data from the Kungarra, using large sample depth tolerances (100 mm) and lower significance levels (0.05; although this conclusion is less clear). The benefit of large sample depth tolerances and low significance levels appears to be common across all datasets used. The increase in R^2 values due to the omission of Boolgeeda samples is likely the result of a decrease in matrix effects in consequence of reduced differences in matrices between samples. Further, it has been noted that in general, finer grained samples produce better XRF patterns, and mud/clay/silt sized samples are the easiest to calibrate as they tend to be more homogenous and have lower errors induced by changes in particle geometry (Weltje and Tjallingii, 2008).

After assessing which program settings were best suited for XRF calibration in a single core, we tested the effects of calibrating all units within the three cores separately (i.e. Kazput Carbonate, Kazput Mudstone, Koolbye Quartzite, Meteorite Bore Member, Kungarra Formation, and Boolgeeda Iron Formation). For all plots, a 100 mm sample depth tolerance, 0.05 significance interval, and the MLC calibration method were used, and 10kV and 30kV XRF data were

calibrated together. A summary table (Appendix A Table 2) and the calibration plots can be found in Appendix A. For comparison, the calibration results acquired by using all bulk-rock chemistry data from the three cores to calibrate all XRF data from all three cores is included in the summary table (i.e. global calibration). Although the goodness of fit as measured by R^2 varies for individual elements depending on which unit is calibrated, the global calibration appears to fit data for all elements better, aside from Mg. We attribute this to the availability of more bulk-rock chemistry calibration points to the program in the global calibration. Simply, by increasing the number of calibration points provided, AvaaXelerate can more accurately fit the XRF data to the "actual" bulk-rock chemistry calibration data.

Finally, we investigated whether solution data from one unit could better calibrate XRF data from all three cores. For all plots, a 100 mm sample depth tolerance, 0.05 significance interval, and MLC calibration method were used, and 10kV and 30kV XRF data were calibrated together. A summary table (Appendix A Table 3) and the calibration plots can be found in Appendix A. For comparison, the global calibration was also included. Again, there is notable variation in the fits of different elements depending on which unit's bulk-rock concentrations are used to calibrate the XRF data. However, the communal best fit for all elements is achieved by the global calibration. We again attribute this to a larger number of calibration points spread over a greater number of lithologies providing a more representative sample of true concentrations for AvaaXelerate to calibrate to.

In summary, when using AvaaXelerate to calibrate XRF data acquired from an Avaatech XRF core scanner, it is best to choose numerous (as many as possible) bulk-rock geochemical calibration points that span multiple lithologies. Cross-calibration plots, such as those included in

Appendix A, and associated R^2 values should always be checked to confirm a good fit for the element of interest.

2.2 Mn Enrichments

X-ray fluorescence core scanning led to the identification of four intervals of Mn enrichment in the TCDP cores; two occur in TCDP1 within the Boolgeeda IF at 150.5-151 m depth (B1) and 130.5-129.5 m depth (B2), and two thicker enrichments with higher Mn concentrations are found in TCDP3 at 182.8-178.65 m depth (K1) and between 162.7-150.55 m depth (K2) (Figure 3.1). Bulk-rock digestions and major element analysis confirmed these enrichments and allowed for the quantitative calibration of XRF data, as discussed in section 2.1. Enrichments B1 and B2 have Mn concentrations of 2.65 wt.% and 1.79 wt.%, respectively. Enrichments K1 and K2 are much larger, reaching Mn concentrations up to 9.76 and 7.10 wt. %, respectively.

Sequential extractions, as described by Poulton and Canfield (2005), suggest Mn in TCDP1 is predominantly associated with carbonate phases (Figure 3.2). Six fractions of total Mn were extracted separately from powdered samples. The exchangeable Mn fraction (Mn_{Ex}) represents the concentration of Mn removed during interaction with 1 M magnesium chloride at pH 7 for 2 hrs at room temperature. This fraction represents Mn adsorbed to the surface of particles and readily exchangeable with fluids. In all samples, this fraction was relatively low to absent. The Mn_{Carb} fraction represents the concentration of Mn collected after powdered samples were reacted with 1 M sodium acetate at pH 4.5 and 50°C for 24 h on a heating block. Under these conditions all carbonates should have been removed from the powers. This fraction represents the largest concentration of Mn in all samples, thus supporting Mn association with carbonate phases. The Mn_{Ox1} extraction represents Mn associated with remaining phases soluble in 1 M hydroxylamine

hydrochloride in 25% v/v acetic acid over 48 h at room temperature. These are typically easily reducible oxides such as ferrihydrite and lepidocrocite. Manganese concentrations in this fraction are generally lower in all samples, aside from intervals containing significant Mn enrichment (i.e. B1). The Mn_{Ox2} fraction represents Mn concentration in reducible oxides such as goethite, akaganéite, and hematite, extracted by reacting remaining sample for 2 h at room temperature with 50g/L sodium dithionite buffered to a pH of 4.8 using 0.35 M acetic acid, 0.2 M sodium citrate, and sodium hydroxide. This fraction hosted low Mn concentrations in all samples. Similarly, the remaining fractions hosting Mn in magnetite, poorly reactive sheet silicates, and pyrite + robust silicates (Mn_{Mag}, Mn_{PRS}, and Mn_{Py+U}) displayed low Mn concentrations. The Mn_{Mag} fraction was extracted using 0.2 M ammonium oxalate and 0.17 M oxalic acid solution at pH 3.2 for 6 h at room temperature. The Mn_{PRS} fraction was extracted by reacting samples with boiling 37% hydrochloric acid for 3-5 min. The final digestion yielding Mn_{Py+U} was performed by adding 5 mL of 70% nitric acid and 3 mL of 48-51% hydrofluoric acid, and subsequently heating mixtures at 155°C until dryness. One mL of 37% hydrochloric acid was then added to the sample and the mixture was again heated at 155°C for 4 h. All sequential extraction solutions were analyzed for Mn, Mo, and Fe using an Agilent 8800 Triple Quadrupole ICP-MS in high matric introduction mode, using Ar as a carrier and dilution gas and He (5 mL/min) as collision gas to minimize polyatomic interferences (Sakai, 2015). Germanium and In were used as internal standards. The certified standard STSD-3 (CANMET Mining and Mineral Science Laboratories, Natural Resources Canada) was used to verify recovery. Average total recovery was 107%.

Carbonate textures visible in Mn enriched sections of both TCDP1 and TCDP3 are similar (Figure 3.3). In both cases, lighter carbonate layers alternate with darker layers of mudstone. The carbonate layers are not uniformly thick across the core, and in some cases appear discontinuous

with oblong carbonate segments not quite extending across intervening mudstone. This is particularly noticeable in interval K2. The association of Mn with carbonate in TCDP1, as confirmed by sequential extractions discussed above, and the similarity of carbonate textures between TCDP1 and TCDP3 supports Mn being hosted in carbonate in both cores (further supported below). Although a similar banded carbonate with enriched Mn concentrations (~1-5 wt. %) is found in the upper sections of enrichment K1, the bottom of the enrichment (182.8-182.2) containing the highest Mn concentrations (~6-9 wt. %) appears texturally different than the other three intervals (see Figure 3.15). Thin carbonate-mudstone banding is not present in this section, but instead, the carbonate forms a thick "mottled" package, capped by a ten-cm thick banded section that contains thin mesobands of jasper. This may suggest the lower section of K1 was formed in a different manner to the other enriched intervals or underwent different diagenetic and/or metamorphic conditions.

Manganese K-edge XANES spectra further support carbonate-hosted Mn (Figure 3.4). Synchrotoron-based XANES spectra were collected using the Hard X-ray MicroAnalysis (HXMA) beamline at the Canadian Light Source (CLS) in Saskatoon, Saskatchewan, Canada. Pelleted rock powder samples were prepared from rock chips of the intervals of interest. Pellets were made by combining rock powder with boron nitride in proportions that varied depending on Mn concentration within the sample. Pellets were subsequently attached to the sample holder and placed in the beamline for analysis. Spectra for braunite, pyrolusite, tephroite, rhodochrosite, manganite, bixbyite, and kutnohorite standards were also acquired for comparison and sample fitting. Scans were completed across an energy range spanning the 1s electron excitation energy (K-shell) for Mn (6537 eV). Samples analyzed from the banded enrichments in intervals B1, B2, and K2 show Mn has an average speciation of 2 (Table 1), and all three intervals are best fit using

a spectrum acquired from a kutnohorite standard. Notably, one sample (T3-182.9) analyzed directly below the K1 interval has a slightly higher average speciation of 2.094. Linear combination fitting suggests the XANES spectrum for this sample is best described by a mixture of kutnohorite (0.375), bixbyite (0.060), pyrolusite (0.016), and tephroite (0.550). However, Mn concentrations in this sample are low and a corresponding powder XRD profile shows no evidence for Mn phases; thus, XANES analysis is likely detecting minor Mn substitution into silicates (Figure 3.5D). As this sample lies outside of the Mn enriched intervals, it will be discussed no further.

Samples analyzed at HXMA were also characterized using powder-XRD (Rigaku Geigerflex Powder Diffractometer equipped with a cobalt tube, graphite monochromator, and scintillation detector) at the XRD Diffraction Laboratory, University of Alberta, Edmonton, Canada. Resulting spectra were matched to crystal structures using the JADE 9.1 software and the ICDD and ICSD databases. Although the kutnohorite XANES standard provided the best fit for Mn rich TCDP1 samples, powder XRD analysis did not support the presence of kutnohorite (Figure 3.5). Instead, powder XRD confirmed the presence of dolomite (Mn-enriched per microprobe analysis) and ankerite. A simple explanation for this discrepancy is as follows: in selecting standards for XANES analysis, we were forced to select a limited number of samples representing the various redox states of Mn (II-IV), as well as different phases that might be present (i.e. carbonates, silicates, oxides). Time limitations on the Canadian Light Source (CLS) synchrotron prevented us from selecting both kutnohorite and ankerite. However, the local coordination environment of Mn in ankerite and kutnohorite is similar (trigonal-rhombohedral crystal lattice; space group R3) and both are Mn carbonates. Because the bonding environment of Mn in both minerals is comparable, kutnohorite and ankerite should result in similar XANES

spectra. XRD patterns, on the other hand, were compared to a large database of crystal structures which contained both ankerite and kutnohorite. It is likely that XRD patterns better represent the specific phase present, while XANES spectra provide information about the Mn bonding environment and average valence. Thus, ankerite is the likely carbonate phase in TCDP1. Interestingly, kutnohorite was identified in powder XRD spectra from TCDP3, in Mn enriched interval K2. Notably, ankerite and kutnohorite form a carbonate series: $Ca(Fe[II],Mg)(CO_3)_2$ to $Ca(Mn[II])(CO_3)_2$. It may be possible that the transition from Mn-enriched dolomite and ankerite to kutnohorite between TCDP1 and TCDP3 represents an increase in background Mn concentrations. Thus, we believe the phase hosting Mn in TCDP cores ranges in composition between Mn-enriched dolomite, ankerite, and kutnohorite.

After locating Mn enrichments and identifying phases hosting Mn, intervals B1, B2, K1, and K2 were investigated in more detail. An in-depth investigation of these Mn enriched intervals will be discussed in the following section.

2.2.1 Enrichment B1

Figure 3.6 shows enrichment B1 in core next to a corresponding XRF profile through the section. Thin section images are included to further highlight changes in lithology and texture that accompany Mn enrichment throughout the interval. Notably, Mn enrichments are strictly associated with sections of the core characterized by alternating bands of carbonate and mudstone. The thin section images highlight a distinct drop in Mn concentrations coinciding with a loss of carbonate bands.

"Eyelet" structures appear at the top of the B1 Mn enrichment. Microprobe maps show the eyelets are composed of Mn-carbonate rims formed around a silicate core (Figure 3.7). Iron and

Mg are also closely associated with Ca and Mn in the microprobe maps. Microprobe analysis and powder XRD suggest the carbonate around the rim is ankerite. A chlorite rim surrounds the ankerite rim, forming the outer boundary of the eyelets. SEM-EDS maps of the eyelet structures and intact carbonate beds further support the close association of Mn and Ca at micron-scale resolution (Figures 3.8 and 3.9). SEM-EDS maps were acquired using a Zeiss Sigma 300 VP-FESEM equipped with secondary and backscattered electron detectors, an in-lens electron detector, a cathodoluminescence (CL) detector, and a Bruker energy dispersive X-ray spectroscopy (EDS) system at the Scanning Electron Microscope Laboratory, University of Alberta, Edmonton, Alberta, Canada. Thin sections were coated in graphite using a Leica EM SCD005 evaporative carbon coater prior to analysis. This association further affirms carbonate-hosted Mn enrichments proposed in the sections above. Micro-X-Ray Fluorescence (μ-XRF) maps acquired using the Very Sensitive Elemental and Structural Probe Employing Radiation from a Synchrotron (VESPERS) beamline at the Canadian Light Source (CLS) show identical results (Figure 3.10). Elemental correlation plots for μ-XRF maps can be found in Appendix B; all plots show a relatively strong correlation between Mn and Ca.

Magnified XRF profiles, at the cm-scale, of major and trace element concentrations across the B1 enrichment are presented in Figure 3.11. As discussed in section 2, these profiles were calibrated using the AvaaXelerate program (Bloemsma, 2015) and bulk-rock chemistry data from samples taken throughout all three TCDP cores. Notably, Si, Al, Ti, Zr, Zn, Ni, and Cr concentrations fall off prior to the Mn enrichment, and then increase slightly within the interval of greatest enrichment. Further, Ca, Mg, and Sr concentrations increase within the Mn enrichment. These trends reflect the transition from mudstone to mudstone containing thin bands of Mn-rich carbonate, which is marked by an interval of higher P content and a modest spike in S.

2.2.2 Enrichment B2

Figure 3.12 shows enrichment B2 in core next to an XRF profile through the corresponding section. Again, there is a noticeable decline in Mn concentration where the carbonate bands disappear. However, carbonate banding in this interval is poorly defined compared to enrichment B1, best demonstrated by the thin section photographs included in Figure 3.12. This may reflect the lower Mn concentrations and relative thinness of this enrichment.

Manganese concentrations appear to increase with Ca, Sr, P, and Fe concentrations, although their association with Fe is less clear (Figure 3.13). Just below the Mn enrichment (~130.7 m depth) concentrations of Al, Ti, Zr, K, Rb, Ni, and Cr spike. This pattern can be explained by an influx of detrital material prior to Mn-carbonate deposition. This influx of material and overlying Mn-carbonate deposition also separate BIF deposition below (Boolgeeda Iron Formation) from grey mudstone-siltstone deposition above (Kungarra Formation). The contact between these two units has traditionally been marked by a thin layer of chert (e.g. Van Kranendonk et al., 2015), which is visible in Figure 3.12 at ~129.60 m depth.

Synchrotron µ-XRF maps acquired at the CLS confirm a similar association of Mn and Ca to that seen in enrichment B1 (Figure 3.14). Elemental correlation plots of µ-XRF counts support this relationship (Appendix B).

2.2.3 Enrichment K1

Texturally, the bottom of enrichment K1 looks different from any interval in B1, B2, or K2 (Figure 3.15). Thin sections taken from this location show a more mottled carbonate lacking well-defined banding. However, banded carbonate is present in two distinct packages lying above the lowermost

section of this enrichment. These packages are apparent in the Mn XRF profile taken through the core and display similar calibrated Mn concentrations to enrichments B1 and B2.

XRF profiles through enrichment K1 show increases in Ca, Fe, Mg, Sr, and P concentrations associated with high Mn concentrations (Figure 3.16). Conversely, Si, Al, Ti, Zr, Zn, Ni, and Cr concentrations fall, reflecting a movement away from detrital sediments of the Koolbye Formation.

2.2.4 Enrichment K2

Manganese enrichment K2 is displayed in Figure 3.17, along with a Mn XRF profile through the section and accompanying thin section photographs. Enrichment K2 is by far the thickest of the four Mn-enriched intervals but displays a remarkably consistent carbonate banding throughout. These bands are most similar to enrichment B1 as demonstrated in Figure 3.18. As mentioned above, however, the dominant carbonate phases are ankerite and kutnohorite opposed to Mn-rich dolomite (Figure 3.5).

XRF profiles of bulk sediments through this interval show no clear spatial association of any element with Mn (Figure 3.18). However, elemental cross-correlation plots of bulk-rock Mn XRF data display slight positive correlations with Ca, Mg, and Sr. Further, element cross-correlation plots of μ-XRF data suggest a strong relationship between Mn and Ca, and weaker relationships with Ni, Cr and S at the micron scale (Appendix B). Micro-XRF maps collected within this interval confirm elemental correlations, and Mn is clearly associated with a carbonate phase (Figure 3.19).

2.3 Major and trace element comparison of enrichments B1 and K2

The new stratigraphic framework presented by Philippot et al. (2018), and ages reported by Caquineau et al. (2018), suggest Mn enrichments in TCDP1 and TCDP3 are separated by more than 140 Ma. Thus, significant changes in environmental conditions may have occurred between deposition of TCDP1 and TCDP3, especially given the fact that this period of time spans the presumed age of the Great Oxidation Event. Differences in major and trace element concentrations have the potential to shed light on variations in environmental conditions separating the two deposits. Thus, major and trace element concentrations through enrichments B1 and K2 were compared as these intervals represent the thickest Mn enrichments in TCDP1 and TCDP3.

Figure 3.20 presents the major element data for samples with >0.1 wt.% MnO throughout enrichments B1 and K2, normalized to upper continental crust (UCC) values (Taylor and McLennan, 1985). Notably, TiO_2 (wt.%) and Al_2O_3 (wt.%) values are much lower in B1 samples while Fe_2O_3 (wt.%) values are higher. Sodium is the only other major element that appears to vary significantly from UCC values and is depleted in both sample sets.

Figure 3.21 presents the trace element data for samples with >0.1 wt.% MnO from enrichments B1 and K2, normalized to UCC values (Taylor and McLennan, 1985). Cobalt, Ni, Cu, Mo, As, Ba, U, and V UCC normalized concentrations are higher in K2 samples compared to B1 samples. Notably, Cu, Cd, As, and U in K2 samples are clearly enriched relative to UCC, while Mo appears slightly enriched, and Co, Ni, Zn, Pb, Ba, and V are close to UCC values. In B1 samples, Cd and As are enriched relative to UCC, while Co, Ni, Cu, Ba, U, and V all appear to be depleted. Zinc is also generally depleted, aside from three samples that are significantly enriched relative to UCC.

Solution data for MnO (wt.%) collected from Mn enriched samples (>0.1 wt.% MnO) throughout intervals B1 and K2 were cross-plotted against all major and trace element data in an attempt to identify geochemical anomalies correlated to Mn enrichments. Manganese XRF data were also cross-plotted against XRF data for all other elements to corroborate correlations using a separate dataset. A summary of the R^2 values from these plots can be found in Table 3. If R^2 values were below 0.1 they were not reported, and the elements are considered to be uncorrelated. A lower case "p" or "n" is located next to each R^2 value to indicate whether the relationship is positive or negative.

MnO (wt.%) concentrations positively correlate with CaO (wt.%) and LOI concentrations in both samples sets of solution data, while Na_2O (wt.%) values are negatively correlated. Silica, K, and P may also be negatively correlated with Mn enrichments but contrasting results between the solution and XRF data make conclusions ambiguous. The trace element data are extremely inconsistent between the two datasets, however, both XRF and solution data suggest a positive correlation between Sr (ppm) and MnO (wt.%) in B1 but not in K2. Further, in both XRF and solution data, Zn is negatively correlated with MnO (wt.%) in enrichment K2 but shows no trend in B1. MnO (wt.%) is also negatively correlated with Cs and Sb in both B1 and K2 bulk rock solution data.

To aid in identifying redox conditions during deposition, Mo_{EF} and U_{EF} concentrations were cross-plotted in a manner identical to Algeo and Tribovillard (2009; Figure 3.22). Enrichment factors (Mo_{EF} and U_{EF}) were calculated using the equation $(X/Al)_{sample}/(X/Al)_{PAAS}$, where X represents either Mo or U and the PAAS subscript refers to post-Archean average shale composition values reported by Taylor and McLennan (1985). Samples from enrichments B1, K2, and the Kazput carbonate form distinct trends within the plot. All three trends show a relative

enrichment in Mo over U when compared to modern seawater. For comparison, the ratio of Mo/U in modern seawater is ~7.5-7.9 (Morris, 1975; Chen et al., 1986; Millero, 1996).

2.4. Stable Isotopes (measured in companion studies)

Stable molybdenum isotope signatures through TCDP1 and TCDP3 are presented in Figure 3.1. These datasets were collected in companion studies conducted on the same suite of rocks, under the umbrella of the Turee Creek Drilling Project (Thoby et al., in prep). It should be stressed that these data were not collected for this thesis but will be referred to here in order to provide further context for the Mn carbonate descriptions discussed above.

Molybdenum concentrations and isotopes were measured in the clean laboratories of the Pôle Spéctrométrie Océan (PSO), Brest, France. Due to the low Mo concentration in some TCDP samples, a rough preliminary measurement of Mo concentration in bulk-rock samples was made to aid in determining the quantity of Mo double-spike to add. The Mo purification protocol follows that of Voegelin et al. (2009), Siebert et al. (2001), and Asael et al. (2013). 1.5 g of powder were digested using 6N HCl, and a ^{97}Mo-^{100}Mo double spike (DS) was added prior to column chemistry to monitor any isotopic fractionation due to Mo extraction procedures and correct for instrumental mass bias during isotope measurement. The DS concentration added was targeted to achieve a DS:Natural Sample ratio close to 1. Column chemistry proceeded in two steps. In the first, Mo and Fe were separated from the bulk-rock samples. In the second step, Mo was isolated. Molybdenum concentrations and stable isotope compositions were determined after chromatographic separation by isotope dilution and MC-ICP-MS measurement (Thermo Scientific Neptune) at the PSO, Brest, France. These analyses were performed across enrichments B1 and K2 within the TCDP cores on samples identical to the ones investigated in this thesis. Molybdenum isotopic signatures (δ^{98}Mo)

across enrichment B1 range between 0.54‰ and 1.36‰, with an average Mo isotope composition of 0.94‰. In TCDP3 δ^{98}Mo measurements are much more consistent, lying between 0-1‰ throughout enrichment K2. Specifically, δ^{98}Mo measurements range from 0.09‰ to 0.80‰, with an average of 0.45‰. Molybdenum isotopes were not measured through enrichments B2 or K1 given time constraints. The reader is referred to the work of Thoby et al. (in prep) for more information regarding the methods and results of Mo isotope analysis in the TCDP cores.

3. Discussion

3.1 Mn Enrichment Mineralogy and Textures

Numerous experimental methods, including XRF scanning, sequential extractions, XANES analysis, microprobe mapping, SEM-EDS mapping, and µXRF mapping have demonstrated the correlation between Mn and carbonates or elemental suites typically associated with carbonates. Manganese enriched carbonates have also been identified in XRD profiles of TCDP1 and TCDP3 (Figure 3.5). Therefore, we can confidently assume that Mn enrichments in the TCDP cores are hosted in carbonates belonging to the ankerite-kutnohorite series [$Ca(Fe[II],Mg)(CO_3)_2$ to $Ca(Mn[II])(CO_3)_2$]. The increased prevalence of kutnohorite in TCDP3 compared to TCDP1 (Figure 3.5) may reflect an increase in background marine Mn concentrations through time.

Manganese enrichments appear to be restricted to carbonate laminations in intervals B1, B2, K1, and K2, aside from a mottled carbonate layer at the base of enrichment K1. It may be possible that Mn enrichments B1, B2, K1, and K2 were formed in a similar manner given the similarity in Mn enriched phases and textures. The greater thickness and higher Mn concentration of Kazput enrichments may be a result of prolonged environmental conditions promoting Mn-rich carbonate deposition, or an expansion of conditions under which Mn-carbonate precipitation was

favoured. Alternatively, the thickness of each Mn enrichment may be influenced by varying basin geometries at the time of deposition (Force and Maynard, 1991). In this case, Kazput enrichments would represent shallower deposits on a more gently inclined slope. Assuming a redox stratified water column, this would allow for conditions promoting Mn enrichment to interact with a larger area of the sea floor as compared to a deeper, more steeply inclined slope.

Eyelet structures in Mn enrichment B1 are clearly secondary, and likely the product of shear strain rotating silicate grains during burial and deformation. However, the presence of intact carbonate beds above and below the eyelet horizon, which also show a spatial association between Ca, Mn, Mg, and Fe (Figure 3.7), suggests the source of Mn-carbonate was likely in place prior to the formation of carbonate rims. Rotation of the silicate grains during deformation likely led to the dissolution and reprecipitation of nearby carbonate, as carbonate dissolved from the high-pressure side of the grain and reprecipitated on the low-pressure side of the grain. This process, continuing over the full rotation of the grain, could have produced the rims. If Mn was preferentially mobilized during deformation, it could explain the increased prevalence of ankerite around the rims opposed to the higher abundance of Mn-rich dolomite in the intact beds, as suggested by powder XRD (Figure 3.5). Thus, it appears that although Mn-rich carbonates are prevalent in the Boolgeeda, higher Mn-enrichments may be partially a result of secondary enrichment during burial. The fact that chlorite forms the outermost layer of the eyelets may constrain the formation of Mn-carbonate layers to conditions below (and prior to) greenschist metamorphism.

The mottled carbonate texture in the bottom of Mn enrichment K1 suggests this portion of the core has undergone different diagenetic and/or metamorphic conditions. This section lies directly above the contact between the Kazput Formation and the Koolbye Quartzite below. It is possible that fluids permeated this contact as a result of increased porosity in the quartzite,

promoting fluid mobility. Alternatively, a density contrast between the two units may have led to preferential deformation at the contact. It is clear that emplacement of the quartzite itself did not contribute to the manganese enrichment as powder-XRD analyses performed on a sample taken from directly below enrichment K1 (T3-182.9; Figure 3.5D) shows no indication of a Mn phase, and Mn concentrations are low at this depth (Figure 3.15). The fact that Mn concentrations are so low in the quartzite lends support to the mottled carbonate texture being a result of deformation opposed to an interaction with secondary fluids; any secondary fluids enriched in Mn should have increased Mn concentrations in the more porous primary sediments of the quartzite. Thus, it may be possible that high Mn concentrations are the result of Mn remobilization and concentrations during deformation, similar to the mechanism of Mn-enrichment in the eyelet rims. The source of Mn may be primary Mn-carbonate beds similar to those visible above the mottled carbonate in enrichment K1.

3.2 Comparison of TCDP Mn enrichments to other global enrichments

Manganese enrichments in the Boolgeeda IF are larger than any previously observed in the Hamersley Basin, particularly the underlying Dales Gorge (Max 0.04 wt. % MnO; Pecoits et al., 2009) or Joffre (Max 0.38 wt.% MnO; Haugaard et al., 2016) Members of the Brockman Iron Formation. However, these enrichments are dwarfed in comparison to the 2.426-2.394 Ga Hotazel Formation and associated Kalahari Mn deposits of South Africa (Gumsley et al., 2017 and Bau et al., 1999, respectively), which host thick packages (15-45 m in places) of Mn enriched sediments with concentrations up to 40 wt.% Mn (Tsikos and Moore, 1997).

Analogous to the Boolgeeda IF's stratigraphic position within the Mount Bruce Supergroup, the Hotazel represents the youngest episode of iron-formation deposition within the

Transvaal Supergroup. Age constraints for the Hotazel (Gumsley et al., 2017; Bau et al., 1999) when combined with the new stratigraphic framework presented by Philippot et al. (2018) place its deposition after the Boolgeeda IF Mn enrichments (B1, B2) but prior to Mn enrichments in the Kapzut Formations (K1, K2). Thus, Hotazel deposition should coincide with deposition of the Kungarra Formation underlying the first glacial unit of the Meteorite Bore Member, the base of which was dated to ~2.31-2.34 Ga using sulfide Re-Os ages (Philippot et al., 2018; 2312±5.6 Ma) and a detrital zircon U-Pb age (Caquineau et al., 2018; 2340±22 Ma).

Manganese rich units of the Hotazel are dominated by braunite (Nel et al., 1986). Tsikos and Moore (1997) also noted an abundance of minerals belonging to the dolomite-ankerite series, and that elevated Ba and Co values characterized all lithologies enriched in Mn. In fact, kutnohorite has been noted to occur pervasively throughout the unit (Gutzmer and Beukes, 1996; Tsikos et al., 2003) as well as manganoan calcite (Johnson et al., 2016). Further, detrital components of the Hotazel were deemed to be negligible, given the low Ti, Al, K, Rb, and Zr concentrations, and Cu, Zn, Ni, Co, and V concentrations were always below 50 ppm, suggesting limited direct volcanogenic hydrothermal input (Tsikos and Moore, 1997). Similar to the Hotazel, the TCDP cores host minerals belonging to the dolomite-ankerite-kutnohorite series (discussed above). Further, Hotazel REE patterns normalized to the North American shale composite are depleted in LREE, contain negative Ce anomalies, and sparse positive Eu anomalies (Tsikos and Moore, 1997), similar to REE signatures for the Boolgeeda IF (Warchola et al., 2018). The Boolgeeda IF also contains relatively low Cu, Zn, Ni, Co, and V concentrations (generally <50 ppm), but shows no correlation between Ba, Co, and Mn (Table 3), and contains comparatively high concentrations of lithogenic elements (Warchola et al., 2018). Thus, the chemical characteristics of Boolgeeda IF Mn enrichments may suggest they were deposited under similar conditions to the Hotazel, but

were more strongly influenced by detrital material. One depositional model presented to explain geochemical trends and Mn enrichments in the Hotazel is fractional precipitation of iron and manganese sourced from distal hydrothermal vents through transgressive-regressive cycles. In fact, each Mn bed in the Kalahari Mn deposit has been suggested to correspond with peak marine transgression (Beukes, 1983; Roy, 1992; Schissel and Aro, 1992). Notably, Mn enrichments B1 and B2 within the Boolgeeda IF appear to bracket sea level rise and fall as highlighted by varying lithogenic element input (e.g. Al, Ti) and Y/Ho ratios (Warchola et al., 2018). It is possible that transgressive-regressive cycles also had an influence on Mn enrichment in the Boolgeeda.

The contrasting correlations between Co, Ba, and Mn may suggest slightly different redox conditions accompanied each Mn deposit. Cobalt and Ba belong to a group of elements known to sorb strongly to Mn oxides. However, Co is not mobile under euxinic conditions as it preferentially forms sulfides. Barium, on the other hand, does not form sulfides but preferentially precipitates from sulfate-rich solutions as barite. The strong correlation between Ba, Mn, and Co in the Hotazel may suggest conditions were not euxinic and sulfate levels were below that of barite oversaturation, allowing both Co and Ba to remain at high concentration in the water column and sorb onto precipitating Mn oxides. A lack of correlation in the Boolgeeda IF may suggest either Co was tied up in sulfides or barite was precipitating in another more oxidizing location, thus hinting at a diverse set of contemporaneous redox conditions separated by multiple chemoclines. Perhaps a more parsimonious explanation is that the supply of Ba and Co to sediments was lower in the Boolgeeda than in the Hotazel. Alternatively, the Hotazel enrichments represent primary Mn oxides diagenetically transformed into Mn carbonates while the contribution of Mn oxides to Boolgeeda enrichments was much smaller, or perhaps non-existent. This conclusion proceeds logically if O_2 concentrations increased steadily through time.

Given that the Hotazel likely represents a younger and more extreme Mn enrichment than B1 and B2 enrichments, it may be more appropriate to make comparisons to the older Koegas Subgroup, South Africa (2.426-2.460 Ga; Gumsley et al., 2017 and Pickard, 2003, respectively). The Koegas is interpreted to have been deposited in a deltaic and near-shore marine environment (Shröder et al., 2011; Johnson et al., 2013; Johnson et al., 2016). Manganese enrichments in the Koegas Subgroup are largely contained within the Rooinekke Formation, which hosts MnO concentrations between 3-5 wt.%, with one excursion reaching concentrations of almost 8 wt.% MnO (Nel, 2013). Johnson et al. (2013) also noted MnO concentrations in bulk rock samples up to 11.6 wt.%. Manganese rich carbonate nodules within the Koegas belong to a solid solution series between ferroan rhodochrosite, manganoan siderite, and manganoan calcite with 'rhodochrosite-like' and 'kutnohorite-like' endmembers (Johnson et al., 2016). Notably, the center of these nodules was determined to be kutnohorite. Further, Mn and Ca concentrations are correlated throughout the Nelani and Rooinekke IF of the Koegas Subgroup, suggesting a relationship between whole rock Mn concentrations and the abundance of carbonate minerals (Nel, 2013), which supports prior suggestions that high Mn abundances were exclusively bound in carbonate phases (Johnson et al., 2013). Thus, mineralogy of Mn phases in the Koegas appears to be similar to that of the TCDP samples. Johnson et al. (2013) suggested that Mn rich carbonates in the Koegas were the result of the reduction of primary Mn oxides. However, the same authors found no evidence for oxygen rich conditions during deposition of the Koegas Formation and therefore concluded that primary Mn oxides may be the extant products of a primitive Mn-based photosynthetic pathway. Notably, negative Ce anomalies have since been reported in the Koegas iron formation (although this data is unpublished; Nel, 2013), perhaps arguing against the biological pathway and instead providing support for abiogenic primary Mn oxides. Interestingly,

Johnson et al. (2016) noted similar textures between Koegas samples and weathered surface samples of the Kungarra Formation, which they suggested may reflect the alteration of primary Mn oxides.

3.3 Primary Phase of Mn Enrichments

Manganese enrichments throughout Earth history have been used to support the presence of oxidizing conditions at the time of deposition. Traditionally it has been thought that Mn enrichments are most likely the result of Mn oxides concentrating at the sea floor and subsequently being reduced to Mn(II) carbonates (e.g. Calvert and Pedersen, 1996). Investigations of modern Mn enrichments, however, have suggested that their formation is much more complex; Mn has even been reported to concentrate in sediments during periods of anoxia. For example, Lepland and Stevens (1996) suggested that Mn-carbonate in the Landsort Deep of the Baltic Sea formed independent of precursor Mn-oxide phases at the sediment-water interface. Instead, they proposed Mn enriched layers formed due to high rates of organic matter deposition and sulphate reduction resulting in increased alkalinity. It remains unknown as to whether Mn enrichments in the TCDP cores are indicative of oxidizing conditions capable of producing primary Mn oxides subsequently reduced to Mn(II) carbonates during diagenesis, or if they were initially deposited as a Mn(II) phase and therefore not a direct indication of the redox state of contemporary seawater.

Given that Mn enrichments in the Boolgeeda IF and Kazput Formation are separated by more than 140 Ma (Philippot et al., 2018; Caquineau et al., 2018), comparing and contrasting their major and trace element signatures may provide valuable information regarding environmental conditions at the time of their deposition, especially considering that major geochemical changes are likely to have occurred in the oceans and atmosphere between 2.45 Ga to <2.31 Ga. For the

sake of simplicity, only the thickest enrichments in each section (intervals B1 and K2) will be discussed.

The relatively high Fe_2O_3 and low TiO_2 and Al_2O_3 concentrations (Figure 3.20) in enrichment B1 are not unexpected as this interval lies within the Boolgeeda IF. Banded iron formation deposition is typically characterized by low detrital input, thus resulting in TiO_2 and Al_2O_3 depletion. Conversely, the K2 enrichment is hosted within the Kazput mudstone which contains no primary Fe precipitate and an abundance of detrital particles. Thus, Fe_2O_3, TiO_2, and Al_2O_3 concentrations are more similar to UCC. Upper continental crust normalized concentrations of Na_2O and K_2O are also lower in the B1 samples which is again attributed to a smaller proportion of detrital materials, including Na and K clays, in the Boolgeeda IF sediments. All other major element concentrations are relatively similar between the two sample sets.

The highly reactive surface of Mn oxides has been noted to strongly sorb numerous metals, including Co, Ni, Cu, Zn, Pb, Cd, Mo, As, and Ba (Goldberg, 1954; Jenne, 1968; Loganathan and Burau, 1973; Nelson et al., 1999a,b; Kay et al., 2001; Matocha et al., 2001; O'Reilly and Hochella, 2003; Toner et al., 2006; Takahashi et al., 2007; Peña et al., 2010). Thus, enrichments in these metals may suggest that primary Mn oxides were present in the sediments at the time of deposition. Notably, Co, Ni, Cu, Mo, As, Ba, U, and V concentrations normalized to upper continental crust are higher in interval K2 than in interval B1; Ni, Cd, Mo, As, and U in K2 are even enriched relative to UCC (Figure 3.21). The enrichment of numerous trace element in K2 may be evidence for primary Mn oxides. This may be supported by the presence of kutnohorite in K2, as Johnson et al. (2016) suggested kutnohorite in the Koegas Subgroup was the direct product of reductive alteration of primary Mn oxides. Conversely, in B1 only Cd and As are enriched relative to UCC while Co, Ni, Cu, Ba, U, and V all appear to be depleted. This inconsistency may be evidence

against primary Mn oxides in B1. Alternatively, it may suggest processes other than the formation of Mn oxides, such as the presence of euxinic conditions within the basin, were influencing the concentrations of these trace elements during deposition of B1.

One of the most striking features of the UCC normalized trace element profiles is the enrichment of As in both B1 and K2 samples (Figure 3.21). Arsenic behaves conservatively in the presence of oxygen (Cullen and Reimer, 1989; Smedley and Kinniburgh, 2002) as As(V) compounds. Thus, higher O_2 concentrations in seawater should promote the mobility of As. If As was more mobile in K2, it may explain the slight enrichment of As in K2 when compared to B1. A similar theory may explain the higher concentrations of Mo, Ba, U, and V, as all behave conservatively under oxic conditions. More oxic conditions during K2 deposition follows logically if a progressive increase in global O_2 concentrations through time is assumed. Alternatively, the spike in As may coincide with a transition from stage III to stage IV of Fru et al.'s (2015) 6 stages of sedimentary As enrichment. Those authors suggest that after the Huronian glaciations, the continental supply of reduced As was "unblocked" as ice retreated and intense weathering resulted in high marine As concentrations. A similar increase in weathering may also explain the Mo, Ba, U, and V enrichments. Temporally this theory fits the new stratigraphic framework proposed by Philippot et al. (2018) as enrichments B1 and K2 occur directly after Huronian glacial sediments, represented in the TCDP cores by the diamictite within the Boolgeeda IF and the Meteorite Bore Member of the Kungarra Formation.

The extreme depletion of Ba in B1 and a few samples of K2 is also interesting. Barium is strongly influence by concentrations of sulfate. Basins with anoxic sulfidic bottom waters have low-SO_4 deep water which makes barite unstable and Ba soluble. In such cases, it is common to see strong correlations of Ba with Mn in sediments (Maynard, 2010), as both Ba and Mn upwell

from the deep sulfidic water and concentrate at the anoxic-oxic chemocline. The fractionation of Mn and Ba in B1 samples may suggest Ba concentrations were low in seawater. If SO_4 concentrations during deposition of B1 were high enough to promote barite precipitation in shallow oxic seawater, this could explain the Ba depletion relative to UCC in interval B1 and interval K2. Alternatively, the depletion of Ba in TCDP1 may be directly related to low detrital input as Ba concentrations appear to be strongly correlated with Al_2O_3 (wt.%) concentrations.

A Mo_{EF} vs U_{EF} plot (Figure 3.22) provides further insight into the benthic redox conditions under which Mn enrichments B1 and K2 were deposited (Algeo Tribovillard, 2009). This proxy relies on the fact that concentrations of both Mo and U in UCC are comparable (3.7 ppm and 2.7 ppm, respectively; Taylor and McLennan, 1985) and both behave conservatively under oxic conditions, resulting in their relatively long residence times in modern seawater (~780 kyr and ~450 kyr, respectively). Although concentrations of both elements are likely to have been lower in less oxic Precambrian seawater, their relative input as a result of increased oxidative weathering as O_2 levels progressively increased throughout the Precambrian should have remained similar.

In marine systems with suboxic bottomwaters, U concentrations in sediments should exceed Mo as oxidizing conditions promote U(VI) stability, which typically forms soluble compounds. Uranium subsequently concentrates at the Fe(II)-Fe(III) redox boundary in the water column (Zheng et al., 2002a,b), given that similar Eh-pH conditions result in the reduction of U(VI) to insoluble U(IV) compounds. This results in low Mo/U ratios. Under reducing conditions approaching euxinia, Mo accumulation in the sediments begins to outpace U due to the formation of particle reactive thiomolybdates (which requires H_2S; Helz et al., 1996; Zheng et al., 2000), resulting in higher Mo/U ratios.

Although Mo enrichment in sediments can also occur through Mn and Fe-oxyhydroxide particle shuttles, this process was likely not significant in the Paleoproterozoic given the shallow depth of the anoxic-oxic chemocline at this time. Any molybdate or thiomolybdate adsorbed to precipitating particles would have likely been re-released during reductive dissolution as Mn or Fe-oxyhydroxides fell through a largely reducing water column. This process has been documented to occur in the modern Black Sea and Framvaren Fjord (Jacobs et al., 1985; Skei et al., 1996; Crusius et al., 1996). The only exception may have been in shallower environments where Mo "shuttling" could have occurred if the anoxic-oxic chemocline was positioned much closer to the sediment water interface. In this case, vertical movement of the chemocline may create a "Mo Pump" such as that observed in the modern Cariaco Basin and Saanich Inlet (Algeo and Lyons, 2006); Mo is scavenged from the water column when Mn and Fe-oxyhydroxides precipitate as the chemocline drops to the sediment water interface, and Mo is released when the chemocline rises and previously formed Mn and Fe-oxyhydroxides are exposed to sulfidic bottom waters which induce reductive dissolution.

On the Mo_{EF} vs U_{EF} plot (Figure 3.22) B1, K2, and Kazput carbonate samples fall along trendlines that are enriched in Mo relative to U compared to the modern seawater trend. This suggests that either conditions in all three cases were more reducing than modern seawater, or that Mn and Fe oxyhydroxide particles acted as Mo shuttles which promoted Mo enrichments relative to U (Algeo and Lyons, 2006; Algeo and Tribovillard, 2009). Notably, the slopes of the three datasets are shifted relative to one another depending on their relative Mo and U enrichment factors. Enrichment factors were calculated as $(X/Al)_{sample}/(X/Al)_{PAAS}$, where X represents the weight concentrations of either Mo or U. B1 samples are located closest to the upper right corner of the plot as a result of the larger Mo and U enrichments in these samples. If Mo and U

enrichments reflect their availability in the water column during deposition, this would suggest B1 samples may have been deposited under slightly more oxidizing conditions compared to Kazput samples. This may also fit with the presence of a negative Ce anomaly in the Boolgeeda IF (Warchola et al., 2018) and a lack of one within carbonates of the Kazput Formation.

Notably, Mo concentrations throughout the TCDP cores are generally low compared to modern Mn enriched sediments. This may be the result of: (1) prolonged euxinia in a restricted basin leading to extensive depletion of Mo in the water column (such as that observed in the Black Sea; Algeo and Lyons, 2006), (2) the reductive dissolution of phases carrying Mo to the sediments (such as Mn- and Fe-oxides), subsequently releasing Mo back to the water column during diagenesis and preventing Mo from being captured in the sediments, or (3) low Mo input from land. An argument against sulfidic conditions in a restricted basin lies in the slope of the Mo_{EF} vs U_{EF} plots; restriction in the Black Sea prevents replenishment of the dissolved Mo pool, resulting in Mo depletion in the water column and a gentler slope of the Mo_{EF} vs U_{EF} trend (Algeo and Lyons, 2006). As mentioned above, all Mo_{EF} vs U_{EF} slopes for TCDP sediments are greater than that of seawater, which argues against restriction. To determine whether Fe- or Mn-oxides acted as shuttles for Mo to the sediment, it is useful to look at Mo isotopic signatures of the TCDP Mn enrichments.

3.4 Environmental context provided by stable isotopes

Molybdenum isotopes are a useful proxy for the redox state of seawater (i.e. Siebert et al., 2003). Modern oxic seawater is enriched in heavy Mo isotopes (modern $\delta^{98}Mo_{SW}$=2.36‰, Siebert et al. 2003) as a result of the removal of light Mo isotopes by sorption to Mn- and Fe-oxides (Barling et al., 2001; Siebert et al., 2003). Sorption to Mn- oxides results in a change in MoO_4^{2-} structure from

tetrahedral to octahedral, which leads to Mo isotopic fractionation (Kashiwabara et al., 2011). Oxidative Mn precipitation requires that atmospheric O_2 levels be higher than $\sim 10^{-2}$ times the present atmospheric level (PAL) assuming solution equilibrium between the atmosphere and oceans. Thus, Mo isotope fraction has been used to track periods in Earth history when marine redox levels breached the threshold for Mn oxide precipitation (e.g. Planavsky et al., 2014; Planavsky et al., 2018). The fact that Mo isotopic signatures are preserved throughout diagenesis or secondary reduction (e.g. Poulson et al., 2009) make them particularly useful for identifying sediments which contained primary Mn oxides, given that the fate of nearly all sedimentary Mn oxides is to be rapidly reduced during early diagenesis (Aller, 1980; Johnson et al., 2013). Thus, Mo isotopic signatures in interval B1 and K2 may confirm or refute conclusions drawn from mineralogical, textural, and major and trace element data.

The δ^{98}Mo signature for the upper crust is estimated to be 0.1‰ and have a Mo concentration of 1.1 ppm (Siebert et al., 2003; Rudnick and Gao, 2003). Seawater δ^{98}Mo signatures are typically measured in carbonates. Notably, carbonate signatures trend towards the composition of the continental crust if there is significant detrital "contamination" in the sample (Voegelin et al., 2009; Thoby et al., in prep). Black shales have also been used to record the δ^{98}Mo signature of seawater, but these records are only accurate if the water column was euxinic (specifically, >11 μM of H_2S) at the time of deposition (Helz et al., 1996). TCDP1 and TCDP3 sediments represent neither pure carbonate sediments nor euxinic black shales; specifically, Ca is $\leq$ 33 wt.% and TOC values are below 0.1 wt.%. Thus, they are not particularly well-adapted samples for capturing global authigenic Mo isotope signatures derived from contemporary seawater. However, these samples are still capable of preserving large Mo isotope fractions indicative of primary Mn-oxides and can help determine whether or not primary Mn-oxides were locally present in the sediment.

The relatively heavy maximum δ^{98}Mo value detected in enrichment B1 (1.36‰) places a minimum constraint on the isotopic composition of seawater and reveals that oxic sinks were important, but muted relative to today, for the global marine Mo cycle at the time of B1 deposition. In fact, if a detrital correction is applied to enrichment B1 (as per Voegelin et al., 2009), the δ^{98}Mo signature approaches 2.47‰. This signature suggests that seawater was at the very least partially oxygenated during deposition of interval B1. However, δ^{98}Mo and Mn concentrations are positively correlated; this is opposite to the trend observed by Planavsky et al. (2014), in which primary Mn oxides were invoked. Thus, Mo isotope data suggests that although oxic conditions were present in the basin at the time of deposition, Mn-oxides did not directly play a role in Mn enrichments in TCDP1. If primary Mn oxides were the source of carbonates that presently host Mn enrichment, the negative δ^{98}Mo values from Mn-oxide rich sediments should have been preserved through reduction and diagenesis (e.g. Poulson et al., 2009).

The lack of negative molybdenum isotope signatures within Mn enrichment K2 similarly argues against the presence of primary Mn-oxides. Intriguingly, δ^{98}Mo values are stable around 0.5‰ across enrichment K2 and into the overlying Kazput Carbonate. Increase Al_2O_3 (wt.%) concentrations also appear to push δ^{98}Mo values towards 0.5‰. The high Al content of K2 samples may suggest the δ^{98}Mo signatures are dominated by a detrital signal. In this case, it may be impossible to tell whether the Mn enrichments were influenced by primary Mn-oxides.

The stability of δ^{98}Mo signatures in K2 may be further influence by low Mo concentrations, which range between 0.01 to 10 ppm throughout the TCDP Mn enrichments. Conversely, Mo is the most abundant trace element in modern seawater and displays a long residence time as a result of its occurrence as the unreactive molybdate anion (MoO_4^{2-}). It is generally assumed that Mo has a long residence time throughout geologic history, making Mo isotope fractionation a good proxy

for global redox conditions. However, with little oxidative weathering of continental sulfides (low Mo source) and a large reduced Mn(II) pool in seawater with the potential to be oxidized by rising O_2 levels (large Mo sink), Mo may have been "consumed" quickly if precipitation of Fe- and Mn-oxides outpaced Mo supply from the continents. Further, oxidation of reduced sulfides would have promoted local euxinic settings resulting in another large Mo sink. If Mo concentrations and residence time remained low, it is possible that Mo was quantitatively scrubbed from the oceans, and the signature we would expect to preserve in marine sediments should be identical to the signature of the input material. Hence, this may explain why the Mo isotope signature in both the Kazput shales and carbonates are fairly similar even though we see relatively large changes in Mo and Mn concentration across the lithologies (Figure 3.1). Essentially, Mo isotope fractionations are muted as they are "buffered" by low Mo concentrations. Thus, although Mo isotopes argue against primary Mn oxides in intervals B1 and K2 this record should be interpreted cautiously.

4. Summary and Conclusion

Like the abundance of Mn in the Transvaal Supergroup Iron Formations (Beukes, 1983; Holland and Beukes, 1990), there appears to be an upward increase in the abundance of Mn in the Mount Bruce Supergroup Iron Formations and overlying Turee Creek Group. Extensive analysis has shown the Mn enrichments in TCDP cores are hosted in carbonates. These carbonates range in composition between manganese rich dolomite [$CaMg(CO_3)_2$], ankerite [$Ca(Fe[II],Mg)(CO_3)_2$], and kutnohorite [$Ca(Mn[II])(CO_3)_2$]. Molybdenum isotopes collected in a companion study (Thoby et al., in prep) suggest these Mn enrichments are not the result of diagenetically altered primary Mn-oxides. Further, Mo isotopes suggest oxic conditions may have been present during deposition of Boolgeeda Mn enrichment but not Kazput Mn enrichments. This supports the

account of a negative Ce anomaly in the Boolgeeda IF (Warchola et al., 2018), and the lack of a negative Ce anomaly in the Kazput sediments. However, Mo isotopic signatures are interpreted under the assumption that Mo has a relatively long residence time in seawater. During the initial stages of the GOE, rapid precipitation of Mn and Fe oxyhydroxides along with the development of localized euxinic sinks may have drastically limited the concentration of Mo in seawater. It is possible that during such conditions, Mo could be quickly and quantitatively removed from seawater, thus pushing the preserved Mo isotopic signature towards that of the initial input (presumably a combination of detrital and hydrothermal sources). Thus Mo, signatures alone cannot rule out the possibility that primary Mn oxides were in fact the source of Mn enrichments in the TCDP cores. As mentioned above, Kutnohorite was identified in XRD spectra of enrichment K2. Johnson et al. (2016) suggested Kutnohorite in the Koegas Subgroup was the direct product of reductive alteration of primary Mn oxides. Given that they also noted similar weathering textures in the Kungarra Formation, it is possible that the same sequence of diagenesis occurred in the TCDP cores and enrichment K2 was in fact sourced from primary Mn oxides. This may be supported by the higher concentrations of trace elements contained within the K2 interval.

7. References (Chapter 3)

Algeo, T.J., Lyons, T.W., 2006. Mo-total organic carbon covariation in modern anoxic marine environments: implication for analysis of paleoredox and paleohydrographic conditions. Paleoceanography 21, PA1016.

Algeo, T.J., Tribovillard, N., 2009. Environmental analysis of paleoceanographic systems based on molybdenum-uranium covariation. Chemical Geology 268, 211-225.

Aller, R.C., Diagenetic processes near the sediment-water interface of long island sound. II. Fe and Mn. Advances in Geophysics 22, 351-415.

Asael, D., Tissot, F.L.H., Reinhard, C.T., Rouxel, O., Dauphas, N., Lyons, T.W., Ponzevera, E., Liorzou, C., Chéron, S., 2013. Coupled molybdenum, iron and uranium stable isootpes as oceanic paleoredox proxies during the Paleoproterozoic Shunga Event. Chemical Geology 362, 193-210.

Barling, J., Arnold, G.L., Anbar, A.D., 2001. Natural mass-dependent variations in the isotopic composition of molybdenum. Earth and planetary Science Letters 193, 447-457.

Bau, M., Romer, R. L., Lüders, V., Beukes, N. J., 1999. Pb, O, and C isotopes in silicified Mooidraai dolomite (Transvaal Supergroup, South Africa): implications for the composition of Paleoproterozoic seawater and 'dating' the increase of oxygen in the Precambrian atmosphere. Earth and Planetary Science Letters 174, 43–57

Beukes, N.J., 1983. Palaeoenvironmental setting of iron-formations in the depositional basin of the Transvaal Supergroup, South Africa. In: Trendall AF, Morris RC (Eds), Iron-Formation: Facts and Problems. Elsevier, Amsterdam, pp. 131-209.

Bloemsma, M.R., 2015. Development of a Modelling Framework for Core Data Integration using XRF Scanning. University of Leuven PhD Thesis Dissertation.

Brewer, P.G., Spencer, D.W., 1974. Distribution of some trace elements in the Black Sea and their flux between dissolved and particulate phases. American Association of Petroleum Geologists Bulletin Memoir 20, 137-143.

Calvert, S.E., Pedersen, T.F., 1996. Sedimentary geochemistry of manganese; implications for the environment of formation of manganiferous black shales. Economic Geology 91, 36-47.

Caquineau, T., Paquette, J.-L., Philippot, P., 2018. U-Pb detrital zircon geochronology of the Turee Creek Group, Hamersley Basin, Western Australia: Timing and correlation of the Paleoproterozoic glaciations. Precambrian Research 307, 34–50.

Chandler, F.W., 1980. Proterozoic redbed sequences of Canada. Canadian Geological Survey Bulletin 311.

Clement, B.G., Luther III, G.W., Tebo, B.M., 2009. Rapid, oxygen-dependent microbial Mn(II) oxidation kinetics at sub-micromolar oxygen concentrations in the Black Sea suboxic zone. Geochimica et Cosmochimica Acta 73, 1878-1889.

Chen, J.H., Edwards, R.L., Wasserburg, G.J., 1986. ^{238}U, ^{234}U and ^{232}Th in seawater. Earth and Planetary Science Letters 80, 241-251.

Crowe, S.A., Døssing, L., Beukes, N.J., Bau, M., Kruger, S.J., Frei, R., Canfield, D.E., 2013. Atmospheric oxygenation three billion years ago. Nature 501, 535-538.

Crusius, J., Calvert, S., Pedersen, T., Sage, D., 1996. Rhenium and molybdenum enrichments in sediments as indicators of oxic, suboxic, and sulfidic conditions of deposition. Earth and Planetary Science Letters 145, 65-78.

Cullen, W.R., Reimer, K.J., 1989. Arsenic speciation in the environment. Chemical Reviews 89, 713-764.

Eigenbrode, J.L., Freeman, K.H., 2006. Late Archean rise of aerobic microbial ecosystems. Proceedings of the National Academy of Sciences of the United States of America 103, 15759-15764.

England, G.L., Rasmussen, B., Krapez, B., Groves, D.I., 2002. Paleoenvironmental significance of rounded pyrite in siliciclastic sequences oft he Late Archean Witwatersrand Basin: oxygen-deficient atmosphere or hydrothermal alteration? Sedimentology 49, 1133-1156.

Farquhar, J., Bao, H.M., Thiemens, M., 2000. Atmospheric influence of Earth's earliest sulfur cycle. Science 289, 756-758.

Force, E.R., Maynard, J.B., 1991. Manganese: Syngenetic deposits on the margins of anoxic basins. Reviews in Economic Geology 5, 147–159.

Fru, E.C., Arvestål, E., Callac, N., Albani, A.E., Kilias, S., Argyraki, A., Jakobsson, M., 2015. Arsenic stress after the Proterozoic glaciations. Scientific Reports 5, 17789.

Godfrey, L.V., Falkowski, P.G., 2009. The cycling and redox state of nitrogen in the Archaean ocean. Nature Geoscience 2, 725-729.

Goldberg, E.D., 1954. Marine geochemistry. I. Chemical scavengers of the sea. Journal of Geology 62, 249-265.

Grandstaff, D.E., 1980. Origin of uraniferous conglomerates at Elliot Lake, Canada and Witwatersrand, South Africa: Implications for oxygen in the Precambrian atmosphere. Precambrian Research 13, 1-26.

Grotzinger, J.P., Kasting, J.F., 1993. New constraints on Precambrian ocean composition. Journal of Geology 101, 235-243.

Gumsley, A.P., Chamberlain, K.R., Bleeker, W., Söderlund, U., de Kock, M.O., Larsson, E.R., Bekker, A., 2017. Timing and tempo of the Great Oxidation Event. Proceedings of the National Academy of Sciences of the United States of America 114, 1811-1816.

Gutzmer J., Beukes, N.J., 1996. Mineral paragenesis oft he Kalahari manganese field, South Africa. Ore Geology Reviews 11, 405-428.

Hansel, C.M., Learman, D.R., 2016. Chapter 18: Geobiology of Manganese. In: Ehrlich HL, Newman DK, Kappler A (Eds.) Ehrlich's Geomicrobiology Sixth Edition. Boca Raton: CRC Press, Taylor & Francis Group.

Haugaard, R., Pecoits, E., Lalonde, S., Rouxel, O., Konhauser, K.O., 2016. The Joffre Banded Iron Formation, Hamersley Gorup, Western Australia: Assessing the palaeoenvironment through detailed petrology and chemostratigraphy. Precambrian Research 273, 12-37.

Helz, G.R., Miller, C.V., Charnock, J.M., Mosselmans, J.F.W., Pattrick, R.A.D., Garner, C.D., Vaughan, D.J., 1996. Mechanisms of molybdenum removal from the sea and its concentration in black shales: EXAFS evidence. Geochimica et Cosmochimica Act 60, 3631-3642.

Hofmann, A., Bekker, A., Rouxel, O.J., Rumble, D., Master, S., 2009. Multiple sulphur and iron isotope composition of detrital pyrite in Archaean sedimentary rocks: a new tool for provenance analysis. Earth and Planetary Science Letters 286, 436-445.

Holland, D.H., Beukes, N.J., 1990. A paleoweathering profile from Griqualand West, South Africa: evidence for a dramatic rise in atmospheric oxygen between 2.2 and 1.9 BYBP. American Journal of Science 290-A, 1-34.

Holland, D.H., 2005. 100th Anniversary Special Paper: Sedimentary Mineral Deposits and Evolution of Earth's Near-Surface Environments. Economic Geology 100, 1489-1509.

Holland, D.H., 2006. The oxygenation of the atmosphere and oceans. Philosophical Transactions of the Royal Society B 361, 903-915.

Jacobs, L., Emerson, S., Skei, J., 1985. Partitioning and transport of metals across the O_2/H_2S interface in a permanently anoxic basin: Framvaren Fjord Norway. Geochimica et Cosmochimica Acta 49, 1433-1444.

Jenne, E.A., 1968. Controls on Mn, Co, Ni, Cu, and Zn concentrations in soil and water: The significant role of hydrous Mn and Fe oxides. In: Gould RF (Ed.), Trace Inorganics in Water. Washinton, DC: American Chemical Society, pp. 337-387.

Johnson, J.E., Webb, S.M., Thomas, K., Ono, S., Kirschvink, J.L., Fischer, W.W., 2013. Manganese-oxidizing photosynthesis before the rise of cyanobacteria. Proceedings of the National Academy of Sciences of the United States of America 110, 11238-11243.

Johnson, J.E., Webb, S.M., Ma, C., Fischer, W.W., 2016. Manganese mineralogy and diagenesis in the sedimentary rock record. Geochimica et Cosmoschimica Acta 173, 210-231.

Kashiwabara, T., Takahashi, Y., Tanimizu, M., Usui, A., 2011. Molecular-scale mechanisms of distribuition and isotopic fractionation of molybdenum between seawater and ferromanganese oxides. Geochimica et Cosmochimica Acta 75, 5762-5784.

Kay, J.T., Conklin, M.H., Fuller, C.C., O'Day, P.A., 2001. Processes of nickel and cobalt uptake by a manganese oxide forming sediment in Pinal Creek, globe mining district, Arizona. Environmental Science and Technology 35, 4719-4725.

Kirkham, R.V., Roscoe, S.M., 1993. Atmospheric evolution and ore deposit formation. Resource Geology Special Issue 15, 1-17.

Kopp, R.E., Kirschvink, J.L., Hilburn, I.A., Nash, C.Z., 2005. The Paleoproterozoic snowball Earth: A climate disaster triggered by the evolution of oxygenic photosynthesis. Proceedings of the National Academy of Sciences of the United States of America 102, 11131-11136.

Loganathan, P., Burau, R.G., 1973. Sorption of heavy metals by hydrous manganes oxides. Geochemica et Cosmochimica Acta 37, 1277-1293.

MacGregor, A.M., 1927. The problem of the Precambrian atmosphere. South African Journal of Science 24, 155-172.

Martin, D.M., Li, Z.X., Nemchin, A.A. Powell, C.M., 1998. A pre-2.2 Ga age for giant hematite ores of the Hamersley Province, Australia? Economic Geology 93, 1084–1090.

Matocha, C.J., Elzinga, E.J., Sparks, D.L., 2001. Reactivity of Pb(II) at the Mn(III,IV) (oxyhydr)oxide-water intervace. Environment Science and Technology 35, 2967-2972.

Maynard, J.B., 2010. The chemistry of manganese ores through time: a signal of increasing diversity of Earth-surface environments. Economic Geology 105, 535-552.

Melezhik, V.A., Fallick, A., Hanski, E.J., Kump, L.R., Lepland, A., Prave, A.R., Strauss, H., 2005. Emergence of the aerobic biosphere during the Archean-Proterozoic transition: challenges of future research. GSA Today 15, 4-11.

Millero, F.J., 1996. Chemical Oceanography. CRC Press, Boca Raton, Florida. 469 pp.

Morris, A.W., 1975. Dissolved molybdenum and vanadium in the northeast Atlantic Ocean. Deep-Sea Research 22, 49-54.

Müller, S.G., Krapez, B., Barley, M.E., Fletcher, I. R., 2005. Giant iron-ore deposits of the Hamersley province related to the breakup of Paleoproterozoic Australia: New insights from in situ SHRIMP dating of baddeleyite from mafic intrusions. Geology 33, 577–5.

Nel, C.J., Beukes, N.J., De Villiers, J.P.R., 1986. The Mamatwan manganese mine of the Kalahari Manganese Field. In: Anhaeusser CR and Maske S (Eds.), Mineral deposits of Southern Africa. Geological Society of South Africa, pp. 963-978.

Nel, B.P., 2013. Petrography and Geochemistry of Iron Formation of the Paleoproterozoic Koegas Subgroup, Transvaal Supergroup, Griqualand West, South Africa. University of Johannesburg Master of Science Thesis Dissertation.

Nelson, Y.M., Lion, L.W., Shuler, M.L., Ghiorse, W.C., 1999a. Lead binding to metal oxide and organic phases of natural aquatic biofilms. Limnology and Oceanography 44, 1715-1729.

Nelson, Y.M., Lion, L.W., Ghiorse, W.C., Shuler, M.L., 1999b. Production of biogenic Mn oxides by Leptothix discophora SS-1 in a chemically defiend growth medium and evaluation of their Pb adsorption characteristics. Applied Environmental Microbiology 65, 175-180.

O'Reilly, S.E., Hochella, M.F., 2003. Lead sorption efficiencies of natural and synthetic Mn and Fe-oxides. Geochimica et Cosmochimica Acta 67, 4471-4487.

Pecoits, E., Gingras, M.K., Barley, M.E., Kappler, A., Posth, N., Konhauser, K.O., 2009. Petrography and geochemistry of the Dales Gorge banded iron formation: Paragenetic sequence, source and implications for palaeo-ocean chemistry. Precambrian Research 172, 163–187.

Pecoits, E., Smith, M.L., Catling, D.C., Philippot, P., Kappler, A., Konhauser, K.O., 2015. Atmospheric hydrogen peroxide and Eoarchean iron formations. Geobiology 13, 1-14.

Peña, J., Kwon, K.D., Refson, K., Bargar, J.R., Sposito, G., 2010. Mechanisms of nickel sorption by a bacteriogenic birnessite. Geochimica et Cosmochimica Acta 74, 3076-3089.

Philippot, P., Ávila, J.N., Killingsworth, B.A., Tessalina, S., Baton, F., Caquineau, T., Muller, E., Pecoits, E., Cartigny, P., Lalonde, S.V., Ireland, T.R., Thomazo, C., van Kranendonk, M.J., Busigny, V., 2018. Globally asynchronous Sulphur isotope signals require re-definition of the Great Oxidation Event. Nature Communications 9, 2245.

Pickard, A.L., 2003. SHRIMP U-Pb zircon ages for the Palaeoproterozoic Kuruman Iron formation, Northern Cape Province, South Africa: Evidence for simultaneous BIF deposition on Kaapvaal and Pilbara Cratons. Precambrian Research 125, 275-315.

Planavsky, N.J., Asael, D., Hofmann, A., Reinhard, C.T., Lalonde, S.V., Knudsen, A., Wang, X., Ossa Ossa, F., Pecoits, E., Smith, A.J.B., Beukes, N.J., Bekker, A., Johnson, T.M., Konhauser, K.O., Lyons, T.W., Rouxel, O.J., 2014. Evidence for oxygenic photosynthesis half a billion years before the Great Oxidation Event. Nature Geoscience 7, 283-286.

Planavsky, N.J., Slack, J.F., Cannon, W.F., O'Connell, B., Isson, T.T., Asael, D., Jackson, J.C., Hardisty, D.S., Lyons, T.W., Bekker, A., 2018. Evidence for episodic oxygenation in a weakly redox-buffered deep mid-Proterozoic ocean. Chemical Geology 483, 581-594.

Pope, M.C., Grotzinger, J.P., 2003, Paleoproterozoic stark formation, Athapuscow Basin, Northwest Canada: a record of cratonic-scale salinity crisis. Journal of Sedimentary Research 73, 280-295.

Poulson, R.L.B., McManus, J., Severmann, S., Berelson, W.M., 2009. Molybdenum behavior during early diagenesis: Insights from Mo isotopes. Geochemistry, Geophysics, Geosystems 10, Q06010.

Poulton, S.W., Canfield, D.E., 2005. Development of a sequential extraction procedure for iron: implications for iron partitioning in continentally derived particulates. Chemical Geology 214, 209-221.

Rasmussen, B., Buick, R., 1999. Redox state of the Archean atmosphere: evidence from detrital heavy minerals in ca. 3250-2750 Ma sandstones from the Pilbara Craton, Australia. Geology 27, 115-118.

Reinhard, C.T., Planavsky, N.J., Lyons, T.W., 2013. Long-term sedimentary recycling of rare Sulphur isotope anomalies. Nature 497, 100-103.

Roscoe, S.M., 1996. Paleoplacer uranium gold. In: Eckstrand, O.R., Sinclair, W.D., Thorpe, R.I. (eds) Geology of Canadian mineral deposit types, vol P-1. Geological Society of America, The Geology of Norther America, Boulder, pp 10-23.

Roy, S., 1992. Environments and processes of manganese deposition. Economic Geology 87, 1218-1236.

Rudnick, R.L., Gao, S., 2003. Composition of the continental crust. Treatise on Geochemistry 3, 1-64.

Rye, R., Holland, H.D., 1998. Paleosols and the evolution of atmospheric oxygen: a critical review. American Journal of Science 198, 621-672.

Satkowski, A.M., Beukes, N.J., Li, W., Beard, B.L., Johnson, C.M., 2015. A redox-stratified ocean 3.2 billion years ago. Earth and Planetary Science Letters 430, 43-53.

Schissel, D., Aro, P., 1992. The major early Proterozoic sedimentary iron and manganese deposits and their tectonic setting. Economic Geology 87, 1367-1374.

Schröder, S., Bekker, A., Beukes, N.J., Strauss, H., van Niekerk, H.S., 2008. Rise in seawater sulphate concentration associated with the Paleoproterozoic positive carbon isotope excursion: evidence from sulphate evaporites in the 2.2-2.1 Gyr shallow-marine Lucknow Formation, South Africa. Terra Nova 20, 108-117.

Schröder, S., Bedorf, D., Beukes, N.J., Gutzmer, J., 2011. From BIF to red beds: Sedimentology and sequence stratigraphy oft he Paleoproterozoic Koegas Subgroup (South Africa). Sedimentary Geology 236, 25-44.

Shih, P.M., Hemp, J., Ward, L.M., Matzke, N.J., Fischer, W.W., 2017. Crown group Oxyphotobacteria postdate the rise of oxygen. Geobiology 15, 19-29.

Siebert, C., Nägler, T.F., Kramers, J.D., 2001. Determination of molybdenum isotope fractionation by double-spike multicollector inductively coupled plasma mass spectrometry. Geochemistry, Geophysics, Geosystems 2, 2000GC000124.

Siebert, C., Nägler, T.F., von Blanckenburg, F., Kramers, J.D., 2003. Molybdenum isotope records as a potential new proxy for paleoceanography. Earth and Planetary Science Letters 211, 159-171.

Skei, J., Loring, D.H., Rantala, R.T.T., 1996. Trace metals in suspended particulate matter and in sediment trap material from a permanently anoxic fjord-Framvaren, south Norway. Aquatic Geochemistry 2, 131-147.

Smedley, P.L., Kinniburgh, D.G., 2002. A review of the source, behaviour and distribution of arsenic in natural waters. Applied Geochemistry 17, 517-568.

Soo, R.M., Hemp, J., Parks, D.H., Fischer, W.W., Hugenholtz, P., 2017. On the origins of oxygenic photosynthesis and aerobic respiration in Cyanobacteria. Science 355, 1436-1440.

Summons, R.E., Jahnke, L.L., Hope, J.M., Logan, G.A., 1999. 2-Methylhopanoids as biomarkers for cyanobacterial oxygenic photosynthesis. Nature 400, 554-557.

Takahashi, Y., Manceau, A., Geoffroy, N., Marcus, M.A., Usui, A., 2007. Chemical and structural control of the partitioning of Co, Ce, and Pb in marine ferromanganese oxides. Geochemica et Cosmochimica Acta 71, 984-1008.

Taylor, S.R., McLennan, S.M., 1985. The continental crust: its composition and evolution. Blackwell Scientific Publication, Oxford.

Thoby, M., Warchola, T., Killingsworth, B., Alam, Md.S., Alessi, D.A., Thomazo, C., Ader, M., Philippot, P., Konhauser, K.O., Lalonde, S.V., in prep. Decoupling Sedimentary Mn enrichments from surface processes.

Thomazo, C., Ader, M., Philippot, P., 2011. Extreme 15N-enrichments in 2.72-Gyr-old sediments: evidence for a turning point in the nitrogen cycle. Geobiology 9, 107-120.

Toner, B., Manceau, A., Webb, S.M., Sposito, G., 2006. Zinc sorption to biogenic hexagonal-birnessite particles within a hydrated bacterial biofilm. Geochimica et Cosmochimica Acta 70, 27-43.

Tsikos, H., Moore, J.M., 1997. Petrography and Geochemistry of the Paleoproterozoic Hotazel Iron-Formation, Kalahari Manganese Field, South Africa: Implications for Precambrian Manganese Metallogenesis. Economic Geology 92, 87-97.

Tsikos, H., Beukes, N.J., Moore, J.M., Harris, C., 2003. Deposition, Diagenesis, and Secondary Enrichment of Metals in the Paleoproterozoic Hotazel Iron Formation, Kalahari Manganese Field, South Africa. Economic Geology 98, 1449–1462.

Van Kranendonk, M.J., Mazumder, R., Yamaguchi, K.E., Yamada, K., Ikehara, M., 2015. Seidmentology of the Paleoproterozoic Kungarra Formation, Turee Creek Group, Western Australia: A conformable record of the transition from early to modern Earth. Precambrian Research 256, 314-343.

Voegelin, A.R., Nägler, T.F., Samankassou, E., Villa, I.M., 2009. Molybdenum isotopic compoisiton of modern and Carboniferous carbonates. Chemical Geology 265, 488-498.

Weltje, G.J., Tjallingii, R., 2008. Calibration of XRF core scanners for quantitative geochemical logging of sediment cores: Theory and application. 274, 423–438.

Weltje, G.J., Bloemsma, M.R., Tjallingii, R., Heslop, D., Röhl, U., Croudace, I.W., 2015. Chapter 21: Prediction of Geochemical Composition from XRF Core Scanner Data: A New Multivariate Approach Including Automatic Selection of Calibration Samples and

Quantification of Uncertainties. In: Croudace IW, Rothwell R.G. (Eds), Micro-XRF Studies of Sediment cores: Applications of a non-destructive tool. Springer Netherlands, pp. 656.

Warchola, T., Lalonde, S.V., Pecoits, E., von Gunten, K., Robbins, L.J., Alessi, D.S., Philippot, P., Konhauser, K.O., 2018. Petrology and Geochemistry of the Boolgeeda Iron Formation, Hamersley Basin, Western Australia. Precambrian Research 316, 155-173.

Wood, J., 1973. Stratigraphy and depositional environments of upper Huronian rocks of the Rawhide Law-Flack Lake area, Ontario. In: Young GM (ed) Huronian Stratigraphy and Sedimentation, vol 12. Geological Association of Canada Special Paper, Geological Assocation of Canada, pp 73-95.

Zheng, Y., Anderson, R.F., van Green, A., Kuwabara, J., 2000. Authigenic molybdenum formation in marine sediments: a link to pore water sulfide in the Santa Barbara Basin. Geochimica et Cosmochimica Acta 64, 4165-4178.

Zheng, Y., Anderson, R.F., van Geen, A., Fleischer, M.Q., 2002a. Preservation of non-lithogenic particulate uranium in marine sediments. Geochimica et Cosmochimica Acta 66, 3085-3092.

Zheng, Y., Anderson, R.F., van Geen, A., Fleischer, M.Q., 2002b. Remobilization of authigenic uranium in marine sediments by bioturbation. Geochimica et Cosmochimica Acta 66, 1759-1772.

8. Figures (Chapter 3)
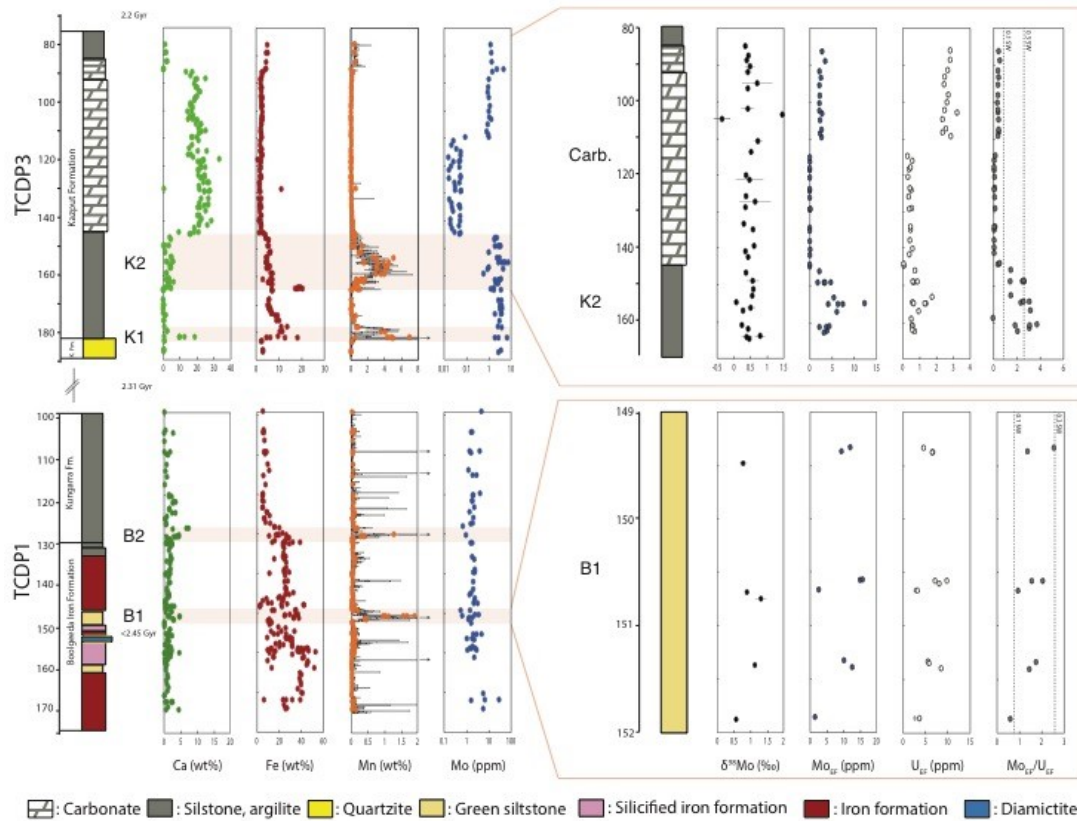
Figure 3.1. Litholog and depth profiles for geochemical variations occurring through cores TCDP1 and TCDP2. It should be noted that carbon and molybdenum isotope data were not collected in this thesis, but were produced in companion studies conducted on the same core. They are referred to here to provide further context for textural observations. A version of this figure will also be included in a forthcoming publication (Thoby et al., in prep).
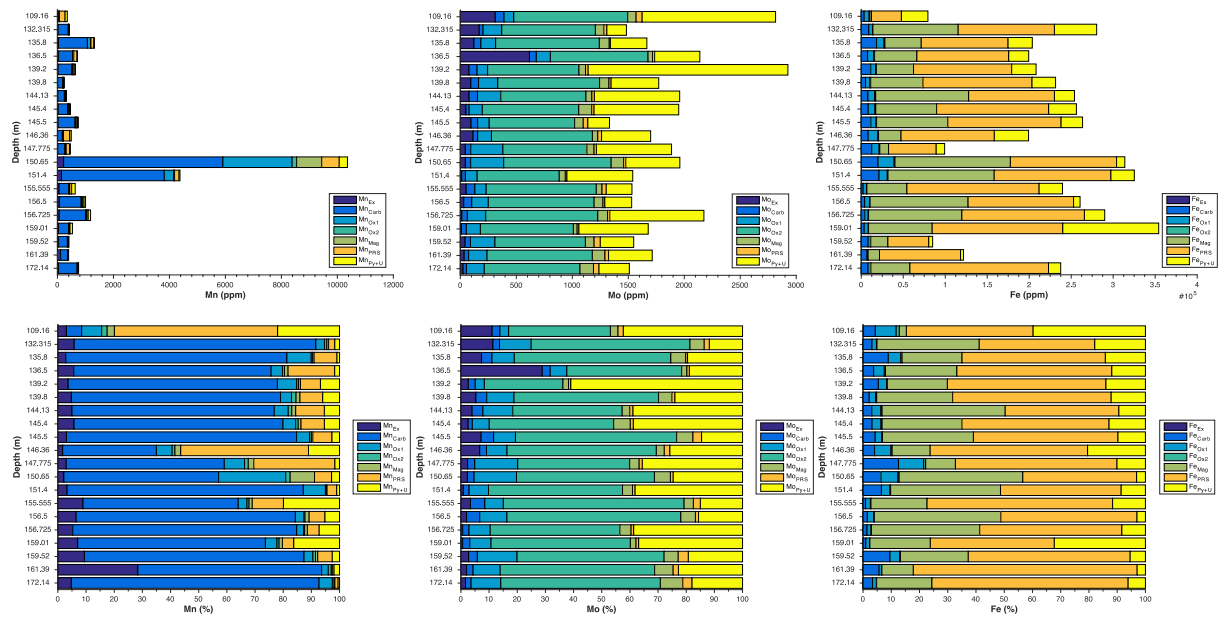
Figure 3.2. Proportion of Mn, Mo, and Fe contained within different sequential extraction fractions. The procedure used for sequential extraction is described by Poulton and Canfield (2005). Note that Mn within the Boolgeeda IF is dominantly found in the carbonate fraction.
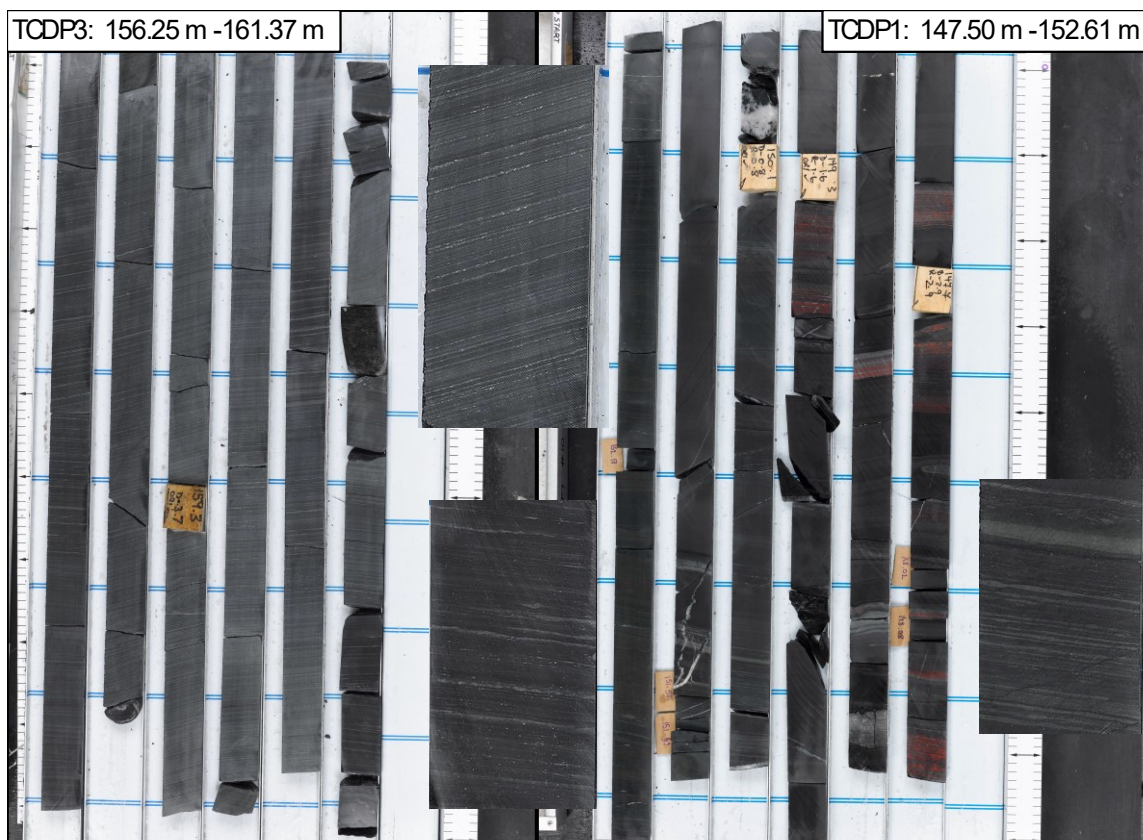
Figure 3.3. Comparison of manganese enriched core segments in TCDP1 and TCDP3.
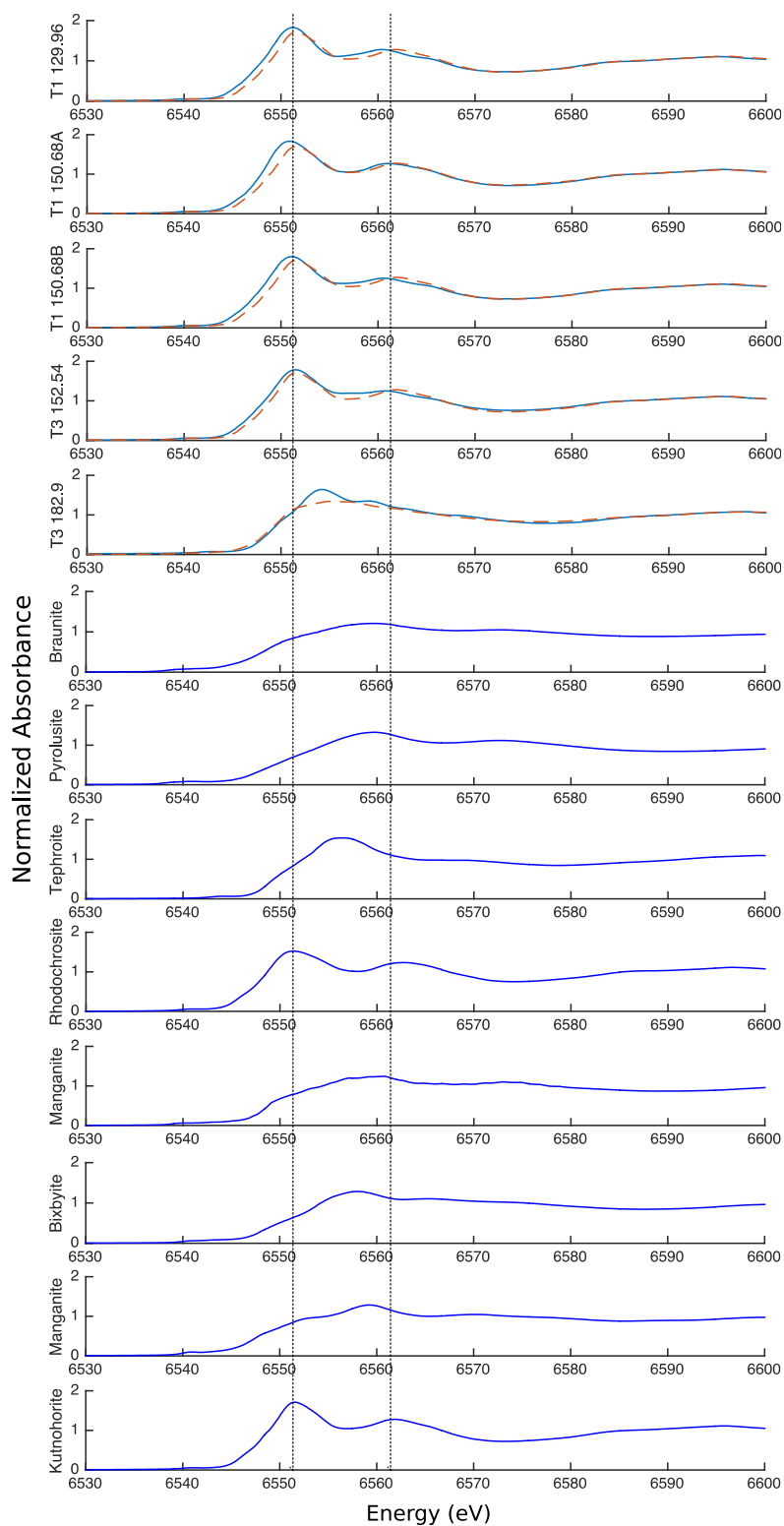
Figure 3.4. Manganese K-edge XANES spectra of selected Mn reference compounds and samples. Solid blue lines represent experimental data and dashed orange lines represent the fit. See tables 1 and 2 to view a summary of Mn speciation for each sample as determined by linear combination fitting of standards.
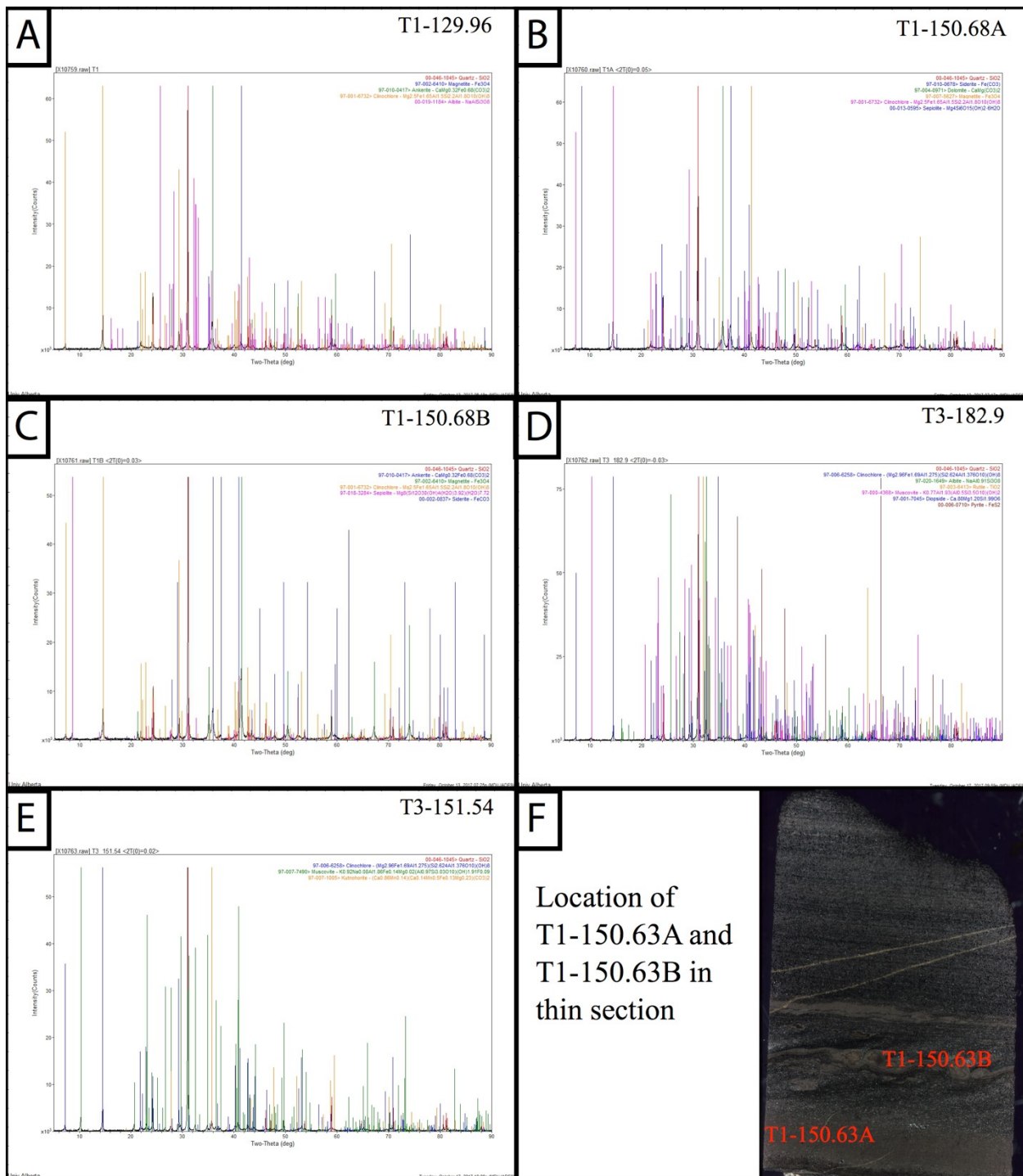
Figure 3.5. Powder XRD spectra for samples on which XANES spectra were collected (shown in Fig. 4). Note the presence of dolomite and ankerite in TCDP1 samples, the presence of kutnohorite in TCDP3 samples associated with interval K2, and the lack of either phase in the sample analyzed just below interval K1.

185
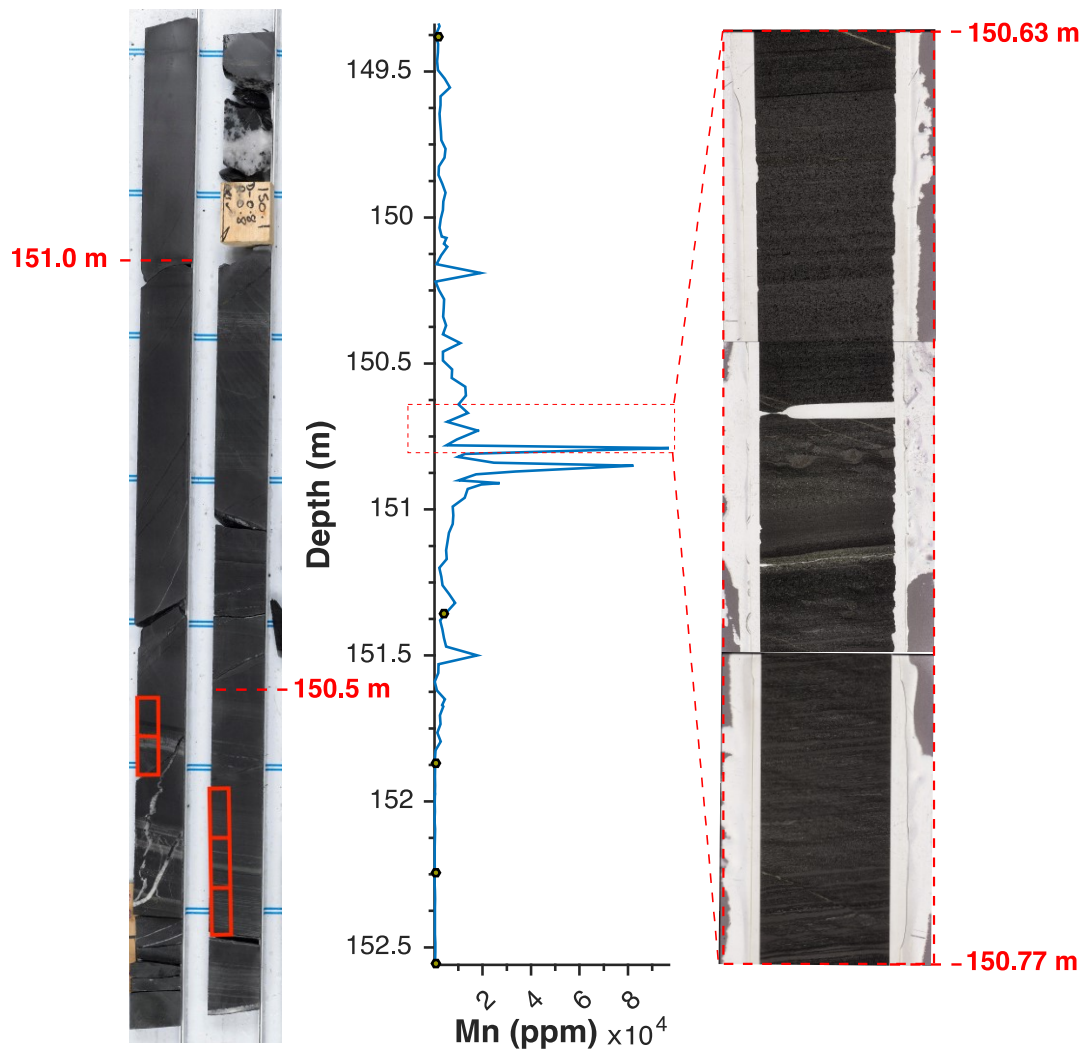
Figure 3.6. Mn enriched interval B1 in core (left), and the Mn XRF profile (center) spanning this section. Magnified images of thin sections (right) have been included to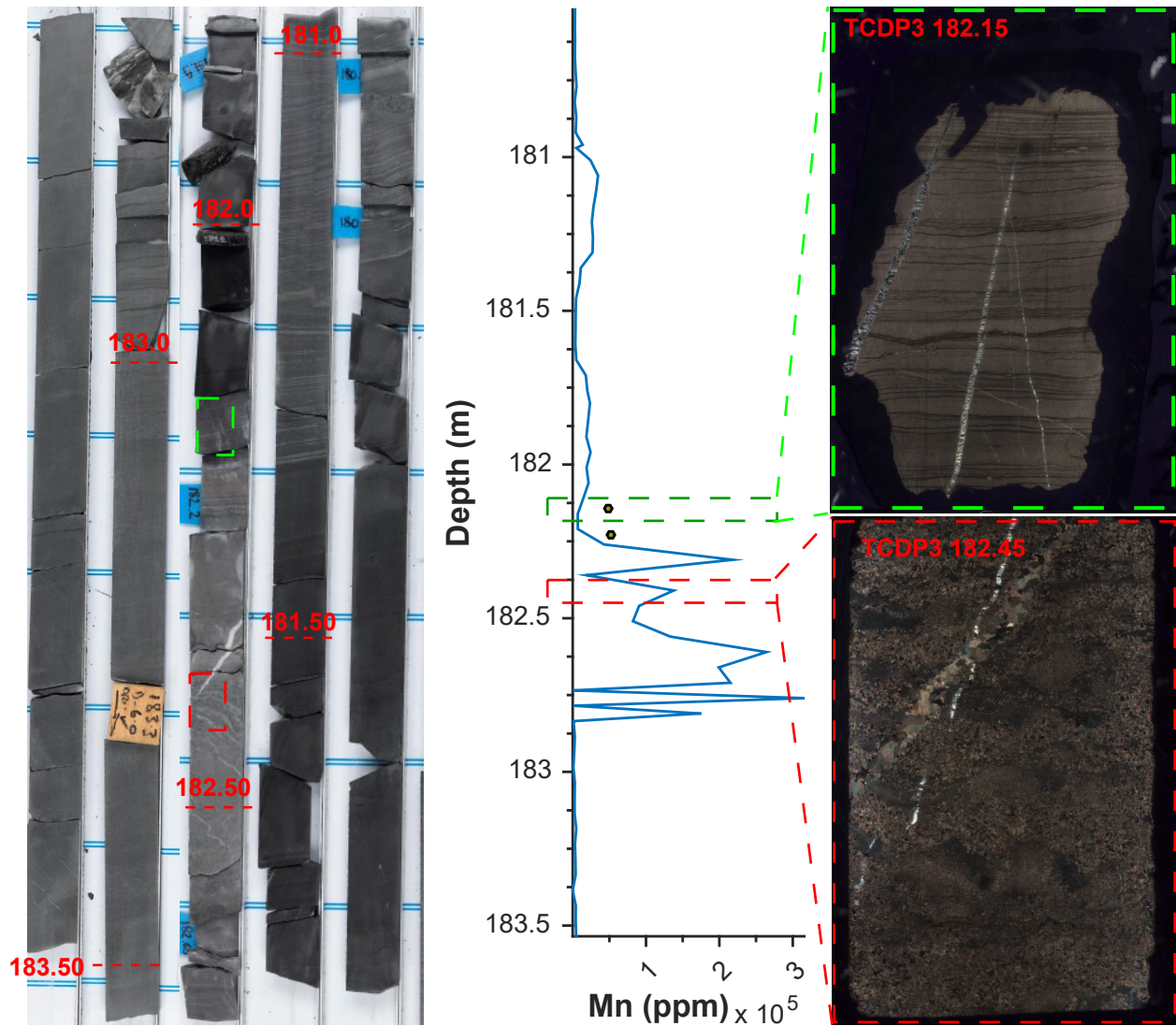 show carbonate textures within the interval. Note the spherical features separating Mn enriched beds below from Mn depleted beds above. Red boxes on the core photos indicate where thin sections were taken.
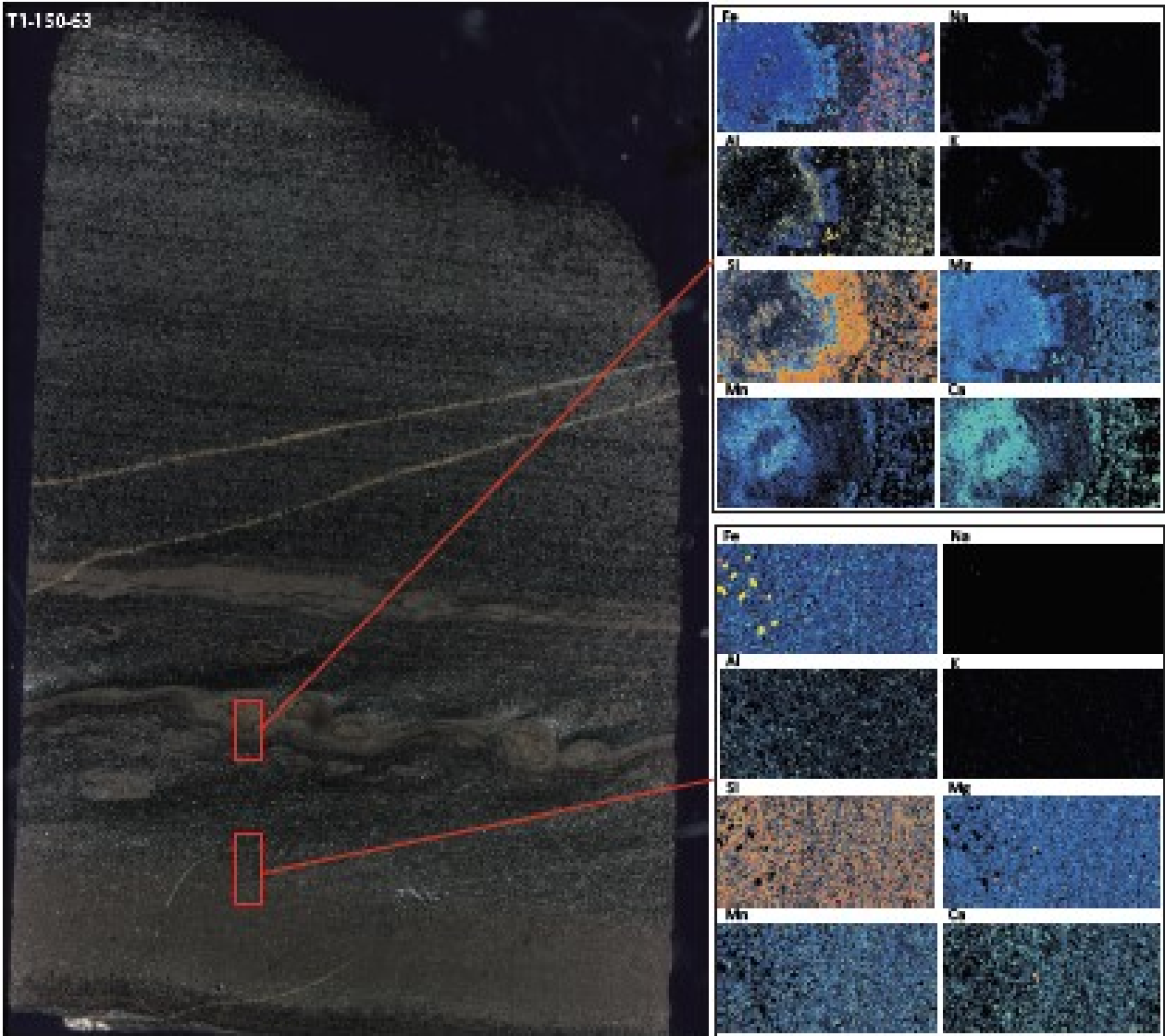
Figure 3.7. Mn textures and major element associations at 150.63 m depth, within the lower Mn enrichment. Maps are 2 mm x 1 mm.
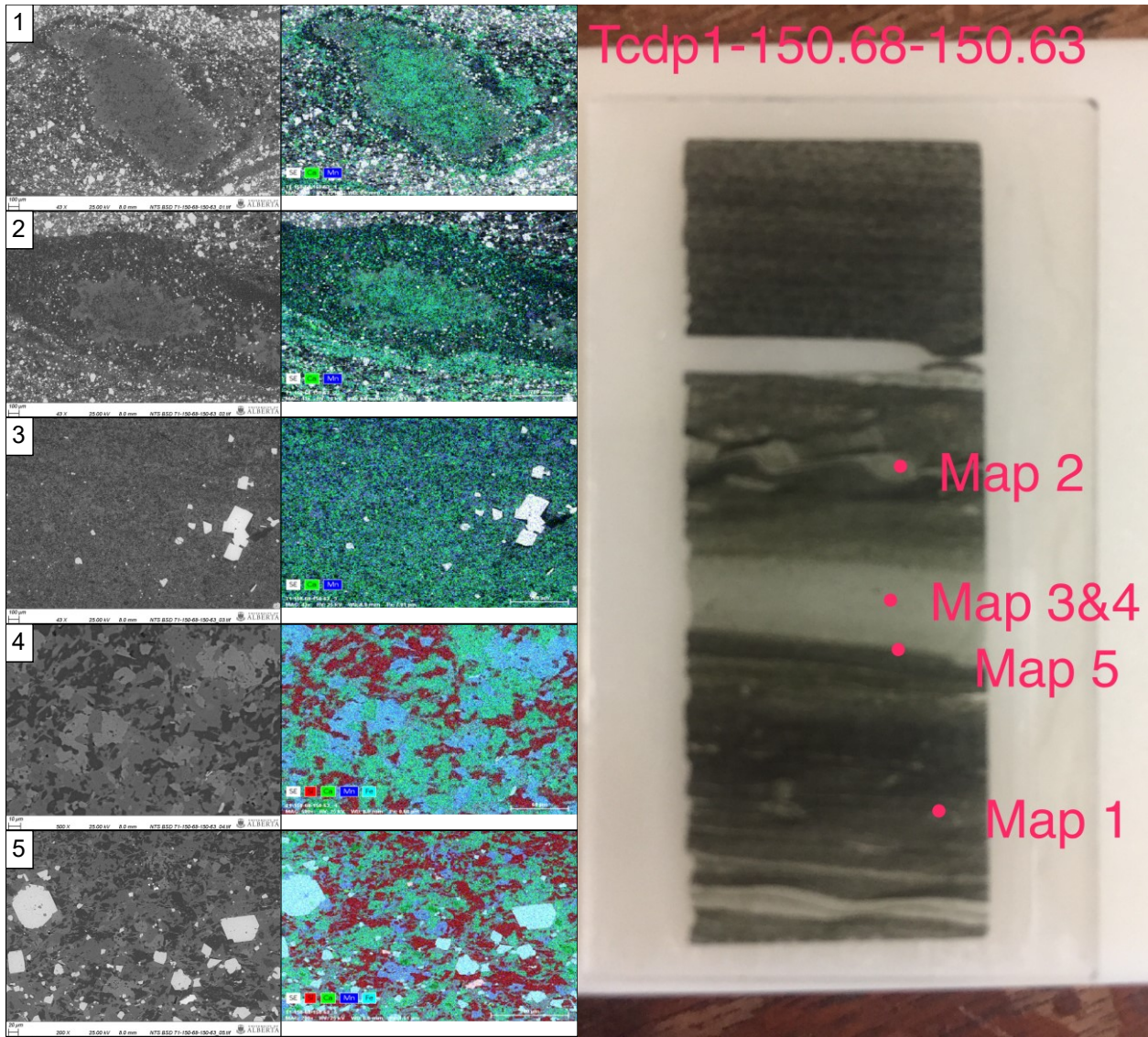
Figure 3.8. SEM-EDS maps of Mn textures in thin section TCDP1-160.68-150.63 corresponding to enrichment B1.
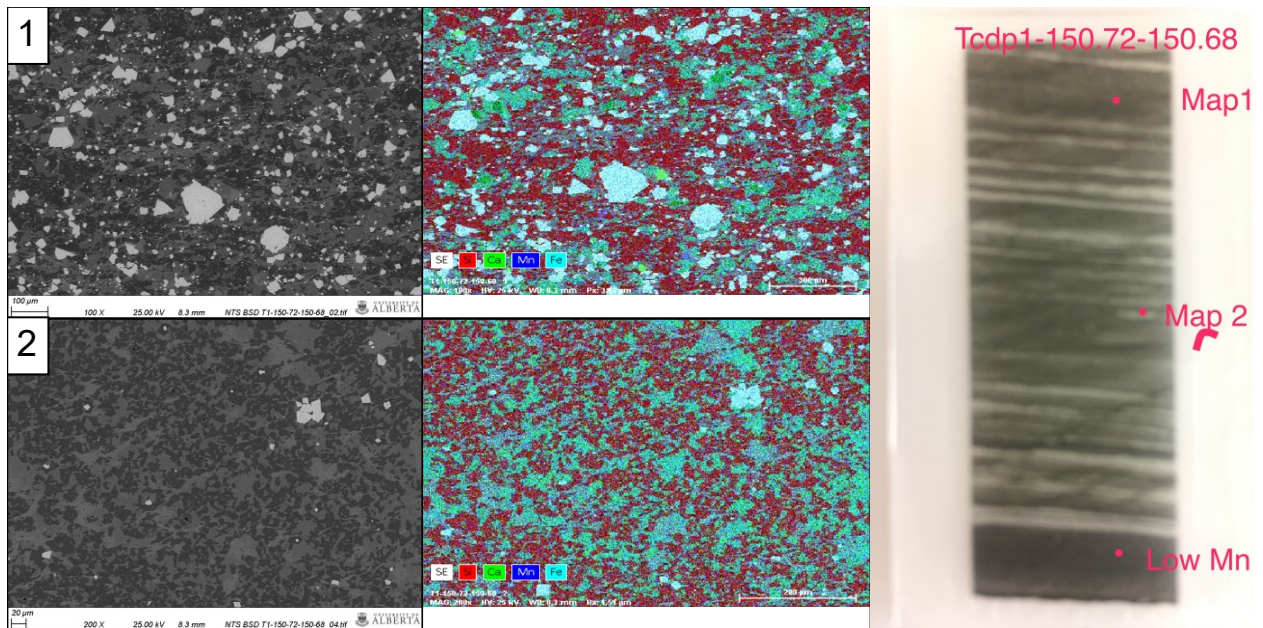
Figure 3.9. SEM-EDS maps of Mn textures in thin section TCDP1-150.72-150.68 corresponding to enrichment B1.
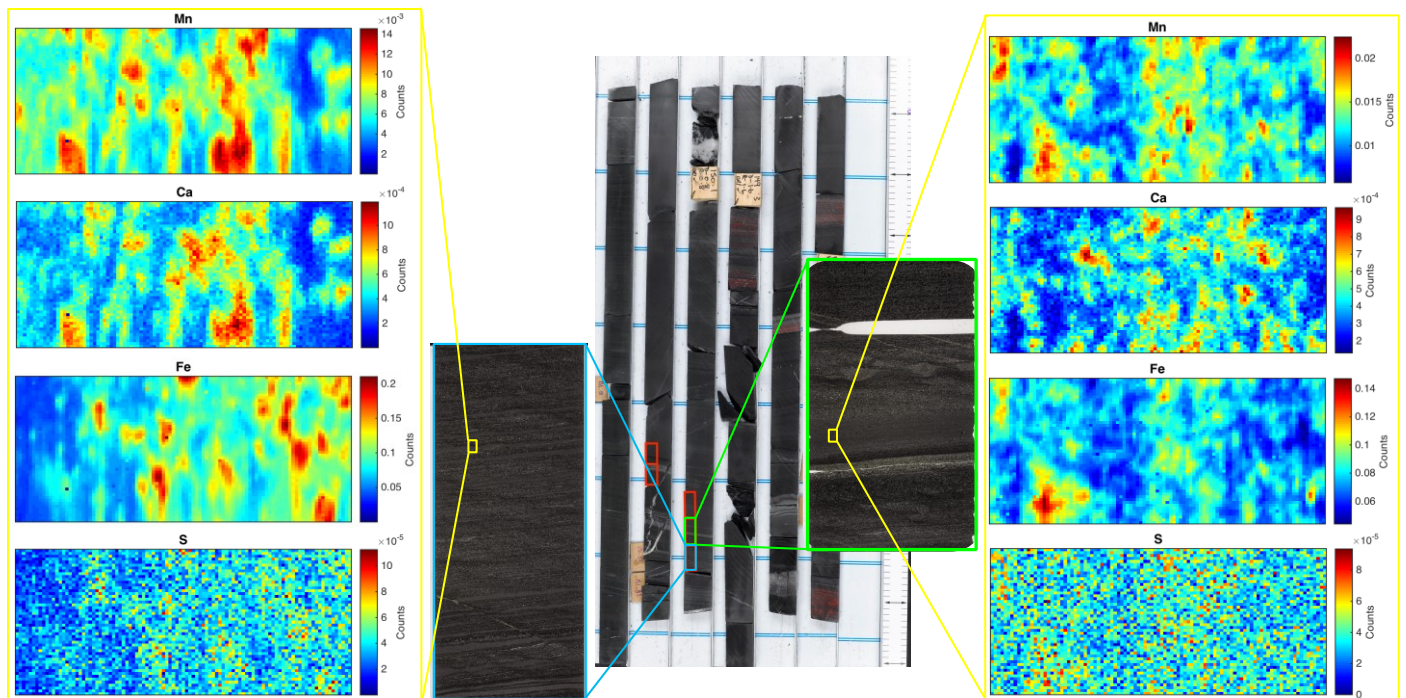
Figure 3.10. µXRF mapping for samples T1-150.73-150.68 and T1-150.68-150.63 (B1). The blue and green boxes highlight the location of thin sections T1-150.73-150.68 and T1-150.68-150.63, respectively. The location of XRF maps is highlighted in yellow. Maps are 1mm x 2mm in size. Mn is concentrated in carbonate grains that concentrate in thin layer, banded on the mm-scale.
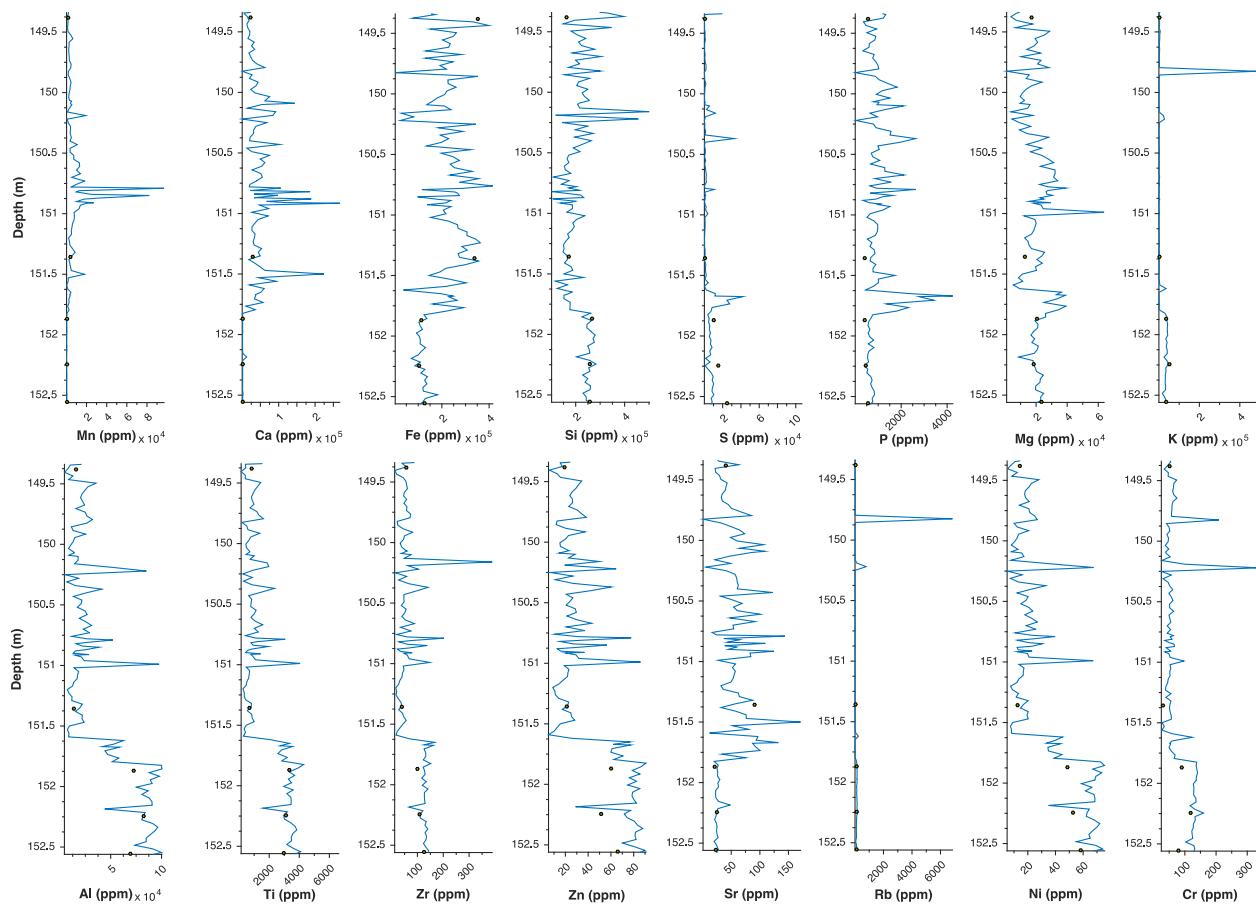
Figure 3.11. Major and trace element XRF profiles through enrichment B1.
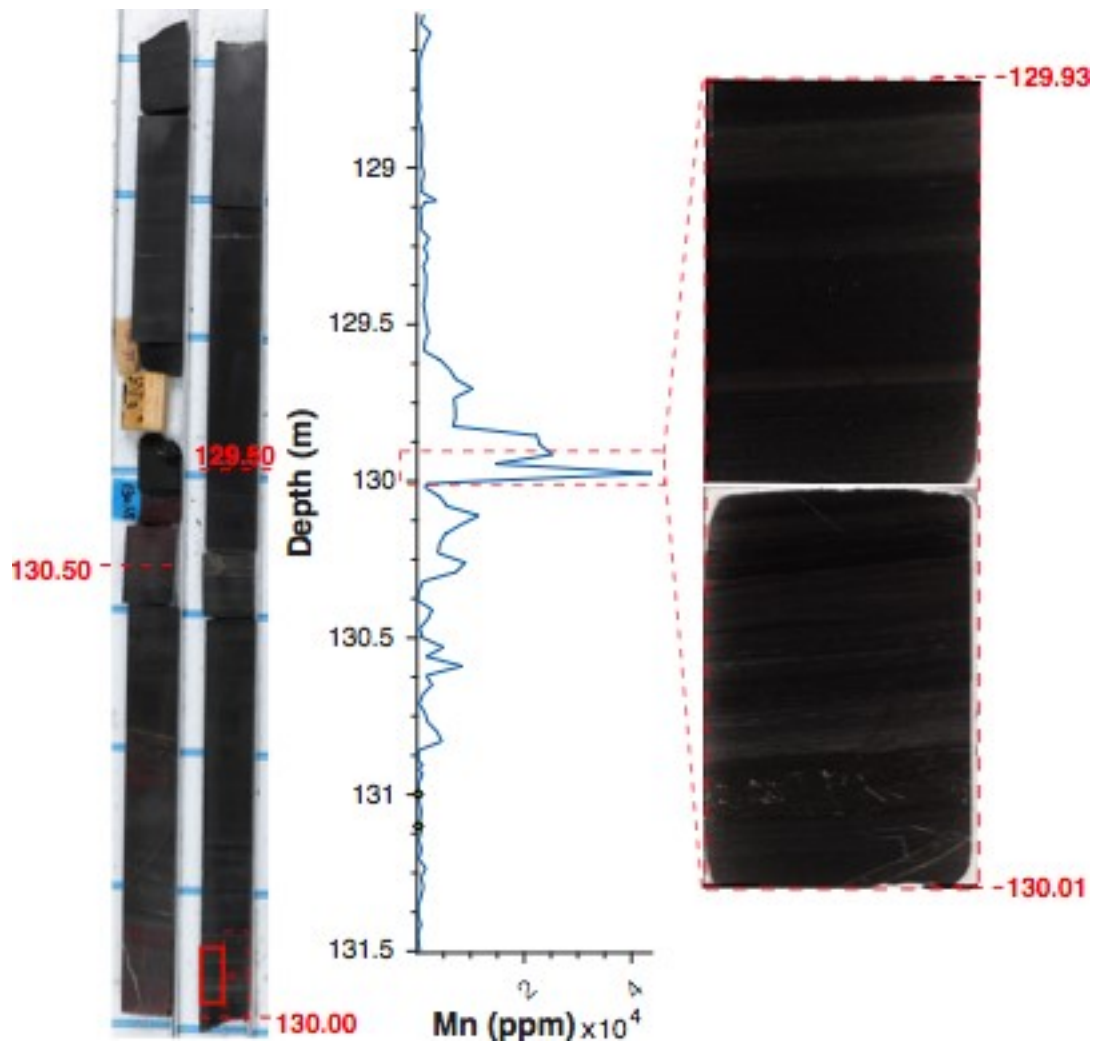
Figure 3.12. Mn enriched interval B2 in core (left), and the Mn XRF profile (center) spanning this section. Magnified images of thin sections (right) have been included to show carbonate textures within the interval. Red boxes on the core photos indicate where thin sections were taken.
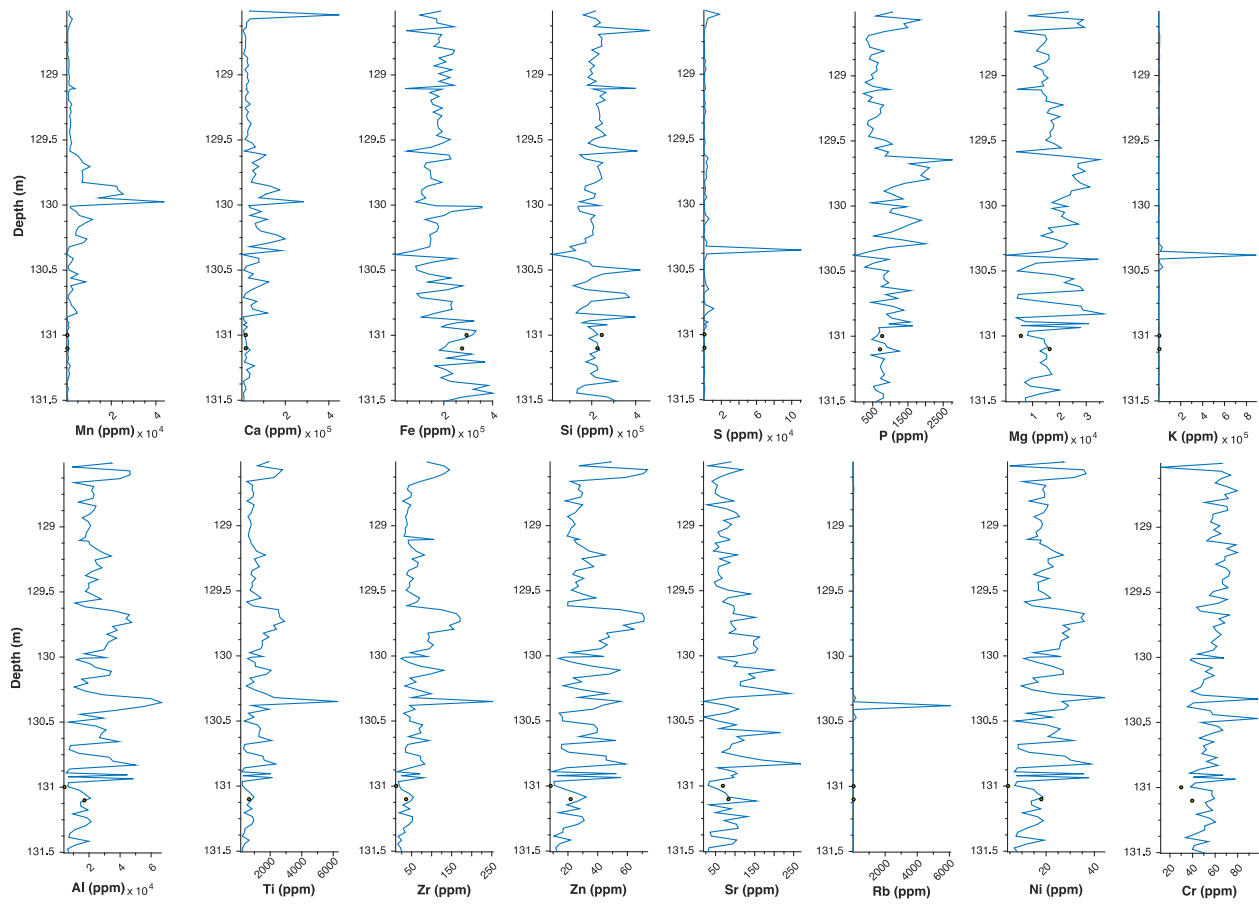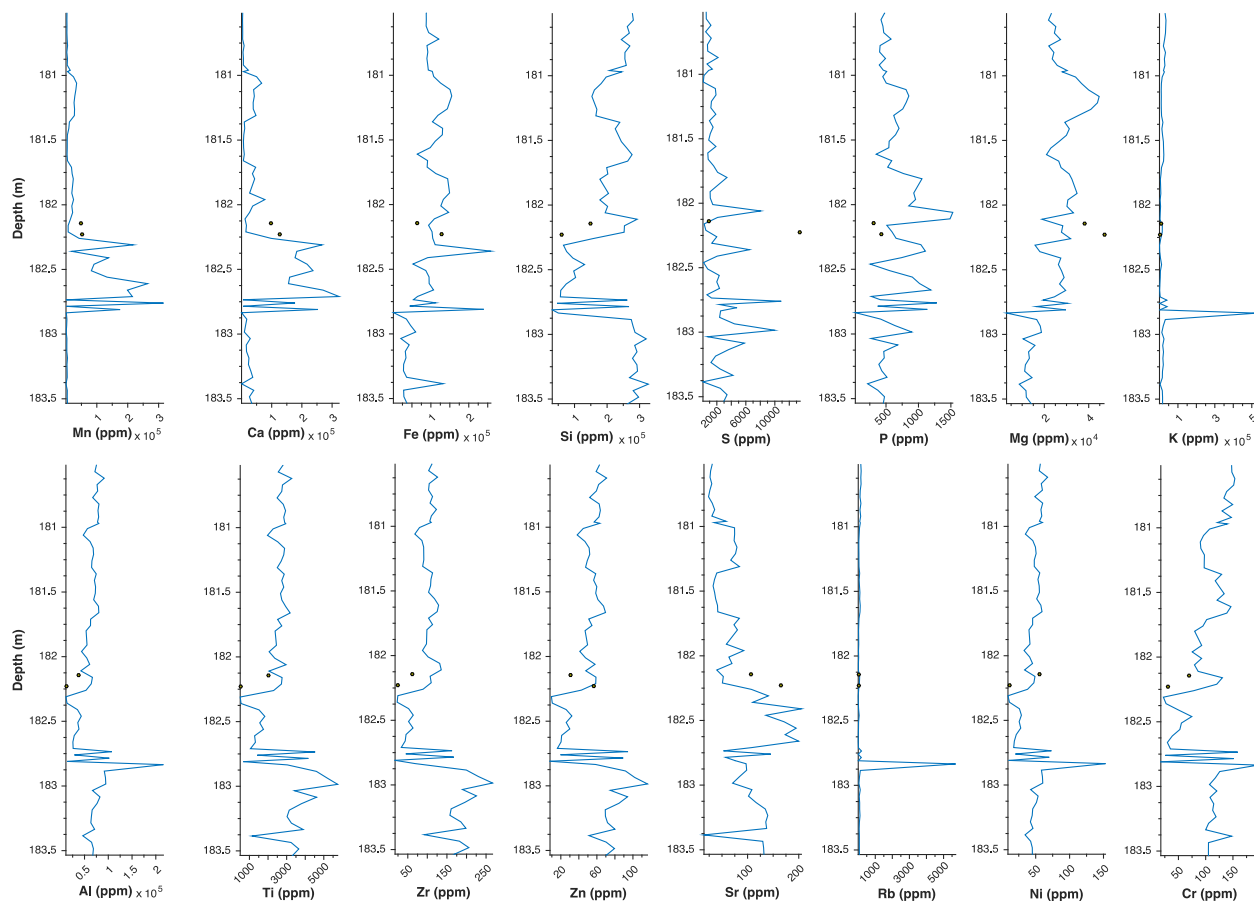
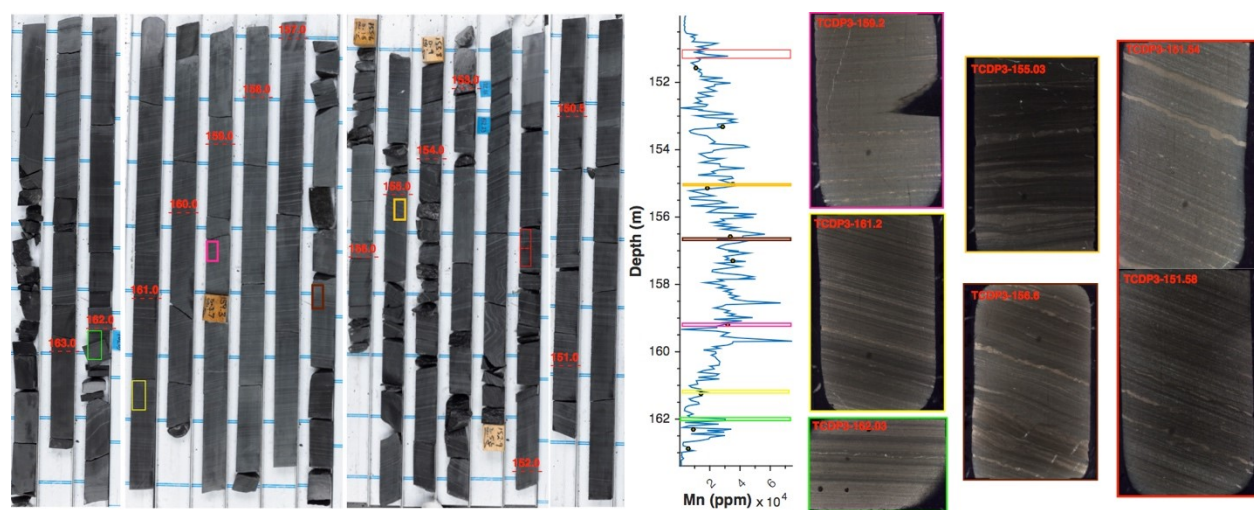**Figure 3.13.** Major and trace element XRF profiles through enrichment B2.
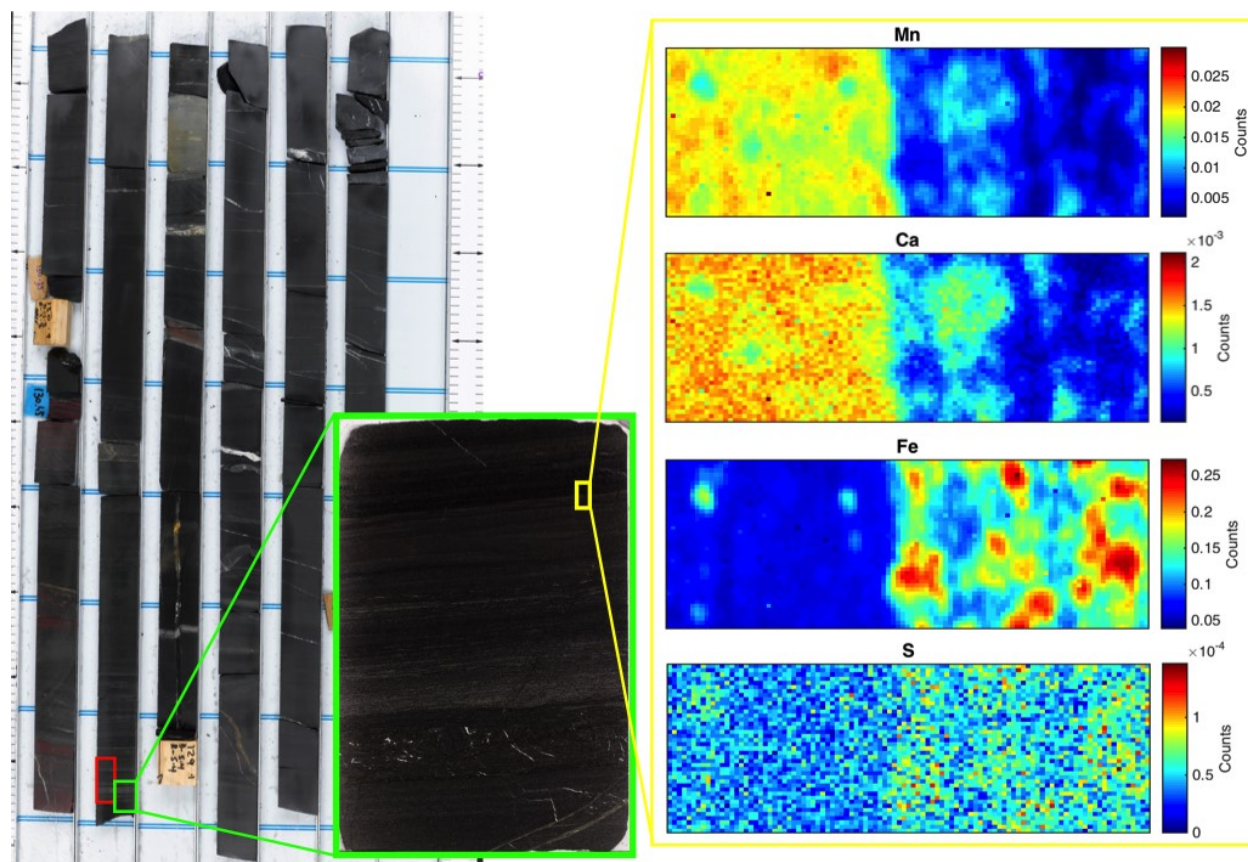
Figure 3.14. µXRF mapping for sample T1-130.01 (B2). The location of the thin section on which analysis was performed is outlined in green. The location where XRF maps were acquired is highlighted in yellow. Maps are 1mm x 2mm in size. Mn is concentrated in thin carbonate layers, banded on the mm-scale.

Figure 3.15. Mn enriched interval K1 in core (left), and the Mn XRF profile (center) spanning this section. Magnified images of thin sections (right) have been included to show carbonate textures within the interval. Red and green boxes on the core photos indicate where thin sections were taken.

**Figure 3.16.** Major and trace element XRF profiles through enrichment K1.

Figure 3.17. Mn enriched interval K2 in core (left), and the Mn XRF profile (center) spanning this section. Magnified images of thin sections (right) have been included to show carbonate textures within the interval. Coloured boxes on the core photos indicate where thin sections were taken.
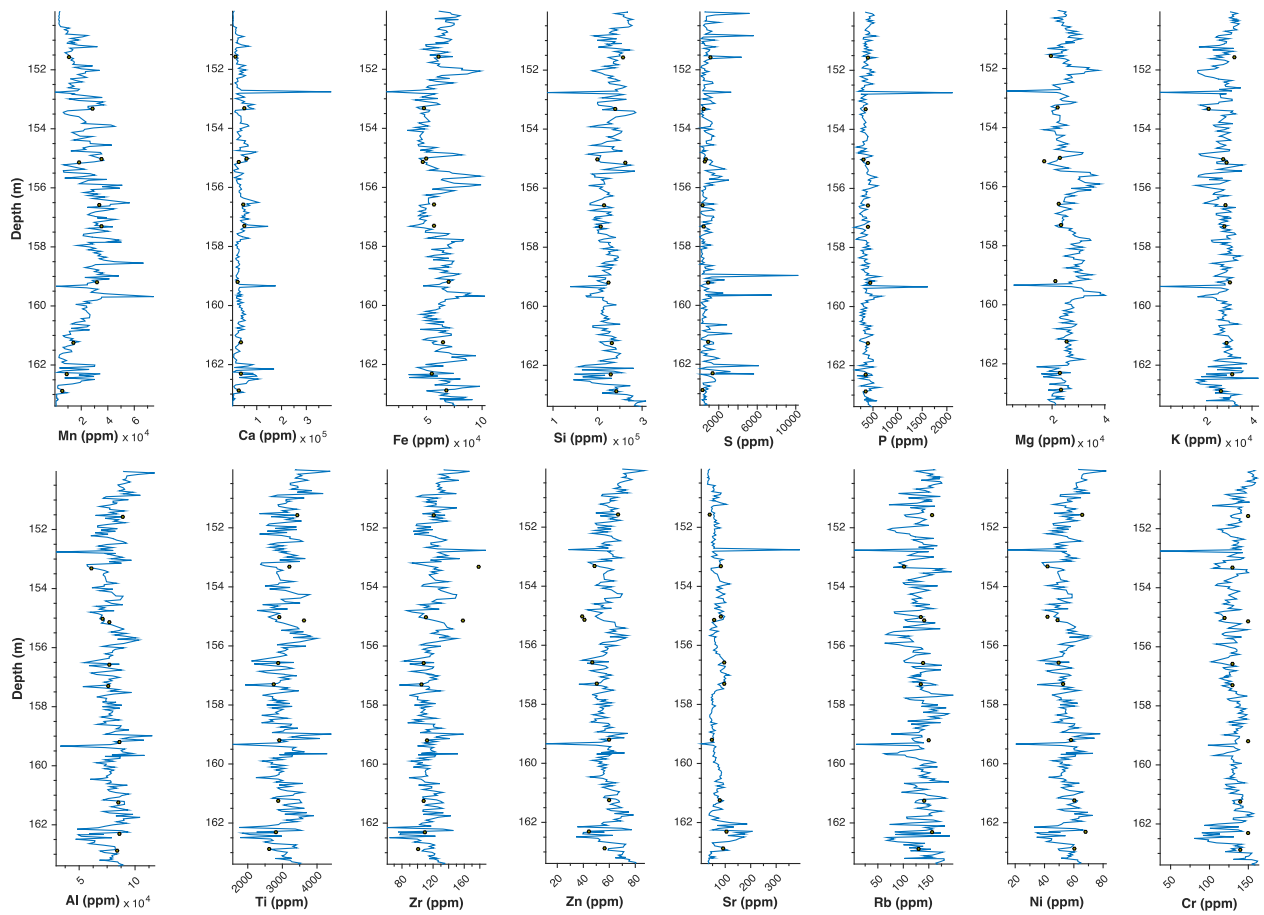
Figure 3.18. Major and trace element XRF profiles through enrichment K2.
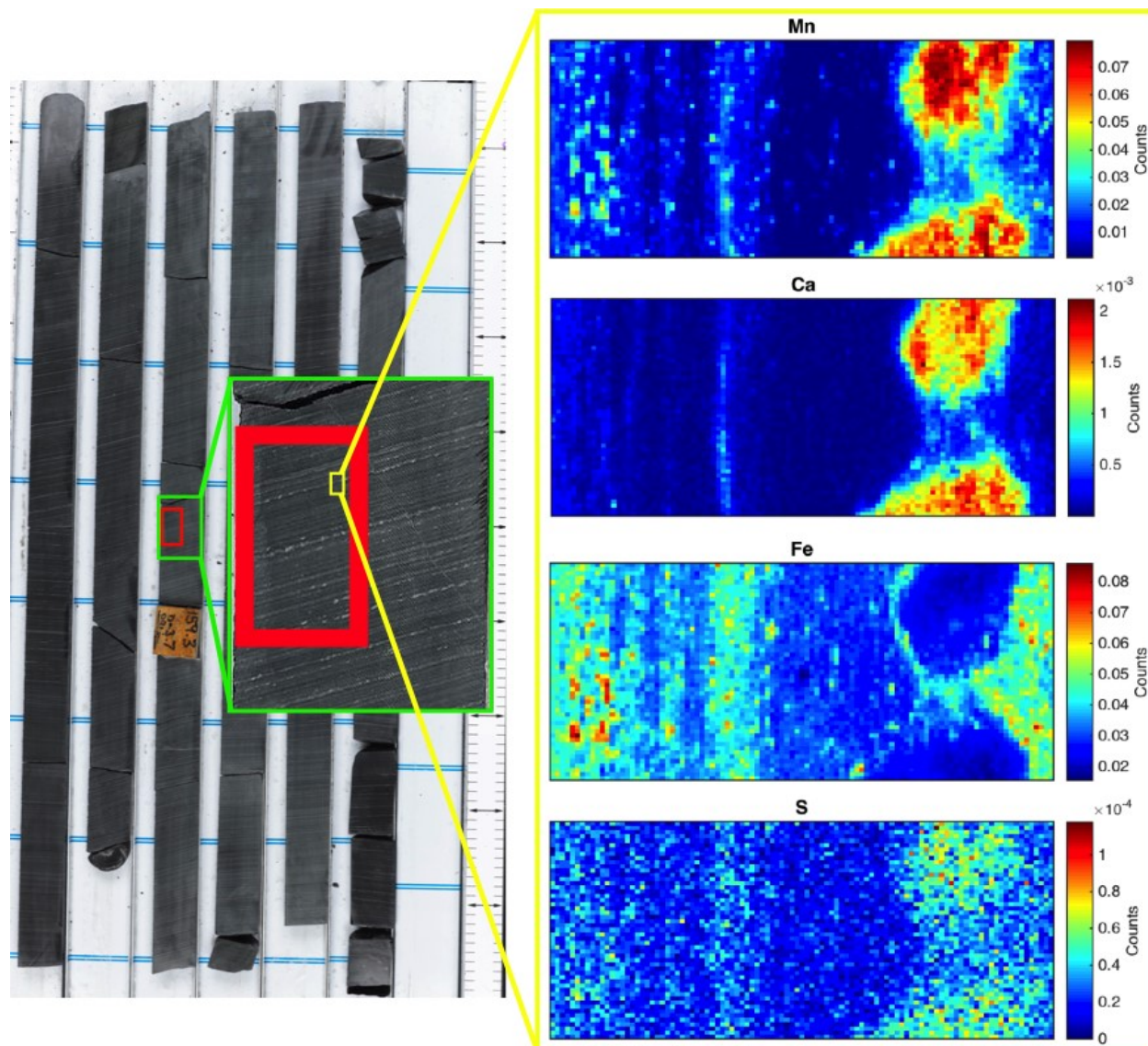
Figure 3.19. µXRF mapping for sample T3-159.2 (K2). The location of the thin section on which analysis was performed is outlined in red. The location where XRF maps were acquired is highlighted in yellow. Maps are 1mm x 2mm in size. Mn is concentrated in thin carbonated layers, banded on the mm-scale. Mn counts are positively correlated with Ca (r^2=0.90), S (r^2=0.69), Cr (r^2=0.45), and Ni (r^2=0.41), and negatively correlated with Mo (r^2=-0.69), Co (r^2=-0.67), and Zr (r^2=-0.49). Bulk rock data indicates Mn enrichments up to 4 wt.% at 159.2 m depth. The carbonate textures and depositional patterns represented by this figure are present between 162.34 m and 151.52 m depth, where Mn concentrations reach up to 7.10 wt.%. According to powder XRD analyses, kutnohorite is the prominent Mn bearing carbonate phase.
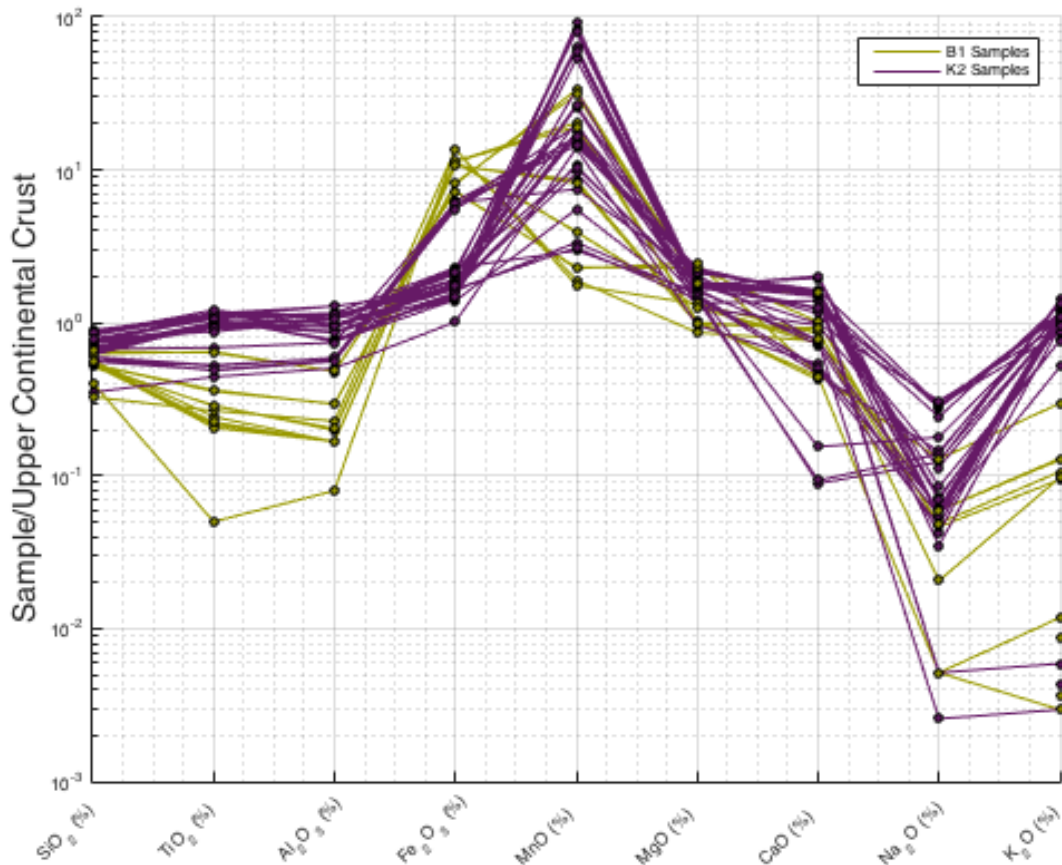
Figure 3.20. Major element data from Mn enriched (>0.1 wt.% MnO) intervals B1 and K2 normalized to upper continental crust values (Taylor and McLennan, 1985). Note that Fe concentrations are higher in B1 samples, as expected given its location within the Boolgeeda IF. Sodium also appears to be depleted in Mn relative to upper continental crust enriched samples. B1 and K2 samples normalized to Archean upper continental crust values (Taylor and McLennan, 1995) show identical patterns.
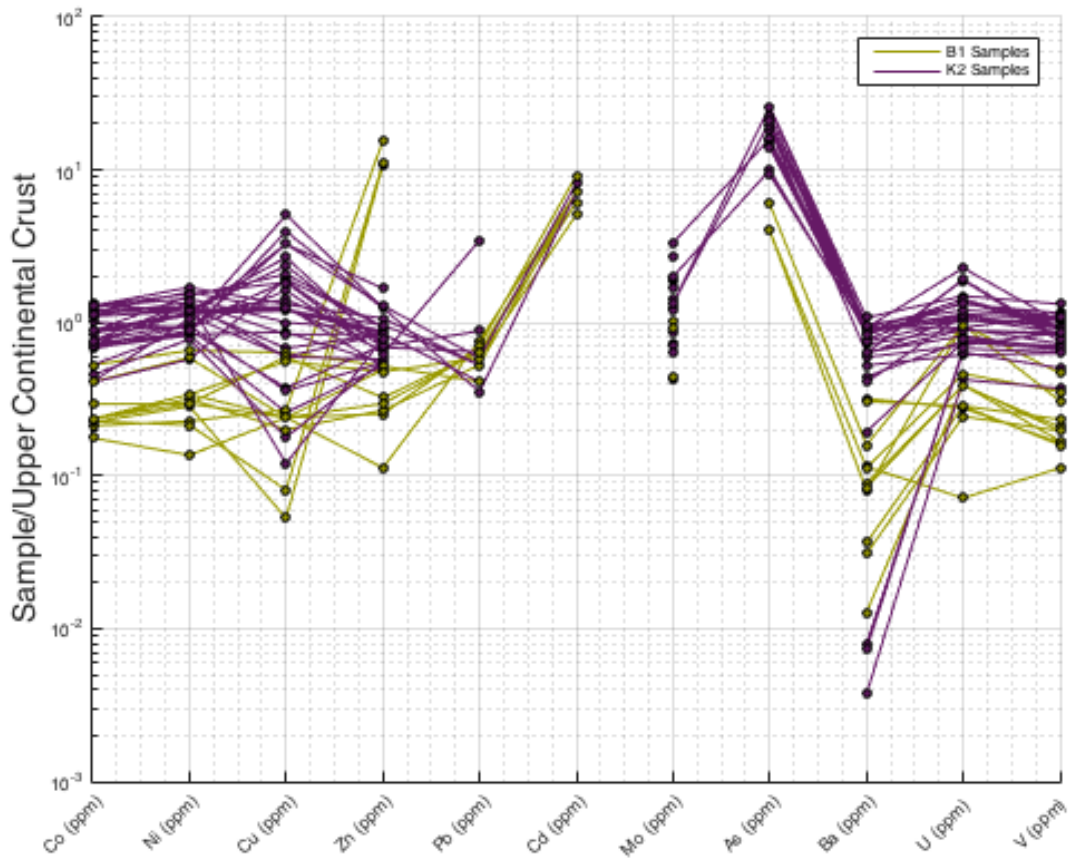
Figure 3.21. Trace element data from Mn enriched (>0.1 wt.%) intervals B1 and K2 normalized to upper continental crust values (Taylor and McLennan, 1985).
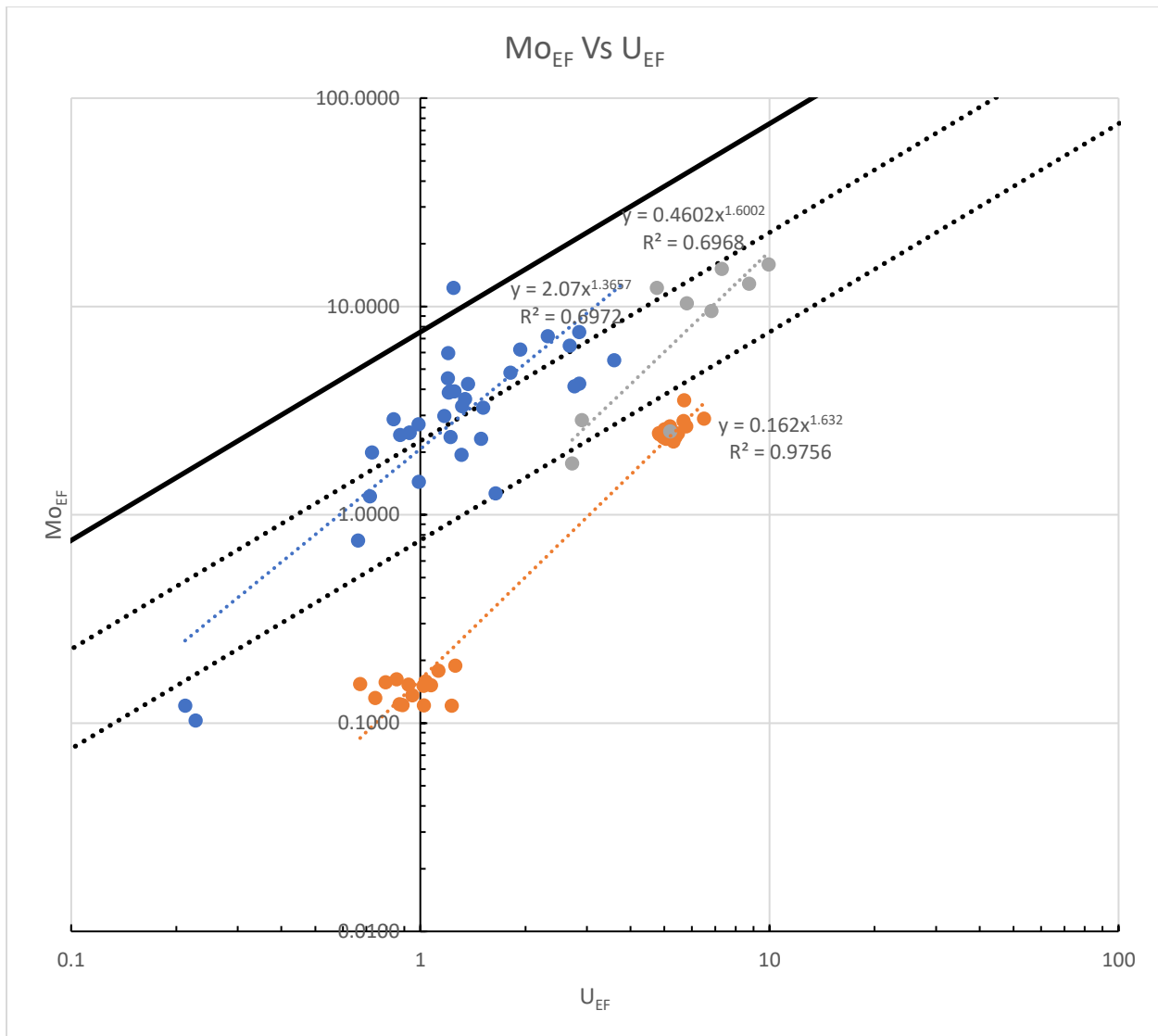
Figure 3.22. MoEF vs UEF for Mn enrichment B1 (grey points), K2 (blue points), and Kazput carbonates (orange points). Dark black and dashed lines represent the modern seawater trend.

9. Tables (Chapter 3)

Table 3.1. Manganese (Mn) speciation calculated from linear combination fitting of reference compounds.

Sample	Manganese (Mn) Speciation
T1-129.96	2.00
T1-150.68A	2.00
T1-150.68B	2.00
T3-152.54	2.00
T3-182.9	2.094

Table 3.2. Proportion of standards used to fit data.

Sample	Standards used (proportions out of 1)
T1-129.96	Kutnohorite (0.999), Rhodochrosite (0.001)
T1-150.68A	Kutnohorite (0.922), Rhodochrosite (0.078)
T1-150.68B	Kutnohorite (0.933), Rhodochrosite (0.067)
T3-152.54	Kutnohorite (0.998), Rhodochrosite (0.002)
T3-182.9	Kutnohorite (0.375), Bixbyite (0.060), Pyrolusite (0.016), Tephroite (0.550)

Table 3.3. Summary of R2 values for Mn cross-plots of solution and XRF data for Mn enriched samples in intervals B1 and K2. R2 values below 0.1 considered "No Fit"; "n" and "p" refer to negative and positive correlations, respectively.

Interval	B1	K2	B1	K2	Interval	B1	K2	B1	K2
Element	MnO (wt.%)	MnO (wt.%)	Mn (XRF)	Mn (XRF)	Element	MnO (wt.%)	MnO (wt.%)	Mn (XRF)	Mn (XRF)
SiO$_2$ (wt.%)	No Fit	No Fit	No Fit	0.3907 (n)	Tm (ppm)	0.1163 (n)	No Fit	-	-
TiO$_2$ (wt.%)	No Fit	No Fit	No Fit	No Fit	Yb (ppm)	0.1362 (n)	No Fit	-	-
Al$_2$O$_3$ (wt.%)	No Fit	No Fit	No Fit	No Fit	Lu (ppm)	0.1109 (n)	No Fit	-	-
Fe$_2$O$_3$ (wt.%)	No Fit	No Fit	No Fit	No Fit	Hf (ppm)	No Fit	No Fit	-	-
MnO (wt.%)	1 (p)	1 (p)	1 (p)	1 (p)	Ta (ppm)	No Fit	No Fit	-	-
MgO (wt.%)	No Fit	No Fit	No Fit	0.2692 (n)	Th (ppm)	No Fit	No Fit	-	-
CaO (wt.%)	0.2342 (p)	0.2195 (p)	0.1612 (p)	No Fit	U (ppm)	No Fit	No Fit	-	-
Na$_2$O (wt.%)	0.2963 (n)	0.1034 (n)	-	-	Sc (ppm)	No Fit	No Fit	-	-
K$_2$O (wt.%)	0.485 (n)	No Fit	No Fit	0.1182 (n)	V (ppm)	No Fit	No Fit	-	-
P$_2$O$_5$ (wt.%)	0.1061 (n)	No Fit	No Fit	No Fit	Cr (ppm)	No Fit	No Fit	No Fit	0.2673 (n)
S (ppm)	No Fit	No Fit	No Fit	No Fit	Co (ppm)	No Fit	No Fit	-	-
LOI	0.2634 (p)	0.3729	-	-	Ni (ppm)	No Fit	0.1187 (n)	No Fit	No Fit
Li (ppm)	No Fit	No Fit	-	-	Cu (ppm)	No Fit	No Fit	-	-
Y (ppm)	0.1029 (n)	No Fit	-	-	Ga (ppm)	No Fit	No Fit	-	-
Zr (ppm)	No Fit	No Fit	No Fit	0.1139 (n)	Rb (ppm)	0.2099 (n)	No Fit	No Fit	0.1294 (n)
Ba (ppm)	No Fit	No Fit	-	-	Sr (ppm)	0.4121 (p)	No Fit	0.2136 (p)	No Fit
La (ppm)	No Fit	No Fit	-	-	Nb (ppm)	No Fit	No Fit	-	-
Ce (ppm)	No Fit	No Fit	-	-	Cd (ppm)	0.6572 (n)	No Fit	-	-
Pr (ppm)	No Fit	No Fit	-	-	Cs (ppm)	0.2646 (n)	0.339 (n)	-	-
Nd (ppm)	No Fit	No Fit	-	-	Pb (ppm)	No Fit	No Fit	-	-
Sm (ppm)	No Fit	No Fit	-	-	Zn (ppm)	No Fit	0.2739 (n)	No Fit	0.2282 (n)
Eu (ppm)	0.1088 (n)	No Fit	-	-	As (ppm)	No Fit	0.3155 (n)	-	-
Gd (ppm)	No Fit	No Fit	-	-	Mo (ppm)	1 (n; 3 pts)	No Fit	-	-
Tb (ppm)	No Fit	No Fit	-	-	Sn (ppm)	No Fit	No Fit	-	-
Dy (ppm)	No Fit	No Fit	-	-	Sb (ppm)	0.567 (n)	0.1497 (n)	-	-
Ho (ppm)	No Fit	No Fit	-	-	W (ppm)	No Fit	No Fit	-	-
Er (ppm)	No Fit	No Fit	-	-					

Chapter 4: Future work investigating signatures for magnetotactic bacteria and microbial mat communities in the Boolgeeda Iron Formation, Hamersley Basin, Western Australia

1. Introduction

Magnetotactic bacteria (MTB) were first identified in marsh sediments in the vicinity of Cape Cod, Massachusetts (Blakemore, 1975). This polyphyletic group is characterized by intracellular chains of magnetite (Fe_3O_4) or greigite (Fe_3S_4; Mann et al., 1990b; Heywood et al., 1990; Bazylinski et al., 1993; Bazylinski et al., 1995) grains, commonly referred to as magnetosomes. It is presumed that magnetosomes allow MTB to orient themselves and move along the Earth's geomagnetic field in a process known as magnetotaxis (Blakemore, 1975). This process allows MTB to reduce a typical 3D "run-and-tumble" strategy for finding preferred microenvironments with a suitable redox gradient to an optimized 1D search along geomagnetic field lines in chemically stratified water or sediment columns (Kirschvink, 1980; Frankel and Bazylinski, 1994; Frankel et al., 1997). As such, MTB commonly live near sharp redox gradients, such as the oxic-anoxic transition zone (OATZ) of aquatic environments and grow preferentially under narrow redox conditions (Figure 4.1; from Kropp and Kirshvink, 2008). Specifically, magnetite producers are typically microaerophiles or nitrate-reducers found in suboxic conditions (Bazylinski and Blakemore, 1983; Bazylinski and Moskowitz, 1997; Bazylinski and Frankel, 2000), often at the top of the OATZ and at the sulphidic hypolimnion (Moskowitz et al., 2008).

Magnetite grains produced by MTB are characterized by their nano-scale size (~50-100 nm), equidimensional cuboidal to octahedral structure, single-domain magnetism, and relatively low Verwey transition temperature (Balkwill et al., 1980; Mann et al., 1990a; Heywood et al., 1990; Moskowitz et al., 1993; Bazylinski et al., 1994; Frankel and Bazylinski, 1994; Bazylinski,

1996). A Verwey transition (Verwey, 1939) refers to a change in magnetite crystal structure from cubic to monoclinic (Iizumi et al., 1982) that results in increased resistivity of magnetite grains, typically occurring at temperatures below 125 K. However, MTB have been shown to produce magnetite grains displaying a Verwey transition between 100-110 K (Prozorov et al., 2007). The latter authors compared the Verwey transition in nanocrystalline bacterial magnetite produced by four different strains of MTB to synthetic magnetite crystals. All four bacterially produced magnetites had lower Verwey transitions temperatures (101-117 K) than the abiogenic synthetic magnetite control (125 K). Magnetite synthesized in an agarose gel, used to mimic the conditions under which magnetite nanocrystals are formed in MTB, also displayed a low Verwey transition temperatures (104 K). The drop in Verwey transition temperature is presumed to be the result of cation depletion and resulting structural changes in biotically produced magnetite that is slightly oxidized (Moskowitz et al., 1993; Kopp et al., 2006).

Recently, Carlut et al. (2015) noted the presence of two Verwey transition temperatures in magnetite within a 2 m interval of the Boolgeeda Iron Formation, Hamersley Basin, Western Australia (Figure 4.2). Their analysis was completed on a ~30 m (163.25-130.45 m depth) section of core capturing the top of the Boolgeeda Iron Formation (2.45 Ga), which represents the terminal iron formation in the Hamersley Basin. The authors attributed the two unique Verwey transition temperatures to two populations of stoichiometrically distinct magnetite phases. The primary magnetite phase, prevalent throughout the Boolgeeda, underwent a Verwey transition between 120-125 K. The second magnetite phase underwent a Verwey transition between 100-110 K. Notably, these two populations of magnetite displaying distinct Verwey transition temperatures are analogous to the experimental groups of Prozorov et al. (2007). The critical question then is:

are the low Verwey transition temperatures detected by Carlut et al. (2015) due to the preservation of magnetite magnetofossils?

Magnetotactic bacteria are theorized to have evolved in the Archean, based on metagenomics and phylogenetic analyses that suggest the persistence of magnetotaxis in multiple lineages that diverged at this time (Lin et al., 2017). Because modern magnetotactic bacteria commonly live near sharp redox gradients, such as the oxic-anoxic transition zone (OATZ) of aquatic environments (Figure 4.1; from Kropp and Kirshvink, 2008), it is likely that their evolution occurred in response to changing geochemical gradients in the Archean environment, such as the development of an OATZ concomitant with the increased oxygenation. The oldest putative record of magnetofossils found to date occurs within the ~1.88 Ga Gunflint Formation, Ontario, Canada (Chang, 1988). However, all putative Precambrian magnetofossils are hosted in outcrop samples of carbonate platform sediments (mostly stromatolitic limestones and cherts), and none are found to meet the strict "magnetofossil robustness criteria" prescribed by Kopp and Kirschvink (2008). The oldest "robust" magnetofossils which meet all criteria proposed by Kopp and Kirschvink (2008) come from Cretaceous (Coniacian-Campanian) chalk deposits in southern England (Hounslow and Maher, 1996; Montgomery et al., 1998; Maher et al., 1999).

The presence of robust magnetofossils in the Boolgeeda Iron Formation (2.45 Ga), as captured by a pristine drill core (TCDP1), would represent a significant extension of the magnetofossil record with profound implications for Palaeoproterozoic water column chemistry. Further, large communities of magnetotactic bacteria at the time of Boolgeeda IF deposition would indirectly suggest extensive oxygenation of the shallow ocean by 2.45 Ga, reinforcing the early onset of the GOE followed by a long period of MIF-S recycling (Philippot et al., 2018).

2. Methods

Detailed methods for magnetic measurements are outlined in Carlut et al. (2015). Petrographic thin-sections observed using plane-polarized light (PPL), cross-polarized light (XPL), and reflected light (RL) microscopy were used for initial investigation and characterization of phases and textures within the 2 m interval of interest. Thin sections were prepared at the University of Alberta (UofA) thin-section preparation facility in Edmonton, Alberta, Canada.

Elemental distribution maps were acquired using a Zeuiss Sigma 300 VP-FESEM equipped with a Bruker energy dispersive X-ray spectroscopy (EDS) system at the UofA scanning electron microscopy (SEM) laboratory. High resolution images were acquired using the backscatter electron detector (BSD) on the same SEM. Petrographic thin-sections were coated in a thin layer of graphite using a Leica EM SCD005 evaporative carbon coater prior to imaging.

3. Results

Petrologic analyses led to the discovery of thin, layered structures with irregular surfaces at the contact between green mudstone/siltstone and overlying banded iron formation (147.8 m depth; Figure 4.3). Predominant phases within the structure include magnetite, Mg-Al-Fe clays, pyrite, quartz, and carbonate. Notably, a stark change in Fe minerology occurs across the approximately 3 mm thickness of the layer. Small euhedral magnetite grains are found at the bottom of the section, which progressively grade over ~750 µm into larger but more sparsely distributed magnetite grains. Above the large euhedral magnetite grains there is a noticeable absence of macroscopic Fe phases in the upper layers of the structure, until large (cm-scale) "pockets" of pyrite are found above the irregular upper surface. These large pyrite "pockets" are interspaced with similarly sized "pockets" of carbonate laterally along the upper surface of the irregular structure. Further, the

"pockets" appear to terminate sharply against and are formed around domal structures comprising the irregular upper surface. Internal laminations within the structure are not uniformly thick laterally; instead, they "pinch in and out" and in some cases terminate within the layer forming discontinuous thin irregular bands. This is particularly noticeable in the brown-green layer in the middle of the structure. Collectively, the internal laminations within the layers, domal upper surface, and mineralogical and textural changes across the structure bear a striking resemblance to a cross-section of a modern microbial mat from Yellowstone National Park (Figure 4.4).

Electron dispersive spectroscopic maps acquired using a Zeiss Sigma 300 VP-FESEM show compositional changes occurring across a transect of the structure (Figure 4.5). Compositional changes appear to mimic visual changes in colour observed in plane-polarized and cross-polarized light. Subtle changes in Mg, Al, Si, and Fe appear to distinguish the middle layers of the structure, where Fe minerals are sparse. Magnesium, Al, and Fe appear to be in relatively greater abundance in the lower middle layer, while Si appears to be more prominent in the upper-middle layer. The large pyrite and carbonate gains along the upper surface of the structure are clearly highlighted by the EDS maps. There is also a clear change in clay morphology that accompanies colour and compositional changes in the middle layers. In both sections, clays are bladed, but in the upper section the blades are much larger and spaced further apart. In the lower section, the blades are smaller in size and intervening space is greatly reduced (Figure 4.6). Notably, the spaces in between the bladed clays in both sections are filled with silica. The higher abundance of Si in the upper layers of the structure, as detected by EDS, may be a result of increased space between grains.

Directly above the boundary between the two distinct middle layers, a thin, laterally-extensive interval containing nano-scale spherical to oblong grains of Fe-oxide is found. The size

of these grains is fairly uniform throughout the interval, and edges of the grains appear rounded. Slightly larger grains found adjacent to the rounded grains display more angular edges, but these grains are significantly less abundant (Figure 4.7). All nano-scale Fe-oxide grains appear to occupy the Si-filled spaces between the bladed clay minerals. In some instances, the rounded grains appear to be arranged linearly, but are rarely in contact with one another and instead separated by gaps roughly the same diameter as the grains themselves (Figure 4.8). The best example of this is in the bottom right image of Figure 4.7, where rounded Fe-oxide grains of roughly the same diameter are arranged in an S-like pattern.

Figure 4.9 presents EDS spectra for various phases discussed above. Carbon peaks are the result of the graphite coating used in sample preparation. Notably, EDS spectra acquired from the rounded grains only display Fe, Si, and O peaks. Blades of the clay minerals display Fe, K, Si, Al, Mg, Na, and O peaks. Spectra from space between the bladed clays only show Si and O peaks.

The image recognition software Image J was used to produced statistical histograms for the size (area) and diameter (calculated assuming spherical grains) of Fe-oxide grains identified using the SEM (Figure 4.10). Analysed grains were split into 100 bins; the majority of Fe-oxide grains analyzed in ImageJ had a diameter between ~250-600 nm, with a peak occurrence of approximately 375 nm. A secondary shoulder appeared in the diameter histogram that appears to peak around 90 nm. Upon further investigation of the SEM images, grains representing this peak may have been identified (red box in Figure 4.10).

4. Discussion

After magnetotactic bacteria die, the magnetosomes can undergo three fates (1) chain breakup, (2) oxidation, and (3) reductive dissolution; a combination of these processes is also possible. The

first of the fates is likely during burial as proteins and lipids that held the chains together are degraded (Kobayashi et al., 2006). The second fate, oxidation, results in the formation of maghemite as Fe^{2+} is lost from the crystal (Xu et al., 1997). However, this process is considered to be the least destructive of the three fates and does not result in significant changes in crystal morphology (Kopp and Kirschvink, 2008). Conversely, fate three can significantly impact the preservation potential of magnetofossils. If oxygen and nitrate are consumed in the sediment during early diagenesis, heterotrophic bacteria turn to Fe(III) as the most efficient electron acceptor, including Fe(III) in magnetite (Kostka and Nealson, 1995; Dong et al., 2000). Thus, if sufficient organic matter is available to fuel microbial metabolism, these dissimilatory iron reducers (termed DIR) will dissolve fine magnetite particles, including magnetofossils. Sulphidic conditions during diagenesis can also promote dissolution of magnetite, and thus the destruction of magnetofossils (Karlin and Levi, 1983; Canfield and Berner, 1987; Karlin, 1990a, 1990b). Collectively, the long-term preservation of magnetofossils depends on the balance between lithification, which should protect magnetofossils, and the metabolic activities of bacteria living in porewaters.

Within the Boolgeeda IF, contacts between green mudstone/siltstone intervals and BIF may represent horizons where rapid emplacement and lithification of Fe(III)-Si gel preserved magnetofossils and associated microbial communities present in shallow porewaters. Figure 4.3 represents such a situation. A 3 mm thick structure is found at the transition from green mudstone/siltstone to BIF. The structure is flat on the bottom contact with green mudstone/siltstone, and irregular to domal at the top contact with the BIF. Four distinct layers are visible in the vertical transect of the structure. The bottom layer consists of euhedral magnetite grains, which are concentrated at the base of the structure and progressively dissipate upwards

within 750 μm. Interestingly, a gradual increase in magnetite grain size accompanies magnetite dissipation, with the largest and most euhedral grains located at the top of the layer and smaller "micrograins" towards the bottom. The top layer is highly irregular and appears to have large domal structures at the surface. Magnetite is again absent. Overlying the top layer, small irregular "pockets" of pyrite and carbonate, approximately 1-2 mm in length, are found alternating laterally along the upper surface. Further, overlying BIF bands appear to terminate obliquely against the irregular domal structures. This may suggest the irregular surface hosting the domal structures was in place prior to the accumulation of primary BIF sediments. We suggest this package represents remnants of a microbial mat community rapidly preserved as overlying Fe(III)-Si gel lithified soon after deposition. The fact that quartz cement fills in the space between bladed clay minerals in the upper layers of the mat may support preservation through silicification. For comparison, a cross-section of a modern mat from Yellowstone has been included in Figure 4.4. Although much thicker than the Boolgeeda structure (perhaps the result of compaction), a similar sequence of minerals and textures can be viewed.

From top to bottom, the layers in the modern microbial mat are composed of cyanobacteria (green), purple sulfur bacteria (pink), and iron and sulfide minerals (black) resulting from sulfate-reducing bacteria (https://www.alpfmedical.info/causative-agent/info-ubv.html). **If** the photic zone extended to the sediment-water interface during deposition of the green mudstone/siltstone, the microbial community composing the mat preserved in the Boolgeeda may have been very similar. The top layers would represent communities of photosynthetic bacteria, including cyanobacteria and underlying purple and green sulfur bacteria. Layers located below may include sulfate reducing bacter (SRB) and methanogens. If the microbial community contained both anaerobic purple-sulfur bacteria and sulfate reducers, an exchange of H_2S and SO_4^{2-} would occur

between the top and bottom of the mat. In the event that H_2S produced by SRB exceeded that required by purple non-S bacteria, reduced sulfide would react with reduced iron in the water column to form pyrite. This would explain the pockets of pyrite visible at the top of the mat. As primary BIF precipitates covered the upper layer of the mat, phototrophs would be prevented from using sunlight for metabolism. The upper layer would therefore die off before the lower layers of sulfate reducers. This would result in an excess of HS^- and HCO_3 reacting with overlying reduced iron to form the pockets of pyrite and carbonate. The small pockets of carbonate and pyrite may thus represent vesicles of HS^- and HCO_3 trapped during burial and diagenetically transformed into carbonate and pyrite. Further, the death of phototrophs in the upper layer of the mat would end the local S cycle, as SO_4^{2-} would not be regenerated. With no sulfate returning to depth, the bottom layers of the mat would also eventually die out.

The abrupt burial and silicification of microbial mat communities, such as the one presented in Figure 4.3, may have promoted the preservation of magnetofossils. If mats persistently occupied the sediment-water interface of the green mudstones/siltstone, vertical movement of the mat would continuously recycle magnetofossils once oxygen and nitrate were consumed in the pore water, assuming sufficient reduced carbon was present. Only when depositional rates outpaced Fe(III) consumption by the microbial community or when delivery of reduced carbon was low would magnetofossils be preserved. The rapid burial of microbial sediments during renewed BIF deposition may have provided the perfect set of conditions for magnetofossil preservation. Silicification would have further inhibited diagenetic and/or metamorphic destruction of magnetofossils over the following 2.45 Ga.

Small (~80-100 nm) spherical to octahedral Fe-oxide particles are found above the boundary between lighter upper layers and lower darker layers of the mat structure (red box within

Figure 4.10; Figures 4.6-4.8). These grains appear to be the proper size, shape, and phase for magnetosomes, and are organized in chains. The larger (averaging ~375 nm) spherical Fe-oxide particles found adjacent to these grains (Figures 4.6-4.8) are the proper shape and phase for magnetosomes, but are much larger than modern magnetosomes and are not organized into the characteristic chains that typically define these structures. However, in some sections of the interval, these larger Fe-oxide grains are organized linearly, separated by small gaps roughly the same distance as the diameter of the grains themselves (Figures 4.7 and 4.8). It may be possible that the larger Fe-oxide grains represent chains of biogenically produced magnetite that were broken apart during early diagenesis. Their larger size may be the result of "ripening" during diagenesis and metamorphism.

The location of the thin layer containing possible magnetosomes within the mat structure is also interesting. If the varying colour, texture, and composition of layers are artifacts of different microbial communities present at the time of silicification, and the communities were comparable to a modern mat, this interval would lie within the theoretical oxic-anoxic transition zone (OATZ) of the mat. Magnetotactic bacteria are documented to inhabit similar niches in modern settings. Thus, if the thin layered interval in the Boolgeeda is indeed a mat and the Fe-oxide structures are magnetofossils, they are located in the exact horizon where we would expect to find them.

The presence of microbial mat communities and associated geochemical cycles in green mudstone/siltstone layers within the Boolgeeda IF may also partially explain the alternating layers of Fe-oxide+apatite+carbonate and quartz+pyrite on the scale of 10s-100s of μm (Supplementary Figure 6 of Philippot et al., 2018). The pyrite within these layers is strongly fractionated (δ^{34}S = -40‰), suggesting it is a product of non-S-limited sulfate reduction by sulfur reducing bacteria. The extremely thin layering may be an artifact of burial and re-establishment of the microbial

community on top of green mudstone/siltstone sediments if depositional rates were low enough to promote vertical movement of the mat. The pyrite layers would result from the same process as discussed above: burial of phototrophs with continued activity from the sulfate reducing bacteria resulting in layers of pyrite. Once the S cycle ended and the mat died, excess carbon and phosphorous from the mat may have been diagetically transformed into apatite and/or carbonate.

5. Summary, Conclusion, and Future Work

The magnetic anomaly detected by Carlut et al. (2015) in conjunction with the Fe-oxide grains displaying similarities to modern magnetosomes identified in this thesis, suggest it is possible that the Boolgeeda Iron Formation hosts the oldest record of magnetofossils found to date. However, identifying magnetofossils using the Verwey proxy is complicated by the fact that oxidation of magnetite may suppress the Verwey transition temperature (Özdemir et al., 1993; Cui et al., 1994; Özdemir and Dunlop, 2010). Therefore, future work will be undertaken in order to confirm that this record is robust and meets all criteria set out by Kopp and Kirschvink (2008).

Moving forward, we plan to analyze the nanoscale Fe-oxide structures identified under the SEM (Figures 4.6-4.10) using transmission electron microscopy (TEM). Thin (~80 nm) foils will be milled from petrographic thin sections using a Ga focused iron beam (Ga-FIB). These foils will be viewed at angstrom-scale under the TEM in hopes of determining the d-spacing of the phases in question, and thus assessing whether the phases present are indeed magnetite. If the grains are magnetite, FORC and MPMS will be used to confirm that these grains are the specific source of the low Verwey transition temperature.

Further, all other possible causes for the low Verwey transition temperature will be ruled out. Carlut et al. (2015) have already disproved diagenetic oxidation as the result of the lower

Verwey transition temperature (Figure 9 in their study). If magnetite had undergone oxidation, hysteresis would be expected during a heating and cooling cycle, and there would be no reversibility in the Verwey transition. The Moskowitz chain test (Moskowitz et al., 1993) and ferromagnetic resonance spectra (Weiss et al., 2004) will also be investigated to confirm the viability of these magnetofossils.

SIMS analyses for S and C isotopes will also be performed on the "pockets" of pyrite and carbonate overlying the irregular surface of the structure. Light stable isotopic signatures hosted in these "pockets" are key to proving or disproving the theory that these they are remnants of biogenic gases being trapped by overlying BIF sediments during burial. This would go a long way in proving or disproving the biotic origin of these structures. If possible, an interesting avenue of future research may be biomarker analysis across the mat structure in hopes of identifying specific members of the bacterial community. If this structure proves to be biotic, it has further implications for the depositional environment of BIF and may confirm reduced Fe upwelling to the shallow shelf, given its inferred location within the photic zone.

The green mudstone/siltstone lying beneath the mat structure should also be investigated for evidence of "magnetosome recycling". If this layer does in fact represent a mat moving vertically upwards through the sediment before being silicified and preserved, it is possible that partially altered magnetosomes are present in small intervals where burial outpaced magnetosome consumption by the microbial community.

If magnetofossils are present within the Boolgeeda IF, this represents a significant extension of the current fossil record. Further, it has vast implications for the depositional environment of BIF and the redox stratification of shallow water environments ~2.45 Gya. Confirming these observations would support an early rise of oxygen and shallow marine

oxygenation within the Hamersley and Turee Creek Basins, as suggested by Philippot et al. (2018) and Warchola et al. (2018).

6. References (Chapter 4)

Balkwill, D.L., Maratea, D., Blakemore, R.P., 1980. Ultrastructure of magnetic spirillum. Journal of Bacteriology 141, 1399-1408.

Bazylinski, D.A., 1996. Controlled biomineralization of magnetic minerals by magnetotactic bacteria. Chemical Geology 132, 191-198.

Bazylinski, D.A., Blakemore, R.P., 1983. Denitrification and assimilatory nitrate reduction in Aquaspirillum magnetotacticum. Applied and Environmental Microbiology 46, 1118-1124.

Bazylinski, D.A., Moskowitz, B.M., 1997. Microbial biomineralization of magnetic iron minerals: microbiology, magnetism and environmental significance. Geomicrobiology: interatctions between microbes and minerals. Reviews in Mineralogy, 181-223.

Bazylinski, D.A., Frankel, R.B., 2000. Biologically controlled mineralization of magnetic iron minerals by magnetotactic bacteria. In: Lovely DR (Ed.), Environmental Microbe-Metal Interactions. ASM Press, Washington, DC, pp. 109-143.

Bazylinski, D.A., Heywood, B.R., Mann, S., Frankel, R.B., 1993. Fe_3O_4 and Fe_3S_4 in a bacterium. Nature 366, 218.

Bazylinski, D.A., Garratt-Reed, A.J., Frankel, R.B., 1994; Electron microscopic studies of magnetosomes in magnetotactic bacteria. Microscopy Research Technique 27, 389-401.

Bazylinski, D.A., Frankel, R.B., Heywood, B.R., Mann, S., King, J.W., Donaghay, P.L., Hanson, A.K., 1995. Controlled biomineralization of magnetite (Fe_3O_4) and Greigite (Fe_3S_4) in a magnetotactic bacterium. Applied and Environmental Microbiology 61, 3232-3239.

Blakemore, R., 1975. Magnetotactic Bacteria. Science 190, 377-379.

Canfield, D.E., Berner, R.A., 1987. Dissolution and pyritization of magnetite in anoxic marine seidments. Geochimica et Cosmochimica Acta 51, 645-659.

Carlut, J., Isambert, A., Bouquerel, H., Pecoits, E., Philippot, P., Vennin, E., Ader, M., Thomazo, C., Buoncristiani, J-F., Baton, F., Muller, E., Deldicque, D., 2015. Low temperature magnetic properties of the Late Archean Boolgeeda iron formation (Hamersley Group, Western Australia): environmental implications. Frontiers in Earth Science 3 (Article 18), 1-14.

Chang, S.B.R., 1988. Bacterial magnetite in sedimentary deposits and its geophysical and paleological implication. Ph.D. Thesis, California Institute of Technology, Pasadena, CA.

Cui, Y.L., Verosub, K.L., Roberts, A.P., 1994. The effect of maghemitization on large multidomain magnetite. Geophysical Research Letters 21, 757-760.

Dong, H., Fredrickson, J.K., Kennedy, D.W., Zachara, J.M., Kukkadapu, R.K., Onstott, T.C., 2000. Mineral transformation associated with the microbial reduction of magnetite. Chemcial Geology 169, 299-318.

Frankel, R.B., Bazylinski, D.A., 1994. Magnetotaxis and magnetic particles in bacteria. Hyperfine Interactions 90, 135-142.

Frankel, R.B., Bazylinski, D.A., Johnson, M.S., Taylor, B.L., 1997. Magneto-aerotaxis in marine coccoid bacteria. Biophysical Journal 73, 994-1000.

Heywood, B.R., Bazylinski, D.A., Garratt-Reed, A.J., Frankel, R.B., 1990. Controlled biosynthesis of greigite (Fe_3S_4) in magnetotactic bacteria. Naturwissenschaften 77, 536-538.

Hounslow, M.W., Maher, B.A., 1996. Quantitative extraction and analysis of carriers of magnetization in sediments. Geophysical Journal International 124, 57-74.

Iizumi, M., Koetzle, T.F., Shirane, G., Chikazumi, S., Matsui, M., Todo, S., 1982. Structure of Magnetite (Fe3O4) below the Verwey Transition Temperature. Acta Crystallographica section B 38, 2121-2133.

Karlin, R., 1990a. Magnetic mineral diagenesis in submoxic sediments at Bettis site W-N- NE Paceific Ocean. Journal of Geophysical Research 95, 4421-4436.

Karlin, R., 1990b. Magnetite diagenesis in marine seidments from the Oregon continental margin. Journal of Geophysical Research 95, 4405-4419.

Karlin, R., Levi, S., 1983. Diagneesis of magnetic minerals in recenct haemipelagic sediments. Nature 303, 327-330.

Kirschvink, J.L., 1980. South-seeking magnetic bacteria. Journal of Experimental Biology 86, 345-347.

Kobayashi, A., Kirschvink, J.L., Nash, C.Z., Kopp, R.E., Sauer, D.A., Bertani, L.E., Voorhout, W.F., Taguchi, T., 2006. Experimental observation of magnetosome chain collapse in magnetotactic bacteria: sedimentological, paleomagnetic, and evolutionary implications. Earth and Planetary Science Letters 245, 538-550.

Kopp, R.E., Nash, C.Z., Kobayashi, A., Weiss, B.P., Bazylinski, D.A., Kirschvink, J.L., 2006. Ferromagnetic resonance spectroscopy for assessment of magnetic anisotropy and magnetostatic interactions: a case study of mutant magnetotactic bacteria. Journal of Geophysical Research 111, B12S25.

Kopp, R.E., Kirschvink, J.L., 2008. The identification and biogeochemical interpretation of fossil magnetotactic bacteria. Earth-Science Reviews 86, 42-61.

Kostka, J.E., Nealson, K.H., 1995. Dissolution and reduction of magnetite by bacteria. Environmental Science and Technology 29, 2535-2540.

Lin, W., Paterson, G.A., Zhu, Q., Wang, Y., Kopylova, E., Li, Y., Knight, R., Bazylinski, D.A., Zhu, R., Kirschvink, J.L., Pan, Y., 2017. Origin of microbial biomineralization and magnetotaxis during the Archean.

Maher, B.A., Thompson, R., Hounslow, M.W., 1999. Introduction. In: Maher, B.A., Thompson, R., (Eds.), Quaternary Climates, Environments, and Magnetism. Cambridge University Press, Cambridge, pp. 1-48.

Mann, S., Sparks, N.H.C., Board, R.G., 1990a. Magnetotactic bacteria: microbiology, biomineralization, paleomagnetism, and biotechnology. Advances in Microbial Physiology 31, 125-181.

Mann, S., Sparks, N.H.C., Frankel, R.B., Bazylinski, D.A., Jannasch, H.W., 1990b. Biomineralization of ferrimagnetic greigite (Fe3S4) and iron pyrite (FeS2) in magnetotactic bacterium. Nature 343, 258-261.

Montgomery, P., Hailwood. E.A., Gale, A.S., Burnett, J.A., 1998. The magnetostratigraphy of Coniacian late Campanian chalk sequences in southern England. Earth and Planetary Science Letters 156, 209-224.

Moskowitz, B.M., Frankel, R.B., Bazylinski, D.A., 1993. Rock magnetic criteria for the detection of biogenic magnetite. Earth and Planetary Science Letters 120, 283-300.

Moskowitz, B.M., Bazylinski, D.A., Egli, R., Frankel, R.B., Edwards, K.J., 2008. Magnetic properties of marine magnetotactic bacteria in a seasonally stratified coastal pond (Salt Pond, Ma, USA).

Özdemir, Ö., Dunlop, D.J., Moskowitz, B.M., 1993. The effect of oxidation on the Verwey transition in magnetite. Geophysical Research Letters 20, 1671-1674.

Özdemir, Ö., Dunlop, D.J., 2010. Hallmarks of maghemitization in low-temperature remanence cycling of partially oxidized magnetite nanoparticles. Journal of Geophysical Research 115, B02101.

Philippot, P., Ávila, J.N., Killingsworth, B.A., Tessalina, S., Baton, F., Caquineau, T., Muller, É., Pecoits, E., Cartigny, P., Lalonde, S.V., Ireland, T.R., Thomazo, C., Van Kranendonk, M.J., and Busigny, V., 2018, Globally asynchronous sulphur isotope signals require re-definition of the Great Oxidation Event. Nature Communications 9, 2245, doi: 10.1038/s41467-018-04621-x.

Prozoroz, R., Prozorov, T., Mallapragada, S.K., Narasimhan, B., Williams, T.J., Bazylinski, D.A., 2007. Magnetic irreversibility and the Verwey transition in nanocrystalline bacterial magnetite. Physical Reviews B 76, 054406.

Verwey, E.J.W., 1939. Electronic conduction of magnetite (Fe3O4) and its transition point at low temperatures. Nature 144, 327-328.

Warchola, T., Lalonde, S.V., Pecoits, E., von Gunten, K., Robbins, L.J., Alessi, D.S., Philippot, P., Konhauser, K.O., in press. Petrology and Geochemistry of the Boolgeeda Iron Formation, Hamersley Basin, Western Australia. Precambrian Research 316, 155-173.

Weiss, B.P., Kim, S.S., Kirschvink, J.L., Kopp, R.E., Sankaran, M., Kobayashi, A., Komeili, A., 2004. Ferromagnetic resonance and low temperature magnetic tests for biogenic magnetite. Earth and Planetary Science Letters 224, 73-89.

Xu, W.X., Peacor, D.R., Dollase, W.A., Van Der Voo, R., Beaubouef, R., 1997. Transformation of titanomagnetite to titanomaghemite: a slow, two-step, oxidation-ordering process in MORB. American Mineralogist 82, 1101-1110.
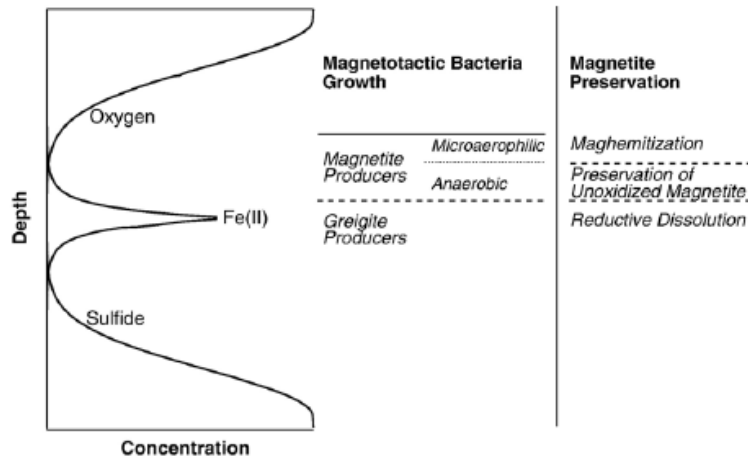
7. Figures (Chapter 4)

Fig. 1. Schematic representation of chemical gradients, typical optimal growth positions of different types of magnetotactic bacteria, and typical diagenetic fates of magnetite. Redox gradients can exist over scales from millimeters to meters.

Figure 4.1. Narrow redox conditions typically inhabited by magnetotactic bacteria.
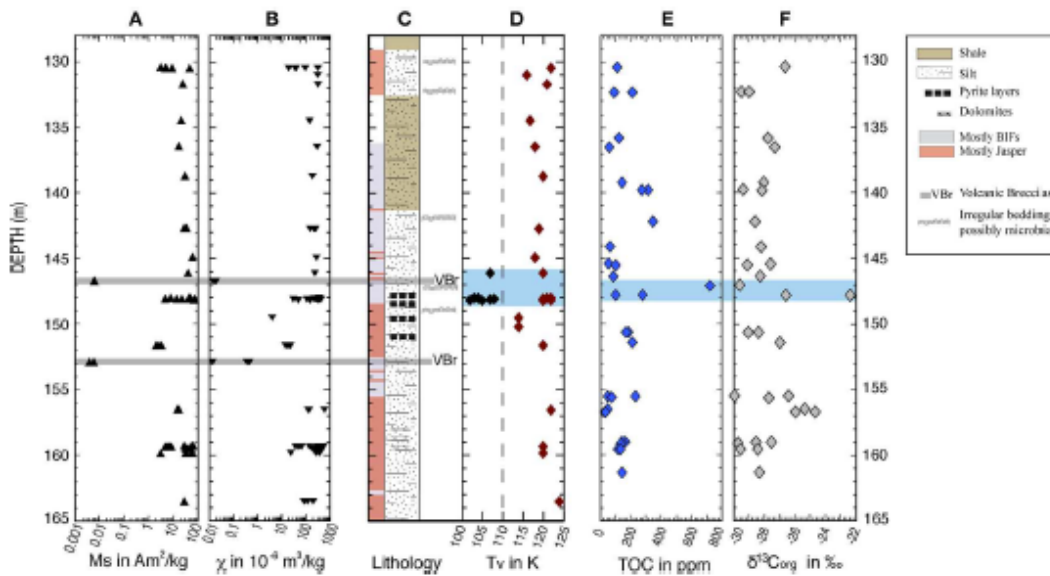

FIGURE 10 | Magnetic parameters, simplified lithology, TOC and $\delta^{13}C_{org}$ results and as a function of depth: (A) saturation magnetization Ms; (B) Mass normalized susceptibility; (C) lithology; **(D) Verwey Temperature; (E) Total Organic Carbon (TOC) and (F) $\delta^{13}C_{org}$. Gray area in (A–C) indicates volcanic breccias; blue area in (D) underlines the two T_V interval and anomalous TOC and $\delta^{13}C_{org}$ in (E,F).**

Figure 4.2. Figure 10 from Carlut et al. (2015) showing the interval containing 2 Verwey transition temperatures.
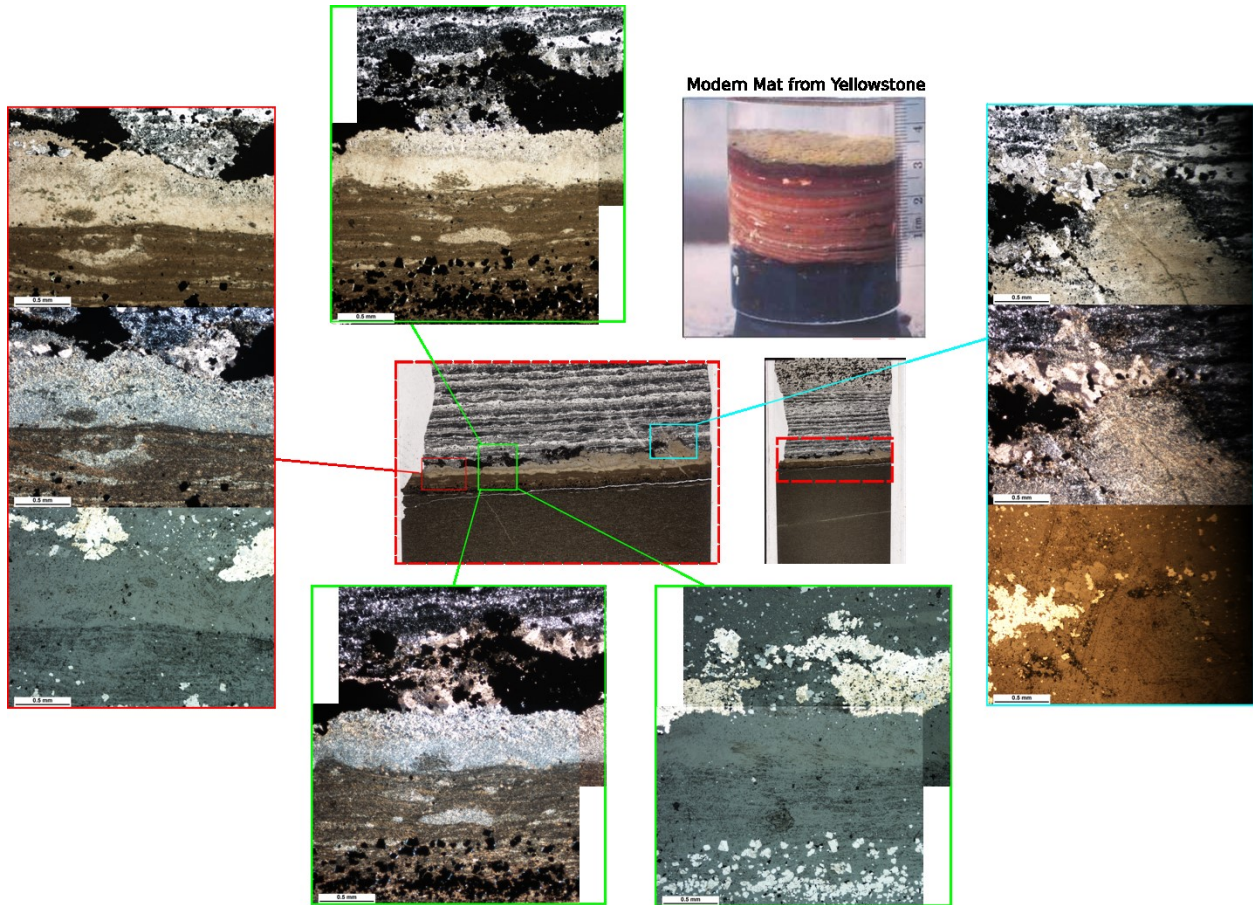
Figure 4.3. Possible microbial mat preserved in the Boolgeeda IF. Note the similarity between a modern mat from Yellowstone Hot Springs and a cross section of the boundary between the green mudstone/siltstone and the overlying BIF. The thin section (center right) is approximately 3 cm in length. The microbial interval is approximately 3 mm thick. Coloured boxes represent enlarged images of the microbial interval, captured by plane-polarized, cross-polarized, and reflected light. Note the domal structures prevalent throughout, and the green-brown to reddish brown banding found above euhedral magnetites at the base. One-two mm "pockets" of pyrite and carbonate appear to alternate laterally along the surface of the domal structures.

Modern Mat from Yellowstone

Boolgeeda Mat in thin section

Figure 4.4. Close up of thin section and mat comparison.

**Figure 4.5. SEM-EDS maps through a segment of the mat structure.**
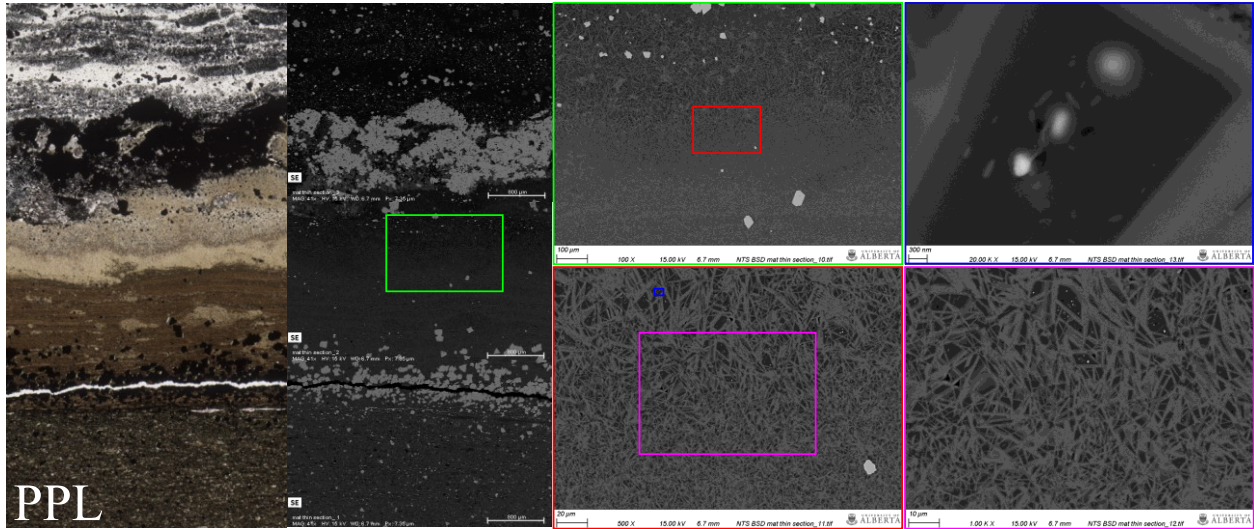
Figure 4.6. Location of nano-scale (~50-100 nm) spherical Fe-oxides. These features are found at the boundary of the dark mat layer and light mat layer. The coloured boxes outline the location of each blown up image.
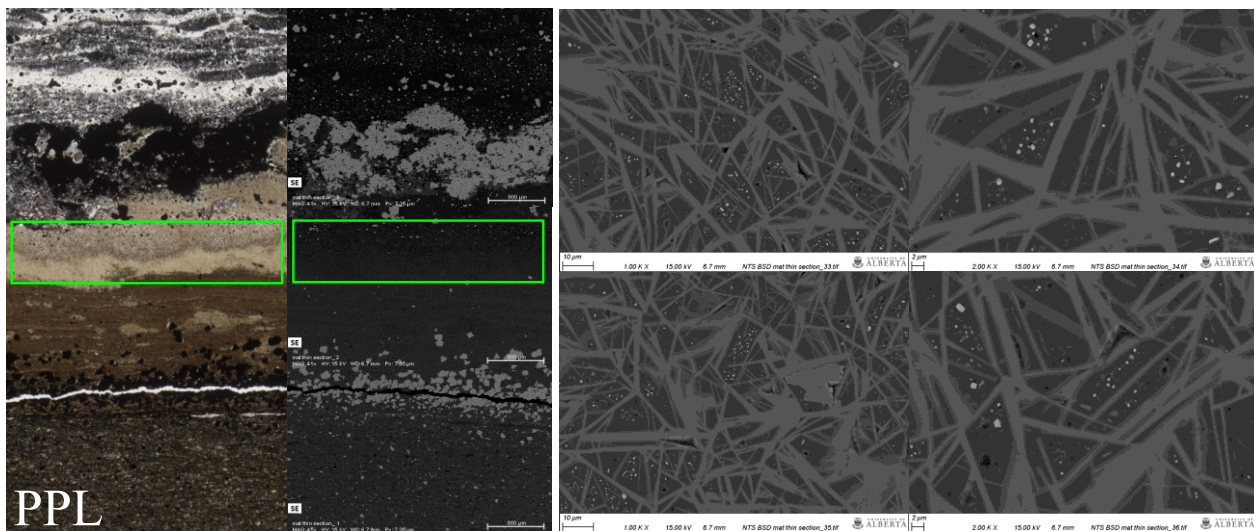

Figure 4.7. Spherical nano-scale magnetite only found in a single layer at the boundary of the light beige colored mat layer and the darker brown-green colored mat layer. This is interesting because we would expect magnetotactic bacteria to inhabit the boundary between oxygen rich and oxygen poor conditions. If this is a mat structure and if these are remnants of magnetotactic bacteria, the magnetofossils are in the location we would expect them to be.
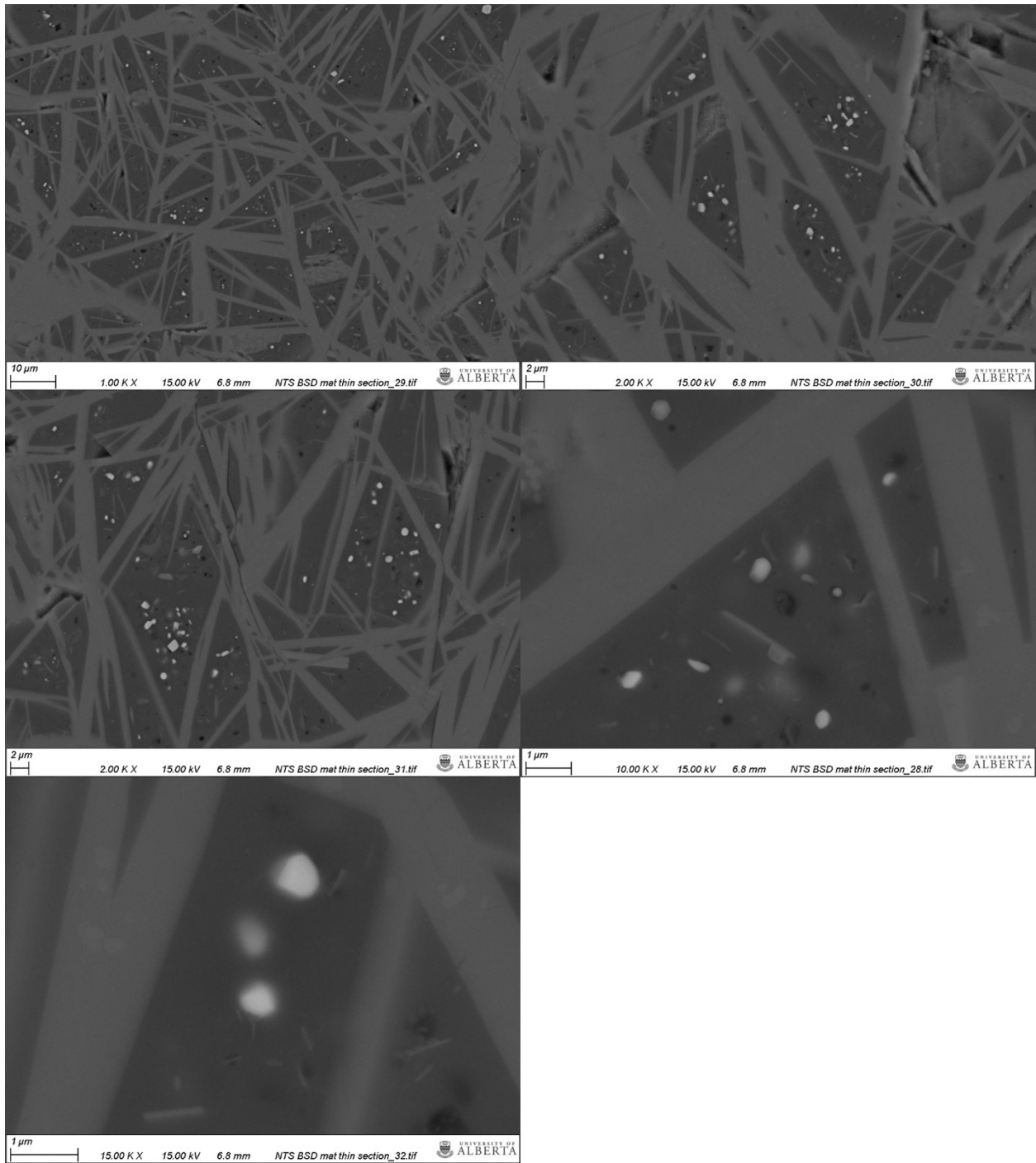
Figure 4.8. More examples of nano-scale spherical Fe-oxide textures.
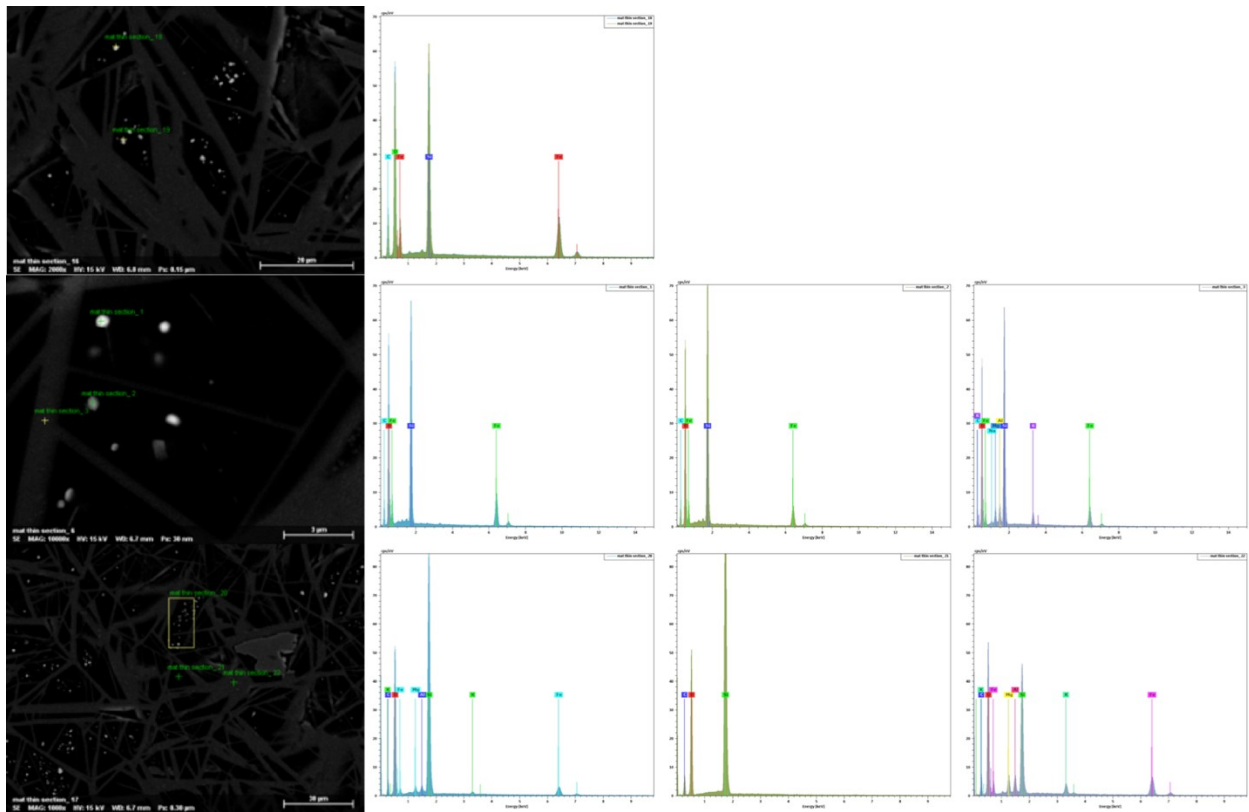
Figure 4.9. EDS spectra of various phases in thin section. The nano-scale spherical features in the mat layer are Fe-oxides. Surrounding matrix is silica. The bladed mineral is some form of Fe, K, Al, Mg clay (perhaps diagenetic product of mat degradation?). The spaces in between the clays are completely silicified. This mat may have been preserved by silicification as overlying BIF deposition took place.
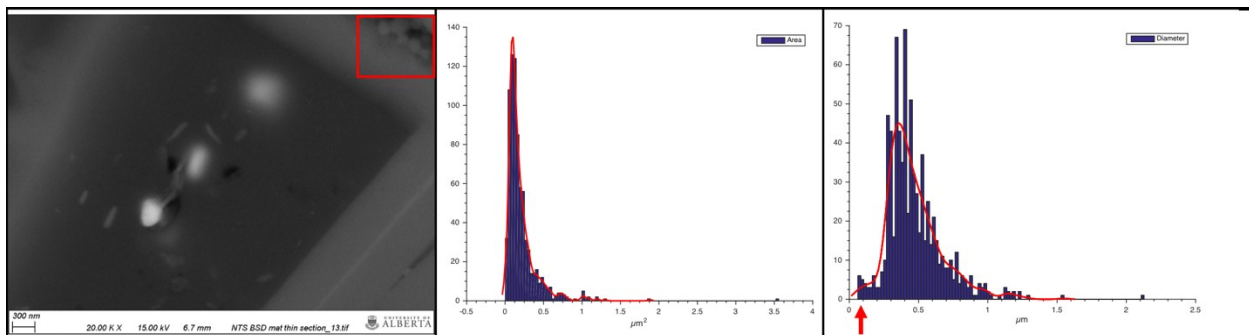
Figure 4.10. Statistical histograms for the area and diameter (calculated assuming spherical grains) of Fe-oxide grains identified using SEM. The majority of grains analyzed were bright white and spherical to elongated, as displayed in the image on the farthest left. However, a small shoulder appeared in the diameter histogram with a secondary peak around 90 nm (red arrow). This shoulder may represent a secondary Fe-oxide phase not previously identified in SEM. This phase may be present in the top right corner of the left SEM image (highlighted by the red box).

Chapter 5: Summary and Conclusions

1. Summary and Conclusions

Three cores collected as part of the Turee Creek Drilling Program (TCDP) were analyzed for major and trace element geochemistry in hopes of identifying geochemical anomalies tied to the rise of atmospheric oxygen at the onset of the Great Oxidation Event (GOE). This search was inspired by the discovery that sulfur isotopic signatures indicative of mass-independent fractionation (MIF-S) had been recycled throughout deposition of sediments comprising the TCDP cores (Philippot et al., 2018). This supports previous theoretical models purporting recycling of MIF-S (Reinhard et al., 2013). The specific goals of this project, listed in the introduction, were to:

(1) Produce a chemostratigraphic dataset of all TCDP cores, with emphasis on TCDP1,

(2) Determine whether redox proxies indicative of oxic conditions at the time of deposition are present within the TCDP sediments,

(3) Assess whether sedimentological processes and/or variations in lithology influence the preservation of reliable redox proxies, and if so, to what degree,

(4) Determine if the Mn enrichments present within the TCDP cores represent primary Mn oxides indicative of highly oxidative conditions at the time of deposition,

(5) Attempt to tie any redox proxies found within the TCDP sediments to those found in other time equivalent deposits, specifically Mn enrichments in South Africa, and

(6) Explore the possibility of preserved magnetofossils in the Boolgeeda Iron Formation and consider implications for environmental conditions at this time.

Goals 1 through 3 were addressed in Chapter 2. Resulting chemostratigraphic profiles and geochemical proxies acquired for TCDP1 were published in:

> Warchola, T., Lalonde, S.V., Pecoits, E., von Gunten, K., Robbins, L.J., Alessi, D.S., Philippot, P., Konhauser, K.O., in press. Petrology and Geochemistry of the Boolgeeda Iron Formation, Hamersley Basin, Western Australia. Precambrian Research 316, 155-173.

Conclusions drawn in the publication suggest shallow oxic water conditions overlying anoxic ferruginous conditions were present during Boolgeeda Iron Formation deposition. The presence of true negative Ce anomalies, particularly in the deeper water banded iron formation units, confirm shallow water oxic conditions. Trace element concentrations and proxies for O_2 levels appeared to be strongly influence by detrital influx. This conclusion was drawn from the sinusoidal pattern of the Y/Ho ratio, Ce anomaly depth plot, and suppression of negative Ce anomalies and positive Eu anomalies with increasing Al_2O_3 (wt.%) concentrations. Iron speciation through the core suggested significant changes in redox conditions moving stratigraphically upward. The most dramatic change in Fe speciation occurred at 160 m depth in TCDP1, which coincide with the disappearance of MIF-S and rampant sulphate reduction as indicated by S-isotopes (Philippot et al., 2018). One sample analyzed from the overlying Kungarra mudstone also suggested conditions approached euxinia. Collectively, all observations suggest oxic weathering of reduced sulfides led to euxinic shallow water conditions close to the continental margin. This interpretation is supported by the Cr/Ti proxy, which fits the trend of progressively increasing Cr/Ti molar ratios leading up to deposition of the Timeball Hill Formation (2.32 Ga), which is interpreted to represent the apogee of sulfide weathering (Konhauser et al., 2011).

Goals 4 and 5 were addressed in Chapter 3. Textural observations, sequential extractions, elemental mapping, and X-ray diffraction all suggested Mn is hosted within carbonates in the TCDP cores. These carbonates range in composition from manganoan dolomite to ankerite to kutnohorite. It appears all Mn rich carbonates belong to the ankerite-kutnohorite series $[Ca(Fe[II],Mg)(CO_3)_2$ to $Ca(Mn[II])(CO_3)_2]$. Textural relationships of Mn carbonates, including interbedding of carbonate and mudstone layers, suggest Mn enrichments are primary, aside from the possibility of further Mn enrichment as a result of dissolution and reprecipitation processes encountered during burial diagenesis. Manganese rich 'eyelet' structures in TCDP1 suggest enrichment occurred prior to greenschist metamorphism. Similar minerology (particularly kutnohorite) has been reported in the Koegas Subgroup of South Africa which was attributed to the reduction of primary Mn oxides (Johnson et al., 2016). However, trace element and Mo isotope data offer inconclusive results as to whether Mn enrichments in the TCDP cores were primary Mn oxides or not. Further work will be conducted to resolve these discrepancies, and a manuscript is in preparation to report the results (Thoby et al., in prep). In general, the progressive increase in the degree of Mn enrichment stratigraphically upwards through the TCDP cores is analogous to that observed in South Africa (Beukes, 1983).

Preliminary work has been completed in working towards goal 6. Initial results, described in Chapter 4, suggest it is worthwhile to further investigate the potential for magnetofossil preservation in TCDP1. A nanoscale Fe-oxide phase concentrated within an interval that perhaps represents the oxic-anoxic transition zone (OATZ) within an ancient silicified microbial mat could represent the oldest magnetofossils ever recorded. Further work using Ga-FIB and TEM to image the d-spacing of the phase in question will confirm whether or not it is magnetite. SIMS analyses for S and C isotopes will also be performed on the "pockets" of pyrite and carbonate overlying the

irregular surface of the structure to confirm whether these "pockets" were produced biogenically. If this record proves to be robust, it would have significant implications for marine redox conditions at the time of TCDP1 deposition and further implications for the depositional environment of BIF.

In conclusion, the period of geological time captured by the TCDP cores (2.45-2.22 Ga) represents one of the most significant periods of environmental change in Earth history. Work conducted in this thesis has provided a record of O_2 proxies which may now be compared with time analogous sections from around the world in hopes of better defining the dynamics of the rise of O_2 throughout the GOE. Although the work in this thesis represents a significant attempt to constrain changes in environmental conditions throughout the GOE, the complete picture has barely begun to take shape. The topic remains an interesting subject for future geoscientists to ponder.

2. References (Chapter 5)

Beukes, N.J., 1983. Palaeoenvironmental setting of iron-formations in the depositional basin of the Transvaal Supergroup, South Africa. In: Trendall AF, Morris RC (Eds), Iron-Formation: Facts and Problems. Elsevier, Amsterdam, pp. 131-209.

Johnson, J.E., Webb, S.M., Ma, C., Fischer, W.W., 2016. Manganese mineralogy and diagenesis in the sedimentary rock record. Geochimica et Cosmoschimica Acta 173, 210-231.

Konhauser, K.O., Lalonde, S.V., Planavsky, N.J., Pecoits, E., Lyons, T.W., Mojzsis, S.J., Rouxel, O.J., Barley, M.E., Rosiere, C., Fralick, P.W., Kump, L.R., Bekker, A., 2011. Aerobic bacterial pyrite oxidation and acid rock drainage during the Great Oxidation Event. Nature 478, 369-373.

Philippot, P., Ávila, J.N., Killingsworth, B.A., Tessalina, S., Baton, F., Caquineau, T., Muller, E., Pecoits, E., Cartigny, P., Lalonde, S.V., Ireland, T.R., Thomazo, C., van Kranendonk, M.J., Busigny, V., 2018. Globally asynchronous sulphur isotope signals require re-definition of the Great Oxidation Event. Nature Communications 9, 2245

Reinhard, C.T., Planavsky, N.J., Lyons, J.R., 2013. Long-term sedimentary recycling of rare sulphur isotope anomalies. Nature 497, 100-104.

Bibliography

Ahn, J.H., Buseck, P.R., 1990. Hematite nanospheres of possible colloidal origin from a Precambrian banded iron formation. Science 250, 111-113.

Alexander, B.W., Bau, M., Andersson, P., Dulski, P., 2008. Continentally-derived solutes in shallow Archean seawater: Rare earth element and Nd isotope evidence in iron formation from the 2.9 Ga Pongola Supergroup, South Africa. Geochimica et Cosmochimica Acta 72, 378-394.

Algeo, T.J., Lyons, T.W., 2006. Mo-total organic carbon covariation in modern anoxic marine environments: implication for analysis of paleoredox and paleohydrographic conditions. Paleoceanography 21, PA1016.

Algeo, T.J., Tribovillard, N., 2009. Environmental analysis of paleoceanographic systems based on molybdenum-uranium covariation. Chemical Geology 268, 211-225.

Alibert, C., McCulloch, M.T., 1993. Rare earth element and neodymium isotopic compositions of banded iron formations and associated shales from Hamersley, Western Australia. Geochimica et Cosmochimica Acta 57, 187-204.

Aller, R.C., Diagenetic processes near the sediment-water interface of long island sound. II. Fe and Mn. Advances in Geophysics 22, 351-415.

Arndt N.T., Nelson D.R., Compston W., Trendall A.F., Thorne A.M., 1991. The age of the Fortescue Group, Hamersley Basin, Western Australia, from iron microprobe zircon U-Pb results. Australian Journal of Earth Science, 38, 261-281.

Asael, D., Tissot, F.L.H., Reinhard, C.T., Rouxel, O., Dauphas, N., Lyons, T.W., Ponzevera, E., Liorzou, C., Chéron, S., 2013. Coupled molybdenum, iron and uranium stable isootpes as oceanic paleoredox proxies during the Paleoproterozoic Shunga Event. Chemical Geology 362, 193-210.

Awramik, S.M., Schopf, J.W., Walter, M.R., 1983. Filamentous fossil bacteria from the Archean of Western Australia. Precambrian Research 20, 357-374.

Ayres, D.E., 1972. Genesis of Iron-bearing minerals in banded iron formation mesobands in the Dales Gorge Member, Hamersley Group, Western Australia. Economic Geology 67, 1214-1233.

Balkwill, D.L., Maratea, D., Blakemore, R.P., 1980. Ultrastructure of magnetic spirillum. Journal of Bacteriology 141, 1399-1408.

Ballantyne, J.M., Moore, J.N., 1988. Arsenic geochemistry in geothermal systems. Geochimica et Cosmochimica Acta 52, 475-483.

Barley, M.E., 1987. The archaean Whim Creek Belt, an ensialic fault-bounded basin in the Pilbara Block, Australia. Precambrian Research 37, 199-215.

Barley, M.E., Pickard, A.L., Sylvester, P.J., 1997. Emplacement of a large igneous province as a possible cause of banded iron formation 2.45 billion years ago. Nature 385, 55-58.

Barling, J., Arnold, G.L., Anbar, A.D., 2001. Natural mass-dependent variations in the isotopic composition of molybdenum. Earth and planetary Science Letters 193, 447-457.

Barlow, E., Van Kranendonk, M. J.., Yamaguchi, K. E., Ikehara, M., 2016. Lithostratigraphic analysis of a new stromatolite – thrombolite reef from across the rise of atmospheric oxygen in the Paleoproterozoic Turee Creek Group, Western Australia.

Barrett, T.J., Fralick, P.W., Jarvis, I., 1988. Rare-earth-element geochemistry of some Archean iron formations north of Lake Superior, Ontario. Canadian Journal of Earth Sciences 25, 570-580.

Bau, M., 1991. Rare-earth element mobility during hydrothermal and metamorphic fluid-rock interaction and the significance of the oxidation state of europium. Chemical Geology 93, 219-230.

Bau, M., 1996. Controls on the fractionation of isovalent trace elements in magmatic and aqueous systems: Evidence from Y/Ho, Zr/Hf, and lanthanide tetrad effect. Contributions to Mineralogy and Petrology 123, 323-333.

Bau, M., 1999. Scavenging of dissolved yttrium and rare earths by precipitating iron oxyhydroxide: experimental evidence for Ce oxidation, Y-Ho fractionation, and lanthanide tetrad effect. Geochimica et Cosmochimica Acta 63, 67-77.

Bau, M., Möller, P., 1993. Rare earth element systematics of the chemically precipitated component in Early Precambrian iron formations and the evolution of the terrestrial atmosphere-hydrosphere-lithosphere system. Geochimica et Cosmochimica Acta 57, 2239-2249.

Bau, M., Dulski, P., 1996. Distribution of yttrium and rare-earth elements in the Penge and Kuruman iron-formations, Transvaal Supergroup, South Africa. Precambrian Research 79, 37–55.

Bau, M., Möller, P., Dulski, P., 1997. Yttrium and lanthanides in eastern Mediterranean seawater and their fractionation during redox-cycling. Marine Chemistry 56, 123-131.

Bau, M., Dulski, P., 1999. Comparing yttrium and rare earths in hydrothermal fluids from the Mid-Atlantic Ridge: implications for Y and REE behavior during near-vent mixing and for the Y/Ho ratio of Proterozoic seawater. Chemical Geology 155, 77-90.

Bau, M., Romer, R. L., Lüders, V., Beukes, N. J., 1999. Pb, O, and C isotopes in silicified Mooidraai dolomite (Transvaal Supergroup, South Africa): implications for the composition of Paleoproterozoic seawater and 'dating' the increase of oxygen in the Precambrian atmosphere. Earth and Planetary Science Letters 174, 43–57

Bau, M., Koschinsky, A., 2009. Oxidative scavenging of cerium on hydrous Fe oxide: Evidence from the distribution of rare earth elements and yttrium between Fe oxides and Mn oxides in hydrogenetic ferromanganese crusts. Geochemical Journal 43, 37-47.

Baur, M.E., Hayes, J.M., Studley, S.A., Walter, M.R., 1985. Millimeter-Scale Variations of Stable Isotope Abundances in Carbonates from Banded Iron-Formations in the Hamersley Group of Western Australia. Economic Geology, 80, 270-282.

Bazylinski, D.A., 1996. Controlled biomineralization of magnetic minerals by magnetotactic bacteria. Chemical Geology 132, 191-198.

Bazylinski, D.A., Blakemore, R.P., 1983. Denitrification and assimilatory nitrate reduction in Aquaspirillum magnetotacticum. Applied and Environmental Microbiology 46, 1118-1124.

Bazylinski, D.A., Moskowitz, B.M., 1997. Microbial biomineralization of magnetic iron minerals: microbiology, magnetism and environmental significance. Geomicrobiology: interatctions between microbes and minerals. Reviews in Mineralogy, 181-223.

Bazylinski, D.A., Frankel, R.B., 2000. Biologically controlled mineralization of magnetic iron minerals by magnetotactic bacteria. In: Lovely DR (Ed.), Environmental Microbe-Metal Interactions. ASM Press, Washington, DC, pp. 109-143.

Bazylinski, D.A., Heywood, B.R., Mann, S., Frankel, R.B., 1993. Fe_3O_4 and Fe_3S_4 in a bacterium. Nature 366, 218.

Bazylinski, D.A., Garratt-Reed, A.J., Frankel, R.B., 1994; Electron microscopic studies of magnetosomes in magnetotactic bacteria. Microscopy Research Technique 27, 389-401.

Bazylinski, D.A., Frankel, R.B., Heywood, B.R., Mann, S., King, J.W., Donaghay, P.L., Hanson, A.K., 1995. Controlled biomineralization of magnetite (Fe_3O_4) and Greigite (Fe_3S_4) in a magnetotactic bacterium. Applied and Environmental Microbiology 61, 3232-3239.

Becker, R. H., Clayton, R. N., 1972. Carbon isotopic evidence for the origin of a banded iron-formation in Western Australia. Geochimica et Cosmochimica Acta 36, 577-595.

Becker, R. H., Clayton, R. N., 1976. Oxygen isotope study of a Precambrian banded iron-formation, Hamersley Range. Western Australia. Geochimica et Cosmochimica Acta 40, 1153-1165.

Bekker, A., Kaufman, A.J., Karhu, J.A., Beukes, N.J., Swart, Q.D., Coetzee, L.L., Eriksson, K.A., 2001. Chemostratigraphy of the Paleoproterozoic Duitschland Formation, South Africa: implications for coupled climate change and carbon cycling. American Journal of Science 301, 261-285.

Bekker, A., Holland, H.D., Wang, P.-L., Rumble III, D., Stein, H.J., Hannah, J.L., Coetzee, L.L., Beukes, N.J., 2004. Dating the rise of atmospheric oxygen. Nature 427, 117-120.

Bekker, A., Slack, J., Planavsky, N., Krapež, B., Hofmann, A., Konhauser, K.O., Rouxel, O.J., 2010. Iron formation: the sedimentary product of a complex interplay among mantle, tectonic, oceanic, and biospheric processes. Economic Geology 105, 467-508.

Bekker, A. and Planavsky, N. and Rasmussen, B. and Krapez, B. and Hofmann, A. and Slack, J. and Rouxel, O. et al. 2014. Iron Formations: Their origins and implications for ancient seawater chemistry, in Holland, H. and Turekian, K. (ed), Treatise on Geochemistry, Vol. 9, pp. 561-628. Netherlands: Elsevier.

Berner, R.A., 1970. Sedimentary pyrite formation. American Journal of Science 268, 1-23.

Beukes, N.J., 1983. Palaeoenvironmental setting of iron-formations in the depositional basin of the Transvaal Supergroup, South Africa. In: Trendall AF, Morris RC (Eds), Iron-Formation: Facts and Problems. Elsevier, Amsterdam, pp. 131-209.

Beukes, N.J., Klein, C., 1990. Geochemistry and sedimentology of a facies transition – from microbanded to granular iron-formation – in the early Proterozoic Transvaal Supergroup, South Africa. Precambrian Research 47, 99-139.

Beukes, N.J., Gutzmer, J., 2008. Origin and paleoenvironmental significance of major iron formations at the Archean-Paleoproterozoic boundary. Society of Economic Geology Reviews 15, 5-47.

Blake, T.S., 1993. Late Archaean crustal extension, sedimentary basin formation, flood basalt volcanism and continental rifting: the Nullagine and Mount Jope Supersequences, Western Australia. Precambrian Research 60, 185-241.

Blake T.S., and Barley M.E., 1992. Tectonic evolution of the Late Archaean to Early Proterozoic Mount Bruce Megasequence. Tectonics II, 1415-1425.

Blake T.S., Buick R., Brown S.J.A., Barley M.E., 2004. Geochronology of a late Archaean flood basalt province in the Pilbara Craton, Australia: constraints on basin evolution, volcanic and sedimentary accumulation and continental drift rates. Precambrian Research 133, 143-173.

Blakemore, R., 1975. Magnetotactic Bacteria. Science 190, 377-379.

Blockley, J.G., 1979. A contribution to the stratigraphy of the Marra Mamba Iron Formation. Geologial Survey of Western Australia Annual Report.

Blockley, J.G., Tehnas, I.J., Mandyczewsky, A., Morris, R.C., 1993. Proposed stratigraphic subdivisions of the Marra Mamba Iron Formation and the lower Wittenoom Dolomite, Hamersley Group, Western Australia. Geological Survey of Western Australia Report.

Bloemsma, M.R., 2015. Development of a Modelling Framework for Core Data Integration using XRF Scanning. University of Leuven PhD Thesis Dissertation.

Boetius A., Ravenschlag K., Schubert C.J., Rickert D., Widdel F., Gieseke A., Amann R., Jorgensen B.B., Witte U., Pfannkuche O., 2000. A marine microbial consortium apparently mediating anaerobic oxidation of methane. Nature, 407, 623-626.

Bolhar, R., Kamber, B.S., Moorbath, S., Fedo, C.M., Whitehouse, M.J., 2004. Characterisation of early Archaean chemical sediments by trace element signatures. Earth and Planetary Science Letters 222, 43-60.

Bolhar, R., Van Kranendonk, M.J., 2007. A non-marine depositional setting for the northern Fortescue Group, Pilbara Craton, inferred from trace element geochemistry of stromatolitic carbonates. Precambrian Research, 155, 229-250.

Bons, P.D., den Brok, B., 2000. Crystallographic preferred orientation development by dissolution-precipitation creep. Journal of Structural Geology 22, 1713-1722.

Brand, U., Veizer J., 1980. Chemical diagenesis of multicomponent carbonate system-1. Trace elements. Journal of Sedimentary Petrology 50, 1219-1250.

Brewer, P.G., Spencer, D.W., 1974. Distribution of some trace elements in the Black Sea and their flux between dissolved and particulate phases. American Association of Petroleum Geologists Bulletin Memoir 20, 137-143.

Bühn, B., Stanistreet, I.G., 1997. Insight into the enigma of Neoproterozoic manganese and iron formations from the perspective of supercontinental break-up and glaciation. Geological Society, London, Special Publications 119, 81-90.

Buick R., 1992. The antiquity of oxygenic photosynthesis: evidence from stromatolites in sulphate-deficient Archean lakes. Science 255, 74-77.

Buick R., 2008. When did oxygenic photosynthesis evolve? Philosophical Transactions of the Royal Society B: Biological Sciences 363, 2731-2743.

Calvert, S.E., Pedersen, T.F., 1996. Sedimentary geochemistry of manganese; implications for the environment of formation of manganiferous black shales. Economic Geology 91, 36-47.

Canfield, D.E., 2001. Isotope fractionation by natural populations of sulfate-reducing bacteria. Geochimica et Cosmochimica Acta, 65, 1117-1124.

Canfield, D.E., Berner, R.A., 1987. Dissolution and pyritization of magnetite in anoxic marine seidments. Geochimica et Cosmochimica Acta 51, 645-659.

Canfield, D.E., Raiswell, R., Bottrell, S.H., 1992. The reactivity of sedimentary iron minerals toward sulfide. American Journal of Science, 296, 818-834.

Caquineau, T., Paquette, J.-L., Philippot, P., 2018. U-Pb detrital zircon geochronology of the Turee Creek Group, Hamersley Basin, Western Australia: timing and correlation of the Paleoproterozoic glaciations. Precambrian Research 307, 34-50.

Carlut, J., Isambert, A., Bouquerel, H., Pecoits, E., Philippot, P., Vennin, E., Ader, M., Thomazo, C., Buoncristiani, J-F., Baton, F., Muller, E., Deldicque, D., 2015. Low temperature magnetic properties of the Late Archean Boolgeeda iron formation (Hamersley Group, Western Australia): environmental implications. Frontiers in Earth Science 3 (Article 18), 1-14.

Catuneanu, O. Principles of Sequence Stratigraphy. Elsevier, Amsterdam, 2006, 375 pp.

Catling D.C. and Clair M.W., 2005. How Earth's atmosphere evolved to an oxic state: a status report. Earth and Planetary Science Letters 237, 1-20.

Chandler, F.W., 1980. Proterozoic redbed sequences of Canada. In: Canadian Geological Survey Bulletin. 311 pp. 1-53.

Chang, S.B.R., 1988. Bacterial magnetite in sedimentary deposits and its geophysical and paleological implication. Ph.D. Thesis, California Institute of Technology, Pasadena, CA.

Chen, J.H., Edwards, R.L., Wasserburg, G.J., 1986. ^{238}U, ^{234}U and ^{232}Th in seawater. Earth and Planetary Science Letters 80, 241-251.

Clement, B.G., Luther III, G.W., Tebo, B.M., 2009. Rapid, oxygen-dependent microbial Mn(II) oxidation kinetics at sub-micromolar oxygen concentrations in the Black Sea suboxic zone. Geochimica et Cosmochimica Acta 73, 1878-1889.

Cloud, P., 1973. Paleoecological significance of the banded iron-formation. Economic Geology 68, 1135-1143.

Compston, W., Arriens, P.A., 1968. The Precambrian geochronology of Australia. Canadian Journal of Earth Sciences 5, 561-583.

Crowe, S.A., Døssing, L.A., Beukes, N.J., Bau, M., Kruger, S.J., Frei, R., Canfield, D.E., 2013. Atmospheric oxygenation three billion years ago. Nature 501, 535-538.

Crusius, J., Calvert, S., Pedersen, T., Sage, D., 1996. Rhenium and molybdenum enrichments in sediments as indicators of oxic, suboxic, and sulfidic conditions of deposition. Earth and Planetary Science Letters 145, 65-78.

Cui, Y.L., Verosub, K.L., Roberts, A.P., 1994. The effect of maghemitization on large multidomain magnetite. Geophysical Research Letters 21, 757-760.

Cullen, W.R., Reimer, K.J., 1989. Arsenic speciation in the environment. Chemical Reviews 89, 713-764.

Davy, R., 1992. Mineralogy and chemical composition of a core from the Weeli Wolli formation in the Hamersley Basin. Record - Geological Survey of Western Australia, 1991/6.

den Brok, S.W.J., Spiers, C.J., 1991. Experimental evidence for water weakening of quartzite by microcracking plus solution-precipitation creep. Journal of the Geological Society of London 148, 541-548.

Derry, L.A., Jacobsen, S.B., 1988. The Nd and Sr isotopic evolution of Proterozoic seawater. Geophysical Research Letters 15, 397-400.

Derry, L.A., Jacobsen, S.B., 1990. The chemical evolution of Precambrian seawater: Evidence from REEs in banded iron formations. Geochimica et Cosmochimica Acta 54, 2965-2977.

Derry, L.A., Kaufman, A.J., Jacobsen, S.B., 1992. Sedimentary cycling and environmental change in the late Proterozoic; evidence from stable and radiogenic isotopes. Geochimica et Cosmochimica Acta 56, 1317-1329.

Dong, H., Fredrickson, J.K., Kennedy, D.W., Zachara, J.M., Kukkadapu, R.K., Onstott, T.C., 2000. Mineral transformation associated with the microbial reduction of magnetite. Chemcial Geology 169, 299-318.

Egglseder, M.S., Cruden, A.R., Tomkins, A.G., Wilson, C.J.L., 2016. Deformation-induced silica redistribution in banded iron formation, Hamersley Province, Australia. Lithos 266-267, 87-97.

Egglseder, M.S., Cruden, A.R., Tomkins, A.G., Wilson, S.A., Langerdam, A.D., 2018. Colloidal origin of microbands in banded iron formations. Geochemical Perspectives Letters 6, 43-49.

Eigenbrode, J.L., Freeman, K.H., 2006. Late Archean rise of aerobic microbial ecosystems. Proceedings of the National Academy of Sciences of the United States of America 103, 15759-15764.

England, G.L., Rasmussen, B., Krapez, B., Groves, D.I., 2002. Paleoenvironmental significance of rounded pyrite in siliciclastic sequences of the Late Archean Witwatersrand Basin: oxygen-deficient atmosphere or hydrothermal alteration? Sedimentology 49, 1133-1156.

Ewers, W.E., Morris, R.C., 1981. Studies of the Dales Gorge Member of the Brockman Iron Formation, Western Australia. Economic Geology 76, 1929-1953.

Farquhar, J., Bao, H., Thiemens, M., 2000. Atmospheric influence of Earth's earliest sulfur cycle. Science 289, 756-758.

Farquhar, J., Bao, H., Thiemens, M., 2001. Atmospheric influence of Earth's earliest sulfur cycle. Science 289, 756-758.

Farquhar, J., Zerkle, A.L., Bekker, A., 2011. Geological constraints on the origin of oxygenic photosynthesis. Photosynthesis Research 107, 11-36.

Fischer, W.W., Knoll, A.H., 2009. An iron shuttle for deepwater silica in late Archean and early Paleoproterozoic iron formation. Geological Society of America Bulletin 121, 222-235.

Force, E.R., Maynard, J.B., 1991. Manganese: Syngenetic deposits on the margins of anoxic basins. Reviews in Economic Geology 5, 147–159.

Frankel, R.B., Bazylinski, D.A., 1994. Magnetotaxis and magnetic particles in bacteria. Hyperfine Interactions 90, 135-142.

Frankel, R.B., Bazylinski, D.A., Johnson, M.S., Taylor, B.L., 1997. Magneto-aerotaxis in marine coccoid bacteria. Biophysical Journal 73, 994-1000.

Frei, R., Crowe, S.A., Bau, M., Polat, A., Fowle, D.A., Dossing, L.N., 2016. Oxidative elemental cycling under the low O2 Eoarchean atmosphere. Scientific Reports 6, 1-9.

Fru, E.C., Arvestål, E., Callac, N., Albani, A.E., Kilias, S., Argyraki, A., Jakobsson, M., 2015. Arsenic stress after the Proterozoic glaciations. Scientific Reports 5, 17789.

Fryer, B.J., 1977a. Rare earth evidence in iron formations for changing Precambrian oxidation states. Geochimica et Cosmochimica Acta 41, 361-367.

Fryer, B.J., 1977b. Trace element geochemistry of the Sokoman Iron Formation. Canadian Journal of Earth Science 14, 1598-1610.

Godfrey, L.V., Falkowski, P.G., 2009. The cycling and redox state of nitrogen in the Archaean ocean. Nature Geoscience 2, 725-729.

Goldberg, E.D., 1954. Marine geochemistry. I. Chemical scavengers of the sea. Journal of Geology 62, 249-265.

Graf, J.L., 1978. Rare earth elements, iron formations and seawater. Geochimica et Cosmochimica Acta 42, 1845-1850.

Grandstaff, D.E., 1980. Origin of uraniferous conglomerates at Elliot Lake, Canada and Witwatersrand, South Africa: Implications for oxygen in the Precambrian atmosphere. Precambrian Research 13, 1-26.

Greene, G.W., Kristiansen, K., Meyer, E.E., Boles, J.R., Israelachvili, J.N., 2009. Role of electrochemical reactions in pressure solutions. Geochimica et Cosmochimica Acta 73, 2862-2874.

Gross, G.A., 1980. A classification of iron-formation based on depositional environments. The Canadian Mineralogist 18, 215-222.

Gross, G.A., 1983. Tectonic systems and the deposition of iron-formation. Precambrian Research 20, 171-187.

Grotzinger, J.P., Kasting, J.F., 1993. New constraints on Precambrian ocean composition. The Journal of Geology 101, 235-243.

Gumsley, A.P., Chamberlain, K.R., Bleeker, W., Söderlund, U., de Kock, M.O., Larsson, E.R., Bekker, A., 2017. Timing and tempo of the Great Oxidation Event. Proceedings of the National Academy of Sciences of the United States of America 114, 1811-1816.

Guo, Q., Strauss, H., Kaufman, A.J., Schröder, S., Gutzmer, J., Wing, B., Baker, M.A., Bekker, A., Jin, Q., Kim, S.-T., Farquhar, J., 2009. Reconstructing Earth's surface oxidation across the Archean-Proterozoic transition. Geology 37, 399-402.

Gutzmer J., Beukes, N.J., 1996. Mineral paragenesis oft he Kalahari manganese field, South Africa. Ore Geology Reviews 11, 405-428.

Hamade, T., Konhauser, K.O., Raiswell, R., Goldsmith, S., Morris, R.C., 2003. Using Ge/Si ratios to decouple iron and silica fluxes in Precambrian banded iron formations. Geology 31, 35-38.

Hansel, C.M., Learman, D.R., 2016. Chapter 18: Geobiology of Manganese. In: Ehrlich HL, Newman DK, Kappler A (Eds.) Ehrlich's Geomicrobiology Sixth Edition. Boca Raton: CRC Press, Taylor & Francis Group.

Haugaard, R., Pecoits, E., Lalonde, S., Rouxel, O., Konhauser, K.O., 2016. The Joffre banded iron formation, Hamersley Gorup, Western Australia: Assessing the palaeoenvironment through detailed petrology and chemostratigraphy. Precambrian Res. 273, 12-37.

Hayes, J.M., 1994. Global methanotrophy at the Archean-Proterozoic transistion. In: Bengtson, S. (Ed.), Early life on Earth. Columbia University Press, New York.

Helz, G.R., Miller, C.V., Charnock, J.M., Mosselmans, J.F.W., Pattrick, R.A.D., Garner, C.D., Vaughan, D.J., 1996. Mechanisms of molybdenum removal from the sea and its concentration in black shales: EXAFS evidence. Geochimica et Cosmochimica Act 60, 3631-3642.

Heywood, B.R., Bazylinski, D.A., Garratt-Reed, A.J., Frankel, R.B., 1990. Controlled biosynthesis of greigite (Fe_3S_4) in magnetotactic bacteria. Naturwissenschaften 77, 536-538.

Hickman, A.H., 1983. Geology of the Pilbara Block and its environs. Geological Survey of Western :Australia, Bulletin 127, 268 pp.

Hinrichs, K.U., 2002. Microbial fixation of methane carbon at 2.7 Ga: was an anaerobic mechanism possible. Geochemistry, Geophysics, Geosystems 3, 1-10.

Hofmann, A., Bekker, A., Rouxel, O.J., Rumble, D., Master, S., 2009. Multiple sulphur and iron isotope composition of detrital pyrite in Archaean sedimentary rocks: a new tool for provenance analysis. Earth and Planetary Science Letters 286, 436-445.

Holland, H.D., 1984. The Chemical Evolution of the Atmosphere and Oceans. Princeton University Press, Princeton NJ, pp. 1-598.

Holland, H.D., 2002. Volcanic gases, black smokers, and the Great Oxidation Event. Geochimica et Cosmochimica Acta 66, 3811-3826.

Holland, H.D., 2005. 100th Anniversary Special Paper: Sedimentary Mineral Deposits and Evolution of Earth's Near-Surface Environments. Economic Geology 100, 1489-1509.

Holland, H.D., 2006. The oxygenation of the atmosphere and oceans. Philosophical Transactions of the Royal Society B: Biological Sciences 361, 903-915.

Holland, D.H., Beukes, N.J., 1990. A paleoweathering profile from Griqualand West, South Africa: evidence for a dramatic rise in atmospheric oxygen between 2.2 and 1.9 BYBP. American Journal of Science 290-A, 1-34.

Horwitz, R.C., 1982. Geological history of the Early Proterozoic Paraburdoo hinge zone, Western Australia. Precambrian Research 19, 191-200.

Hounslow, M.W., Maher, B.A., 1996. Quantitative extraction and analysis of carriers of magnetization in sediments. Geophysical Journal International 124, 57-74.

Iizumi, M., Koetzle, T.F., Shirane, G., Chikazumi, S., Matsui, M., Todo, S., 1982. Structure of Magnetite (Fe3O4) below the Verwey Transition Temperature. Acta Crystallographica section B 38, 2121-2133.

Irwin, H., Curtis, C.D., Coleman, M.L., 1977. Isotopic evidence for the source of diagenetic carbonates formed during the burial of organic-rich sediments. Nature 269, 209-213.

Isley, A.E., 1995. Hydrothermal plumes and the delivery of iron to banded iron formations. The University of Chicago Press Journals 103, 169-185.

Isley, A.E., Abbott, D.H., 1999. Plume-related mafic volcanism and the deposition of banded iron formation. Journal of Geophysical Research 104, 15461-15477.

Jacobs, L., Emerson, S., Skei, J., 1985. Partitioning and transport of metals across the O_2/H_2S interface in a permanently anoxic basin: Framvaren Fjord Norway. Geochimica et Cosmochimica Acta 49, 1433-1444.

James, H.L., 1954. Sedimentary facies of iron-formation. Economic Geology 49, 235-293.

Jenne, E.A., 1968. Controls on Mn, Co, Ni, Cu, and Zn concentrations in soil and water: The significant role of hydrous Mn and Fe oxides. In: Gould RF (Ed.), Trace Inorganics in Water. Washinton, DC: American Chemical Society, pp. 337-387.

Johnson, J.E., Webb, S.M., Thomas, K., Ono, S., Kirschvink, J.L., Fischer, W.W., 2013. Manganese-oxidizing photosynthesis before the rise of cyanobacteria. Proceedings of the National Academy of Sciences of the United States of America 110, 11238-11243.

Johnson, J.E., Webb, S.M., Ma, C., Fischer, W.W., 2016. Manganese mineralogy and diagenesis in the sedimentary rock record. Geochimica et Cosmoschimica Acta 173, 210-231.

Kakegawa, T., Nanri, H., 2006. Sulfur and carbon isotope analyses of 2.7 Ga stromatolites, cherts and sandstones in the Jeerinah Formation, Western Australia. Precambrian Research, 148, 115-124.

Karlin, R., 1990a. Magnetic mineral diagenesis in submoxic sediments at Bettis site W-N- NE Paceific Ocean. Journal of Geophysical Research 95, 4421-4436.

Karlin, R., 1990b. Magnetite diagenesis in marine seidments from the Oregon continental margin. Journal of Geophysical Research 95, 4405-4419.

Karlin, R., Levi, S., 1983. Diagneesis of magnetic minerals in recenct haemipelagic sediments. Nature 303, 327-330.

Kashiwabara, T., Takahashi, Y., Tanimizu, M., Usui, A., 2011. Molecular-scale mechanisms of distribuition and isotopic fractionation of molybdenum between seawater and ferromanganese oxides. Geochimica et Cosmochimica Acta 75, 5762-5784.

Kay, J.T., Conklin, M.H., Fuller, C.C., O'Day, P.A., 2001. Processes of nickel and cobalt uptake by a manganese oxide forming sediment in Pinal Creek, globe mining district, Arizona. Environmental Science and Technology 35, 4719-4725.

Khim, B.K., Yoon, H.I., 2003. Postglacial marine environmental changes in Maxwell Bay, King George Island, West Antarctica. Polar Research 22, 341-353.

Kirkham, R.V., Roscoe, S.M., 1993. Atmospheric evolution and ore deposit formation. Resource Geology Special Issue 15, 1-17.

Kirschvink, J.L., 1980. South-seeking magnetic bacteria. Journal of Experimental Biology 86, 345-347.

Klein, C., Beukes, N.J., 1989. Geochemistry and sedimentology of a facies transition from limestone to iron-formation deposition in the Early Proterozoic Transvaal Supergroup, South Africa. Economic Geology 84, 1733-1742.

Klein, C., Beukes, N.J., 1993. Sedimentology and geochemistry of the glaciogenic late Proterozoic Rapitan Iron-Formation in Canada. Economic Geology 88, 542-565.

Klein, C., 2005. Some Precambrian banded iron-formations (BIFs) from around the world: Their age, geologic setting, mineralogy, metamorphism, geochemistry, and origin. American Minerologist 90, 1473-1499.

Kobayashi, A., Kirschvink, J.L., Nash, C.Z., Kopp, R.E., Sauer, D.A., Bertani, L.E., Voorhout, W.F., Taguchi, T., 2006. Experimental observation of magnetosome chain collapse in magnetotactic bacteria: sedimentological, paleomagnetic, and evolutionary implications. Earth and Planetary Science Letters 245, 538-550.

Koeppenkastrop, D., De Carlo, E.H., 1992. Sorption of rare-earth elements from seawater onto synthetic mineral particles: An experimental approach. Chemical Geology 95, 251-263.

Konhauser, K.O., Hamade, T., Raiswell, R., Morris, R.C., Ferris, F.G., Southam, G., Canfield, D.E., 2002. Could bacteria have formed the Precambrian banded iron formations? Geology 30, 1079-1082.

Konhauser, K.O., Newman, D.K., and Kappler, A., 2005. The potential significance of microbial Fe(III)-reduction during Precambrian banded iron formations. Geobiology 3, 167-177

Konhauser K.O., Pecoits E., Lalonde S.V., Papineau D., Nisbet E.G., Barley M.E., Arndt N.T., Zahnle K., Kamber B.S., 2009. Oceanic nickel depletion and a methanogen famine before the Great Oxidation Event. Nature 458, 750-753.

Konhauser, K.O., Lalonde, S.V., Planavsky, N.J., Pecoits, E., Lyons, T.W., Mojzsis, S.J., Rouxel, O.J., Barley, M.E., Rosiere, C., Fralick, P.W., Kump, L.R., Bekker, A., 2011. Aerobic bacterial pyrite oxidation and acid rock drainage during the Great Oxidation Event. Nature 478, 369-373.

Konhauser, K.O., Robbins, L.J., Pecoits, E., Peacock, C., Kappler, A., Lalonde, S.V., 2015. The Archean nickel famine revisited. Astrobiology 15, 804-815.

Konhauser, K.O., Planavsky, N.J., Hardisty, D.S., Robbins, L.J., Warchola, T.J., Haugaard, R., Lalonde, S.V., Partin, C.A., Oonk P.B.H., Tsikos, H., Lyons, T.W., Bekker, A., Johnson, C.M., 2017. Iron Formations: A global record of Neoarchaean to Palaeoproterozoic environmental history. Earth-Science Reviews 172, 140-177.

Kopp, R.E., Kirschvink, J.L., Hilburn, I.A., Nash, C.Z., 2005. The Paleoproterozoic snowball Earth: A climate disaster triggered by the evolution of oxygenic photosynthesis. Proceedings of the National Academy of Sciences of the United States of America 102, 11131-11136.

Kopp, R.E., Nash, C.Z., Kobayashi, A., Weiss, B.P., Bazylinski, D.A., Kirschvink, J.L., 2006. Ferromagnetic resonance spectroscopy for assessment of magnetic anisotropy and magnetostatic interactions: a case study of mutant magnetotactic bacteria. Journal of Geophysical Research 111, B12S25.

Kopp, R.E., Kirschvink, J.L., 2008. The identification and biogeochemical interpretation of fossil magnetotactic bacteria. Earth-Science Reviews 86, 42-61.

Kostka, J.E., Nealson, K.H., 1995. Dissolution and reduction of magnetite by bacteria. Environmental Science and Technology 29, 2535-2540.

Krapež, B., 1996. Sequence-stratigraphic concepts applied to the identification of basin-filling rhythms in Precambrian successions. Australian Journal of Earth Sciences, 43, 355-380.

Krapež, B., Barley, M.E., 1987. Archaean strike-slip faulting and related ensialic basins: evidence form the Pilbara Block, Australia. Geological Magazine 1124, 555-567.

Laajoki, K., 1975. Rare-earth elements in Precambrian iron formations in Vayrlankyla, South Puolanka area, Finland. Bulletin of the Geological Society of Finland 47, 93-107.

Lascelles, D.F., 2000. Marra Mamba Iron Formation stratigraphy in the eastern Chichester Range, Western Australia. Australian Journal of Earth Sciences 47, 799-806.

Lin, W., Paterson, G.A., Zhu, Q., Wang, Y., Kopylova, E., Li, Y., Knight, R., Bazylinski, D.A., Zhu, R., Kirschvink, J.L., Pan, Y., 2017. Origin of microbial biomineralization and magnetotaxis during the Archean.

Lindsay, J.F., Brasier, M.D., 2000. A carbon isotope reference curve for ca. 1700-1575 Ma, McArthur and Mount Isa Basins, Northern Australia. Precambrian Research 99, 271-308.

Lindsay, J.F., Brasier, M.D., 2002. Did global tectonics drive early biosphere evolution? Carbon isotope record from 2.6 to 1.9 Ga carbonates of Western Australian basins. Precambrian Research, 114, 1-34.

Loganathan, P., Burau, R.G., 1973. Sorption of heavy metals by hydrous manganes oxides. Geochemica et Cosmochimica Acta 37, 1277-1293.

Lowe, D.R., 1980. Stromatolites 3,400-myr old from the Archean of Western Australia. Nature 284, 441-443.

Luo, G., Ono, S., Beukes, N.J., Wang, D.T., Xie, S., Summons, R.E., 2016. Rapid oxygenation of Earth's atmosphere 2.33 billion years ago. Science Advances 2, 1-9.

MacGregor, A.R., 1927. The problem of the Precambrian atmosphere. South African Journal of Science 24, 155-172.

Machel, H.G., Krouse, H.R., Sassen, R., 1995. Products and distinguishing criteria of bacterial and thermochemical sulfate reduction. Applied Geochemistry 10, 373-389.

Maher, B.A., Thompson, R., Hounslow, M.W., 1999. Introduction. In: Maher, B.A., Thompson, R., (Eds.), Quaternary Climates, Environments, and Magnetism. Cambridge University Press, Cambridge, pp. 1-48.

Mann, S., Sparks, N.H.C., Board, R.G., 1990a. Magnetotactic bacteria: microbiology, biomineralization, paleomagnetism, and biotechnology. Advances in Microbial Physiology 31, 125-181.

Mann, S., Sparks, N.H.C., Frankel, R.B., Bazylinski, D.A., Jannasch, H.W., 1990b. Biomineralization of ferrimagnetic greigite (Fe3S4) and iron pyrite (FeS2) in magnetotactic bacterium. Nature 343, 258-261.

Martin, D.M., Li, Z.X., Nemchin, A.A., Powell, C.M., 1998. A pre-2.2 Ga age for giant hematite ores of the Hamersley Province, Australia? Economic Geology 93, 1084-1090.

Martin, D.M., 1999. Depositional setting and implications of Paleoproterozoic glaciomarine sedimentation in the Hamersley Province, Western Australia. Geological Society of America Bulletin 111, 189-203.

Martin, D.M., Powell, C.M., George, A.D., 2000. Stratigraphic architecture and evolution of the early Paleoproterozoic McGrath Trough, Western Australia. Precambrian Research 99, 33-64.

Martindale, R. C., Strauss, J. V, Sperling, E. A., Johnson, J. E., Van Kranendonk, M. J., Flannery, D., French, K., Lepot, K., Mazumder, R., Rice, M.S., Schrag, D.P, Summons, R., Walter, M., Abelson, J., Knoll, A. H., 2015. Sedimentology, chemostratigraphy, and stromatolites of lower Paleoproterozoic carbonates, Turee Creek Group, Western Australia. Precambrian Research 266, 194–211.

Matocha, C.J., Elzinga, E.J., Sparks, D.L., 2001. Reactivity of Pb(II) at the Mn(III,IV) (oxyhydr)oxide-water intervace. Environment Science and Technology 35, 2967-2972.

Maynard, J.B., 2010. The chemistry of manganese ores through time: a signal of increasing diversity of Earth-surface environments. Economic Geology 105, 535-552.

Mazumder, R., Van Kranendonk, M. J., 2013. Palaeoproterozoic terrestrial sedimentation in the Beasley River Quartzite, lower Wyloo Group, Western Australia. Precambrian Research 231, 98–105.

Mazumder, R., Van Kranendonk, M.J., Altermann, W., 2015. A marine to fluvial transition in the Paleoproterozoic Koolbye Formation, Turee Creek Group, Western Australia. Precambrian Research 258, 161-170.

McConchie, D.M., 1984. The geology and geochemistry of the Joffre and Whaleback Shale members of the Brockman Iron Formation, Western Australia. University of Western Australia.

Melezhik, V.A., Fallick, A.E., Hanski, E.J., Kump, L.R., Lepland, A., Prave, A.R., Strauss, H., 2005. Emergence of the aerobic biosphere during the Archean-Proterozoic transition: challenges of future research today. GSA Today 15, 4-11.

Millero, F.J., 1996. Chemical Oceanography. CRC Press, Boca Raton, Florida. 469 pp.

Montgomery, P., Hailwood. E.A., Gale, A.S., Burnett, J.A., 1998. The magnetostratigraphy of Coniacian late Campanian chalk sequences in southern England. Earth and Planetary Science Letters 156, 209-224.

Morris, A.W., 1975. Dissolved molybdenum and vanadium in the northeast Atlantic Ocean. Deep-Sea Research 22, 49-54.

Morris, R.C., 1993. Genetic modelling for banded iron-formation of the Hamersley Group, Pilbara Craton, Western Australia. Precambrian Research 60, 243-286.

Morris, R.C., Horwitz, R.C., 1983. The origin of the iron-formation-rich Hamersley Group of Western Australia – deposition on a platform. Precambrian research 21, 273-297.

Moskowitz, B.M., Frankel, R.B., Bazylinski, D.A., 1993. Rock magnetic criteria for the detection of biogenic magnetite. Earth and Planetary Science Letters 120, 283-300.

Moskowitz, B.M., Bazylinski, D.A., Egli, R., Frankel, R.B., Edwards, K.J., 2008. Magnetic properties of marine magnetotactic bacteria in a seasonally stratified coastal pond (Salt Pond, Ma, USA).

Müller, S.G, Krapež, B., Barley, M.E., Fletcher, I.R., 2005. Giant iron-ore deposits of the Hamersley province related to the breakup of Paleoproterozoic Australia: New insights from in situ SHRIMP dating of baddeleyite from mafic intrusions. Geology 33, 577-580.

Myers, J.S., 1993. Precambrian History of the West Australian Craton and Adjacent Orogens. Annual Review of Earth and Planetary Sciences, 21, 453-485.

Nel, C.J., Beukes, N.J., De Villiers, J.P.R., 1986. The Mamatwan manganese mine of the Kalahari Manganese Field. In: Anhaeusser CR and Maske S (Eds.), Mineral deposits of Southern Africa. Geological Society of South Africa, pp. 963-978.

Nel, B.P., 2013. Petrography and Geochemistry of Iron Formation of the Paleoproterozoic Koegas Subgroup, Transvaal Supergroup, Griqualand West, South Africa. University of Johannesburg Master of Science Thesis Dissertation.

Nelson, Y.M., Lion, L.W., Shuler, M.L., Ghiorse, W.C., 1999a. Lead binding to metal oxide and organic phases of natural aquatic biofilms. Limnology and Oceanography 44, 1715-1729.

Nelson, Y.M., Lion, L.W., Ghiorse, W.C., Shuler, M.L., 1999b. Production of biogenic Mn oxides by Leptothix discophora SS-1 in a chemically defiend growth medium and evaluation of their Pb adsorption characteristics. Applied Environmental Microbiology 65, 175-180.

Nesbitt, H.W., Young, G.M., 1989. Formation and diagenesis of weathering profiles. The Journal of Geology 97, 129-147.

Nozaki, Y., Zhang, J., Amakawa, H., 1997. The fractionation between Y and Ho in the marine environment. Earth and Planetary Science Letters 148, 329-340.

O'Reilly, S.E., Hochella, M.F., 2003. Lead sorption efficiencies of natural and synthetic Mn and Fe-oxides. Geochimica et Cosmochimica Acta 67, 4471-4487.

Ohmoto, H., 1992. Biogeochemistry of sulfur and the mechanisms of sulfide-sulfate mineralization in Archean oceans, In: M. Schidlowski (Ed.), Early Organic Evolution: Implications for Mineral and Energy Sources, Springer-Verlag, Berlin, 378-397.

Ohmoto, H., Goldhaber, M., 1997. Applications of sulfur and carbon isotopes in ore deposit research. In: Barnes H.L (Ed.), Geochemistry of Hydrothermal Ore Deposits, third ed. John Wiley and Sons, 517-611.

Ohta, A., Kawabe, I., 2001. REE (III) adsorption onto Mn dioxide (delta-MnO2) and Fe oxyhydroxide: Ce(III) oxidation by delta-MnO2. Geochimica et Cosmochimica Acta 65, 695–703.

Ono, S., Eigenbrode, J.L., Pavlov, A.A., Khareecha, P., Rumble III, D., Kasting, J.F., Freeman, K.H., 2003. New insights into Archean sulfur cycle from mass-independent sulfur isotope records from the Hamersley Basin, Australia. Earth and Planetary Science Letters, 213, 15-30.

Özdemir, Ö., Dunlop, D.J., Moskowitz, B.M., 1993. The effect of oxidation on the Verwey transition in magnetite. Geophysical Research Letters 20, 1671-1674.

Özdemir, Ö., Dunlop, D.J., 2010. Hallmarks of maghemitization in low-temperature remanence cycling of partially oxidized magnetite nanoparticles. Journal of Geophysical Research 115, B02101.

Pack, A., Russell, S.S., Shelley, J.M.G., van Zuilen, M., 2007. Geo- and cosmochemistry of the twin elements yttrium and holmium. Geochimica et Cosmochimica Acta 71, 4592-4608.

Partin, C.A., Lalonde, S.V., Planavsky, N.J., Bekker, A., Rouxel, O.J., Lyons, T.W., Konhauser, K.O., 2013a. Uranium in iron formations and the rise of atmospheric oxygen. Chemical Geology 362, 82–90.

Partin, C.A., Bekker, A., Planavsky, N.J., Scott, C.T., Gill, B.C., Li, C., Podkovyrov, V., Maslov, A., Konhauser, K.O., Lalonde, S.V., Love, G.D., Poulton, S.W., Lyons, T.W., 2013b. Large-scale fluctuations in Precambrian atmospheric and oceanic oxygen levels from the record of U in shales. Earth and Planetary Science Letters 369-370, 284–293.

Partridge, M.A., Golding, S.D., Baublys, K.A., Young, E., 2008. Pyrite paragenesis and multiple sulfur isotope distribution in late Archean and early Paleoproterozoic Hamersley Basin sediments. Earth and Planetary Science Letters 272, 41-49.

Pavlov A.A., Kasting J.F., Eigenbrode J.L., Freeman K.H., 2001. Organic haze in Earth's early atmosphere: Source of low-C-13 Late Archean kerogens? Geology 29, 1003-1006.

Pavlov, A.A., Kasting, J.F., 2002. Mass-independent fractionation of sulfur isotopes in Archean sediments: strong evidence for an anoxic Archean atmosphere. Astrobiology 2, 27-41.

Pecoits, E., Gingras, M.K., Barley, M.E., Kappler, A., Posth, N., Konhauser, K.O., 2009. Petrography and geochemistry of the Dales Gorge banded iron formation: Paragenetic sequence, source and implications for palaeo-ocean chemistry. Precambrian Research 172, 163–187.

Pecoits, E., Smith, M.L., Catling, D.C., Philippot, P., Kappler, A., Konhauser, K.O., 2015. Atmospheric hydrogen peroxide and Eoarchean iron formations. Geobiology 13, 1-14.

Peña, J., Kwon, K.D., Refson, K., Bargar, J.R., Sposito, G., 2010. Mechanisms of nickel sorption by a bacteriogenic birnessite. Geochimica et Cosmochimica Acta 74, 3076-3089.

Percak-Dennett, L., Roden, E.E., Beard, B.L., Johnson, C.M., 2011. Iron isotope fractionation during dissimilatory iron reduction under simulated Archean conditions. Geobiology 9, 205-220.

Philippot, P., Ávila, J.N., Killingsworth, B.A., Tessalina, S., Baton, F., Caquineau, T., Muller, E., Pecoits, E., Cartigny, P., Lalonde, S.V., Ireland, T.R., Thomazo, C., van Kranendonk, M.J., Busigny, V., 2018. Globally asynchronous sulphur isotope signals require re-definition of the Great Oxidation Event. Nature Communications 9, 2245.

Pickard, A.L., 2003. SHRIMP U-Pb zircon ages for the Palaeoproterozoic Kuruman Iron formation, Northern Cape Province, South Africa: Evidence for simultaneous BIF deposition on Kaapvaal and Pilbara Cratons. Precambrian Research 125, 275-315.

Pickard, A.L., Barley, M.E., Krapež, B., 2004. Deep-marine depositional setting of banded iron formation: Sedimentological evidence from interbedded clastic sedimentary rocks in the early Palaeoproterozoic Dales Gorge Member of Western Australia. Sedimentary Geology 170, 37-62.

Planavsky, N., Bekker, A., Rouxel, O.J., Kamber, B., Hofmann, A., Knudsen, A., Lyons, T.W., 2010. Rare Earth Element and yttrium compositions of Archean and Paleoproterozoic Fe formations revisited: new perspectives on the significance and mechanisms of deposition. Geochimica et Cosmochimica Acta 74, 6387-6405.

Planavsky, N.J., Asael, D., Hofmann, A., Reinhard, C.T., Lalonde, S.V., Knudsen, A., Wang, X., Ossa Ossa, F., Pecoits, E., Smith, A.J.B., Beukes, N.J., Bekker, A., Johnson, T.M., Konhauser, K.O., Lyons, T.W., Rouxel, O.J., 2014. Evidence for oxygenic photosynthesis half a billion years before the Great Oxidation Event. Nature Geoscience 7, 283-286.

Planavsky, N.J., Slack, J.F., Cannon, W.F., O'Connell, B., Isson, T.T., Asael, D., Jackson, J.C., Hardisty, D.S., Lyons, T.W., Bekker, A., 2018. Evidence for episodic oxygenation in a weakly redox-buffered deep mid-Proterozoic ocean. Chemical Geology 483, 581-594.

Pope, M.C., Grotzinger, J.P, 2003. Paleoproterozoic stark formation, Athapuscow Basin, Northwest Canada: record of cratonic-scale salinity crisis. Journal of Sedimentary Research 73, 280-295.

Posamantier, H.W., Jervey, M.T., Vail, P.R., 1988. Eustatic controls on clastic depositional sequeces and systems tract models. In: C.K. Wilgus et al. (Eds.), Sea Level Changes: An Integrated Approach. Special publications of the Society of Economic Paleontologists and Mineralogists 42, 109-124.

Posamantier, H.W., James, D.P., 1993. An overview of sequence stratigraphic concepts: uses and abuses. In : H.W. Posamentier, C.P. Summerhayes, B.U. Haq, G.P. Allen (Eds.), Sequence Stratigraphy and Facies Associations. International Association of Sedimentologists Special Publication 18, 3-18.

Poulson, R.L.B., McManus, J., Severmann, S., Berelson, W.M., 2009. Molybdenum behavior during early diagenesis: Insights from Mo isotopes. Geochemistry, Geophysics, Geosystems 10, Q06010.

Poulton, S.W., Krom, M.D., Raiswell, R., 2004. A revised scheme for the reactivity of iron (oxyhydr)oxide minerals towards dissolved sulfide. Geochimica et Cosmochimica Acta 68, 3703-3715.

Poulton, S.W., Canfield, D.E., 2005. Development of a sequential extraction procedure for iron: implications for iron partitioning in continentally derived particulates. Chemical Geology 214, 209-221.

Powell, C.M., Horwitz, R.C., 1994. Late Archaean and Early Proterozoic tectonics and basin formation of the Hamersley Ranges. In: 12th Australian Geological Convention, Geological Society of Australia, Perth, Excursion Guidebook 4.

Prozoroz, R., Prozorov, T., Mallapragada, S.K., Narasimhan, B., Williams, T.J., Bazylinski, D.A., 2007. Magnetic irreversibility and the Verwey transition in nanocrystalline bacterial magnetite. Physical Reviews B 76, 054406.

Raiswell, R., Canfield, D.E., 1998. Sources of iron for pyrite formation in marine sediments. American Journal of Science 298, 219-245.

Rasmussen, B., Buick, R., 1999. Redox state of the Archean atmosphere: Evidence from detrital heavy minerals in ca. 3250-2750 Ma sandstones from the Pilbara Craton, Australia. Geology 27, 115-118.

Rasmussen, B., Fletcher, I.R., Sheppard, S., 2005. Isotopic dating of the migration of a low-grade metamorphic front during orogenesis. Geology, 33, 773-776.

Rasmussen, B., Krapež, B., Meier, D.B., 2014. Replacement origin for hematite in 2.5 Ga banded iron formation: evidence for postdepostional oxidation of iron-bearing minerals. Geological Society of America Bulletin 126, 438-446.

Rasmussen, B., Krapež, B., Muhling, J.R., Suvorova, A., 2015. Precipitation of iron silicate nanoparticles in early Precambrian oceans marks Earth's first iron age. Geology 43, 303–306.

Rasmussen, B., Muhling, J.R., Suvorova, A., Krapež, B., 2016. Dust to dust: evidence for the formation of "primary" hematite dust in banded iron formations via oxidation of iron silicate nanoparticles. Precambrian Research 284, 49-63.

Rasmussen, B., Muhling, J.R., Suporova, A., Krapež, B., 2017. Greenalite precipitation linked to the deposition of banded iron formations downslope from a late Archean carbonate platform. Precambrian Research. 290, 49-62.

Reinhard, C.T., Planavsky, N.J., Lyons, J.R., 2013. Long-term sedimentary recycling of rare sulphur isotope anomalies. Nature 497, 100-104.

Roscoe, S.M., 1996. Paleoplacer uranium gold. In: Eckstrand OR, Sinclair WD, Thorpe RI (eds) Geology of Canadian mineral deposit types, vol P-1. Geological Society of America, The Geology of North America, Boulder, 10-23.

Roy, S., 1992. Environments and processes of manganese deposition. Economic Geology 87, 1218-1236.

Rudnick, R.L., Gao, S., 2003. Composition of the continental crust. Treatise on Geochemistry 3, 1-64.

Rye, R., Holland, H.D., 1998. Paleosols and the evolution of atmospheric oxygen: a critical review. American Journal of Science 298, 621-672.

Sakai, K., 2015. Routine soil analysis using an Agilent 8800 ICP-QQQ. Application note 5991-6409EN. Agilent Technologies.

Satkowski, A.M., Beukes, N.J., Li, W., Beard, B.L., Johnson, C.M., 2015. A redox-stratified ocean 3.2 billion years ago. Earth and Planetary Science Letters 430, 43-53.

Schissel, D., Aro, P., 1992. The major early Proterozoic sedimentary iron and manganese deposits and their tectonic setting. Economic Geology 87, 1367-1374.

Schopf, J.W., Packer, B.M., 1987. Early archean (3.3-billion to 3.5-billion-year-old microfossils from Warrawoona Group, Australia. Science 237, 70-73.

Schröder, S., Bekker, A., Beukes, N.J., Strauss, H., van Niekerk, H.S., 2008. Rise in seawater sulphate concentration associated with the Paleoproterozoic positive carbon isotope excursion: evidence from sulphate evaporites in the 2.2-2.1 Gyr shallow-marine Lucknow Formation, South Africa. Terra Nova 20, 108-117.

Schröder, S., Bedorf, D., Beukes, N.J., Gutzmer, J., 2011. From BIF to red beds: Sedimentology and sequence stratigraphy of the Paleoproterozoic Koegas Subgroup (South Africa). Sedimentary Geology 236, 25-44.

Scott, C., Lyons, T.W., Bekker, A., Shen, Y., Poulton, S., Chu, X., Anbar, A., 2008. Tracing the stepwise oxygenation of the Proterozoic ocean. Nature 452, 456-459.

Shih, P.M., Hemp, J., Ward, L.M., Matzke, N.J., Fischer, W.W., 2017. Crown group Oxyphotobacteria postdate the rise of oxygen. Geobiology 15, 19-29.

Siebert, C., Nägler, T.F., Kramers, J.D., 2001. Determination of molybdenum isotope fractionation by double-spike multicollector inductively coupled plasma mass spectrometry. Geochemistry, Geophysics, Geosystems 2, 2000GC000124.

Siebert, C., Nägler, T.F., von Blanckenburg, F., Kramers, J.D., 2003. Molybdenum isotope records as a potential new proxy for paleoceanography. Earth and Planetary Science Letters 211, 159-171.

Skei, J., Loring, D.H., Rantala, R.T.T., 1996. Trace metals in suspended particulate matter and in sediment trap material from a permanently anoxic fjord-Framvaren, south Norway. Aquatic Geochemistry 2, 131-147.

Smedley, P.L., Kinniburgh, D.G., 2002. A review of the source, behaviour and distribution of arsenic in natural waters. Applied Geochemistry 17, 517-568.

Smith R.E., Perdrix J.L., Parks J.C., 1982. Burial metamorphism in the Hamersley province, Western Australia. Journal of Petrology 23, 75-102.

Soo, R.M., Hemp, J., Parks, D.H., Fischer, W.W., Hugenholtz, P., 2017. On the origins of oxygenic photosynthesis and aerobic respiration in Cyanobacteria. Science 355, 1436-1440.

Spencer, E., Percival, F.G., 1952. The structure and origin of the banded hematite jaspers of Singhbhum, India. Economic Geology 47, 365-383.

Steinhofel, G., von Blackenburg, F., Horn, I., Konhauser, K.O., Beukes, N., Gutzmer, J., 2010. Deciphering formation processes of banded iron formations from the Transvaal and the Hamersley Sequence by combined Si and Fe isotope analysis using UV femtosecond laser ablation. Geochimica et Cosmochimica Acta 74, 2677–2696.

Summons, R.E., Jahnke, L.L., Hope, J.M., Logan, G.A., 1999. 2-Methylhopanoids as biomarkers for cyanobacterial oxygenic photosynthesis. Nature 400, 554-557.

Summons R.E., Bradley A.S., Jahnke L.L., and Waldbauer J.R., 2006. Steroids, triterpenoids and molecular oxygen. Philosophical Transactions of the Royal Society B: Biological Sciences 361, 951-968.

Sun, S., Konhauser, K.O., Kappler, A., Li, Y-L., 2015. Primary hematite in Neoarchean to Paleoproterozoic oceans. Geological Society of America Bulletin 127, 850-861.

Swanner, E.D., Bekker, A., Pecoits, E., Konhauser, K.O., Cates, N.L., Mojzsis, S.J., 2013. Geochemistry of pyrite from diamictites of the Boolgeeda Iron Formation, Western Australia with implications for the GOE and Paleoproterozoic ice ages. Chemical Geology 362, 131-142.

Takahashi, Y., Manceau, A., Geoffroy, N., Marcus, M.A., Usui, A., 2007. Chemical and structural control of the partitioning of Co, Ce, and Pb in marine ferromanganese oxides. Geochemica et Cosmochimica Acta 71, 984-1008.

Taylor, S.R., McLennan, S.M., 1985. The continental crust: Its composition and its evolution, Blackwell, Oxford, 312 pp.

Thoby, M., Warchola, T., Killingsworth, B., Alam, Md.S., Alessi, D.A., Thomazo, C., Ader, M., Philippot, P., Konhauser, K.O., Lalonde, S.V., in prep. Decoupling Sedimentary Mn enrichments from surface processes.

Thomazo C., Ader M., Farquhar J., Philippot P., 2009. Methanotrophs regulated atmospheric sulfur isotope anomalies during the Mesoarchean (Tumbiana Formation, Western Australia). Earth and Planetary Science Letters, 279, 65-75.

Thomazo, C., Ader, M., Philippot, P., 2011. Extreme 15N-enrichments in 2.72-Gyr-old sediments: evidence for a turning point in the nitrogen cycle. Geobiology 9, 107-120.

Thorne, A.M., Trendall, A.F., 2001. Geology of the Fortescue Group, Pilbara Craton, Western Australia. Geological Survey of Western Australia Bulletin 144.

Thorne, A.M., Tyler, L.M., 1996. Roy Hill, Western Australia Sheet 50-12: Geological Survey of Western Australia. 1:250 000 Map Series.

Thorpe, R.A., Hickman, A.H., Davis, D.W., Mortensen, J.K., Trendall, A.F., 1992. U-Pb zircon geochronology of Archaean felsic units in the Marble Bar region, Pilbara Craton, Western Australia. Precambrian Research 56, 169-189.

Toner, B., Manceau, A., Webb, S.M., Sposito, G., 2006. Zinc sorption to biogenic hexagonal-birnessite particles within a hydrated bacterial biofilm. Geochimica et Cosmochimica Acta 70, 27-43.

Tosca, N.J., Guggenheim, S., Pufahl, P.K., 2016. An authigenic origin for Precambrian greenalite: implications for iron formation and the chemistry of ancient seawater. Geological Society of America Bulletin 128, 511-530.

Trendall A.F., and Blockley J.G., 1970. The iron formations of the Precambrian Hamersley Group, Western Australia. Geological Survey of Western Australia Bulletin, 119.

Trendall, A.F., 1973. Varve Cycles in the Weeli Wolli Formation of the Precambrian Hamersley Group, Western Australia. Economic Geology 68, 1089-1097.

Trendall, A.F., 1976. Striated and faceted boulders from the Turee Creek Formation – Evidence for a possible Huronian glaciation on the Australian continent: Geological Survey of Western Australia Annual Report 1975, 88-92.

Trendall, A.F., Pepper, R.S., 1977. Chemical composition of the Brockman Iron Formation. Geological Survey of Western Australia, 1976/25.

Trendall A.F., 1979. A revision of the Mount Bruce Supergroup. Geological Survey of Western Australia Annual Report for 1978, 63-71.

Trendall, A.F., 1981. The Lower Proterozoic Meteorite Bore Member, Hamersley Basin Western Australia. In: Hambrey, M.J., Harland, W.B. (Eds.), Earth's Pre-Pleistocene Glacial Record. Cambridge University Press, Cambridge, 555-557.

Trendall, A.F., 1990. Hamersley Basin, in Geology and mineral resources of Western Australia. Western Australia Geological Survey, Memoir 3, 77-119, in Geology and mineral resources of Western Australia. Western Australia Geological Survey, Memoir 3, 163-191.

Trendall, A.F., Nelson, D.R., De Laeter, J.R., Hassler, S.W., 1998. Precise zircon U-Pb ages from the Marra Mamba Iron Formation and Wittenoom Formation, Hamersley Group, Western Australia. Australian Journal of Earth Sciences 45, 137-142.

Trendall, A.F., 2002. The significance of iron-formation in the Precambrian stratigraphic record. In: Altermann W. & Corcorane P.L. eds. Precambrian Sedimentary Environments: a Modern Approach to Depositional Systems, pp. 33-66. International Association of Sedimentologists Special Publication 44.

Trendall, A.F., Conpston, W., Nelson, D.R., De Laeter, J.R., Bennett, V.C., 2004. SHRIMP zircon ages constraining the depositional chronology of the Hamersley Group, Western Australia. Australian Journal of Earth Sciences 51, 621-644.

Trompette, R., De Alvarenga, C.J.S., Walde, D., 1998. Geological evolution of the Neoproterozoic Corumbá graben system (Brazil). Depositional context of the stratified Fe and Mn ores of the Jacadigo Group. Journal of South American Earth Sciences 11, 587-597.

Trudinger, P.A., Chamber, L.A., 1985. Low-temperature sulphate reduction: biological versus abiological. Canadian Journal of Earth Sciences 22, 1910-1918.

Tsikos, H., Moore, J.M., 1997. Petrography and Geochemistry of the Paleoproterozoic Hotazel Iron-Formation, Kalahari Manganese Field, South Africa: Implications for Precambrian Manganese Metallogenesis. Economic Geology 92, 87-97.

Tsikos, H., Beukes, N.J., Moore, J.M., Harris, C., 2003. Deposition, Diagenesis, and Secondary Enrichment of Metals in the Paleoproterozoic Hotazel Iron Formation, Kalahari Manganese Field, South Africa. Economic Geology 98, 1449–1462.

Van Kranendonk, M. J., Mazumder, R., 2015. Two Paleoproterozoic glacio-eustatic cycles in the Turee Creek Group, Western Australia, (3), 596–607.

Van Kranendonk, M. J., Mazumder, R., Yamaguchi, K. E., Yamada, K., Ikehara, M., 2015. Sedimentology of the Paleoproterozoic Kungarra Formation, Turee Creek Group, Western

Australia: A conformable record of the transition from early to modern Earth. Precambrian Research, 256, 314–343.

Verwey, E.J.W., 1939. Electronic conduction of magnetite (Fe3O4) and its transition point at low temperatures. Nature 144, 327-328.

Viehmann, S., Bau, M., Hoffmann, J.E., Muenker, C., 2015. Geochemistry of the Krivoy Rog Banded Iron Formation, Ukraine, and the impact of peak episodes of increased global magmatic activity on the trace element composition of Precambrian seawater. Precambrian Research 270, 165-180.

Viehmann, S., Bau, M., Bühn, B., Dantas, E.L., Andrade, F.R.D., Walde, D.H.G., 2016. Geochemical characterisation of Neoproterozoic marine habitats: Evidence from trace elements and Nd isotopes in the Urucum iron and manganese formations, Brazil. Precambrian Research 282, 74-96.

Voegelin, A.R., Nägler, T.F., Samankassou, E., Villa, I.M., 2009. Molybdenum isotopic compoisiton of modern and Carboniferous carbonates. Chemical Geology 265, 488-498.

Waldbauer J.R., Sherman L.S., Sumner D.Y., and Summons R.E., 2009. Late Archean molecular fossils from the Transvaal Supergroup record the antiquity of microbial diversity and aerobiosis. Precambrian Res. 169, 28-47.

Walde, D.H.G., Hagemann, S.G., 2007. The Neoproterozoic Urucum/Mutun Fe and Mn deposits in W-Brazil/SE-Bolivia: assessment of ore deposits models. Zeitschrift-Deutschen Gesellschaft Fur Geowissenschaften 158, 45-56.

Walter, M.R., Buick, R., Dunlop, J.S.R., 1980. Stromatolites 3,400-3,500 Myr old from the North Pole area, Western Australia: Nature 284, 443-445.

Warchola, T., Lalonde, S.V., Pecoits, E., von Gunten, K., Robbins, L.J., Alessi, D.S., Philippot, P., Konhauser, K.O., in press. Petrology and Geochemistry of the Boolgeeda Iron Formation, Hamersley Basin, Western Australia. Precambrian Research 316, 155-173.

Weiss, B.P., Kim, S.S., Kirschvink, J.L., Kopp, R.E., Sankaran, M., Kobayashi, A., Komeili, A., 2004. Ferromagnetic resonance and low temperature magnetic tests for biogenic magnetite. Earth and Planetary Science Letters 224, 73-89.

Weltje, G.J., Tjallingii, R., 2008. Calibration of XRF core scanners for quantitative geochemical logging of sediment cores: Theory and application. 274, 423–438.

Weltje, G.J., Bloemsma, M.R., Tjallingii, R., Heslop, D., Röhl, U., Croudace, I.W., 2015. Chapter 21: Prediction of Geochemical Composition from XRF Core Scanner Data: A New Multivariate Approach Including Automatic Selection of Calibration Samples and Quantification of Uncertainties. In: Croudace IW, Rothwell R.G. (Eds), Micro-XRF Studies of Sediment cores: Applications of a non-destructive tool. Springer Netherlands, pp. 656.

Williford, K. H., Van Kranendonk, M. J., Ushikubo, T., Kozdon, R., Valley, J. W., 2011. Constraining atmospheric oxygen and seawater sulfate concentrations during Paleoproterozoic glaciation: In situ sulfur three-isotope microanalysis of pyrite from the Turee Creek Group, Western Australia. Geochimica et Cosmochimica Acta, 75, 5686–5705.

Wood, J., 1973. Stratigraphy and depositional environments of upper Huronian rocks of the Rawhide Lake-Flack Lake area, Ontario. In: Young GM (ed) Huronian Stratigraphy and Sedimentation, vol 12. Geological Association of Canada Special Paper, Geological Association of Canada, 73-95.

Xu, W.X., Peacor, D.R., Dollase, W.A., Van Der Voo, R., Beaubouef, R., 1997. Transformation of titanomagnetite to titanomaghemite: a slow, two-step, oxidation-ordering process in MORB. American Mineralogist 82, 1101-1110.

Zhang, J., Amakawa, H., Nozaki, Y., 1994. The comparative behaviors of yttrium and lanthanides in the seawater of the north Pacific. Geophysical Research Letters 21, 2677-2680.

Zheng, Y., Anderson, R.F., van Green, A., Kuwabara, J., 2000. Authigenic molybdenum formation in marine sediments: a link to pore water sulfide in the Santa Barbara Basin. Geochimica et Cosmochimica Acta 64, 4165-4178.

Zheng, Y., Anderson, R.F., van Geen, A., Fleischer, M.Q., 2002a. Preservation of non-lithogenic particulate uranium in marine sediments. Geochimica et Cosmochimica Acta 66, 3085-3092.

Zheng, Y., Anderson, R.F., van Geen, A., Fleischer, M.Q., 2002b. Remobilization of authigenic uranium in marine sediments by bioturbation. Geochimica et Cosmochimica Acta 66, 1759-1772.

Appendix A

Appendix A Table 1

Element/Method-R^2	(1)	(2)	(3)	(4)	(5)	(6)	(7)	(8)	(9)
Al	0.55	0.41	0.55	0.55	-	0.56	0.71	0.7	-
Ca	0.43	0.27	0.43	0.43	-	0.43	0.45	0.45	-
Cr	0.24	0.29	0.24	0.24	-	0.24	0.66	0.68	-
Fe	0.66	0.48	0.66	0.66	0.43	0.7	0.71	0.91	0.6
K	0.72	0.59	0.72	0.72	-	0.73	0.78	0.88	-
Mg	0.03	0.03	0.03	0.03	-	0.03	0.31	0.17	-
Mn	0.19	0.01	0.19	0.19	-	0.56	0.75	0.75	-
Ni	0.54	0.43	0.54	0.54	0.37	-	0.72	-	0.45
P	0.25	0.05	0.25	0.25	-	0.2	0.42	0.13	-
Rb	0.64	0.52	0.64	0.64	0.6	-	0.81	-	0.61
S	0.48	0.07	0.48	0.48	-	0.42	0.12	0.41	-
Si	0.19	0.15	0.19	0.19	-	0.22	0.74	0.78	-
Sr	0.26	0.15	0.26	0.26	0.37	-	0.35	-	0.63
Ti	0.5	0.33	0.5	0.5	-	0.51	0.68	0.71	-
Zn	0.45	0.31	0.45	0.45	0.25	-	0.28	-	0.41
Zr	0.41	0.25	0.41	0.41	0.25	-	0.15	-	0
Undef	0.21	0.13	0.21	0.21	0.43	0.34	0.1	0.22	0.6

1) XRF calibration using concentration data from all TCDP1 samples - 30kV and 10kV
2) XRF calibration using concentration data from all TCDP1 samples - 50 mm depth tolerance - 30kV and 10kV
3) XRF calibration using concentration data from all TCDP1 samples - 1% significance level - 30kV and 10kV
4) XRF calibration using concentration data from all TCDP1 samples - 20% significance level - 30kV and 10kV
5) XRF calibration using concentration data from all TCDP1 samples - 30kV only
6) XRF calibration using concentration data from all TCDP1 samples - 10kV only
7) XRF calibration using concentration data from Kungarra samples only - 30kV and 10kV
8) XRF calibration using concentration data from Kungarra samples only - 10kV only
9) XRF calibration using concentration data from Kungarra samples only - 30kV only

Appendix A Table 2

Element/Method-R^2	(1)	(2)	(3)	(4)
Al	0.39	0.69	0.17	0.76
Ca	0.54	0.65	0.51	0.84
Cr	0.28	0.51	0.05	0.53
Fe	0.17	0.73	0.24	0.87
K	0.53	0.7	0.47	0.81
Mg	0.48	0.7	0	0.4
Mn	0.61	0.63	0.2	0.9
Ni	0.46	0.55	0.22	0.78
P	0.33	0.28	0.26	0.29
Rb	0.48	0.67	0.28	0.82
S	0.48	0.51	0.54	0.49
Si	0.49	0.55	0.1	0.62
Sr	0.62	0.73	0.21	0.76
Ti	0.54	0.3	0.17	0.73
Zn	0.52	0.44	0.09	0.74
Zr	0.5	0.09	0.1	0.66
Undef	0.1	0.3	0.08	0.55

1) Kazput Carbonate Calibration
2) Kungarra Formation Calibration
3) Boolgeeda Iron Formation Calibration
4) All XRF data calibrated using all concentration data

*** This dataset contains no "contaminated" data (i.e. ACTLABS only) - fewer formations could be calibrated because the bulk-rock chemistry calibration dataset contains fewer data points to calibrate with

Appendix A Table 3

Element/Method-R^2	(1)	(2)	(3)	(4)	(5)	(6)
Al	0.63	0.5	0.3	0.72	0.11	0.75
Ca	0.61	0.74	0.19	0.69	0.47	0.82
Cr	0.2	0.35	0.04	0	0	0.21
Fe	0.52	0.42	0.23	0.81	0.21	0.89
K	0.35	0.43	0.13	0.72	0.36	0.75
Mg	0.67	0.44	0.17	0.83	0	0.46
Mn	0.9	0.86	0.57	0.67	0.4	0.92
Ni	-	-	-	-	-	-
P	0.31	0.17	0	0.38	0.07	0.27
Rb	0.42	0.55	0.03	0.52	0.38	0.78
S	0.13	0.3	0.01	0.24	0.38	0.39
Si	0.59	0.41	0.23	0.68	0.06	0.55
Sr	0.54	0.61	0	0.59	0.14	0.69
Ti	0.55	0.5	0.21	0.64	0.15	0.72
Zn	0.52	0.45	0	0.47	0.09	0.72
Zr	0.21	0.51	0.04	0.16	0.1	0.62
Undef	0.31	0.09	0.03	0.3	0.11	0.58

1) Kazput carbonate bulk-rock data used to calibrate XRF data from all three cores
2) Kazput mudstone bulk-rock data used to calibrate XRF data from all three cores
3) Meteorite Bore Member bulk rock data used to calibrate XRF data from all three cores
4) Kungarra Formation bulk-rock data used to calibrate XRF data from all three cores
5) Boolgeeda Iron Formation bulk-rock data used to calibrate XRF data from all three cores
6) All XRF data calibrated using all concentration data

*** This dataset contains "contaminated" data from Nancy and Brest - Ni was therefore not included in the XRF calibration because Ni values were contaminated in bulk-rock chemistry used for calibration
*** Cr data may be contaminated too
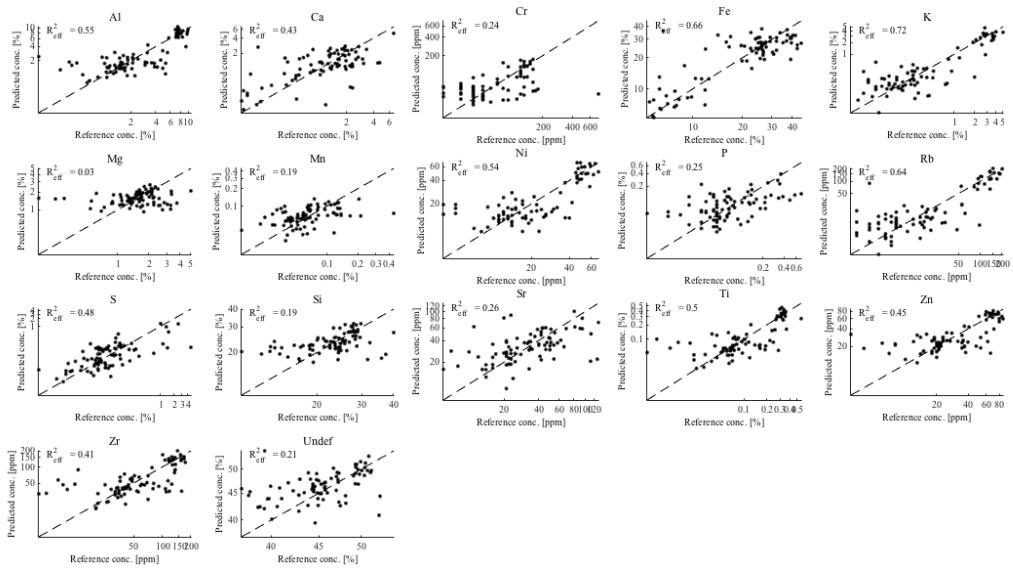
Appendix A Table 1 Cross-plot (1) – All TCDP1 Samples, 30kV and 10kV
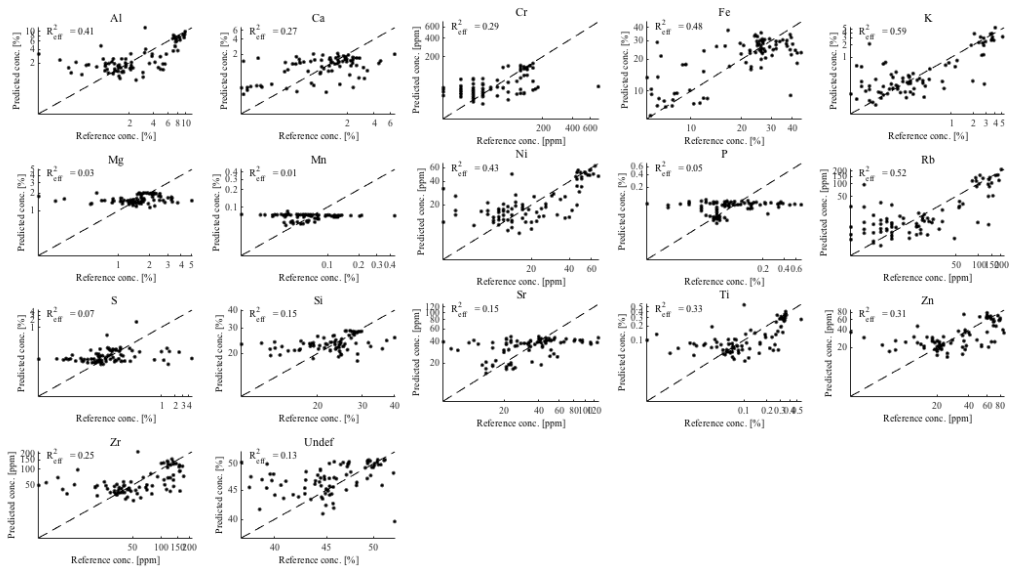
Appendix A Table 1 Cross-plot (2) – All TCDP1 samples, 50 mm depth tolerance, 30kV and 10kV
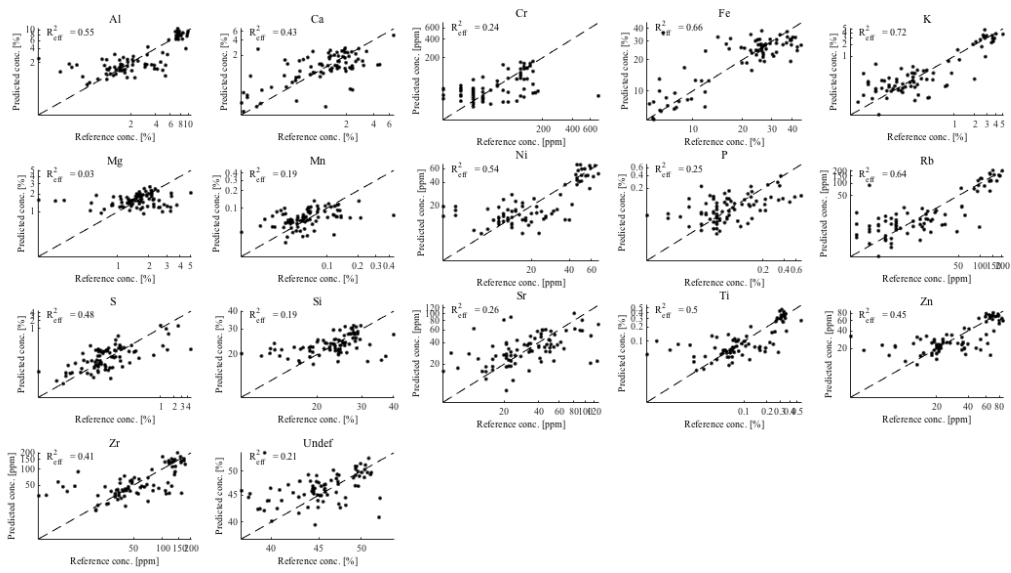
Appendix A Table 1 Cross-plot (3) – All TCDP1 samples, 1% significance interval, 30kV and 10kV
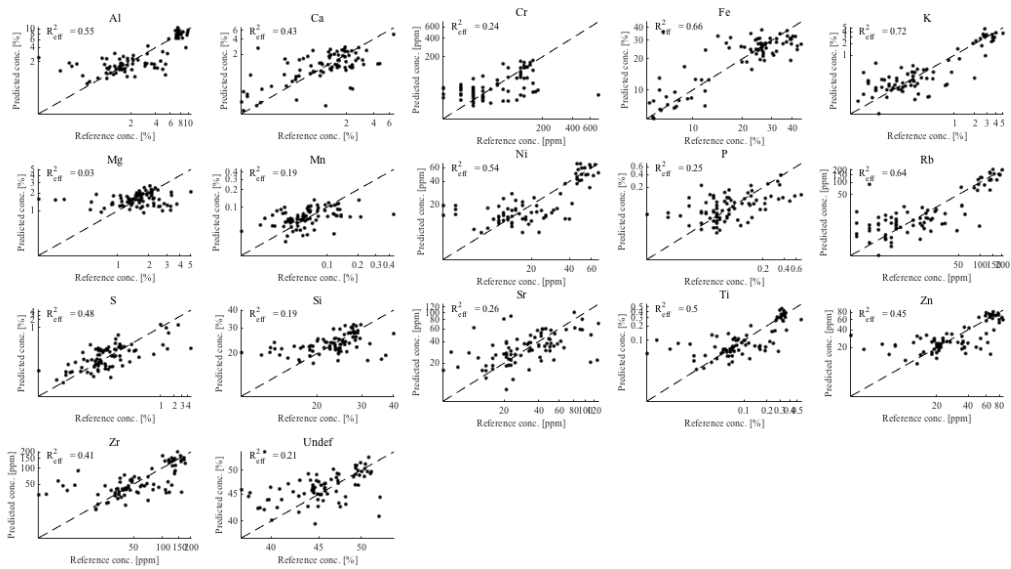
Appendix A Table 1 Cross-plot (4) – All TCDP1 samples, 20% significance interval, 30kV and 10kV

252
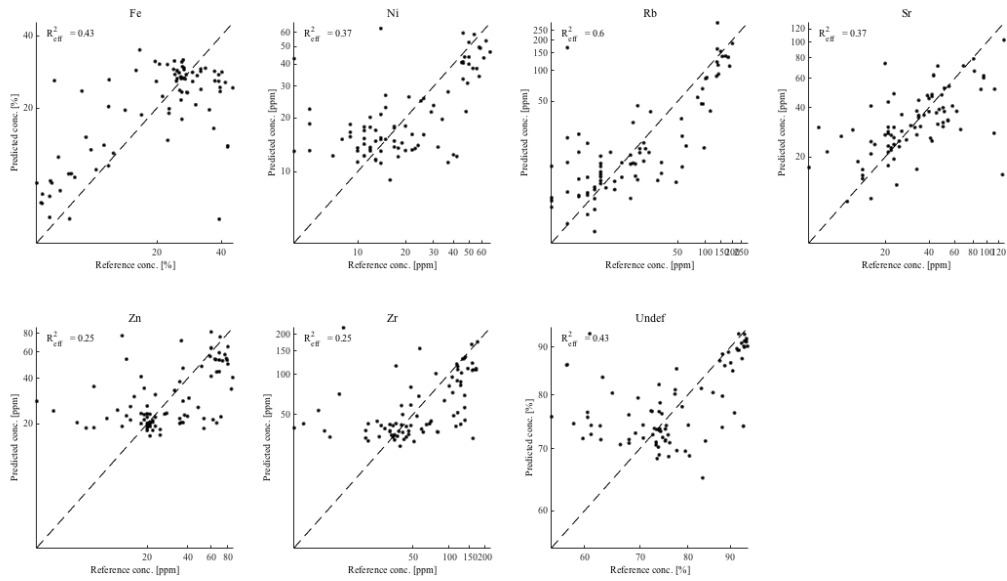
Appendix A Table 1 Cross-plot (5) – All TCDP1 samples, 30kV only
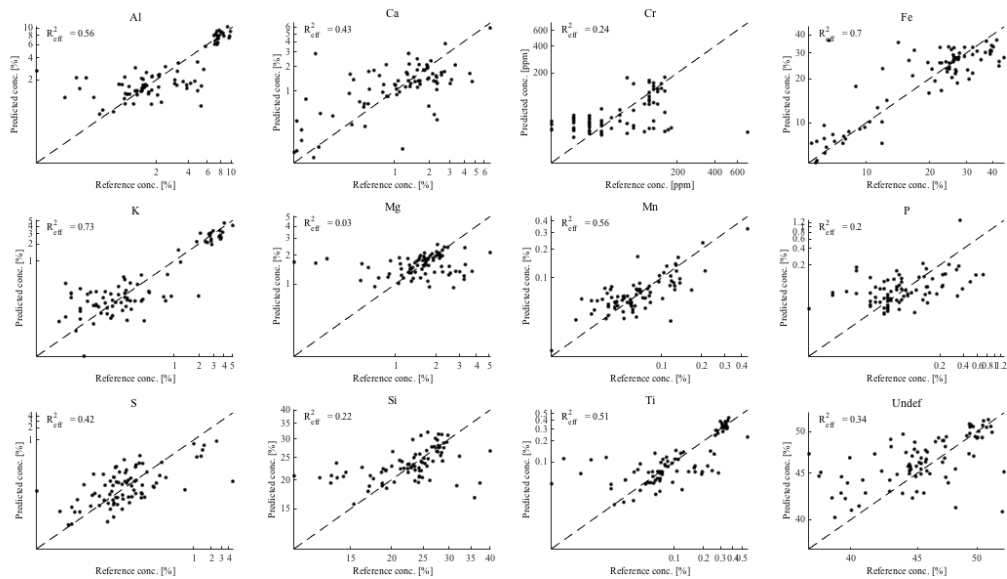
Appendix A Table 1 Cross-plot (6) – All TCDP1 samples, 10kV only
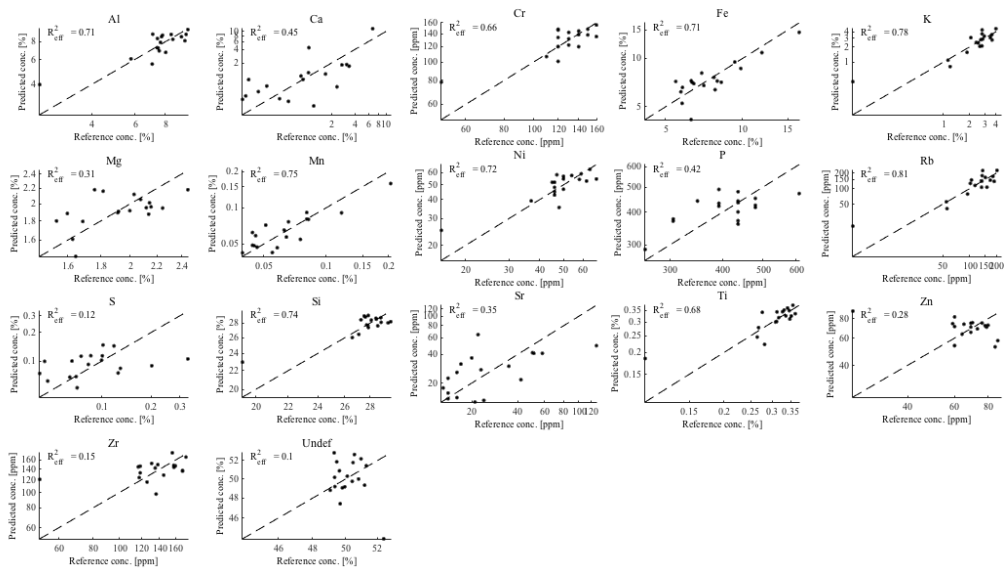
Appendix A Table 1 Cross-plot (7) – Kungarra samples only, 30kV and 10kV
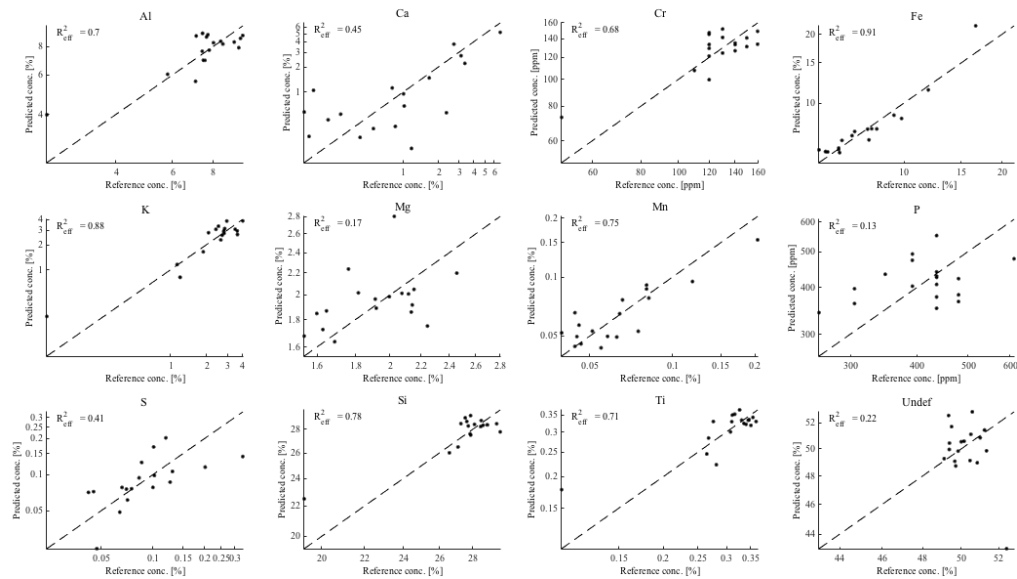
Appendix A Table 1 Cross-plot (8) – Kungarra samples only, 10kV only
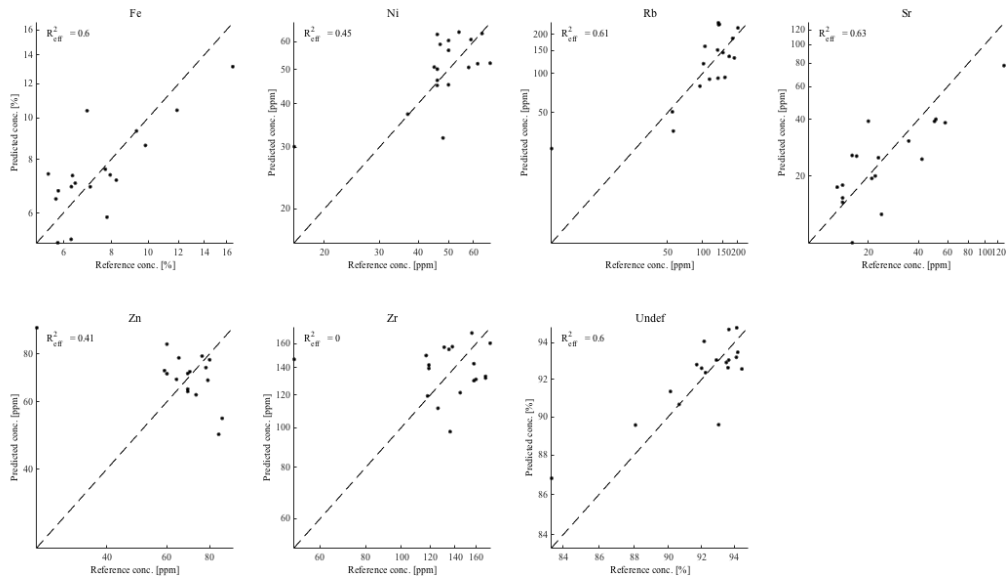
Appendix A Table 1 Cross-plot (9) – Kungarra samples only, 30kV only
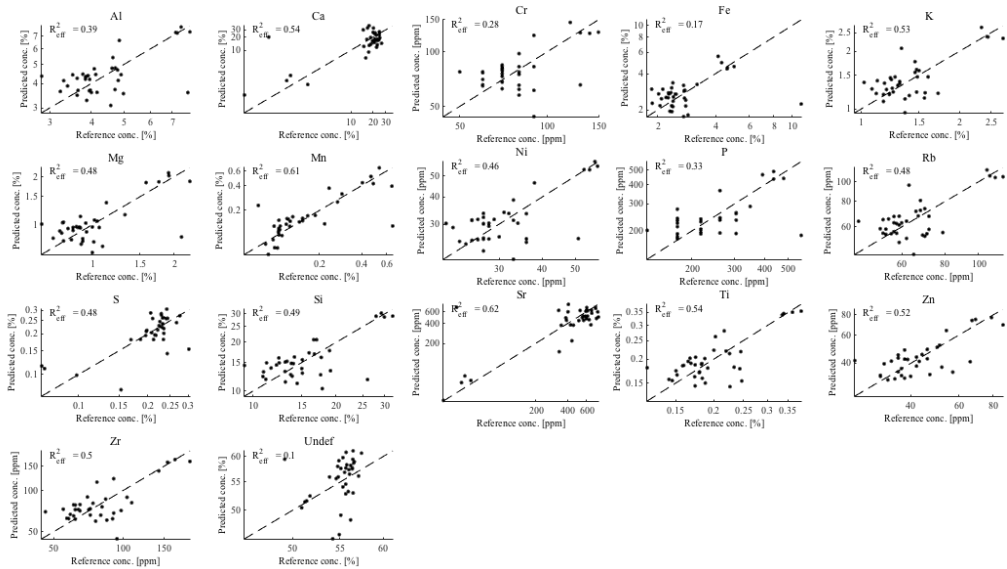
Appendix A Table 2 Cross-plot (1) – Kazput carbonate calibration
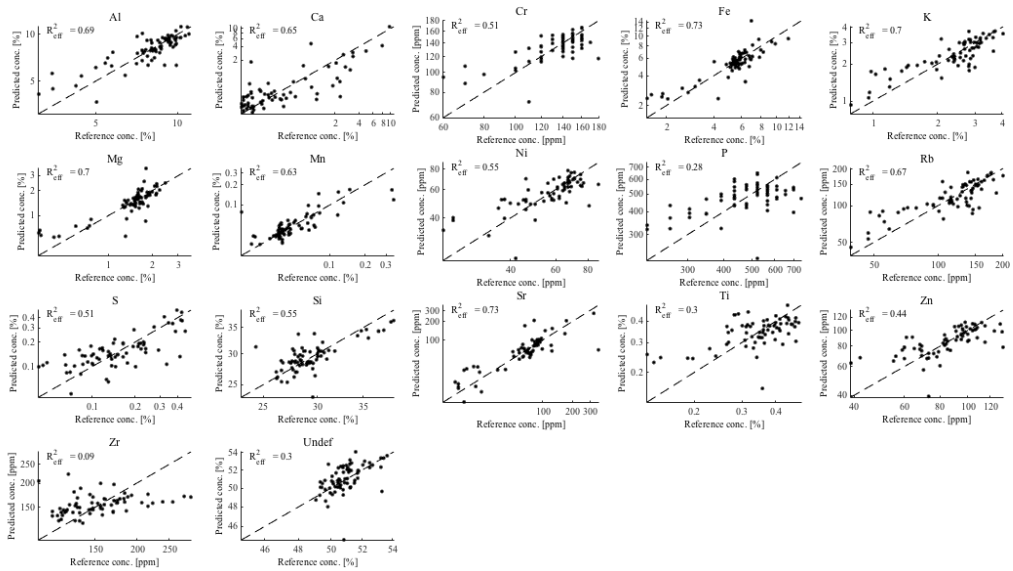
Appendix A Table 2 Cross-plot (2) – Kungarra Formation calibration
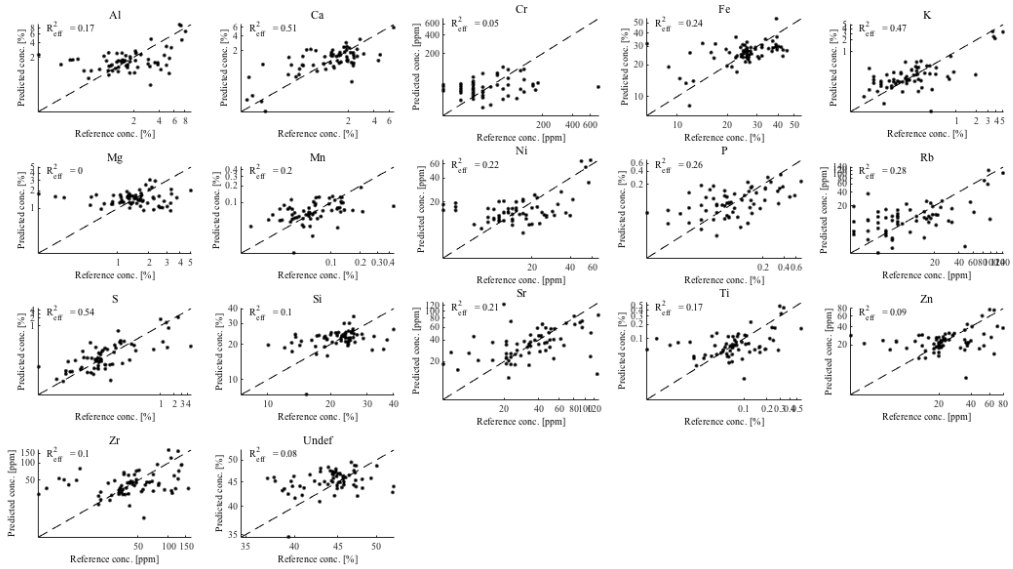
Appendix A Table 2 Cross-plot (3) – Boolgeeda Iron Formation calibration

256
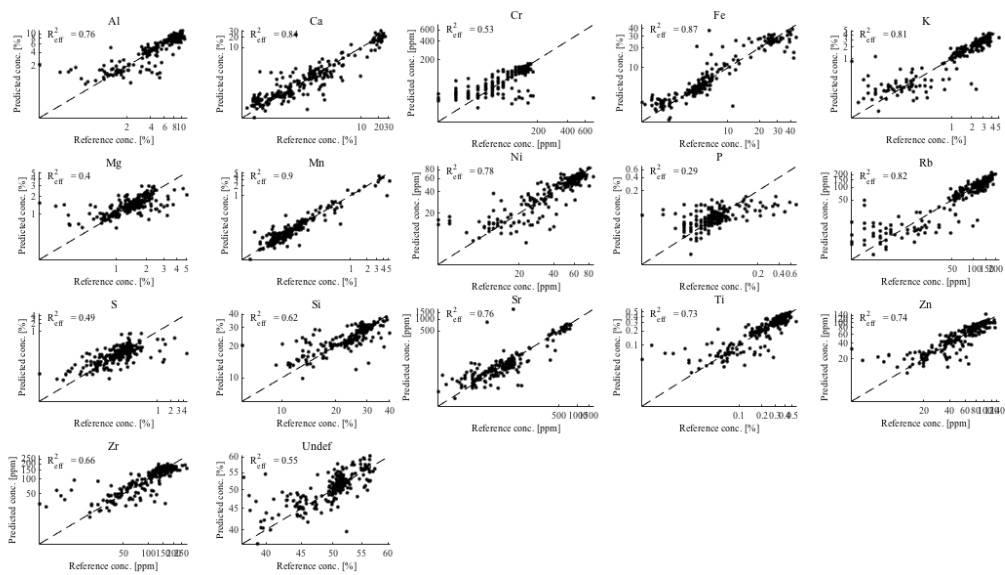
Appendix A Table 2 Cross-plot (4) – All XRF data calibrated using all concentration data
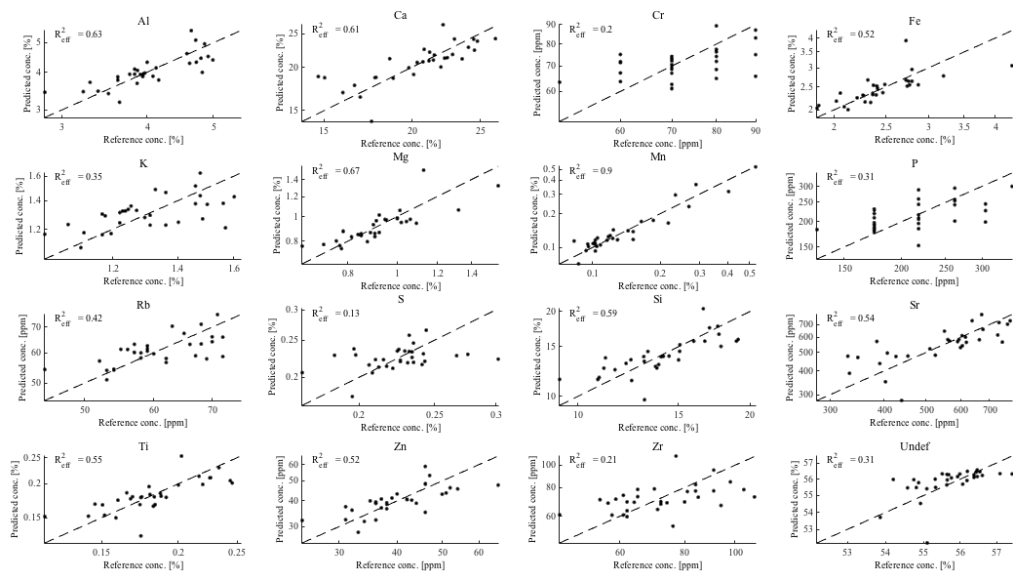
Appendix A Table 3 Cross-plot (1) – Kazput carbonate bulk-rock data used to calibrate XRF data from all three cores
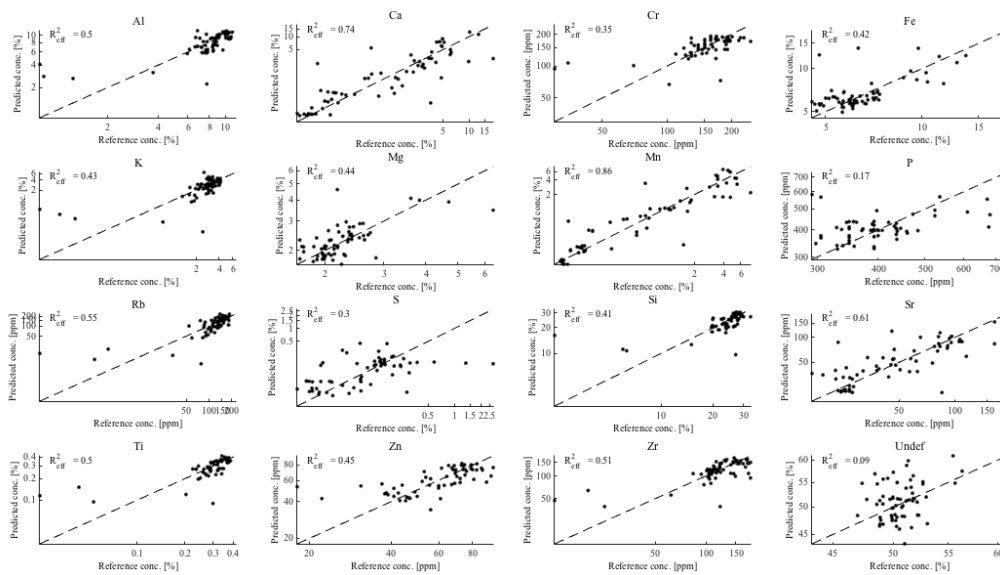
Appendix A Table 3 Cross-plot (2) – Kazput mudstone bulk-rock data used to calibrate XRF data from all three cores
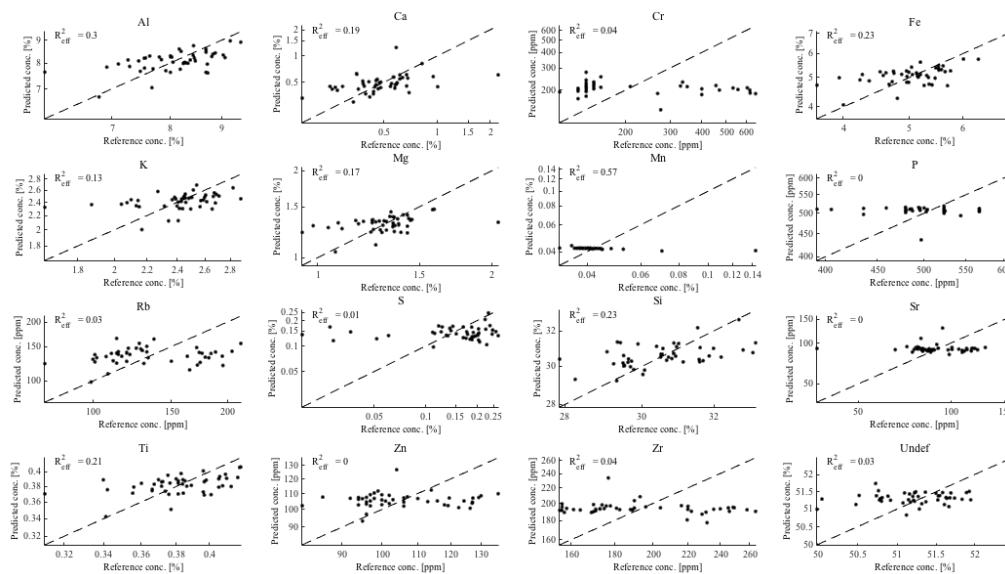
Appendix A Table 3 Cross-plot (3) – Meteorite Bore Member bulk-rock data used to calibrate XRF data from all three cores
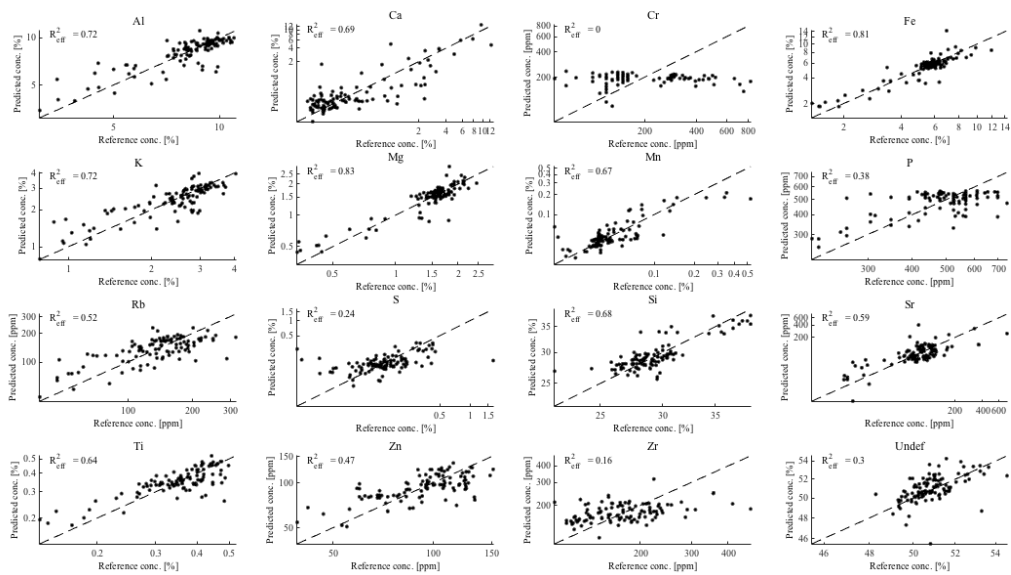
Appendix A Table 3 Cross-plot (4) – Kungarra Formation bulk-rock data used to calibrate XRF data from all three cores
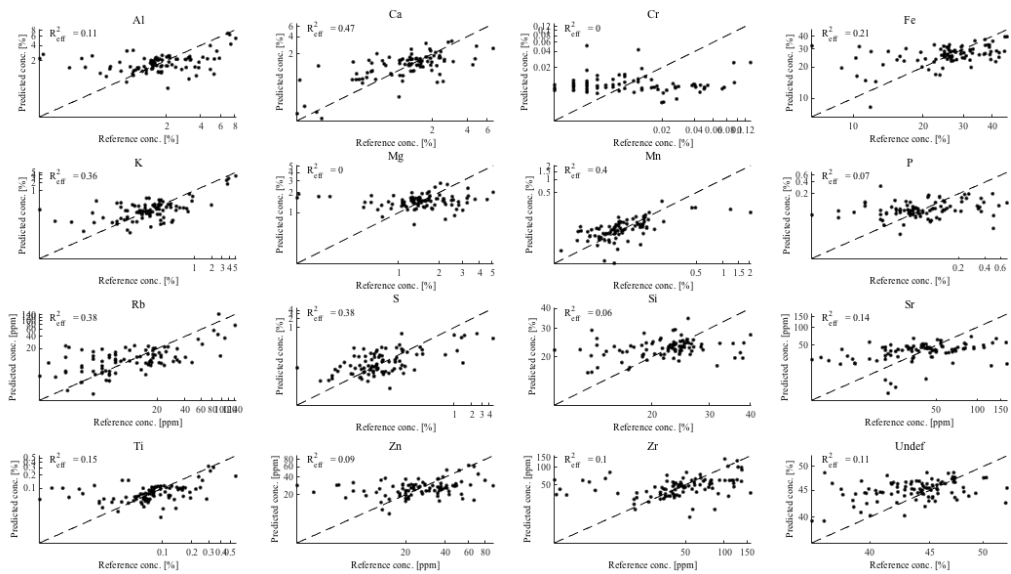
Appendix A Table 3 Cross-plot (5) – Boolgeeda Iron Formation bulk-rock data used to calibrate XRF data from all three cores
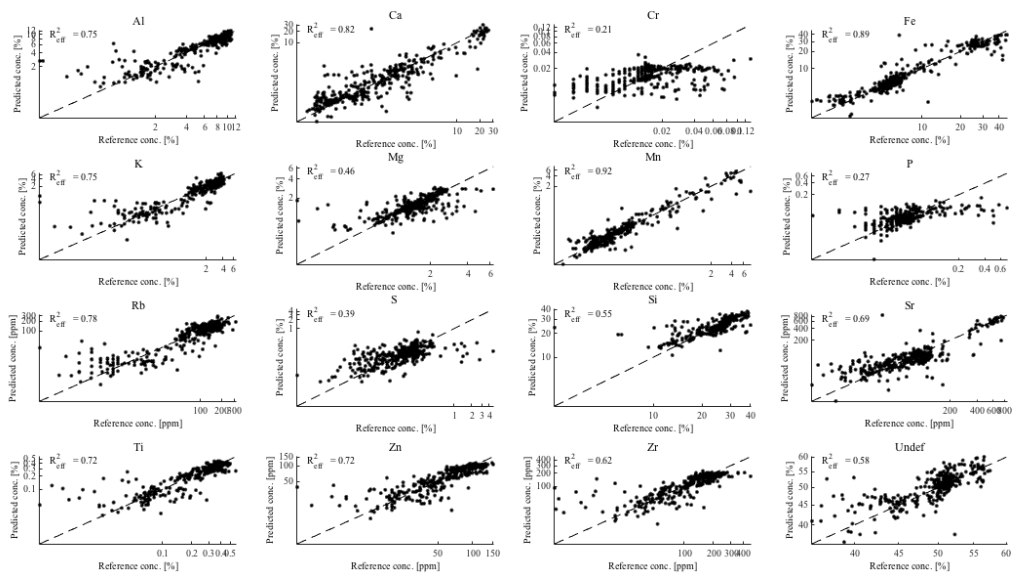
Appendix A Table 3 Cross-plot (6) – All XRF data calibrated using all concentration data

Element/Method-R^2	(1)	(2)
Al	0.76	0.75
Ca	0.84	0.82
Cr	0.53	0.21
Fe	0.87	0.89
K	0.81	0.75
Mg	0.4	0.46
Mn	0.9	0.92
Ni	0.78	-
P	0.29	0.27
Rb	0.82	0.78
S	0.49	0.39
Si	0.62	0.55
Sr	0.76	0.69
Ti	0.73	0.72
Zn	0.74	0.72
Zr	0.66	0.62
Undef	0.55	0.58

1) All XRF data calibrated using all concentration data (no "contaminated" points included)
2) All XRF data calibrated using all concentration data (with "contaminated" points included)

*** Notably, the global XRF calibrations for both the "contaminated" and non-"contaminated" datasets show similar fits. This may suggest the program is able to statistically eliminate contaminated calibration points. However, it may be safer just to use the ACTLABS data moving forward.
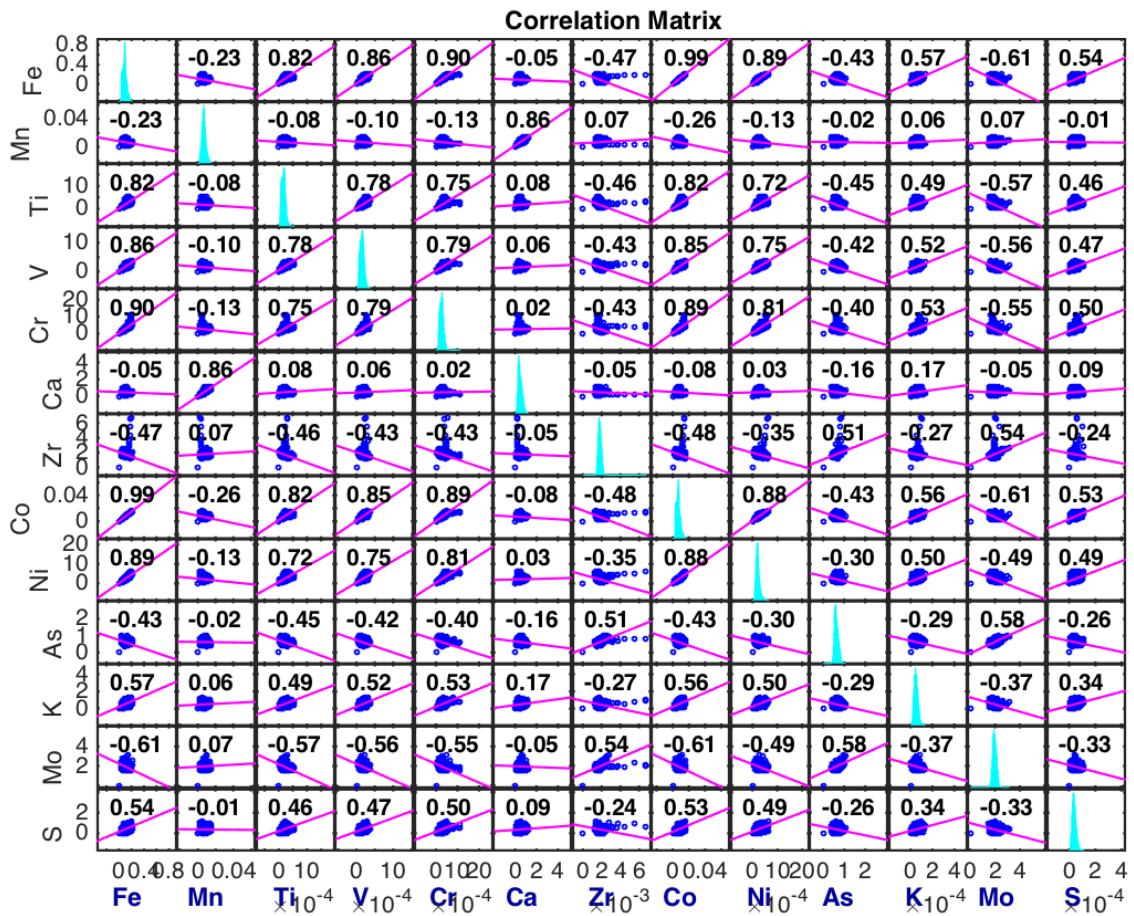
Appendix A Figure 1. Correlation matrix for XRF map of sample T1-150.73-150.68 A (B1). Manganese shows a strong correlation with Ca, but no other elements.
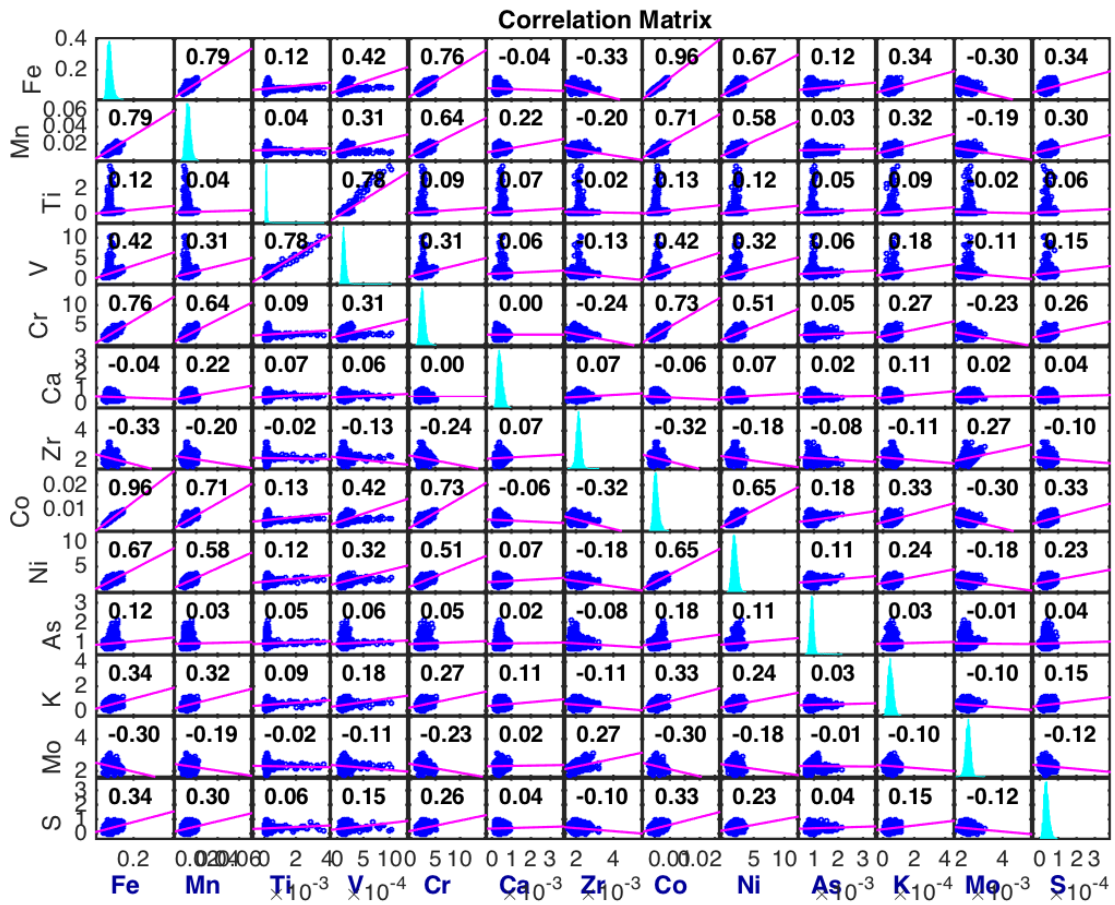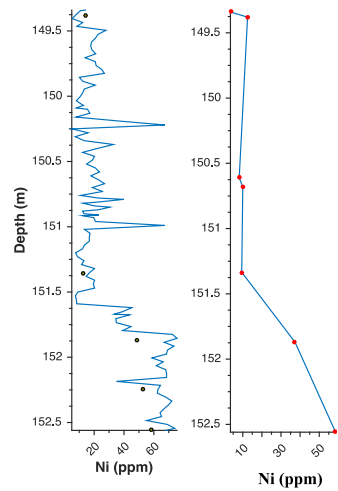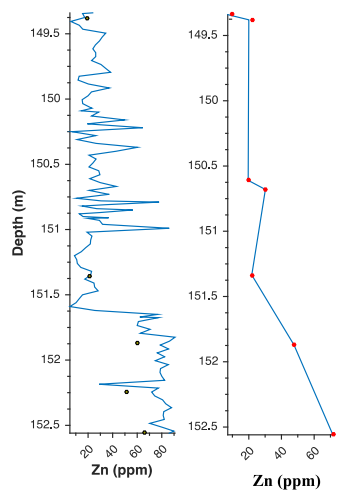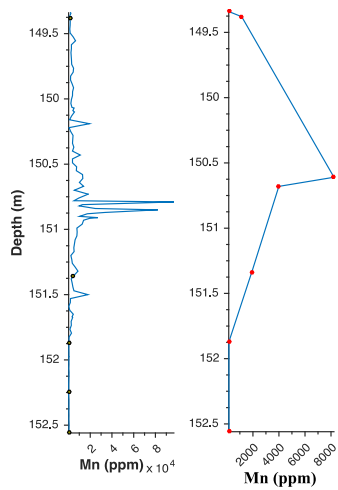
Appendix A Figure 2. Correlation matrix for XRF map of sample T1-150.68-150.63 B (B1). Noticeably higher correlation with Fe, V, Cr, Co, Ni, K, and S.
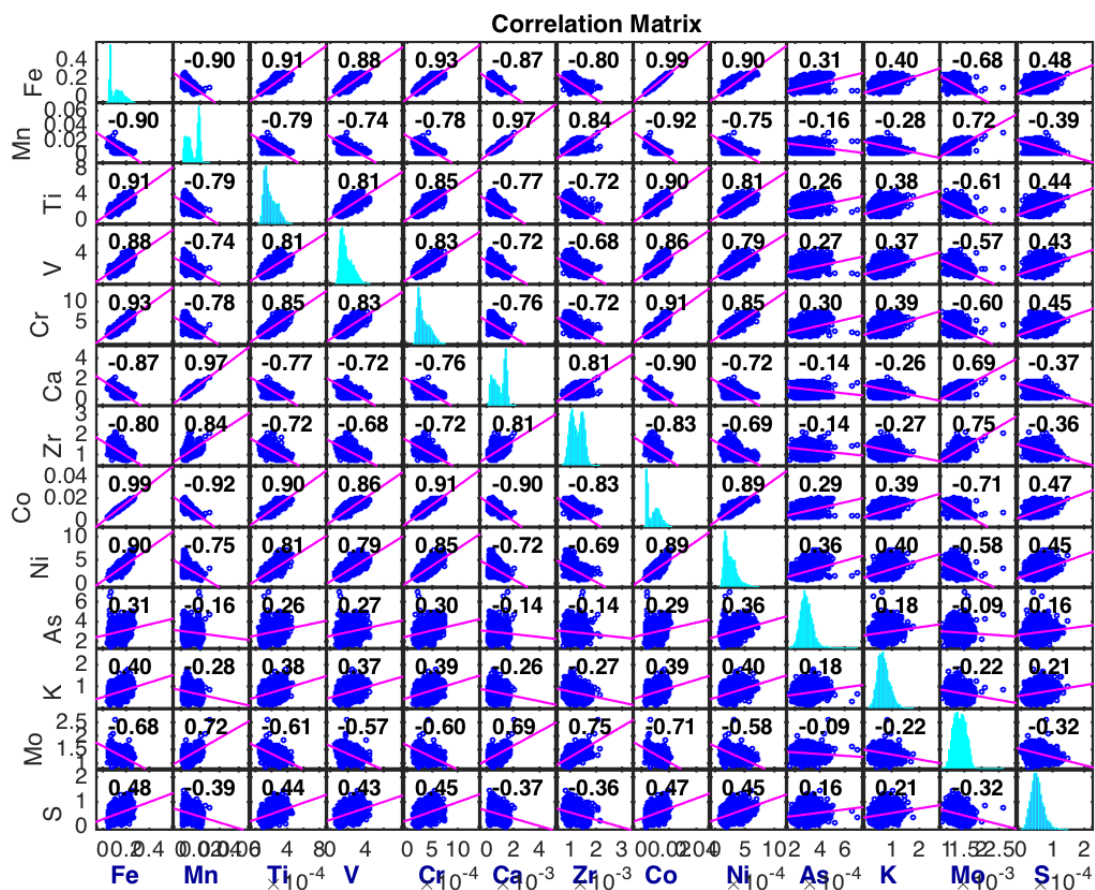
Appendix A Figure 3. Correlation matrix for sample XRF map of sample T1-130.01 (B2).

Appendix A Figure 4. Correlation matrix for XRF maps of sample T3-159.2 (K2).

Appendix A Figure 5. Comparison of XRF and bulk=rock chemistry depth profiles through Mn enriched interval B1. Profiles produced using calibrated XRF data are on the left, while bulk-rock geochemical profiles are on the right. Note the significantly higher resolution of the XRF profiles. Further, note how sparse sampling of bulk-rock samples could lead to the misidentification of the depth at which peak Mn concentration occurs.